
**Proceedings for the 31st Annual Conference of the Society
for Astronomical Sciences**



**Joint Meeting of
The Society for Astronomical Sciences
The American Association of Variable Star Observers**

Society for Astronomical Sciences

Symposium on Telescope Science

Editors:
Brian D. Warner
Robert K. Buchheim
Jerry L. Foote
Dale Mais

May 22-24, 2012
Big Bear Lake, CA

Disclaimer

The acceptance of a paper for the SAS proceedings can not be used to imply nor should it be inferred as an endorsement by the Society for Astronomical Sciences or the American Association of Variable Star Observers of any product, service, or method mentioned in the paper.

Published by the Society for Astronomical Sciences, Inc.
Rancho Cucamonga, CA

First printing: May 2012

Photo Credits:

Front Cover: NGC 7293, Alson Wong

Back Cover: Sagittarius Milky Way, Alson Wong

Table of Contents

PREFACE	I
----------------	----------

CONFERENCE SPONSORS	II
----------------------------	-----------

SYMPOSIUM SCHEDULE	III
---------------------------	------------

PRESENTATION PAPERS	1
----------------------------	----------

PHOTOMETRY OF HUBBLE'S FIRST CEPHEID IN THE ANDROMEDA GALAXY, M31	3
<i>BILL GOFF, MATT TEMPLETON, RICHARD SABO, TIM CRAWFORD, MICHAEL COOK</i>	

BK LYNCIS: THE OLDEST OLD NOVA? OR: ARCHAEO-ASTRONOMY 101	7
<i>JONATHAN KEMP, JOE PATTERSON, ENRIQUE DE MIGUEL, GEORGE ROBERTS, TUT CAMPBELL, FRANZ-J. HAMBSCH, TOM KRAJCI, SHAWN DVORAK, ROBERT A. KOFF, ETIENNE MORELLE, MICHAEL POTTER, DAVID CEJUDO, JOE ULOWETZ, DAVID BOYD, RICHARD SABO, JOHN ROCK, ARTO OKSANEN</i>	

PHOTOMETRIC MONITORING BY AMATEURS IN SUPPORT OF A YY GEM PROFESSIONAL OBSERVING PROJECT	17
<i>BRUCE L. GARY, DR. LESLIE H. HEBB, JERROLD L. FOOTE, CINDY N. FOOTE, ROBERTO ZAMBELLI, JOAO GREGORIO, F. JOSEPH GARLITZ, GREGOR SRDOC, TAKESHI YADA, ANTHONY I. AYIOMAMITIS</i>	

THE LOWELL AMATEUR RESEARCH INITIATIVE	25
<i>DEIDRE ANN HUNTER, JOHN MENKE, BRUCE KOEHN, MICHAEL BECKAGE, KLAUS BRASCH, SUE DURLING, STEPHEN LESHIN</i>	

LUNAR METEOR IMPACT MONITORING AND THE 2013 LADEE MISSION	29
<i>BRIAN CUDNIK</i>	

FIRST ATTEMPTS AT ASTEROID SHAPE MODELING	37
<i>MAURICE CLARK</i>	

DIURNAL PARALLAX DETERMINATIONS OF ASTEROID DISTANCES USING ONLY BACKYARD OBSERVATIONS FROM A SINGLE STATION	45
<i>EDUARDO MANUEL ALVAREZ, ROBERT K. BUCHHEIM</i>	

ON THE MAXIMUM AMPLITUDE OF HARMONICS OF AN ASTEROID LIGHTCURVE	59
<i>ALAN HARRIS</i>	
PV CEPHEI AND GYULBUDAGHIAN'S VARIABLE NEBULA	65
<i>DAVID BOYD</i>	
WHY VISUAL OBSERVATIONS OF MU CEPHEI ARE IMPORTANT	69
<i>DAVID G. TURNER</i>	
ROAD (REMOTE OBSERVATORY ATACAMA DESERT): INTENSIVE OBSERVATIONS OF VARIABLE STARS	75
<i>FRANZ-JOSEF HAMBSCH</i>	
ER URSAE MAJORIS: A DWARF NOVA WITH SURPRISES	79
<i>ENRIQUE DE MIGUEL, JOE PATTERSON, JONATHAN KEMP, WILLIAM STEIN, GEORGE ROBERTS, T. CAMPBELL, FRANZ-J. HAMBSCH, TOM KRAJCI, SHAWN DVORAK, ROBERT A. KOFF, ETIENNE MORELLE, MICHAEL POTTER, DAVID CEJUDO, STEVE BRADY, KENNETH MENZIES</i>	
SMALL TELESCOPE SPECTROSCOPY OF EPSILON AURIGAE	89
<i>JEFFREY L. HOPKINS</i>	
OBSERVATIONS USING A BESPOKE MEDIUM RESOLUTION FAST SPECTROGRAPH	97
<i>JOHN MENKE</i>	
HIGH RESOLUTION SPECTROSCOPY FOR THE AMATEUR: EXPERIENCES WITH THE LHIRES III SPECTROGRAPH	105
<i>STANLEY A. GORODENSKI</i>	
EXTREMELY LOW-COST POINT-SOURCE SPECTROPHOTOMETRY (ELCPSS)	113
<i>JOHN BEAVER, CHARLES CONGER</i>	
SPECTROSCOPIC ANALYSIS OF ALGOL DURING ECLIPSE CYCLE	121
<i>JONATHAN BOYD, KODIAK DARLING, ELISE SPARKS, LAJEANA WEST, DOUGLAS WALKER</i>	
A FRESH LOOK AT THE ALGOL-LIKE ECLIPSING BINARY, AO SER	127
<i>KEVIN B. ALTON, ANDREJ PRŠA</i>	
THE LIGHT AT NIGHT MAPPING PROJECT: LAN MAP 1, THE TUCSON BASIN	139
<i>E.R. CRAINE, B.L. CRAINE, P.R. CRAINE, E.M. CRAINE</i>	
OBSERVING DOUBLE STARS	147
<i>RUSSELL M. GENET, B.J. FULTON, FEDERICA B. BIANCO, JOHN MARTINEZ, JOHN BAXTER, MARK BREWER, JOSEPH CARRO, SARAH COLLINS, CHRIS ESTRADA, JOLYON JOHNSON, AKASH SALAM, VERA WALLEN, NAOMI WARREN, THOMAS C. SMITH, JAMES D. ARMSTRONG, STEVE MCGAUGHEY, JOHN PYE, KAKKALA MOHANAN, REBECCA CHURCH</i>	
AMATEUR IMAGE PIPELINE PROCESSING USING PYTHON PLUS PYRAF	159
<i>WAYNE GREEN</i>	

HIGH TIME RESOLUTION ASTRONOMY OR HIGH SPEED PHOTOMETRY <i>GARY A. VANDER HAAGEN</i>	165
PHOTON COUNTING – ONE MORE TIME <i>RICHARD H. STANTON</i>	177
TRACKING BOLIDES, 3D VISUALIZATION AND DATA <i>THOMAS G. KAYE, ROBERT CRAWFORD, MARK BOWLING, JOHN KALAS</i>	185
TOOLS AND TECHNIQUES FOR MEASURING ASTEROID OCCULTATIONS WITH DSLR AND CCD CAMERAS <i>JOHN E. HOOT</i>	191
<u>PAPERS WITHOUT PRESENTATION AND POSTERS</u>	<u>201</u>
A VIRTUAL ASTRONOMICAL RESEARCH MACHINE IN NO TIME (VARMINT) <i>JOHN BEAVER</i>	203
THE CONFUSING CASE OF 16666 LIROMA <i>ROBERT K. BUCHHEIM, JOHN RUTHROFF</i>	209
STUDENT PROJECT AND CURRICULUM BASED ON LIGHT AT NIGHT DATA COLLECTION <i>ERIN M. CRAINE, JENNIFER C. DEBENEDETTI</i>	215
ENHANCING THE EDUCATIONAL ASTRONOMICAL EXPERIENCE OF NON-SCIENCE MAJORS WITH THE USE OF AN IPAD AND TELESCOPE <i>ROBERT M. GILL, MICHAEL J. BURIN</i>	219
THE ROTATIONAL PERIOD OF THE SUN USING THE DOPPLER SHIFT OF THE HYDROGEN ALPHA SPECTRAL LINE <i>ROBERT M. GILL</i>	225
FAST SPECTROMETER CONSTRUCTION AND TESTING <i>JOHN MENKE</i>	229
ADILS: AN AMATEUR DUAL IMAGING LITTROW SPECTROGRAPH <i>WAYNE GREEN</i>	233
HIGH ACCURACY RA/DEC ENCODERS FOR A CA 1890 GEM <i>WAYNE GREEN</i>	234
A SINGLE BEARM POLARIMETER <i>JERRY D. HORNE</i>	235

Preface

We welcome the American Association of Variable Star Observers (AAVSO) to the 31st annual SAS Symposium on Telescope Science. The first joint meeting between the Society for Astronomical Sciences and the AAVSO, held in 2009, was a tremendous success, bringing in presenters from around the world and in record numbers. Current plans are for the AAVSO to make this a biannual affair, merging its annual Spring meeting in even-numbered years with the SAS Symposium. The SAS Board of Directors is looking forward to a long and rewarding partnership that brings together some of the world's best backyard and professional astronomers to share their experiences and expertise in the name of promoting astronomical research to advance our knowledge of the Universe.

Not everyone wants to give a presentation but they still want to contribute to the Symposium by submitting a paper for the proceedings. So, this year, partly because of the unprecedented number of papers received, the proceedings include a section not just for poster papers but "papers without presentation." We may try to do this in future years as well but, as always, our first goal is to get presenters who also submit papers. The live presentations are vital for spurring discussion both during Q&A and in groups outside the formal paper sessions.

It takes many people to have a successful conference, starting with the Conference Committee. This year the regular committee members are:

Lee Snyder	Robert D. Stephens
Robert Gill	Jerry L. Foote
Cindy Foote	Margaret Miller
Brian D. Warner	Robert K. Buchheim
Dale Mais	

There are many others involved in a successful conference. The editors take time to note the many volunteers who put in considerable time and resources. We also thank the staff and management of the Northwoods Resort in Big Bear Lake, CA, for their efforts at accommodating the Society and our activities.

Membership dues alone do not fully cover the costs of the Society and annual conference. We owe a great debt of gratitude to our corporate sponsors: Sky and Telescope, Software Bisque, Santa Barbara Instruments Group, PlaneWave Instruments, Apogee Instruments, Inc., and DC-3 Dreams. Thank you!

Finally, there would be no conference without our speakers and poster presenters and those sitting attentively in the audience (you're not doing your email right now, are you?). We thank them for making this one of the premiere pro-am events in the world.

Brian D. Warner
Robert K. Buchheim
Jerry L. Foote
Dale Mais

2012 April 27

Conference Sponsors

The conference organizers thank the following companies for their significant contributions and financial support. Without them, this conference would not be possible.



Apogee Instruments, Inc.

Manufacturers of astronomical and scientific imaging cameras
<http://www.ccd.com>



Sky Publishing Corporation

Publishers of Sky and Telescope Magazine
<http://skyandtelescope.com>



Software Bisque

Developers of TheSky Astronomy Software and the
Paramount Telescope Mount
<http://www.bisque.com>



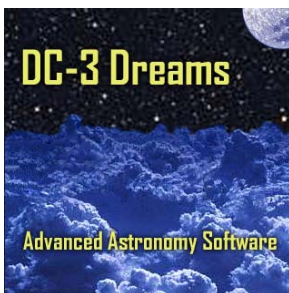
Santa Barbara Instruments Group

Makers of astronomical instrumentation
<http://www.sbig.com>



PlaneWave Instruments

Makers of the CDK line of telescopes
<http://www.planewaveinstruments.com:80/index.php>



DC-3 Dreams Software

Developers of ACP Observatory Control Software
<http://www.dc3.com/>

Symposium Schedule

The schedule is subject to change without notice.

Meeting Courtesies

Please turn off cell phones, pagers, and alarms during presentations.

Please be kind to the presenters and wait until breaks to check your email and browse the Internet. Yeah, we know.

Please be considerate of those in the meeting room near the wall with the vendor's room. If visiting the vendor's room during presentations, please keep voices down and do not use the direct entrance between the vendor's and meeting rooms. Enter the meeting room from the hallway.

If you do not want your presentation to be recorded (video/audio) and/or not posted on the SAS web site, please let us know before your talk begins.

Thanks!

SAS Program Committee

2012 SAS/AAVSO Joint Meeting Schedule

Wednesday 5/23

<i>Coffee/Registration</i>		08:00	08:30	
<i>Welcome</i>	<i>Lee Snyder and Arne Henden</i>	08:30	09:00	
Pro-Am Collaborations				
Bill Goff	Photometry of Hubble's First Cepheid in the Andromeda Galaxy, M31	09:00	09:20	
Joe Patterson	The Tortured Accretion Disk of BK Lyncis	09:20	09:40	
Bruce Gary	Photometric Monitoring of YY Gem	09:40	10:00	
Deidre Hunter	The Lowell Amateur Research Initiative	10:00	10:20	
<i>Coffee Break</i>		10:20	10:40	20 MINUTES
Solar System Research				
Brian Cudnik	Lunar Meteor Impacts	10:40	11:00	
Maurice Clark	Shape Modeling of Three Asteroids	11:00	11:20	
Eduardo Alvarez	Diurnal parallax determinations of asteroid distance	11:20	11:40	
Alan W. Harris	On the maximum amplitude of harmonics of an asteroid lightcurve	11:40	12:00	
<i>Lunch</i>		12:00	13:40	100 MINUTES
Variable Stars				
David Boyd	PV Cephei and Gyulbudaghian's Variable Nebula	13:40	14:00	
David Turner	Why Visual Observations of Mu Cephei are Important	14:00	14:20	
Josch Hamsch	Remote Observations of Variable Stars	14:20	14:40	
Enrique de Miguel	ER Uma: A Dwarf Nova with Surprises	14:40	15:00	
<i>Coffee</i>		15:00	15:20	20 MINUTES
Campaign Champions				
Tim Puckett	Supernova Searching	15:20	15:40	
Jeffrey Hopkins	Small Telescope Spectroscopy of epsilon Aurigae	15:40	16:00	
<i>Sponsor Infomercials</i>		16:00	17:00	
<i>AAVSO Membership Meeting</i>		19:00	21:00	

Thursday 5/24

<i>Coffee</i>		08:00	08:40	
Spectroscopy and Such				
John Menke	Observations Using a Medium Resolution Home-built Fast Spectrograph	08:40	09:00	
Stan Gorodenski	High Resolution Spectroscopy for the Amateur	09:00	09:20	
John Beaver	Extremely Low-Cost Point-Source Spectrophotometry (ELCPSS)	09:20	09:40	
Doug Walker	Low Resolution Spectroscopy of the Eclipsing Binary Star Algol	09:40	10:00	
Kevin B. Alton	A Fresh Look at the Algol-like Eclipsing Binary AO Ser	10:00	10:20	
<i>Coffee</i>		10:20	10:40	20 MINUTES
Special Projects I				
Eric Crane	The Light at Night Mapping Project	10:40	11:00	
Russ Genet	CCD Double Star Observations	11:00	11:20	
Wayne Green	Imaging Pipeline Processing using Python plus PyRAF	11:20	11:40	
Gary Vander Haagen	High Speed Photometry	11:40	12:00	
<i>Group Photo / Lunch</i>		12:00	14:00	2 HOURS
Special Projects II				
Richard Stanton	Photo Counting - One More Time	14:00	14:20	
Tom Kaye	Tracking Bolides, 3D Visualization and Data	14:20	14:40	
John E. Hoot	DSLR and CCD Occultation Methods	14:40	15:00	
<i>Good Night, and Good Luck</i>		15:20	15:30	
<i>Dinner</i>		17:30		
<i>Banquet Speaker</i>	<i>Dava Sobel</i>	19:00	20:00	

Presentation Papers

Photometry of Hubble's First Cepheid in the Andromeda Galaxy, M31

Bill Goff
AAVSO
13508 Monitor Lane
Sutter Creek, CA 95685
b-goff@sbcglobal.net

Matt Templeton
AAVSO
49 Bay State Rd.
Cambridge, MA 02138, USA
Matthewt@aavso.org

Richard Sabo
AAVSO
Richard@theglobal.net

Tim Crawford
AAVSO
tcarchcape@yahoo.com

Michael Cook
AAVSO
michaeljcook@rogers.com

Abstract

In the 1920s Hubble discovered a variable star in the Andromeda Galaxy, M31 which later was revealed to be a Cepheid type variable. Hubble's observations confirmed that M31 was indeed a remote star system separate from our own Milky Way. We present here recent photometry of this object made during 2010 and 2011. These observations were made by members of the AAVSO at the request of the Space Telescope Science Institute's Heritage Project. Over 300 Rc, V and unfiltered observations have been made. These are the first observations in current times to establish a period for the object. The period of this Cepheid as measured here is in agreement with the earlier data from 1920s and 1950s.

1. Introduction

Edwin Hubble settled one of astronomy's biggest puzzles in 1925 when he published light curves of Cepheid variables he had located in the Andromeda Galaxy, M31. At the time astronomy was at a crossroads. Many astronomers believed that the 'nebulae' in the night sky were just parts of our own Milky Way Galaxy, and others believed they were external objects far away. There wasn't a good way to measure their distances

Hubble began monitoring M31 and a few other galaxies with the largest telescope in the world of the time, the 100-inch Hooker telescope on Mt. Wilson in California. The "great telescope" as Hubble re-

ferred to it, was capable of resolving many individual stars in that galaxy (Hubble, 1936).

Hubble's work hinged on the recently revealed relationship between period and luminosity for Cepheid variables. Henrietta Leavitt had surveyed hundreds of variables in the Magellanic Clouds and noticed that the brighter Cepheids had longer periods. Since they were nearly all at the same distance it meant that absolute luminosity could be gauged. This relationship later became known as the Leavitt Law.

Calibrating the Leavitt Law had significant interest and difficulties. There are very few Cepheids close enough for parallax measurements. Shapely used Cepheids in globular clusters, whose distances were known through other means, to establish what was seen as a good calibration. Hubble utilized this

calibration and noted that further revisions were expected to be of minor importance. After Hubble published his work on the galactic distance scale, it was discovered there are two types of Cepheids. The cluster Cepheids used by Shapely were older, smaller and fainter than the brighter classic Cepheids in the disk of the galaxy and recalibrating the Leavitt Law caused the size of the universe to double! (Percy, 2007).

2. Observations

The Space Telescope Science Institute's Heritage Project drew AAVSO to this object. They were interested in re-imaging the target with Hubble's namesake, Hubble Space Telescope, as a tribute to his achievement and wanted to know if a current ephemeris existed. As the object had not been observed by the AAVSO, an Alert Notice (Waagan, 2010) was published to invite observations so that a light curve could be established. The object was reported at 19th magnitude by Hubble so, while a challenging target, it is not out of reach for amateurs with CCD cameras and large-aperture scopes. Over the course of the next several months, 214 observations were made via CCD imaging. Most all observations were done with Cousin R filter, but some were done with a standard V filter. Total exposure times were normally in the 60-minute range for one observation, which were normally stacked groups of shorter exposures. Images were processed using standard available software packages and techniques such as flat-fielding and dark subtraction. Results were then uploaded to the AAVSO database.

ObsCode	Name	Location	Obs
GFB	Goff	California	66
CMIA	Cook	Ontario, Ca	12
SRIC	Sabo	Montana	7
CTX	Crawford	Oregon	3

Observers for the 2011 data. The 2010 observer list is reported by Templeton et al. (2011).

The observations are not on a standard photometric system though the observers did use a standard set of comparison stars established by the AAVSO and similar filters. This required that the observation be adjusted to a common zero point. Templeton (2011) reported on a technique to make these adjustments to the 2010 data for the object.

Observations continued in the 2011 season by four observers. They made an additional 89 observations all in Cousins R; and they too were processed as above and added to the AAVSO database.

3. Analysis of 2010 Data

As noted above, Templeton *et al.* (2011) had reported on the analysis of the 2010 data and the ephemeris for the object. A Fourier function had been used with a result of 31.4 ± 0.1 day period. This period was used to establish the ephemeris needed by the Heritage Project.

In order to evaluate the two combined seasons of data, we first needed to insure we agreed with Templeton's result. The 2010 data were downloaded from AAVSO and then divided into separate sets by observer. One observer's (GFB) data were loaded first into Peranso software, as it covered more than two cycles of variation. Then the second observer's (HQA) data were loaded and used for a standard magnitude. The two sets were adjusted by using a Fourier phase diagram which overlays the data onto one cycle, which made the differences appear obvious. Binning the data by the day also helped. The program reports the standard deviations of the bins so those days where the value was high indicated differences between the two sets. After the two sets were in agreement, the remaining sets were loaded one at a time and adjusted as well. The 2010 phased data are shown in Figure 1.

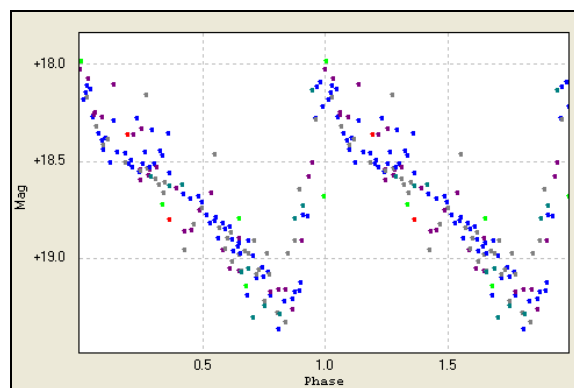


Figure 1. Phased 2010 data. All observations are folded onto two phases.

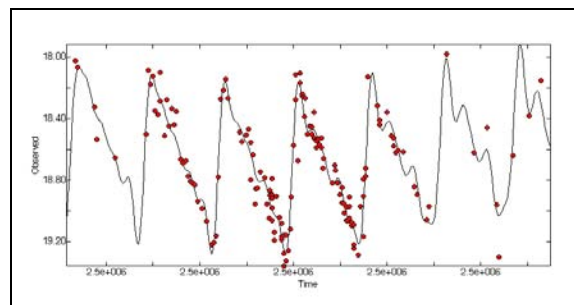


Figure 2. Light curve for 2010 data. Period is shown as 31.38 ± 0.09 days.

We used Period04 software for our Fourier analysis. The program uses a discrete Fourier Transform algorithm and provides least squares fitting for a number of frequencies. Fitting the 2010 data resulted in a period of 31.38 ± 0.09 , which we considered a good result. Our light curve for the 2010 data is shown on Figure 2. The light curve is not smooth due to the fitting of multiple frequencies.

4. Analysis of 2011 Data

The same process was repeated with the 2011 data. One observer's (GFB) data set was first loaded then the others loaded individually and zero pointed using the phase diagram and binning until all were loaded. The phase diagram is shown in Figure 3.

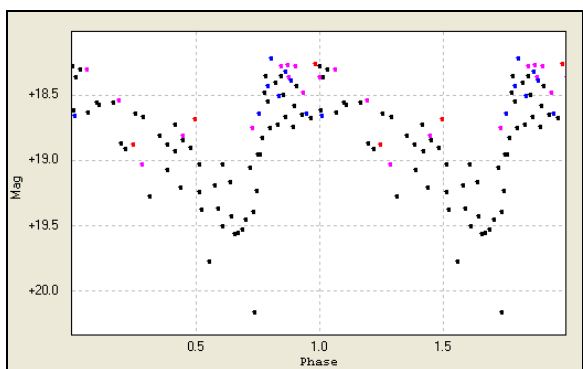


Figure 3. Phased 2011 data. All observations are folded onto two phases.

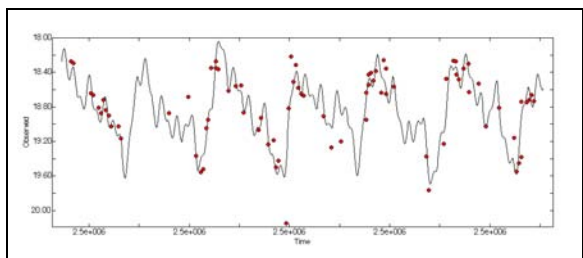


Figure 4. Light curve for 2011 data. Period is shown as 31.26 ± 0.26 days.

The 2011 data set is a smaller one. Fourier analysis and fitting the data with the Period04 program resulted in a period of 31.26 ± 0.26 d. The light curve is shown in Fig. 4. The reduced observations have made it appear more erratic and the error is considerably higher.

5. Combined 2010-2011

The goal of continuing the observations through the second year was to further refine the period over the longer time span. Having two years of data now at hand, we imported them both into one session with

the Period04 software. The Fourier analysis and fitting proceeded as before, and as a final result, the period was reported as 31.47 ± 0.03 d. The light curve for the combined 2010-2011 data is shown on Figure 5. Templeton has suspected that by adding an additional season's observation the period error would reduce, and this appears to be true.

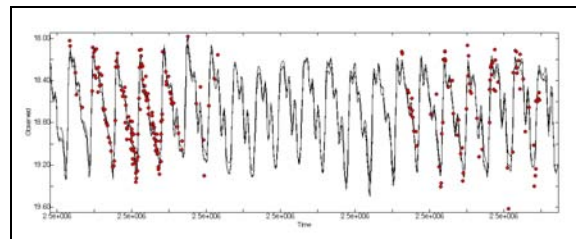


Figure 5. Light curve for combined 2010-2011 data. Period is shown as 31.47 ± 0.03 days.

6. Discussion

Templeton *et al.* (2011) noted that the first year's results were in agreement the results of Hubble and Baade done in the 1920 and 1950 and that the object is unchanged over this time span. We substantially agree that the two-year results add support to that result. We also note that Hubble's first results came from 10 years of images from a dozen observers so the greater span aided his result. Some members of the team have expressed interest in continuing with this target for another year. Gathering data on another color band would be of value as Cepheids change color during their cycle.

7. Acknowledgements

The authors would like to thank Arne Henden for his encouragement in undertaking this project during the SAS conference in May 2010. Matt Templeton's paper of 2011 set a very high benchmark for our work and his participation in this work have been essential in directing our efforts here.

8. References

- Hubble, E. (1939, 1982). *The Realm of the Nebulae*, Yale University Press, New Haven, US.
- Lenz, P., Breger, M. (2010). Period04, astronomical time series analysis software.
<http://www.univie.ac.at/tops/Period04/>
- Peranso 2010, Peranso, period analysis software.
<http://www.peranso.com/>

Hubble's First M31 Cepheid – Goff et al.

Percy, R. (2007). *Understanding Variable Stars*, Cambridge University Press, Cambridge, UK

Templeton, M., Henden, A., Goff, W., Smith, S., Sabo, R., Walker, G., Buchheim, R., Belcheva, G., Crawford, T., Cook, M., Dvorak, S., Harris, B. (2011). *PASP* **123**, 1347.

Waagen, E.O. (2010). *AAVSO Alert Notice* 422 (2010 July 16).

BK Lyncis: The Oldest Old Nova? or: Archaeo-Astronomy 101

*Jonathan Kemp
Gemini Observatory, Hilo, HI 96720
jk@155west.org*

*Joe Patterson
Department of Astronomy, Columbia University, 550 West 120th Street, New York, NY 10027
jop@astro.columbia.edu*

*Enrique de Miguel
CBA (Huelva), Observatorio del CIECEM, Matalascañas, 21076 Almonte, Huelva, Spain
edmiguel63@gmail.com*

*George Roberts
CBA (Tennessee), 2007 Cedarmont Dr., Franklin, TN 37067*

*Tut Campbell
CBA (Arkansas), 7021 Whispering Pine, Harrison, AR 72601*

*Franz-J. Hambsch
CBA (Mol), Oude Bleken 12,B-2400 Mol, Belgium*

*Tom Krajci
CBA (New Mexico), PO Box 1351 Cloudcroft, NM 88317*

*Shawn Dvorak
CBA (Orlando), AAVSO, 1643 Nightfall Dr., Clermont, FL 34711*

*Robert A. Koff
CBA (Colorado), Antelope Hills Observatory, 980 Antelope Drive West, Bennett, CO 80102*

*Etienne Morelle
CBA (France), Sirene ObservatoryLagarde d'Apt, France*

*Michael Potter
CBA (Baltimore), 3206 Overland Ave., Baltimore, MD 21214*

*David Cejudo
CBA (Madrid), Observatorio El Gallinero, El Berrueco, Madrid, Spain*

*Joe Ulowetz
CBA (Illinois), 855 Fair Lane, Northbrook, IL 60062*

*David Boyd
CBA (Wantage), 5 Silver Lane, West Challow, Wantage, OX12 9TX, United Kingdom*

*Richard Sabo
CBA (Montana), 2336 Trailcrest Drive, Bozeman, MT 59718*

*John Rock
CBA (Wilts), 2 Spa Close, Highworth, Swindon, Wilts SN6 7PJ, United Kingdom*

Abstract

We summarize the results of a 20-year campaign to study the light curves of BK Lyncis, a nova-like star strangely located below the 2-3 hour orbital period gap in the family of cataclysmic variables. Two “superhumps” dominate the nightly light curves – with periods 4.6% longer, and 3.0% shorter, than P_{orb} . The first appears to be associated with the star's brighter states ($V \sim 14$), while the second appears to be present throughout and becomes very dominant in the low state ($V \sim 15.7$). It's plausible that these arise, respectively, from a prograde apsidal precession and a retrograde nodal precession of the star's accretion disk. In 2011-2, the star's light curve became indistinguishable from that of a dwarf nova – in particular, that of the ER UMa subclass. No such transition has ever been observed in a cataclysmic variable. Reviewing all the star's oddities, we speculate: (a) BK Lyn is the remnant of the probable nova on 30 December 101, and (b) it has been fading ever since, but has taken ~ 2000 years for the accretion rate to drop sufficiently to permit dwarf-nova eruptions. If such behavior is common, it can explain two other puzzles of CV evolution. One: why the ER UMa class even exists (because all can be remnants of recent novae). And two: the relative space densities of short- and long-period CVs, and of known nova remnants (set by the durations of these transient phases).

1. Introduction

BK Lyncis was discovered in the Palomar-Green survey for objects with ultraviolet excess (Green *et al.*, 1986), and was listed as PG0917+342 in the preliminary catalog of cataclysmic-variable stars in that survey (Green *et al.*, 1982). A subsequent radial-velocity study confirmed the CV identification and revealed an orbital period of 107.97 minutes (Ringwald *et al.*, 1996). Two years of time-series photometry revealed “superhumps” in the star's light curve – large-amplitude waves interpreted as resulting from apsidal precession of the accretion disk (Skillman and Patterson, 1993; hereafter SP). These studies showed only small variability in the range $V = 14.5-14.7$. Thus the star became well-established as a “novalike variable”, a class which would be unremarkable, except for the star's short orbital period. Of the few hundred CVs known with orbital period below 2 hours, BK Lyn is the *only* novalike variable.

BK Lyn is also a good candidate as the “oldest old nova.” Several studies of ancient Chinese records have suggested that a nova appeared very close to its position on 101 December 30 (His, 1958; Pskovskii, 1972; Clark and Stephenson, 1977), and Hertzog (1986) concluded that BK Lyn is the remnant of Nova Lyncis 101. This would certainly qualify as the oldest old nova – far exceeding the closest challenger, CK Vul = Nova Vulpeculae 1670 (Shara *et al.*, 1985).

Such curiosities have kept BK Lyn on our observing lists for years. In this paper we report the results of many observational campaigns: spanning 20 years, and including ~ 400 nights and ~ 2500 hours of time-series photometry. Among the several re-

wards, detailed here, was the star's spectacular transformation into a *bona fide* dwarf nova in 2012.

2. Observational Techniques

Essentially all the data reported here comes from the Center for Backyard Astrophysics (CBA), a global network of telescopes cooperating in campaigns of time-series photometry of variable stars. Most of the observational techniques were discussed in the second paper of our series (SP), but the network expanded in later years to include ~ 20 telescopes, spread sufficiently over the Earth to give very long time series relatively untroubled by local weather and daily aliasing. Our typical telescope is a 35-cm reflector, equipped with a CCD camera and recording images every 60 s for many hours per night. Most of the data is unfiltered (white-light, or perhaps more correctly, “pink”, with an effective wavelength near 6000 Å) differential photometry, although we always obtain some coverage in V light to express results on a standard scale. Data from several telescopes are then spliced together to form a one-night light curve, with minimal gaps. We take advantage of overlaps in data to determine additive constants which put all our measurements on one scale (usually that of the most prolific or best-calibrated observer). These constants are usually in the range 0.01-0.05 mag, probably due to variations in transparency and camera sensitivity. Most telescopes use the same comparison star, although we also use data with other comparisons (requiring larger and more uncertain additive constants) if there is sufficient overlap. In this case we used GSC 2496-00893, which is 3.6 arcmin NE from BK Lyn. On 5

Observer		2012	2011	2005	2002	1999
TOTAL nights/hours	CBA-	157/925	58/324	19/94	42/306	34/225
Tom Krajci	New Mexico	33/214	-	-	-	-
David Cejudo	Spain (Madrid)	22/149	-	-	-	-
Enrique de Miguel	Spain (Huelva)	29/135	13/63	-	-	-
Tut Campbell	Arkansas	18/113	11/44	-	-	-
Shawn Dvorak	Florida	19/92	4/15	-	-	-
Josch Hambsch	Belgium	12/64	21/126	-	-	-
John Rock	England	6/30	-	-	-	-
David Boyd	England	2/9	-	-	-	-
Etienne Morelle	France	4/27	-	-	-	-
Joe Ulowetz	Illinois	4/16	-	-	-	-
Others		3/15	-	6/30	-	-
Arto Oksanen	Finland	-	5/15	-	-	-
Gianluca Masi	Italy	-	1/3	-	-	-
Mike Potter	Baltimore	-	3/14	-	-	-
Tonny Vanmunster	Belgium	-	-	7/36	-	2/7
Anthony Kroes	Wisconsin	-	-	4/19	-	-
Brian Martin	Alberta	-	-	2/9	9/61	-
Jerry Foote	Utah	-	-	-	17/145	-
Dave Skillman	Maryland	-	-	-	10/67	7/40
Robert Fried	Flagstaff	-	-	-	4/25	8/47
Jonathan Kemp	MDM	-	-	-	2/8	2/8
Dave Harvey	Tucson	-	-	-	-	8/80
Lasse Jensen	Denmark	-	-	-	-	7/43

Table 1. Observation Details

good nights in 2011, we measured that star to have $V = 13.897(8)$, $B-V = 0.533(10)$.

Research programs on faint stars with small telescopes often use white light, to enable high time resolution and to improve signal-to-noise. In the case of cataclysmic variables, it usually makes good astrophysical sense too, since the underlying sources of light are broad-band emitters (accretion disk, white dwarf). It is common practice to report magnitudes as “C” (or often “CV”, though we will avoid this term for obvious reasons): the result of differential photometry in clear light, added to the comparison star’s known V magnitude. This is also our practice. However, because the white-light passbands are typically $\sim 4000 \text{ \AA}$ wide, the effective wavelengths of the variable and comparison stars can easily be 500 \AA apart. Therefore, C/CV magnitudes are not V magnitudes. We nevertheless prefer the C/CV scale and use it here, because it is our natural measurement scale, and because it expresses the true changes in light very accurately.

For archival purposes, a standard V magnitude is more desirable. Our C magnitudes transform to V magnitudes via

$$\Delta V = \Delta C + 0.37 \Delta(B-V)$$

which implies $\Delta V = -0.20$ in this case, where the variable is assumed (and observed) to have $B-V$ near 0.0. The latter assumption is pretty good for the great majority of cataclysmic variables accreting at a high rate.

Atmospheric extinction is significant for us, because the program stars are usually much bluer than comparison stars (although we avoid very red stars, which are the bane of all stellar photometry). We know from experience that this differential extinction amounts to $\sim 0.04 \text{ mag/airmass}$ for most CVs. Nevertheless, in the spirit of keeping human hands off the data as much as possible, we usually make *no correction for extinction*.

The summary observing log in the five new observing seasons (adding to the two seasons reported by SP) is given in Table 1. (A “night” denotes a time-series of good quality lasting at least 3 hours.)

3. Seasonal Light Curves

During all years prior to 2011, the star lived up to its billing as a novalike variable, showing quite small excursions about a mean $V = 14.7$. This is also consistent with the snapshot *Roboscope* data reported by Ringwald *et al.* (1996), which found the star always in the range 14.6-14.7 on 116 nights in 1994 and 1995. And it’s consistent with the range (14.5-14.8) listed in the 1980s-90s versions of the General Catalogue of Variable Stars (GCVS).

However, in 2011 the star clearly had excursions to a fainter state (15.5), as well as a brighter state (13.5). This seasonal light curve is shown in the upper frame of Figure 1. In 2012, the variations were closely monitored over a long baseline, and revealed a pattern which bore all the earmarks of a dwarf-nova – in particular, a dwarf nova of the ER UMa class. This is shown in the middle frame of Figure 1.

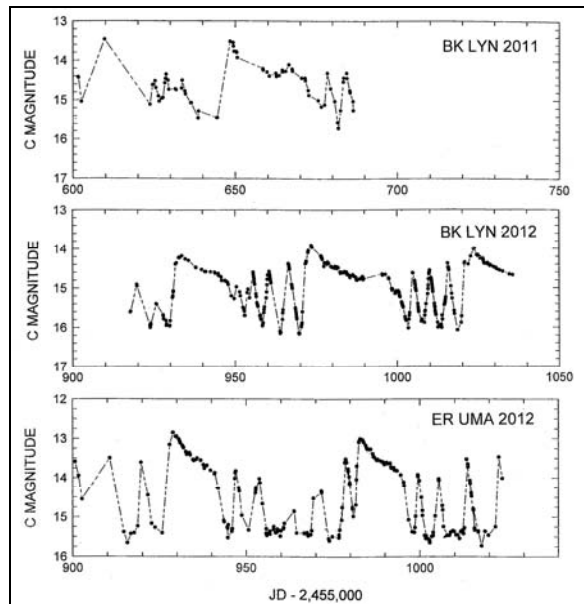


Figure 1. *Top*: BK Lyn 2011 light curve. For the first time, the star showed bright and faint states. *Middle*: BK Lyn 2012 light curve, showing the well-defined “ER UMa” pattern of variability. *Bottom*: the contemporaneous 2012 light curve of ER UMa – apparent quite a close relative of BK Lyn. The two stars also show great similarity in their complex, yet virtually identical, pattern of superhumps. In this figure, all points are averages over 1-3 superhump cycles.

In fact, by coincidence we were simultaneously carrying out a long monitoring campaign on ER UMa itself, and that seasonal light curve was practically indistinguishable – even in small details – from that of BK Lyn in 2012. This is shown in the lower frame of Figure 1. In both cases, apparent superoutbursts occurred every 40 days, followed by smaller excursions – possibly “normal” outbursts – repeating every 4-5 days. Furthermore, as will be discussed in the next section, the two stars revealed a complex and identical morphology of periodic signals (positive and negative superhumps). Within the limits of data now available, it appears that BK Lyn, after ~30 years of living as a novalike variable, became a dwarf nova in 2011-2.

4. Nightly and Spliced Light Curves

Our main program was to study the time series for periodic signals. The first two seasons have been published (SP: 1992 and 1993). BK Lyn then stayed always near $V=14.6$, and showed rather stable waves with a period slightly exceeding P_{orb} : a “positive superhump”. The full amplitude was ~0.07 mag, and the period excess was 4.6%, fairly typical of superhumps in CVs of comparable P_{orb} .

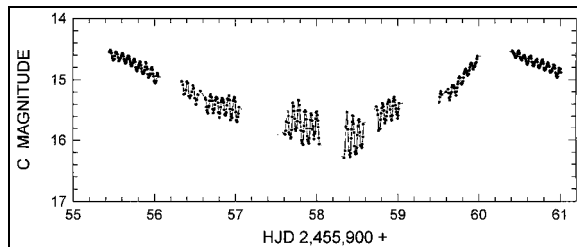


Figure 2. Five nights in 2012, showing the basic pattern of the negative superhump: large amplitude when the star is faint and small amplitude when the star is bright. The amplitude is roughly constant in intensity units. Points are 10-minute averages over the original 1-minute integrations.

Later years showed a much stronger signal, which we illustrate in Figure 2, a 4-day segment obtained in 2012. This dominated all the later data (1999-2012), and was especially strong, approaching 0.6 mag, when the star became faint. In this section, we report on this and other signals in the various years’ light curves.

Throughout this paper, we adopt a date convention of truncated Julian dates (“JD” = true JD – 2,400,000), and a frequency convention of cycles $d^{-1} = c/d$ (for compactness, and as the natural unit of frequency in programs affected by daily aliasing). Since this paper is equally a story of classical and dwarf novae, we also need a convention for describing their shenanigans: classical novae have *eruptions*, whereas dwarf novae will be described as having “outbursts” or “maxima”. Finally, we use the term *novalike* to describe noneruptive and nonmagnetic CVs whose spectrum, excitation, and M_V are similar to the prototype, UX Ursae Majoris. This is the most common use of the term, although some authors use it more expansively – to describe any CV not known to be a dwarf nova, old nova, or magnetic.

4.1 1999 Coverage

The 1999 coverage spanned 26 days, with good instrumental magnitudes and a dense segment during JD 51218-32. The power spectrum of this segment is shown in the upper frame of Figure 3. The dominant signals, by far, occur at 0.400(11) and 13.738(9) c/d; these are sensibly phase-stable over the 26 days, and have full amplitudes – respectively – of 0.17 and 0.13 mag. After subtracting these two powerful signals, the time series shows weaker but significant features at 12.770(10) and 25.560(11) c/d. Shown in the lower frame of Figure 3, these latter signals are apparently a manifestation of the positive superhump, familiar from 1992/3. The strong signals are new, and are very likely manifestations of a “negative superhump”, a fairly common phenomenon in CVs of

short P_{orb} and high accretion rate. The mean waveforms are shown in the inset figures. The negative superhump is closely sinusoidal, while the positive superhump has a very strong second harmonic.

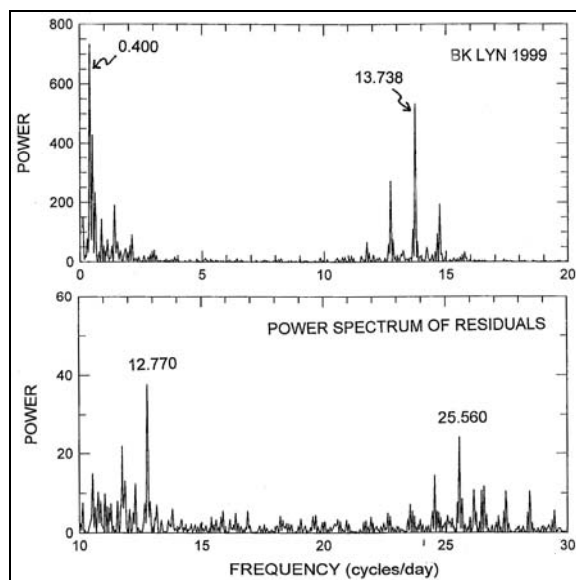


Figure 3. *Top:* power spectrum of BK Lyn in 1999, with significant signals flagged with their frequencies in c/d. The negative superhump dominates, along with its associated “wobble” signal. *Bottom:* the power spectrum of the residuals, after these two strong signals are subtracted from the time series. A weak positive superhump remains, with much of the power at the second harmonic (“double-humped”).

Unfortunately, the negative and positive superhumps are separated by a frequency close to 1 c/d, a cruel blow to astronomers on our planet. Still, the star never promised us a rose garden, and this long campaign with good alias rejection was able to separate the two signals.

At the risk of injecting some interpretation into matters of reportage (seldom wise, and we properly hate ourselves for doing it), we will call the positive superhump “apsidal” and express the frequency as $\omega - A$ and the negative superhump “nodal” and express the frequency as $\omega + N$ (where ω is the orbital frequency). The 1999 signals are then N , $\omega - A$, $\omega + N$, $2\omega - 2A$, and $2\omega - A$. In fact, for all years of observation, all detected frequencies obey these simple rules:

1. All apparitions of N are in the form $+N$, $+2N$, etc.
2. All apparitions of A are in the form $-A$, $-2A$, etc.
3. Whenever a $+N$ sideband appears, a strong low-frequency signal at N appears.

4. Whenever a $-A$ sideband appears, a low-frequency signal at A never appears.

In fact, for virtually all our data on all superhumping CVs, *these rules appear to be strictly followed* – although data quality does not always yield high confidence for frequencies below 2 c/d.

This terminology accords with a common modern interpretation, and will help our reportage in this complicated story of periodic signals. A primer on periodic-signal and superhump zoology in cataclysmic variables can be found in Appendix A of Patterson *et al.* (2002).

4.2 2002 Coverage

The 2002 coverage spanned 58 days, with a dense segment during JD 52264-318. The powerful signals occurred again at 0.394(2) and 13.740(2) c/d. After subtracting these, weaker signals appeared at 25.521(2), 27.475(2), 12.760(2), and 13.344(2) c/d, in order of decreasing power. These appear to be the N , $\omega + N$, $2(\omega - A)$, $2(\omega + N)$, $\omega - A$, and ω signals – in order of decreasing power. Full analysis awaits a subsequent paper. But we note that these frequency assignments agree within the quite small errors, with the basic underlying clocks taken to be the orbital frequency, the “nodal” frequency (that of disk wobble, in the popular interpretation), and the frequency of apsidal motion – respectively at $\omega = 13.344(2)$, $N = 0.395(2)$, and $A = 0.584(2)$ c/d.

4.3 2005 Coverage

The 2005 coverage spanned 20 days, when the star stayed always close to $V = 14.8$. The runs were sufficiently short that no reliable analysis was feasible for signals of very low frequency. But the power spectrum showed the usual superhump signals at 13.740(4) and 12.751(4) c/d and their second harmonics, with full amplitudes of 0.140 and 0.024 mag, respectively. The $\omega + N$ negative superhump is highly sinusoidal, while the $\omega - A$ signal has the distinctive fast-rise-slow-decline pattern characteristic of positive superhumps (in virtually all cataclysmic variables).

4.4 2011 Coverage

The star’s 2011 light curve covered 324 hours and 58 nights. We defer detailed analysis to a later paper. However, the seasonal light curve, seen in Figure 1, clearly shows the star to have significantly different brightness states – both fainter and brighter

than anything seen (by us, or by anybody) in previous years. We resolved to do a more thorough job in the 2012 campaign.

4.5 2012 Coverage

As of 2012 early April, our observing campaign is ongoing. However, Table I shows details of the coverage (~1000 hours and climbing), and Figures 1 and 2 show the seasonal and several-day light curves. Full details await the end of the campaign, but we've learned a lot from all this close scrutiny:

1. The star now shows recurrent high and low states. The high states are either bright and long, or faint and short – and follow the guidelines of “supermaxima” and “normal maxima” familiar from the study of dwarf novae, especially the ER UMa class. [See Robertson et al. (1995) for the standard treatment of this class, and Osaki (1996) for a lucid theoretical account.] Supermaxima occur every 45 days, and normal maxima occur every 5 days.
2. An apsidal superhump grows suddenly to very large amplitude (0.3 mag) at the beginning of superoutburst, and decays slowly as the outburst does, over ~15 days. Its waveform initially shows the nearly universal fast-rise-slow-decline pattern, but then mutates to a double-humped shape after a few days.
3. A negative superhump is present all the time, with an amplitude which is practically constant in intensity units (~0.6 mag at $V = 16$, 0.07 mag at $V = 14$). This signal appears to pay no attention, in phase or amplitude, to any outbursts which may be occurring. And it always dominates when the star is faint; the pattern obvious in Figure 2 repeats exactly every time the star shuffles between bright and faint states.

5. Interpretation

Those are the facts. We now proceed to the challenge of interpretation. In that task we appeal to numerous elements of today's conventional wisdom regarding the common interpretation, and in some cases outright theory, of cataclysmic variables.

Of course, such reliance on theory and popular interpretation always brings with it some hazard of going wrong.

5.1 A Precessing and Wobbling Disk

The periodic signals (ω , N , A , and their children) are the most straightforward, because they fit into a detailed pattern of behavior which is familiar from the study of numerous other CVs.

BK Lyn is a dwarf nova (nee novalike) with a short orbital period, and outbursts showing a long/short dichotomy. During all long outbursts of such stars, a strong apsidal superhump (ω - A) is quickly born, and decays after a few weeks. Short eruptions never hatch such signals. Stars like this are called “SU UMa-type” dwarf novae. There are hundreds of such stars, and therefore thousands of eruptions sufficiently studied to test the universality of these statements, and there are *no known exceptions*; you can “take it to the bank”.

Present-day nomenclature also ordains subclasses. The superoutbursts of so-called WZ Sge stars happen very rarely ($P > 10$ years), while those of ER UMa stars happen very frequently ($P < 100$ days). Stars in between are just plain old SU UMas. In our opinion, these subclasses do not reflect any essential difference in physics, but merely accretion rate. Osaki (1996; see his Figure 2) shows simply and lucidly why outburst recurrence rate should vary smoothly with accretion rate; Patterson (2011, hereafter P11) shows ploddingly that observations bear this out, and in particular that recurrence period scales as $(\dot{M})^{-1}$ (Figures 7 and 11 of that paper).

Superhumps are a great distinguishing feature of all such stars, and are sometimes taken to be a *defining* feature of the SU UMa class. Our enthusiasm doesn't go quite that far, however. It is more general, and more interesting, to say that (apsidal) superhumps inevitably result when stars of sufficiently short P_{orb} , and containing accretion disks, achieve sufficiently high \dot{M} for a sufficiently long time. It's then up to observers to determine what constitutes “sufficient”. Patterson et al. (2005) estimated these sufficiency conditions as follows: $P_{\text{orb}} < 3.5$ hours, $\dot{M} \approx 3 \times 10^{-9} M_{\odot}/\text{yr}$, $t \sim$ a few days.

In all respects that we have been able to measure, or ponder, it certainly appears that BK Lyn's positive superhump is a fully credentialed member of the dwarf-nova family. In particular, it resembles in detail that of the ER UMa family, with behavior patterns reminiscent of other class members: V1159 Ori (Patterson et al., 1995), V503 Cyg (Harvey et al., 1995), and ER UMa itself (Gao et al., 1999). We take that to mean, in the now-popular interpretation, that in superoutburst, BK Lyn's disk becomes quickly eccentric, with a line of apsides precessing prograde at 0.58 c/d.

The negative superhump is more challenging to understand, because this phenomenon has been seen

in only 10-20 CVs, and they have not shown the uniform behavior patterns nicely presented to us by positive superhumpers. We defer full analysis to a later paper.

5.2 The Classical Nova

The “guest star” of 101 A.D. has been previously discussed by Hsi (1958) and Clark and Stephenson (1978), and especially by Hertzog (1986). Unlike most guest stars, it is at relatively high galactic latitude (40 degrees), and can be placed with unusual precision in the sky, since it is described as very close to a star which all students of ancient records take to be Alpha Lyncis. Hertzog argues that a compelling case can be made for BK Lyn, a scant 29 arcminutes away from α Lyn. The modern-day BK Lyn is an extremely unusual star – the only short-period novalike among the ~1000 known CVs, and now the only novalike to have morphed into a dwarf nova. Positional coincidence with a very unusual object is evidence of physical association. The modern-day GCVS apparently accepts this, since it lists BK Lyn's range of variability as 0.3-14.6.

The ancient records describe the star as “not bright”, which, in the context of other brightness reports in those records, is taken to mean a magnitude near zero. Outbursts of the modern-day dwarf nova reach $V = 13.8$ (allowing for the difference between V and C magnitudes), and outbursting dwarf novae are pretty good “standard candles” with $M_V = +4.6$. Allowing an additional 0.2 mag for absorption on this line of sight, we estimate BK Lyn to lie at a distance of 600 pc. If the guest star is actually BK Lyn, then it apparently rose to $M_V = -9$ (0.3 minus 0.2, with a distance modulus $m-M = 9$). This is about right for a moderately fast classical nova, and a cataclysmic variable is exactly what's needed as a classical-nova progenitor. Finally, we note that BK Lyn has just executed the move which theorists have long predicted must occur for very old novae: it has settled back into a dwarf-nova state. These arguments from physics and brightness strengthen the argument from positional agreement, and we conclude, following Hertzog, that BK Lyn is very likely to be the remnant of Nova Lyn 101.

5.3 BK Lyn as a Milestone for Nova Evolution

There has long been a paradox – or at least an oddity – in the census of cataclysmic variables. All such stars should become classical novae as their envelopes of accreted hydrogen grow to a certain threshold, and the great majority of CVs (>90%) are

stars of short orbital period. Yet the great majority of known old novae (~90%) are stars of *long* orbital period. We still don't have a satisfactory explanation for this oddity. However, identification of BK Lyn with an ancient nova will shed considerable light upon it.

In a classic study of old novae, mainly from the 20th century, Robinson (1975) found that novae have the same brightness before and after eruption. But since most known novae arise in stars of long P_{orb} , this finding only applies to that class. To express this in terms of accretion rate, Robinson found that (long- P_{orb}) postnovae fade to $\sim 10^{-8} M_{\odot}/\text{yr}$ within 10-20 years after eruption... and then, within the limits of data on photographic surveys, seem to have the same brightness, and therefore accretion rate, a few years before the eruption. The simplest interpretation is that these stars are similarly bright throughout the long interval between eruptions. We strongly suspect that this is true – because the present census of long- P_{orb} CVs, which are presumably the ancestors of future novae, really *does not contain any stars which substantially differ from this description*. Among long- P_{orb} stars, prenovae, postnovae, and nova suspects all look about the same (aside from fireworks associated with the eruption itself: ejected gas and dust shells, supersoft X-rays, etc.).

The situation for short- P_{orb} stars should be radically different. Why? *Because these stars are not naturally entitled to accrete at $10^{-8} M_{\odot}/\text{yr}$* . Their only reliable driver of mass transfer is GR, which only provides $10^{-10} M_{\odot}/\text{yr}$. Therefore they have to wait ~100x longer to pile up enough matter to fuel another eruption, and that may be plenty of time to cool sufficiently to join their natural compadres at short P_{orb} – the garden-variety dwarf novae, with a quiescent M_V near +10 and brief outbursts every 100-1000 days.

In this scenario, BK Lyn is the product of a recent nova eruption – probably the eruption of 101 December 30. With a mere 2000 years of cooling, the white dwarf is still fairly hot, and the secondary star sufficiently agitated to transfer matter at an unnaturally high rate – near $10^{-8} M_{\odot}/\text{yr}$. This explains the high temperature component seen in the ultraviolet spectrum (35000 K; Zellem *et al.*, 2009), and the star's intrinsic brightness ($\langle M_V \rangle = 4$, Patterson, 2011). Somewhere between 2005 and 2011, the star faded sufficiently to allow dwarf-nova outbursts to occur.

This empirically sets an important and previously unknown timescale: 2000 years to resume life as a dwarf nova, viz. of the ER UMa persuasion. However, ER UMa stars are themselves quite rare; P11 estimated that they comprise only 1% of the population of short-period dwarf novae. If the ER UMa stage lasts ~10000 years, the numbers work out

about right: 2000 for the BK Lyn era, 10000 for the ER UMa era, and 1,000,000 for dwarf-nova normalcy. That satisfies the available space-density constraints, and allows the correct amount of time for binaries accreting at $10^{-10} M_{\odot}/\text{yr}$ to accumulate the $10^{-4} M_{\odot}$ needed to trigger a nova eruption.

Shouldn't we then expect most short-period novae to be much fainter prior to eruption, contrary to Robinson's study? Yes – but that study concerned mainly long-period novae. Schaefer and Collazzi (2010) recently studied archival photographic magnitudes for a group of short-period novae, and found them to be much fainter before eruption. So all the evidence to date seems to be consistent with this account of relaxation following a classical nova in a short-period CV.

5.4 The Transition to Dwarf Nova: a Singular Event?

Does the observed 2005-2011 transition to a dwarf-nova state represent a singular event in BK Lyn's postnova evolution? Well, maybe. Our 20-year observation span, and the 6-year window for this event, are short – but not ridiculously short compared to the putative 2000-year wait. Also, we obtain similar photometric coverage of many old novae and novalikes (dozens), and we have not observed such a transition in any other star. So even as a singular event, not to be repeated until the next nova cycle, it does not seem wildly improbable.

But there is no need to hypothesize a singular event. Secular decline in \dot{M} over a few thousand years could easily be punctuated by small fluctuations about the temporary mean; indeed, many cataclysmic variables show small luminosity variations on timescales of decades (Warner, 1988, Richman *et al.*, 1991). It's plausible that such fluctuations could now be swinging the disk between states of stable and unstable accretion. Indeed, that is our current understanding of Z Cam stars: dwarf novae near that threshold accretion rate, with their disks fluctuating irregularly between stable and unstable. In this version of our scenario, BK Lyn could be considered the first short-period Z Cam star.

If this latter version were correct, then we might well see other ER UMa stars – especially RZ LMi with its whirlwind 20-day superoutburst cycle – mutating temporarily into novalike variables, pausing slightly in their inevitable decline towards a long and simple life as a garden-variety dwarf nova.

6. Summary

1. We began this long campaign to study the superhump signals of BK Lyn, but detailed analysis still lies ahead. Both positive and negative superhumps appear to fit into the known categories of similar objects – and, in particular, strongly resemble those of two known ER UMa stars: V503 Cyg and ER UMa itself. Probably they arise from apsidal advance and nodal regression in an eccentric and tilted accretion disk.
2. Seasonal light curves demonstrate that somewhere in the interval 2005-2011, the novalike variable BK Lyn mutated into a card-carrying dwarf nova of the ER UMa class, with superoutbursts occurring every 45 days. The dwarf-nova standard-candle relation implies a distance of about 600 pc.
3. Arguments from positional coincidence, galactic latitude, nova physics, and the rarity of short-period novalikes suggest that BK Lyn is the old-nova remnant of the “guest star” of 101 A.D.
4. This suggests the following timescales for a short-period dwarf nova's relaxation following a classical-nova eruption: 2000 years as a novalike, 10000 years as an ER UMa dwarf nova (gradually declining to an ordinary SU UMa), and 1,000,000 years in true quiescence.
5. This can explain why ER UMa stars exist (because they are remnants of recent novae), why they're rare (because that phase is only 1% of a nova's full eruption cycle), and why short-period stars are rare among known old novae (because they spend most of their quiescence very faint, where they hide from our telescopes).
6. If this story of smooth decline is correct, then the superoutburst recurrence period – a rather easily determined number – is very strongly affected by *time since the last classical-nova eruption*. That might be the “second parameter” (besides orbital period) needed to understand the scatter in the various \dot{M} -related quantities of dwarf novae (see the figures in P11). For example, it could explain the tremendous difference between the frenetic RZ LMi (P~20 days) and the somnolent WZ Sge (P~30 years) – two stars of practically identical P_{orb} .
7. You can learn an awful lot from a patient research program with 14-inch telescopes.

7. References

- Clark, D. H., Stephenson, F. R. (1977). *The Historical Supernovae*. Pergamon New York.
- Gao, W., et al. (1999). *Ap. J.* **527**, L55.
- Green, R. F., Schmidt, M., Liebert, J. (1986). *Ap. J. S.* **61**, 305.
- Green, R. F., Ferguson, D. H., Liebert, J. E., Schmidt, M. (1982) *PASP* **94**, 560.
- Harvey, D. A., et al. (1995) *PASP* **107**, 551.
- Hertzog, K. P. (1986) *Observatory* **106**, 38.
- Honeycutt, R. K., Robertson, J. W., Kafka, S. (2011). *Astron. J.* **141**, 121.
- Hsi, T.-T. (1958). *Smithson. Contr. Astrophys.* **2**, 109.
- Osaki, Y. (1996). *PASP* **108**, 39.
- Patterson, J., et al. (1995). *PASP* **107**, 1183.
- Patterson, J., et al. (2002). *PASP* **114**, 721.
- Patterson, J., et al. (2005). *PASP* **117**, 1204.
- Patterson, J. (2011). *MNRAS* **411**, 2695.
- Pskovskii, Y. P. (1972). *Sov. Astr.* **16**, 23.
- Richman, H. R., Applegate, J. H., Patterson, J. (1994). *PASP* **106**, 1075.
- Ringwald, F. A., Thorstensen, J. R., Honeycutt, R. K., Robertson, J. W. (1996). *MNRAS* **278**, 125.
- Robertson, J. R., et al. (1995). *PASP* **107**, 443.
- Robinson, E. L. (1975). *Astron. J.* **80**, 515.
- Schaefer, B. E., Collazzi, A. (2010). *Astron. J.* **139**, 1831.
- Shara, M. M., Moffat, A. F. J., Webbink, R. F. (1985). *Ap. J.* **294**, 271.
- Skillman, D. R., Patterson, J. (1993). *Ap. J.* **417**, 298.
- Thorstensen, J. R., Taylor, C. J. (2000) *MNRAS* **312**, 629.
- Warner, B. (1988). *Nature* **336**, 129.
- Zellem, R., et al. (2009) *PASP* **121**, 942.

Photometric Monitoring by Amateurs in Support of a YY Gem Professional Observing Project

Bruce L. Gary

*Hereford Arizona Observatory, 5320 E. Calle Manzana, Hereford, AZ 85615 USA
BLGary@umich.edu*

Dr. Leslie H. Hebb

*Department of Physics and Astronomy, Vanderbilt University, Nashville, TN 37235 USA
Leslie.Hebb@Vanderbilt.edu*

Jerrold L. Foote

*Vermillion Cliffs Observatory, Kanab, UT 84741 USA
jfoote@scopecraft.com*

Cindy N. Foote

*Vermillion Cliffs Observatory, Kanab, UT 84741 USA
cindyf@kanab.net*

Roberto Zambelli

*Societa Astronomica Lunae, 19030, Castelnuovo Magra, Italy
Robertozambelli.rz@libero.it*

Joao Gregorio

*Affiliation, Atalaia, Portugal
j.gregorio@netcabo.pt*

F. Joseph Garlitz

*Elgin Amateur Observatory, Elgin, Oregon 97827 USA
garlitzj@eoni.com*

Gregor Srdoc

*Physical Therapist, Trainer, Viskovo, Croatia
gregor@vip.hr*

Takeshi Yada

*The Shimane Nature Museum of Mt. Sanbe, Ohda, Shimane 694-0003, Japan
yada@nature-sanbe.jp*

Anthony I. Ayiomamitis

*Perseus Observatory, Nea Palatia-Oropou, Greece 19015
anthony@perseus.gr*

Abstract

When a professional observatory is used in the study of an active star, it may be necessary to establish activity level “context,” such as the star’s flaring frequency, presence of star spots and brightness changes. Characterizing these aspects of star activity requires time-consuming observations, which can often be obtained by amateurs. This article describes coordinated photometric monitoring by a selected team of advanced amateurs in support of a 10-day intensive spectropolarimetry observation of YY Gem, an M dwarf eclipsing binary. One of the authors (LH) used the 3.6-meter Canadia-France-Hawaii Telescope in Hawaii for determining magnetic field strength maps, and she initiated the request for photometric monitoring by amateurs. The observations are undergoing analysis, yet preliminary results demonstrate the value of a coordinated professional/amateur approach in the conduct of this type of observing campaign.

1. Introduction

M-dwarf stars outnumber all other spectral classifications, so it is understandable that stellar modelers are anxious to understand why their models under-estimate M-dwarf radii by 5 or 10%. Could these stars have magnetic fields that inhibit convection in a way that swells their size? To find out, professional astronomer Dr. Leslie Hebb led a team of investigators in obtaining 10 nights of telescope time on the 3.6-meter Canada-French-Hawaii Telescope (CFHT) in Hawaii to conduct spectropolarimetry observations of a pair of eclipsing M-dwarfs, YY Geminorum (YY Gem).

A complex picture is starting to emerge where three different phenomena, all related to magnetic fields, are invoked to explain the observed radii of M dwarf stars over the entire mass range. In particular, the existence of large star spots near the poles of the eclipsing binary component stars could be causing a systematic overestimate of measured radii during the light curve analysis procedure. This project involves constructing a new eclipsing binary model that incorporates light curve data while constraining star spot properties from a Doppler Imaging analysis of the spectropolarimetric spectra (explained in Section 4). This analysis will provide the most accurate radius and temperature estimates of the component stars. When combined with magnetic fields maps, we hope to better understand if and how magnetic fields are causing the radii of YY Gem to be larger than predicted by previous models.

In order for the CFHT observations to be fully interpreted it was necessary to supplement these observations with high-precision light curves at many wavelengths. These data are necessary for the eclipsing binary modeling and thus essential to the success of the project. In addition, M-dwarfs are also prone to flaring, perhaps due to magnetic field disturbances. Star spot variations and flaring activity of the YY Gem pair can be evaluated using light curve monitoring, with special emphasis on the 10-day CFHT observations (2012 January 4 to 13).

Professional telescopes can cost hundreds of dollars per observing minute, so the cost of including light curve monitoring in the proposed YY Gem project would have been prohibitive. Instead, amateurs were considered for providing this support. After all, eclipsing binary light curves have been made by amateurs for decades and, since the advent of CCD cameras and computer-controlled telescopes, amateur capabilities have improved greatly.

One of the authors (BLG) has a history of recruiting amateurs for special observing projects (e.g., Amateur Exoplanet Archive, Pro-Am White Dwarf

Monitoring), and he agreed to coordinate advanced amateurs with experience in exoplanet light curve measurements to support the YY Gem project, from 2011 October and to 2012 January.

2. Amateur Team

Continuous observing during the 10-day CFHT observations would have been desirable, but since no Earth-based site has clear skies all the time it is impossible for a ground-based network of observatories to provide continuous coverage – except on rare, brief occasions. For example, if clear skies exist half the time at three observing sites equally spaced in longitude, they can be expected to provide complete coverage of any target on only ~13% of dates. Even if the sites have clear skies 2/3 of the time the complete coverage statistics increases to only ~23%. Another strategy is to use multiple sites at each longitude, but spaced apart so that their clear sky statistics are uncorrelated. With two sites at each longitude, and half of nights clear for each site, complete coverage can be expected for ~43% of dates. Therefore, it is unrealistic to expect complete coverage for any network of observatories when several dates are involved.

This monitoring project recruited 9 observers in 3 longitude regions: 4 in Europe, 4 in the US and one in Japan, as summarized in Table I.

Longitude	Observer	Location	Filters
+024	Ayiomamitis	Greece	Bs
+014	Srdoc	Croatia	Rs
+010	Zambelli	Italy	Bs & V
-009	Gregorio	Portugal	V
-110	Gary	Arizona	g'r'i'z'
-112	J. Foote	Utah	V & Rc
-112	C. Foote	Utah	B & Ic
-118	Garlitz	Oregon	Bs
-227	Yada	Japan	Bs

Table I. Observer list and their filter assignments. Rs, Vs and Bs are SBIG's RGB filters.

With only one observer at Pacific longitudes there was no expectation of continuous coverage. With 4 observers at two longitude regions, however, good coverage was expected for ~ 2/3 of each date; and indeed this was achieved. During the 10-dates of interest 93 light curves were obtained, with a median coverage of 18.3 hours (76%). During the preceding 3 months 31 LCs were obtained. Following the intensive 10-day observations two light curves were obtained (for refining the orbital period).

3. YY Gem and Reference Star

This is a difficult target for photometry because YY Gem is only 71 arcseconds away from the bright star Castor. The V-magnitudes for these two stars is 9.06 and 1.58; the difference of 7.5 magnitudes corresponds to a flux ratio of 980:1.

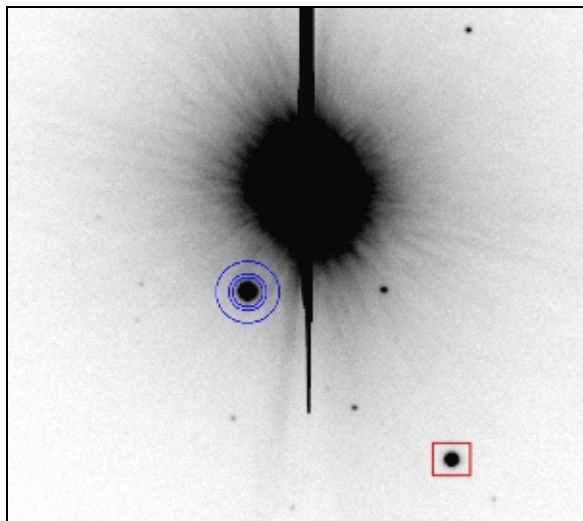


Figure 1. YY Gem (blue circles) and Castor, 71 “arc apart, and nearby star used for reference (red square).

In all images Castor was saturated and “bleeding.” Most images also had pixel edge reflections in 4 directions. Some observers rotated their CCD assembly so that YY Gem was not close to the bleeding, pixel reflection and spider diffraction spike features (Fig. 1 has a rotation of 11 degrees). A nearby star was used for reference for all filter bands. An all-sky observation produced B, V, Rc and Ic magnitudes, from which magnitudes for other bands were calculated.

YY Gem undergoes a 19.5-hour variation in brightness, slightly greater at shorter wavelengths, so in Table II, the magnitudes for YY Gem and the reference star are for phase 0.35.

Band	Wavelength [nm]	YY Gem	Reference Star
B	441	10.451	10.917
V	540	9.062	9.947
Rc	624	8.156	9.419
Ic	800	7.193	8.988
Bs	450	10.39	10.83
Vs	540	9.06	9.95
Rs	640	8.06	9.36
g'	478	9.775	10.409
r'	620	8.589	9.650
i'	755	7.912	9.459
z'	910	7.342	9.318

Table II. YY Gem and reference star magnitudes. Rs, Vs and Bs are SBIG RGB filters.

The RA/DE coordinates for YY Gem and the reference star are 07:34:37.45, +31:52:10.2 and 07:34:26.32, +31:51:00.1. Meridian transit occurred near local midnight in mid-January. Based on these all-sky calibrations YY Gem is a very red star, with $B-V = +1.389 \pm 0.023$, and the reference star is moderately red, with $B-V = +0.970 \pm 0.026$.

4. Previous Publications

Observations by Kron (1952) show a 40 mmag amplitude (80 mmag peak-to-peak) variation of the out-of-transit (OOT) V-band magnitude associated with the orbital period (19.5-hours). Both transits had depths of about 0.6 mag, so the transit geometry has a “grazing” V-shape.

In 1971 Leung and Schneider (1978) observed transits with V, R and I filters (Figure 8), and these data showed OOT amplitude decreasing with wavelength. Torres and Ribas (2002), hereafter TR2002, measured radial velocities spectroscopically, reviewed previous mid-transit timing data to derive an improved ephemeris, and modeled the 1971 light curves using a star spot model. Their model solution showed that both stars were virtually identical, with radii of 0.62 solar and masses of 0.60 solar. Their ephemeris is $HJD = 2449345.112327(87) + 0.814282212(12) \times E$, where E is an integer number of orbits.

TR2002 found that the 1971 transit depths decrease with wavelength differently for the primary transit (611, 596, 563 mmag for V, R and I) and secondary transit (544, 539, 544 mmag). Between primary and secondary transits the OOT level is constant. However, from phase 0.4 to 0.6 (including secondary transit) the OOT level fades ~ 45 mmag and fully recovers by primary ingress (phase 0.9).

Qian et al. (2002), hereafter referred to as Q2002, suggest that the orbital period exhibits a secular decrease, which might be due to mass loss due to magnetic fields and stellar winds. Their ephemeris for the primary transit is $HJD = 2424595.8178(1) + 0.81428258(1) \times E - 1.20(2) \times 10^{-11} \times E^2$. This ephemeris corresponds to a continuous period decrease of $dP/dt = -1.08 \times 10^{-8}$ day/year (-90 milliseconds/century).

Both the TR2002 and Q2002 ephemerides ignore the possibility that changing star spots will affect mid-transit timings, so their quoted SEs overlook this source of systematic uncertainty.

5. Results of Present Observations

Normally, it is a trivial matter to assign one transit of an eclipsing binary as the primary. But when

the transits have almost the same depth, and when star spots are present, it is possible that transit depth relationships can change on yearly timescales. This problem is greater when the period is short and the interval between observations is large. The latest published YY Gem ephemeris (Q2002) is based on observations from 1971 to 1998, and since the orbital period is ~ 0.814 days there are >5800 periods between 1998 and the present observations. Confusion is compounded by the possibility that the period may be decreasing, or is variable.

An assignment of “primary” was made for the high quality 2011 November 27 transit, which occurred 8.1 ± 0.2 minutes late compared to the TR2002 ephemeris. If this transit were a secondary then it would be occurring 578 minutes early. A provisional identification was needed for archiving purposes so this event was provisionally adopted as primary.

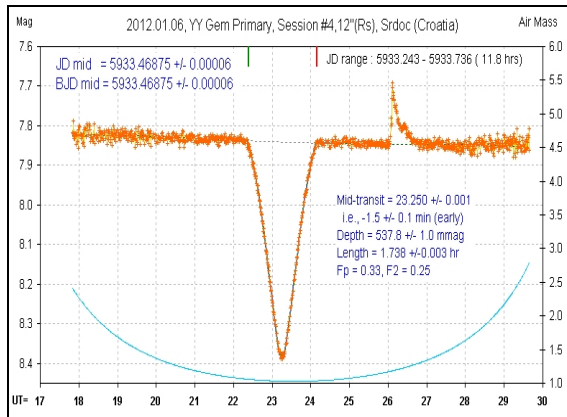


Figure 2. Typical light curve, showing a “primary” transit followed by a flare.

A typical light curve (LC) is shown in Figure 2. It was obtained by Gregor Srdoc (Croatia) on 2012 January 6 using a 0.30-m telescope with a Rs-band filter. The information boxes state that transit depth is 538 ± 1 mmag, transit length = 1.738 ± 0.003 hours, mid-transit occurs at 23.250 ± 0.001 UT, or JD = $2455933.46875 \pm 0.00006$ (with a BJD equivalent). On this observing session overlapping transits lasted 21.1 hours, and three flares were observed.

An analysis of transit depths is shown in Figure 3. The deepest transits are the ones identified for the current analysis as “secondary.” These transits vary greatly with wavelength, in contrast with the shallower “primary” transits. Also shown in this figure are the depths of the 1971 transits. It is curious that the 1971 primary transit depths exhibit a similar behavior to the current “secondary” transits; and the 1971 secondary transit depths resemble the current “primary” transits.

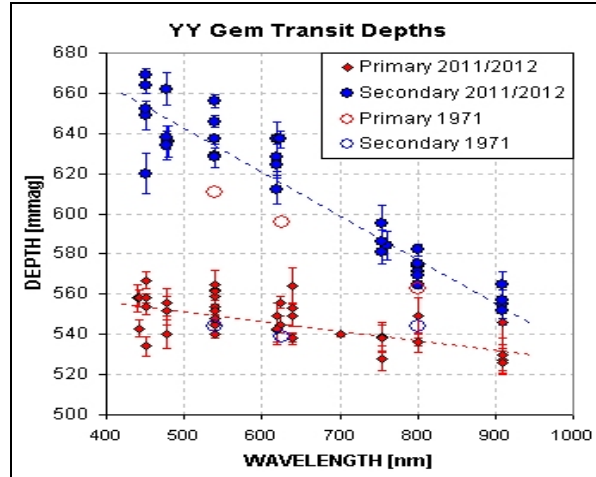


Figure 3. Depths of “primary” (red) and “secondary” (blue) transits. The 1971 transit depths are shown with large circles.

During the 2011 observations (56 non-overlapping hours) only one small flare was observed. However, during the 10-day intensive observing dates (180 non-overlapping hours), 20 flares were present (on 9 of the 10 days). That’s 1.1 ± 0.2 flares per 10-hour nominal observing session, versus 0.2 ± 0.2 flares per 10 hours from 2011 October through December. In other words, the 10-day intensive observing period occurred when YY Gem was actively flaring. Flare activity was present at all phases, although 5 occurred between 0.69 and 0.83.

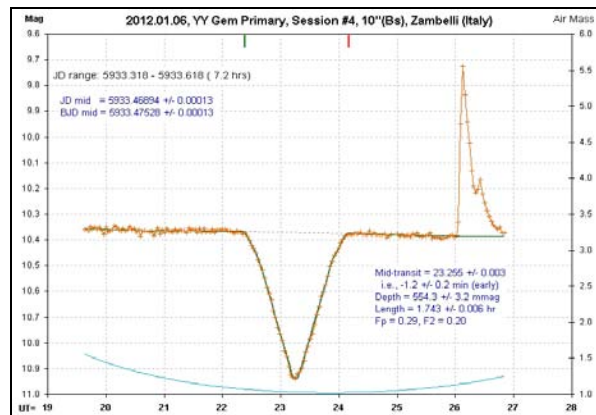


Figure 4. Light curve of the same transit shown in Fig. 2 but made with a Bs-band filter, showing that the flare amplitude is greater at shorter wavelengths.

Flare rise and decay times can be estimated from Fig. 2 data (using un-averaged data, with 8-second spacing); from onset to peak takes 2.6 minutes, while the one-half life decay time is 7.9 minutes. The decay appears to be complete in 40 minutes. Each of the 21 flares observed exhibit an intensity that decreases with wavelength.

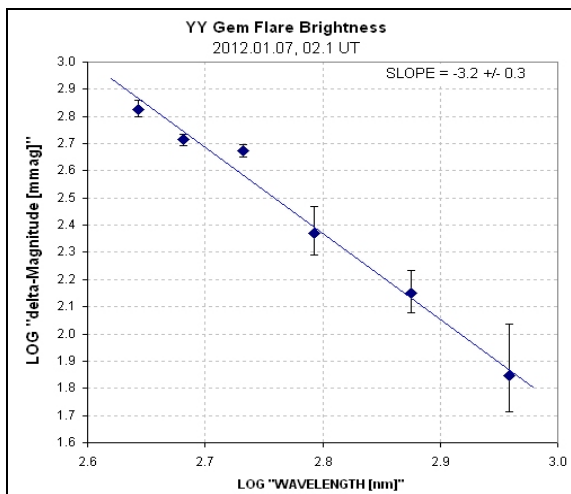


Figure 5. Flare brightness versus wavelength for the event of 2012 January 7, 02.1 UT.

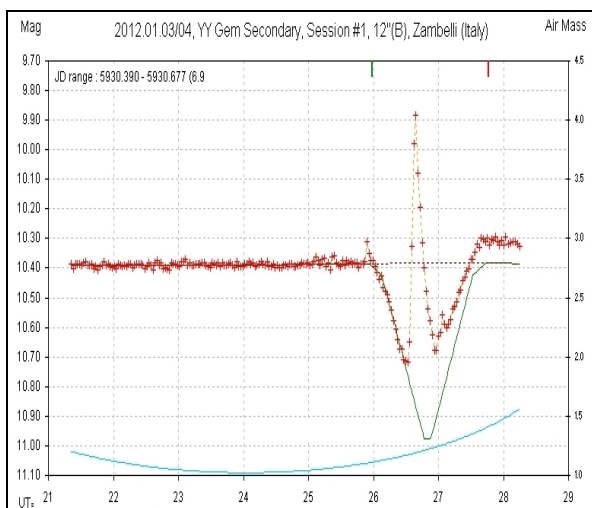


Figure 6. Flare during a transit, observed by Zambelli in Italy with Bs-band filter.

The flare in Fig.'s 2 and 4 were observed by four observers using 7 different filters, which allows a determination of the flare's "spectral index" to be made over a wide range of wavelengths. This is shown in Figure 5, where the logarithm of brightness and wavelength are used to achieve a linear relationship. The slope of such a line is "spectral index" which in this case is -3.2 ± 0.3 . This spectral index requires that the flare emission have a non-thermal origin, and it is reasonable to speculate that a magnetic disturbance is involved. Flaring activity was maximum on the first of the 10 intensive observing dates (Session #1, 2012 January 3/4), and gradually subsided to zero on the last date (January 12/13).

Figure 6 shows the largest flare encountered, which occurred during a transit (on the first of the 10-days of intensive observations). After the flare recov-

ered there appears to be a residual brightness of ~ 80 mmag that persists for > 1 hour.

Out-of-transit (OOT) brightness varied in an interesting way as a function of orbital phase and wavelength. Establishing OOT shape is difficult due to differences in extinction between the target star (YY Gem) and the reference star. Since YY Gem is redder than the reference star it will fade at a lower rate with increasing air mass, leading to a "bowl" shaped LC. Model-fitting LC observations involves removal of this differential extinction effect. For stars that don't vary in brightness during the LC the model fitting is correctly identifying "bowl" shapes that are correlated with air mass and removing this "air mass curvature" (AMC) variation by adjusting a differential extinction parameter. Provided that every LC uses the same reference star, AMC should be the same for all LCs, so the same value should be found for the differential extinction parameter for all such LCs.

However, if there is a real OOT variation with a minimum near the middle of the LC the fitting procedure will attempt to remove this component of curvature as if it was being produced by a differential extinction unique to that LC. This would lead to removal, or an underestimate, of the actual OOT variation. Similarly, if the OOT really exhibits a maximum near the middle of the LC the fitting procedure will reduce the amplitude of any real "inverted bowl" OOT shape. In other words, the LC fitting procedure will reduce the amplitude of any OOT variation that is actually present. This problem would not exist if the target and reference stars were the same color, but with YY Gem being so extremely red there were no similarly colored stars within a typical field-of-view that could be used for reference.

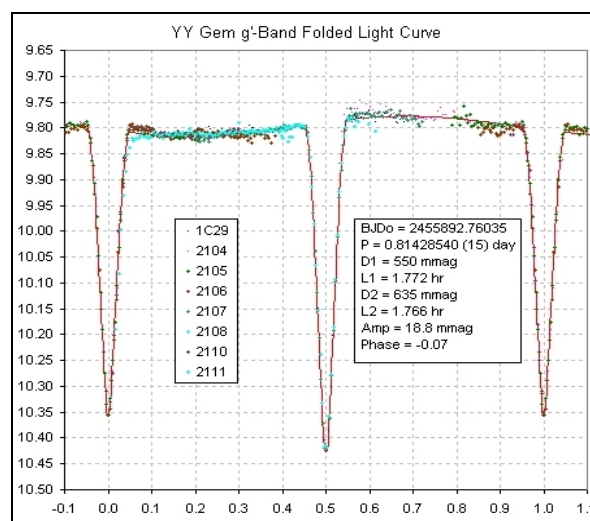


Figure 7. Phase-folded g'-band light curve for 8 dates, using a 16-parameter model.

One solution for this problem is to simultaneously solve for both AMC and OOT shape, in a procedure that involves all LCs for a given filter band. A more straightforward solution is to first estimate AMC for a given filter band, based on all LCs for that band, then re-do the model fitting using the average AMC, and finally phase-fold the resulting LCs. This is a less elegant approach, but it is simpler to implement, and it is the approach used for this analysis. Figure 7 is an example of a g' -band phase folded LC using this 3-step procedure.

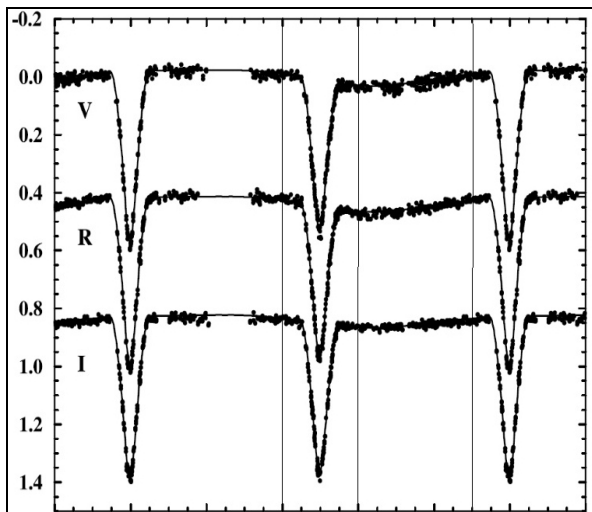


Figure 8. Phase-folded light curve for 3 bands, based on measurements in 1971 (Leung and Schneider, 1978) and model-fitted by Torres and Ribas (2002). The ordinate is a magnitude scale. Phases of 0.4, 0.6 and 0.9 are indicated by vertical lines.

Notice in Fig. 7 that OOT shows a minimum at phase 0.2, just after egress of the transit provisionally identified in this analysis as “primary.” Compare the OOT feature with what was found in a phase-folded LC based on 1971 measurements, shown as Figure 8. Each of the filter bands show a minimum just after a secondary transit, at a phase of 0.6 or 0.7. As noted by Leung and Ribas, who performed the model fit to the 1971 data, all of the fade near the secondary transit occurs between phases 0.4 and 0.6, and a recovery occurs between 0.6 and 0.9 – just before primary ingress. Most of this OOT variation can be seen in the present data, but with a 0.5 phase shift. In other words, if the present data had an incorrect primary/secondary identification, the OOT shapes for 1971 and 2012 would exhibit a better match.

The 1971 phase-folded LC shows a slightly convex shape (brightening in the middle) between primary and secondary transit. If we reverse the primary/secondary identification for the 2012 OOT, then it would exhibit a concave shape. If the primary/secondary assignments for the 2012 data are

correct, and assuming the OOT shapes are due to star spots that persist for decades, then there must have been a major change in star spots between 1971 and 2012.

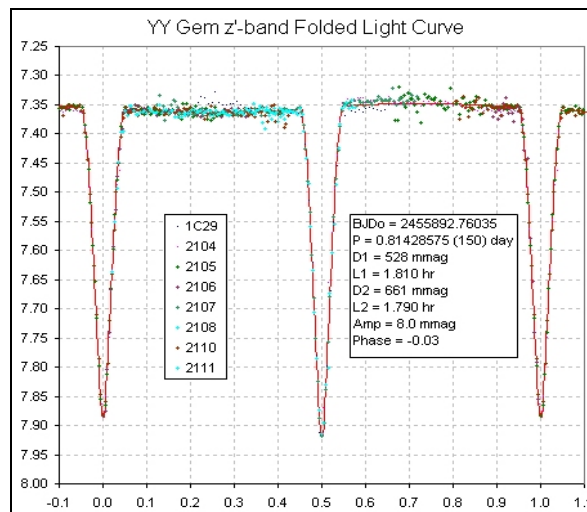


Figure 9. Phase-folded z' -band light curve for 8 dates, using a 16-parameter model.

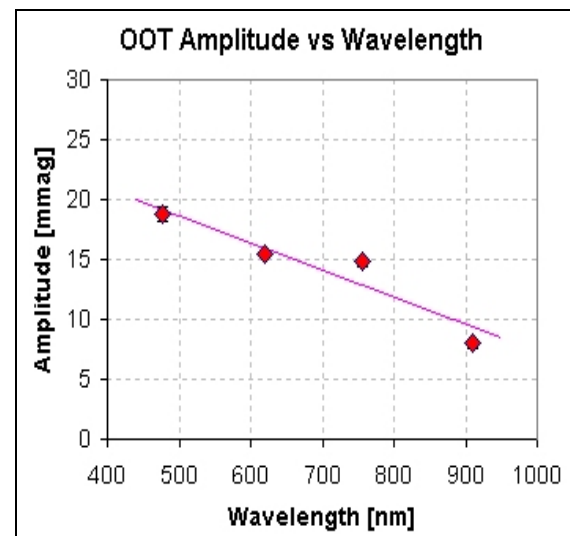


Figure 10. OOT variation amplitude (1/2 peak-to-peak) versus wavelength.

Figure 9 is a z' -band version of Fig. 7. It exhibits a much smaller OOT variation: ~8 mmag versus ~19 mmag at g' -band. The phase-folded LCs at r' - and i' -band (not shown) have OOT amplitudes of 15 and 14 mmag. Figure 10 shows OOT variation amplitude versus wavelength.

Assuming the OOT variation is caused by star spots they must have less temperature contrast at the stellar atmosphere altitude where z' -band emission originates. This will constrain the atmosphere model

If star spot changes are not responsible for the change in OOT pattern between 1971 and 2012, the re-assigning of primary/secondary to the 2012 data will require a period change. The implications of this are important, for it would require speculations about mass loss (Q2002). Before discussing this interesting possibility let's consider the information present in the 2012 LCs about P, and a possible discrepancy between P for 2011/2012 and those derived by TR2002 and Q2002.

From 2011 October to 2012 April a total of 127 LCs were obtained (31 in 2011, 93 during the 10-day CFHT observations, and 2 following); 44 of these included complete transits. Some of the mid-transit times were measured with an accuracy of ~ 10 seconds. Figure 11 is a plot of differences between measured mid-transit time and a best-fitting period solution. For this plot it was assumed that the secondary transit occurs exactly mid-way between primary transits, which doubles the number of transits available for such an analysis.

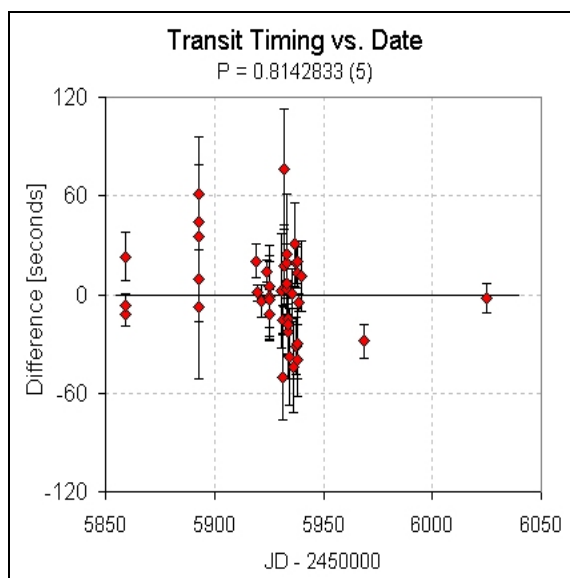


Figure 11. Mid-transit time differences versus date, using both primary and secondary transits, from 2011 October to 2012 April. The differences are with respect to a solved-for period.

The best-fitting P, used for reference in Fig. 11, is 0.81428330(46) day. This period was solved for using chi-square minimization. The Q2002 ephemeris calls for a P on 2012 January 7 of 0.81428372(2) day. The difference between these two periods is $+36 \pm 43$ milliseconds, which means that the present data are compatible with the Q2002 suggested P decay rate. An alternative ephemeris is given by Q2002 (that assigns weights to measurements slightly differently) which assumes that P does not change: $HJD = 2424595.8172 + 0.81428254 \times E$. The difference

between the current P measurement and this “constant P” solution is -66 millisecond (no SE is given by Q2002 for the constant P, but we may assume that $SE \sim 60$ ms). The current P estimate is therefore insufficiently accurate to favor either of the Q2002 period solutions.

The P solution in Fig. 11 differs from the TR2002 P by 35 ± 49 millisecond. Therefore, the P solution from the 2011/2012 transit timing data (Fig. 11) produce a P value that is compatible with the TR2002 P solution. Whereas the P determinations are compatible, the 2011/2012 transits all occur ~ 8.0 minutes later than predicted by the TR2002 ephemeris. The TR2002 P is assigned an accuracy based on precision, and since star spot effects were not considered as a systematic source of uncertainty in their 73-year database we suggest that the 8 minute offset for all 2011/2012 transit events can be used to refine the TR2002 ephemeris. Specifically, we suggest the following ephemeris: $BJD = 2456024.67475(6) + 0.81428290(5) \times E$.

We should ask if a primary/secondary reassignment to the 2011/2012 data is compatible with TR2002 and Q2002 P solutions, and also compatible with the P measurement from the present data. Let's consider reassigning a 2012 transit from “secondary” to “primary” status, and calculate the smallest change to a linearly decreasing P that would be consistent with this reassignment. Consider the LC on 2012 January 7 by Gregorio; mid-transit time is $BJD = 2455934.69633(6)$, and this transit's designation was “secondary.” If we use the Q2002 ephemeris and change the number of orbits for it by the smallest fraction of an orbit that would make this transit correspond to a primary transit, then for this JD interval the average P would be 0.81427179(2) day. Such a P value is statistically incompatible with the Q2002 constant P, the Q2002 decreasing P (both by 400-sigma) and the TR2002 P (400-sigma). Moreover, it is incompatible with the P determined from the 2011/2012 data (21-sigma). We conclude that YY Gem is not undergoing period changes by amounts that have been measured. Instead, we suggest that star spot changes on yearly to decade timescales distort the LC timings in ways that can be misinterpreted as a changing ephemeris.

6. Spectropolarimetric Observations

Magnetic fields can be directly measured on low mass stars through observations of the Zeeman Effect. This can be done when an atom or molecule is in the presence of a magnetic field, once degenerate energy levels undergo a small separation. This phenomenon can be detected in stars through both the

splitting and the polarization of the absorption features in observed stellar spectra.

In practice, the polarization signature is sensitive to both the field strength and its orientation. Furthermore, as the star rotates, an individual magnetic feature on the surface will produce a slowly varying distortion in the spectral line profile over time. Thus, by obtaining a time series of polarized spectra over the full range of rotational phases of a star it is possible to construct images of the large-scale component of the surface magnetic field. This technique is referred to as Zeeman Doppler Imaging (ZDI) (Donati *et al.*, 1997; Semel, 1989). If a time series of unpolarized spectra is also obtained, a large-scale brightness map of the stellar surface (i.e. star spot map) can be derived through a Doppler Imaging (DI) analysis.

We obtained a series of circularly polarized spectra of YY Gem during the 10-night CFHT observing run, densely covering all orbital (and rotational) phases of the binary. We also obtained a corresponding series of unpolarized spectra. These data will be used to derive magnetic field maps and surface brightness maps of both M dwarf stars in the binary using ZDI and DI analysis techniques.

The ultimate goal of the project to explore in detail how magnetic fields and the resulting surface spots influence the structure and temperature of low mass stars. It is now well established that theoretical stellar evolution models underestimate the radii of M dwarf stars by 5-10% and overestimate their temperatures by a few 100 degrees.

Preliminary maps of magnetic field and star spots on both of the YY Gem stars have been produced, so we are confident that final results will contribute to our understanding of model adjustments needed to account for M dwarf sizes.

7. Conclusion

When a professional astronomer is conducting observations of an object that is likely to be photometrically variable it may be possible to rely upon a network of advanced amateurs to document that variability. In the case of the eclipsing binary YY Gem, spectropolarimetric observations were made at the CFHT during a 10-day observing run, and on the same dates a network of amateurs monitored flare activity, transit depth, transit timing, transit shape and OOT variability with ~76% coverage. Similar photometric observations were made before and after the 10-day run, which permitted flare activity context. These features were characterized as a function of wavelength, from B-band to z'-band.

The amateur photometry light curves show a significant change in transit depth, depth versus

wavelength and OOT shapes, compared with 1971 light curves. Two explanations were considered: 1) the orbital period has changed by one-half orbit during the past few decades, or 2) star spots have changed significantly during that time in a way that produces the above changes. We conclude in favor of the second explanation. This was an unexpected finding and further illustrates the merits of extensive photometric support of professional observations.

All light curves and additional results can be found at a web page maintained by one of the authors (BLG, <http://brucegary.net/yygem/>).

8. References

- Donati, J.-F., Brown, S. F. (1997) “Zeeman-Doppler Imaging of Active Stars. V. Sensitivity of Maximum Entropy Magnetic Maps to Field Orientation.” *Astron. & Astrophys.*, **326**, 1135-1142.
- Leung, K. C., Schneider, D. P. (1978). “YY Geminorum I. Photometry and Absolute Dimensions.” *AJ*, **83**, 618-625.
- Qian, S, Liu, D., Tan, W., Soonthornthum, B. (2002) “YY Geminorum: A Very Late Type Close Binary with Possible Magnetic Stellar Wind.” *AJ*, **124**, 1060-1063.
- Semel, M. (1989). “Zeeman-Doppler Imaging of Active Stars. I – Basic Principles.” *Astron. & Astrophys.*, **225**, 456-466.
- Torres, G., Ribas, I. (2002) “Absolute Dimensions of the M-Type Eclipsing Binary YY Geminorum (Castor C): A Challenge to Evolutionary Models in the Lower Main Sequence.” *AJ*, **567**, 1140-1165.

The Lowell Amateur Research Initiative

*Deidre Ann Hunter
Lowell Observatory
1400 West Mars Hill Road
Flagstaff, AZ 86001
dah@lowell.edu*

*John Menke
MenkeScientific
25000 Old Hundred Road
Barnesville, MD 20838
john@menkescientific.com*

*Bruce Koehn
Lowell Observatory
1400 West Mars Hill Road
Flagstaff, AZ 86001
koehn@lowell.edu*

*Michael Beckage
370 Clipper Way
Seal Beach, CA 90740
michael@discoverthestars.net*

*Klaus Brasch
krbrasch@earthlink.net*

*Sue Durling
900 Switzer Canyon Drive #101
Flagstaff, AZ 86001
sdurling@juno.com*

*Stephen Leshin
Sedona AZ
sleshin@yahoo.com*

Abstract

Lowell Observatory has a rich history of amateur research, starting with its founder Percival Lowell. With this SAS meeting, we are announcing the launch of a new initiative to involve amateurs in scientific research: The Lowell Amateur Research Initiative (LARI). This program pairs qualified amateurs with professional astronomers at Lowell Observatory to carry out collaborative research projects. I outline the process for becoming involved, starting with a web-based interface for submitting applications, and the projects that are currently available. We look forward to engaging with the amateur community and expect the program to grow in scope as we gain experience.

1. Introduction

Lowell Observatory has a long history of professional/amateur collaborations. Lowell himself was an amateur, but collaborated with professional astronomers all over the world. With this meeting, we are

announcing the Lowell Amateur Research Initiative (LARI), which enables research collaborations between amateur and professional astronomers. Although amateur-professional collaborations have taken place at Lowell Observatory in the past, this program provides a more formal means of promoting

the involvement of amateur astronomers in research at Lowell.

2. Past Collaborations

Amateur astronomers have contributed significantly to research at Lowell. Here are a few recent examples.

2.1 LONEOS

The Lowell Observatory Near-Earth Object Search, directed by Ted Bowell, was aimed at discovering Earth-crossing asteroids. From 1993 to 2008, LONEOS discovered hundreds of NEAs and honed their positions. Four amateurs – Paul Johnson, James Ashley, Robert Cash, and G. H. Bliss – searched LONEOS images for asteroids that were missed by an automatic software procedure. They discovered numerous objects too faint for the LONEOS software, including 2003 SQ₂₂₂, which came within one-fifth of the distance to the moon (Cash *et al.*, 2003). Amateur Charles Juels also undertook follow-up observations to determine the orbits of hundreds of LONEOS discoveries.

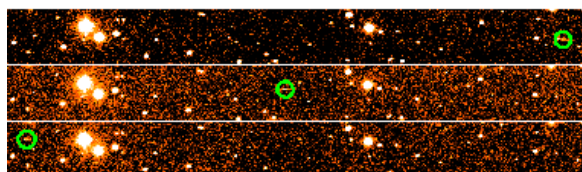


Figure 1. NEA 2003 SQ₂₂₂ was discovered by volunteer Robert Cash. These images show its motion over 41 minutes. The day before, 2003 SQ₂₂₂ had passed just one fifth of the Moon's distance from Earth. Image obtained from online What's Happening Magazine, June 10, 2011; article by Ted Bowell.

2.2 Mars

Amateur Jeff Beish worked with Leonard Martin at Lowell Observatory on monitoring dust storms on Mars (for example, *Martin et al.*, 1991).

2.3 Comets

Amateur Joseph Marcus has analyzed sunlight scattering from Sun-grazing comets (for example, Marcus, 2007). David Schleicher at Lowell used his analysis to build a full phase angle dust scattering model for Comet Halley and determine the comet's emission properties.

3. Current Projects

Lowell Observatory astronomers are currently conducting several projects that would benefit from participation by amateur astronomers. More are likely to be added to this list as the program becomes established and as our scientific staff grows.

3.1 LITTLE THINGS (Deidre Hunter)

LITTLE THINGS is a multi-wavelength study of 41 dwarf irregular galaxies. The goal of the project is to understand how the tiniest galaxies in the universe form stars from the gas between the stars (<http://www2.lowell.edu/users/dah/littlethings/index.html>). Determining the extent to which external interactions with other galaxies have affected their star formation histories is very important.

An amateur with a large telescope, a high quality CCD, and dark skies could contribute significantly by obtaining ultra-deep, stacked images of the LITTLE THINGS galaxies over a wide field of view. People who have done this for other galaxies have found amazing debris left over from galaxy-galaxy interactions or satellite cannibalism (see, for example, Martínez-Delgado *et al.*, 2012), and this has changed our understanding of the factors influencing galaxy evolution.



Figure 2. Dwarf irregular galaxy IC 1613. What lies hidden to our eyes because it is faint or lies outside the field of view of our current images? In this image of IC 1613, blue is far ultraviolet light from young stars, green is green (V-band) light from middle-aged stars, and red is atomic hydrogen gas—the fuel for new star formation. The data are from the LITTLE THINGS project. The color composite image was produced by Lauren Hill.

3.2 Asteroid Recovery (Bruce Koehn)

Data mining of old LONEOS frames could potentially lead to the discovery of new asteroids and old asteroid positions that were not found the first time and to improved photometry of all asteroids. A test on a few frames yielded several asteroids that were missed in the automated search.

3.3 Asteroid Light Curves (Bruce Koehn)

Amateurs with a modest telescope and a CCD camera can participate in an asteroid light curve campaign. The primary targets will be slowly rotating asteroids since they are difficult for a single observer to cover successfully. Additional targets will be Near Earth Asteroids. Web page assistance would be greatly appreciated for this project.

3.4 Monitoring Low-mass Stars (Evgenya Shkolnik)

Stars with masses less than about half the mass of the Sun make up 75% of the Galaxy's stars. An amateur with a good photometer and an optical or H α filter will monitor young and active low mass stars to determine their rotation periods as a function of age, look for eclipsing binary stars, and look for evidence of transiting giant planets. Stellar magnitudes are primarily 12-13 mag in V-band.

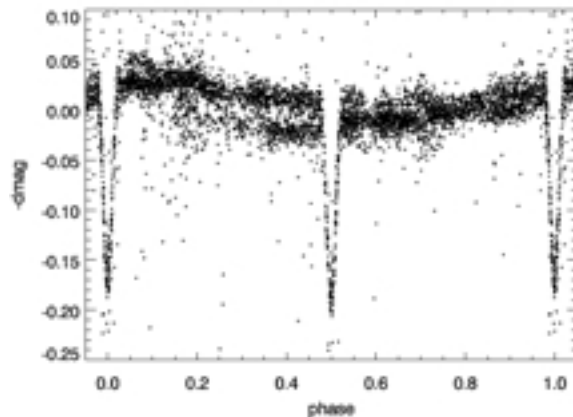


Figure 3. Light curve of the low mass star BD -22 5866, with an eclipse period of 2.21 days. The difference in starspot intensity from two different epochs is clear in the light curve. From Shkolnik et al. (2008).

3.5 Orbits of Centaurs and Kuiper Belt Objects (Larry Wasserman)

Centaur asteroids and Kuiper Belt Objects often have relatively short orbital arcs, resulting in inaccurate sky-plane positions. The amateur involved in this

project would take images of these objects for purposes of astrometry. Because the objects are faint (>18 for Centaurs and >20 for KBOs), this project requires a fairly large telescope, large field view, and dark skies.

3.6 Transiting Exoplanets (Georgi Mandushev)

Help Georgi discover exoplanets, variable stars, and other transient objects through data mining. He has reduced photometric data for several fields near the Milky Way. The fields are 6x6 degrees and contain tens of thousands of stars 10th magnitude and fainter. The data are suitable for identifying and classifying variable stars, other objects, and unidentified transiting planets.

4. How to Participate

Here are the steps for becoming involved in LARI:

1. Go to the LARI web site:
http://www.lowell.edu/LARI_welcome.php.
2. Create a LARI login account.
3. Set up your research profile.
4. A committee at Lowell identifies an amateur whose skills and interests appear to be well matched to a particular project.
5. The astronomer contacts the amateur and they get to work.

5. Acknowledgements

We appreciate the work that Antoinette Beiser has put into organizing LARI and bringing the Lowell Pro/Am Committee together. We also acknowledge Tom Vitron for providing text for the LARI web site. We are grateful to Lowell Observatory and John and Meg Menke for funding participation in this SAS meeting.

6. References

Cash, R. A., Van Ness, M. E., Skiff, B. A. (2003). (2003). "2003-RO3." *Minor Planet Electronic Circular*.

Marcus, J. N. (2007). “Forward-Scattering Enhancement of Comet Brightness. I. Background and Model.” *International Comet Quarterly* **29**, 39-66.

Martin, L. J., Beish, J. D., Parker, D. C. (1991). “Martian Dust Storms in 1990.” *Bulletin of the American Astronomical Society* **23**, 1217.

Martínez-Delgado, D., Romanowsky, A. J., Gabany, R. J., *et al.* (2012). “Dwarfs Gobbling Dwarfs: A Stellar Tidal Stream Around NGC 4449 and Hierarchical Galaxy Formation on Small Scales.” *Astrophysical Journal Letters* **748**, L24.

Shkolnik, E., Liu, M. C., Reid, I. N., Hebb, L., Collier Cameron, A., Torres, C. A., Wilson, D. M. (2008). “BD -22 5866: A Low-Mass, Quadruple-lined Spectroscopic and Eclipsing Binary.” *Astrophysical Journal* **682**, 1248-1255.

Lunar Meteor Impact Monitoring and the 2013 LADEE Mission

Brian Cudnik

Department of Chemistry & Physics

Prairie View A&M University

P.O. Box 519, M.S. 2230

Prairie View, Texas 77446

Abstract

For over twelve years, amateur and professional astronomers have been monitoring the moon regularly for the tell-tale point-like flashes of impacting meteoroids. This endeavor started with my own visual sighting of a lunar Leonid meteor impacting the dark hemisphere of the waxing gibbous Moon on 1999 November 18 (UT). Since then, the Association of Lunar and Planetary Observers (ALPO) has established the Lunar Meteoritic Impact Search (LMIS) section, which I have served as coordinator since early 2000, and we have logged over 80 lunar meteor impact candidates. In this presentation I will provide a brief overview of lunar meteor monitoring techniques, including some of the equipment that people have been using in the field. I will outline how anyone can become involved in this ongoing, fruitful study of this dynamic aspect of our solar system. Finally I will introduce the upcoming LADEE moon mission and discuss how amateur astronomers can be involved in gathering useful scientific data during the Perseid 2013 maximum, and afterwards, in support of this mission.

1. Introduction

Since the invention of the telescope, and even before that, the occurrence of Lunar Transient Phenomena (LTP) has perplexed astronomers, challenging (especially in more recent centuries) the paradigm that the moon is changeless and “dead”. LTP has taken on many forms, including point flashes that appear and disappear in a fraction of a second, but have only been documented by single observers of varying skill levels. There are relatively rare instances of small groups of people at the same telescope or the same observing site documenting LTP, but no reports of two well-separated observers (by at least 50 km), to my knowledge, have been recorded – until 1999.

Since 1999, when the first scientifically confirmed observations of lunar meteor phenomena were recorded, astronomers at various levels have recorded, fairly regularly, the occurrence of point flashes on the moon caused by meteoroid impacts. These turned out to be much more common than lunar eclipses, but their random nature confounded observations of them for centuries. A handful of systematic attempts at observing and cataloging lunar meteoroid impacts have been attempted throughout the 20th century, with one of the most notable being the Association of Lunar and Planetary Observers’ Lunar Meteor Search program which lasted from 1955 to 1965 but failed to provide simultaneous independent observations of lunar meteors. This is not surprising given that the observations were visual at

the time, and it is extremely challenging to document a lunar meteor strike solely by pure visual means. But technology (and a little serendipity) would change that near the dawn of the 21st century.

NASA is planning to launch the latest in a series of spacecraft to the moon, in 2013. The spacecraft, dubbed Lunar Atmosphere and Dust Environment Explorer (LADEE) is scheduled to launch in 2013 July. Collaborations with universities and the amateur astronomy community are sought for this worthwhile project.

2. Historical Background

2.1 The First Confirmed Lunar Meteor Impact Observations and the Formation of ALPO-LMIS

Prior to the uneventful impact of Lunar Prospector in 1999 July, during the fall of 1998, Martin Beech and Simona Nikolova, of the University of Regina, made specific predictions about lunar Leonids, published in their paper (Beech *et al.*, 1998). They realized that the moon would be entering an especially dense filament of meteoroids during the November Leonid meteor shower. David Dunham, president of IOTA (International Occultation Timing Association) coordinated an effort to videotape the unilluminated side of the waxing gibbous Moon during the peak of activity November 18 (3h to 6h UT). At that time, most setups involving video cameras and telescopes were unable to take in the entire

Moon, so the job was partitioned into thirds. People whose last names began with A through H would monitor the northern third of the moon, etc. so as to cover the entire darkened crescent of the waxing Gibbous moon.

Not being equipped with video but having access to a 14-inch f/11 Cassegrain, I visually monitored the moon for impacts and spotted one at 4:46 UT. This was subsequently confirmed on Dunham's video and this confirmation motivated others to check their videos for additional impacts. Initially, six impact events, showing themselves as point flashes of light, were observed and confirmed. New software, developed by Peter Gural, of SAIC (Science Applications International Corporation) for fireball detection was used to locate additional impact events on people's videotapes. This method resulted in five additional, unconfirmed impact candidates being found.

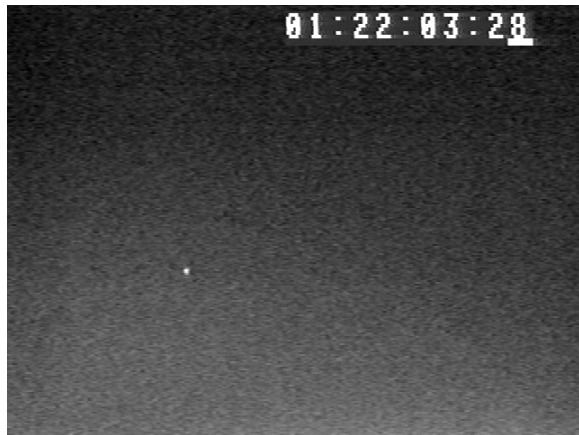


Figure 1. Image of Leonid impact "A" recorded on 18 November 1999 by David Dunham (image courtesy of David Dunham).

In early 2000, the Association of Lunar and Planetary Observers formed the Lunar Meteoritic Impact Search section, for which I was made the coordinator (and remain so to this day). The section enjoyed much activity in the first year of operation, with many observers reported what would later be deemed as spurious (non-impact) events caused by retinal flashes or cosmic ray hits. By the second year, the activity had tapered off, but enjoyed a brief resurgence in 2001 November when the Moon was once again favorably placed to receive impacts from a relatively dense ribbon of meteoroids from the Leonid stream. Two confirmed and two probable impact candidates were recorded with this event.

2.2 More Organizations get Involved

In addition to ALPO-LMIS, IOTA, the Italian Geologic Lunar Researches Group, and the British

Astronomical Association, more groups, individuals, and organizations become involved toward the middle of the first decade of the 21st century. A group from Japan, observing the moon during the Perseid meteor shower of 2004, netted a confirmed Perseid meteoroid impact, the first confirmed non-Leonid lunar meteor. A year later, the Meteoroid Environment Office of NASA Marshall Space Flight Center, Alabama, USA, began a regular program to monitor the moon for two weeks per month with multiple telescopes and video cameras. The first impact event candidate was recorded in early 2005 November, a likely Taurid meteoroid. Since then, this program has recorded over 200 meteor impact events on the Moon.

The observers who contributed to ALPO-LMIS have, over the years, recorded some 80 viable candidates, but only a handful of these were scientifically confirmed. In most cases, the observer was working alone or happened to be looking at the moon for other reasons when he/she is surprised by an impact event. In recent years, however, with the collaboration with NASA-MSFC, several of our active members have recorded impacts that have been confirmed by NASA and vice versa. Figure 2 shows an image of a lunar Geminid impact that I recorded by video in 2010 December.

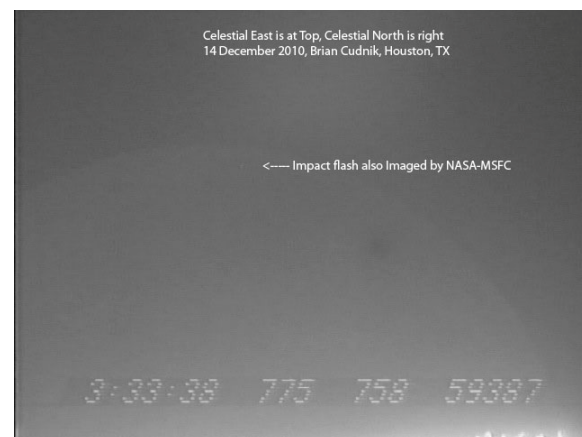


Figure 2. Image of a confirmed lunar Geminid impact, recorded on 14 December 2010 by Brian Cudnik.

2.3 Watching Spacecraft Crash

The ALPO-LMIS, NASA-MSFC MEO and other organizations were active in monitoring any ground-based flashes or plumes produced by the impact of several spacecraft. The first was SMART-1 (European Space Agency) which was commanded to crash-land on the Moon on 2006 September 3. A campaign of ground-based amateur and professional telescopes and observatories was carried out, and nearly everyone observed a negative (i.e., no flash)

result. However, professional astronomers at the Canada-France-Hawaii Telescope Corporation recorded a flash in the infrared (2,122 nm) with the WIRCam wide-field infrared camera on the 3.6-meter optical/infrared telescope on the summit of Mauna Kea in Hawaii. The gif-animation posted on their website, <http://www.cfht.hawaii.edu/News/Smart1/> shows nicely the flash followed by the resultant dust cloud of material kicked up by the impact.

Nearly three years later, the Japanese Kaguya spacecraft was commanded to crash into the moon on 2009 June 10 at 18:25UT. This was daylight for North America so ALPO-LMIS did not coordinate this one. Astronomers in Asia were able to observe the impact flash resulting from this man-made event.

Five months later, in 2009 October, the twin impacts of LCROSS (Lunar CRater Observation and Sensing Satellite) centaur upper stage rocket and LCROSS itself were observed from ground-based observatories all over the moon-facing hemisphere of the Earth. Nothing was observed from the ground, but LCROSS did capture plume images on its way to its own demise (Figure 3). It also detected signs of water (not the water itself, but two convincing signs that water is present, from the profile of the near infrared spectrum recorded by LCROSS's spectrometer to the ultraviolet signature of the hydroxyl (OH) molecule formed when H₂O encounters solar radiation and is disassociated into H and OH molecules.

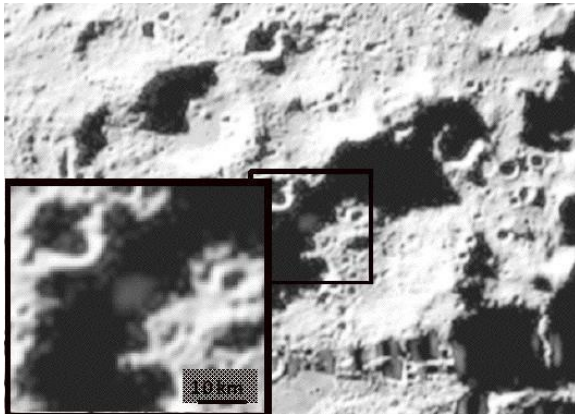


Figure 3. LCROSS image of impact plume generated by the crash of a centaur upper stage rocket seconds earlier. This event was instrumental in providing conclusive evidence for water ice existing in the permanently shadowed craters of the Moon's polar regions. Image courtesy of NASA.

3. Current Work on Lunar Meteors

3.1 "Lunar Meteoroid Impacts and how to Observe Them"

Published in 2010, this first-of-its-kind volume describes the various considerations that go into a lunar meteor monitoring program. It is a collection of work from various sources on all the stages involved in this sort of endeavor. This book provides a useful reference and training reference for those getting started with lunar meteor monitoring. It also provides resources for those who have been involved in astronomy for some time.

As the name of the book implies, it starts with some background information about the cratering history of the moon and the history of LTP sightings from the 1500's onward. The LTP catalog it provides focuses on events that resemble manifestations of meteoroid impacts and includes only the events that have the highest confidence ranking. Many of these were observed by skilled observers, giving the events significant credibility.

The second half of the book focuses on the tools and techniques of lunar meteor observation. I focus on the video-equipped observer, but I also do not leave out the visual observer. I provide references and resources to provide observers with what is needed to carry out a fruitful campaign, and I share the dates of some of the more significant lunar meteor opportunities for years to come.

3.2 Current and Ongoing Efforts

The ALPO-LMIS continues to coordinate a world-wide effort in monitoring the moon for meteoroid impacts. It does so through its website, through informal e-mail communication, papers at local conferences, and a list-server called lunar-impacts@yahoo.com. The level of activity and participation varies from year to year depending on the circumstances of the moon's position during annual meteor showers.

NASA-MSFC also continues to monitor the moon regularly and has, as of 2011 November, recorded 233 impact candidates. Most of these are from sporadic meteors, but a number of annual showers are represented in the impact list. They monitor the moon about 10 nights per month, when the illumination is between 10 and 55 percent. The distribution of impacts may be more a reflection of where the monitoring is centered (from roughly ± 30 degrees latitude and from 20% radius from disk center along the lunar equator to the limb).

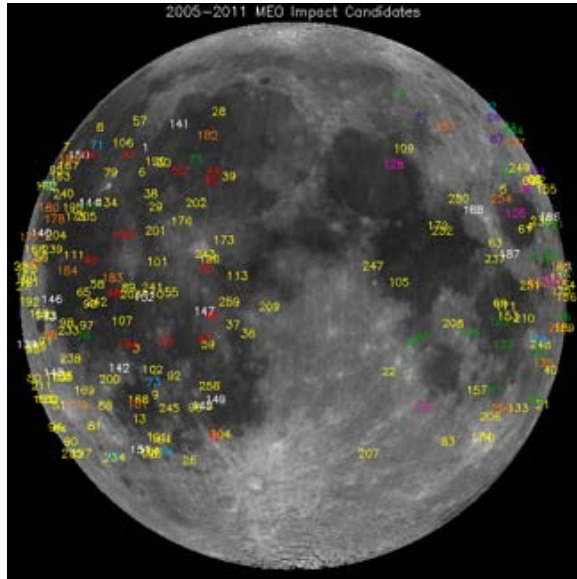


Figure 4. Map showing the locations of the 233 meteoroid impacts observed by NASA-MSFC from late 2005 to late 2011. The clustering of impact sites visible in the image may be more of a selection effect, refer to the text for more details. This image is courtesy of NASA-MSFC Meteoroid Environment Office.

In both the ALPO and the NASA cases, monitoring takes place during a one week period from a few days after new until a day or two after first quarter, then again a day or two before last quarter until a few days before new. In these cases, the “few days” will last between 3 and 5 days, depending on ecliptic angle at a given observing location. If an annual shower is active, it will be monitored as part of the two week monitoring period, with a possible extension beyond the set periods to accommodate a shower peak or extend the monitoring due to lingering shower activity.

Collaboration continues between NASA-MSFC and ALPO-LMIS. In both cases, the preferred monitoring method involves video and in both cases the video is analyzed by programs such as LunarScan or UFOCapture to capture the transient flashes. Usually one party discovers the event while the other party confirms with their videotapes and vice versa.

3.3 CMOS Imaging

As part of our program to include new technologies (or at least technologies not widely used but potentially beneficial for research), we are also employing still imagery of the moon. We are using a CMOS (Complementary Metal Oxide Semiconductor) imager, assembled by Holland *et al.* (2008, 2009) to do systematic imaging of the illuminated lunar disk to look for several things (Cudnik *et al.*, 2011a):

- Systematic imaging to study the ray structures of the moon at various phases not limited to full moon
- Imaging for photometric and radiometric studies
- Imaging of earthshine to gather information of the Earth’s albedo over time
- Filtered and unfiltered imaging of the moon throughout its phase cycle to look for and characterize other forms of LTP
- High cadence observations of lunar eclipses to determine crossing times of lunar features by the Earth’s shadow as well as estimates of contact times of the shadow with the lunar disk



Figure 5. Ground-based image of the entire lunar disk taken on 23 November 2010, obtained with a CMOS electronic detector and a Celestron NexStar 8-inch (20 cm) Cassegrain telescope. Image Credit: Prem Saganti, Gary Erickson, and Brian Cudnik.

We will be working on the above in conjunction with other groups such as ALPO to maximize the value of our collaborative efforts. The goal is to enable the determination of a viable cause for other form of LTP in a similar manner as lunar meteor observations have been successfully used to validate and explain the point flash form of LTP.

3.4 Observing Program Nuts and Bolts

We are always welcoming observations of the moon in search of lunar meteoroid impacts. Although we prefer the video method for observing and recording lunar meteors, we do not want to leave the visual observer out. Visual observers may be such due to personal preference or economics (financial difficulty preventing the purchase of equipment for video observation and data reduction). The advice I offer visual observers is this: ensure you are well rested and focused before your first observing ses-

sion, use a short wave radio and tape recorder and blank moon map to record your observed candidates, take frequent breaks after 10 or 15 minutes of observation to minimize fatigue (and resultant lost impact events), and finally, if there is any doubt, call it out anyway. Given the extremely transient nature of lunar meteoroid impacts, a very quick but noticed flash may very well turn out to be a genuine event. This, of course, is dependent on simultaneous video observation of the same region of the moon at the same time.

This brings me to video observations. The active lunar meteor observer George Varros has an excellent tutorial on his website, www.lunarimpacts.com, which provides a handy walkthrough, from start to finish, of a typical observing run. A typical setup includes a telescope with a wide field of view, or a focal reducer, a low light black and white CCD video camera (like what people find with security vendors, an example is a Watec 902H2 Ultimate) a video time insertion / GPS device for recording time and geographic position, a recording device such as a digital video camcorder or a portable DVD recorder, and the means to store vast amounts of data. The equipment is set up to monitor the moon for one or more hours and the video is recorded for later analysis. One may also record nearby stars for magnitude estimates of any recorded impact candidate.

Once the observing run is complete, or during the observing run if one is capable of doing so, the data is streamed into a program called LunarScan 1.5 written by Peter Gural, which takes 1 GB chunks of data and “looks for” impact candidates. The video stream is broken up into these chunks using a program called Virtual Dub. These chunks are then scanned frame by frame to look for meteoroid impact point flashes. Once a set of candidate impacts are found by the software, it is up to the user to weed out transients such as video noise or cosmic ray hits.

After a list of likely candidates, including date, time, position, estimated magnitude, etc. is generated, this information is reported to NASA-MSFC and ALPO-LMIS. The observing team at NASA-MSFC may have been observing at the same time and can provide confirming observations of one or more of the impact candidates; the ALPO-LMIS serves to coordinate the former along with interested individuals and groups, they may be able to contact someone else observing at the same time to obtain a confirmation of one or more of the events observed.

3.5 Lessons Learned

We have come a long way as far as lunar meteor monitoring is concerned. The technology has greatly improved since the early Leonid days of late 1999, and over twelve years of experience on many fronts

have improved the techniques and approaches to lunar meteor observation. These are quite common events, but are randomized enough and of extremely short duration (20 to 100 milliseconds) so as to make them a significant challenge to observe.

The presence of spurious events such as cosmic ray hits were quickly found to mimic real lunar meteor impact flashes, but closer inspection of these transients revealed subtle differences between these and true impact events. These differences include a fuzzy versus sharp flash profile, the flash appearing over multiple frames versus a single frame, etc. While these differences are not always easily discernible, knowing them did go a long way in helping to narrow down which events were more likely to be genuine events and which were not.

The best, most foolproof means of determining whether an event is a genuine impact event remains this: to use two independent setups spaced at least 30 km apart observing at the same time to document the same event, within less than a second difference in event time and less than 5” difference in position on the moon’s disk.

4. Upcoming Project: Observations in Support of the LADEE Mission

The Lunar Atmosphere and Dust Environment Explorer (LADEE, Fig. 6) is a NASA spacecraft that will orbit the Moon and explore the dust and atmosphere environment at the moon. The mission is currently set for launch on a Minotaur-V launch vehicle in early 2013 July. After a 32 day cruise phase and a 30 day checkout period, the satellite will be ready to take data by mid-September. Unfortunately this is too late for a favorable Perseid encounter with the moon, which was originally going to be the focus of the collaborative effort. However, sporadic meteor impacts, regularly observed, will become the focus of observational efforts during the 60 day mission.

The purpose of supplementing the LADEE mission with ground-based observations is to identify distinct impact events that are expected to kick up dust and inject it into the near-moon environment, replicating in some ways the days of Apollo 17 when sketches made by Eugene Cernan from lunar orbit showed some unusual optical phenomena minutes to seconds before orbital sunrise. Most noticeable of this is a set of crepuscular rays that seem to be caused by scattering attributed to particles or molecules of some type. In the airless environment of the moon, one would not expect to see any such phenomena. This leads to the question of what is replenishing the dust or material and how does it remain suspended above the lunar surface.

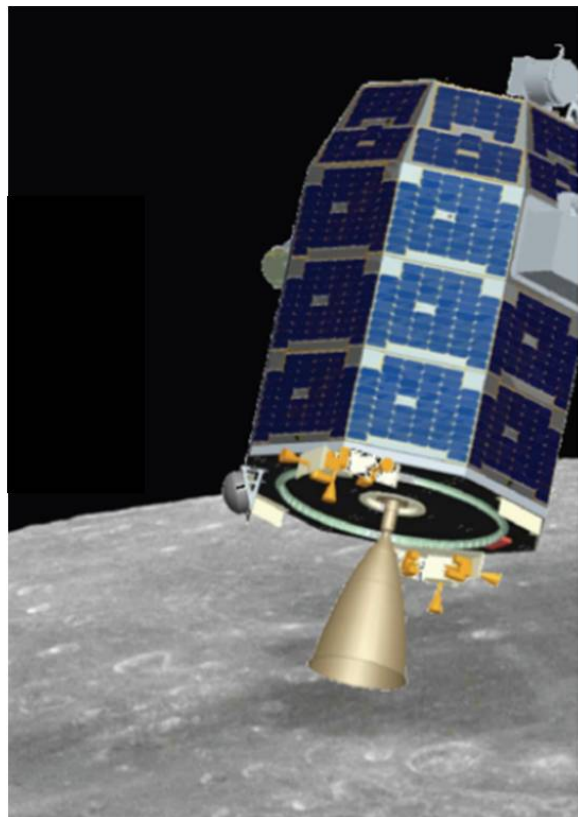


Figure 6. The LADEE spacecraft at the Moon, artist's conception. Image courtesy of NASA.

To answer these questions, Dr. Brian Day of NASA-Ames has requested ground-based observations in collaborative support of the mission. These will be observations of lunar meteoroid impacts, made by interested amateur astronomers and participants at universities. The idea would be to characterize the source of the dust aloft by correlating increased fluxes of dust with impact events. If enough of these correlative events are documented, this effort will go a long way in answering the questions about what the Apollo astronauts (and unmanned Surveyor spacecraft) saw from the moon: the crepuscular rays and the horizon brightening just prior to sunrise.

In preparation for this campaign, I will be upgrading the astronomical aspect of the department of Chemistry and Astronomy at Prairie View A&M University. The plan is to employ our physics majors to make the routine observations of the moon to match what NASA-MSFC is doing: for 10 days per month, monitor the moon (between 10% and 55% illumination) with a video camera and telescope system in search for meteoritic impacts. I plan to upgrade existing equipment to handle the expected heavy data load, and I plan to enable a semi-automated system to be run for each observing session. Data will be collected and analyzed in near real

time at the University, and candidates will be logged, evaluated, reported, and catalogued.

In addition to the university's efforts, I will be contacting existing and new collaborators to encourage them to put forward the effort to monitor the moon as often as they are able to each month, in support of existing regular campaigns. Ideally I would like to have a global network, monitoring the moon continuously (24 hours a day) for five days waxing and five days waning. But weather and a host of other influences will likely curtail this, but we will observe as much as we can.

The monthly 10-day campaign will begin sometime later in 2012 and will continue prior to the launch of LADEE, and will continue through the science phase and afterwards. Impacts will be catalogued with me as coordinator of ALPO-LMIS and with NASA-MSFC, the Meteoroid Environment Office as part of their ongoing program. Sporadic meteoroid impacts happen fairly regularly and are expected to provide stimuli for, as well as an agent to maintain, the existing dusty environment in the vicinity of the moon. Meteoroid impacts are also thought to play a role in the replenishment of the lunar sodium exosphere (Bellot Rubio, *et al.*, 2000).

5. Conclusion

Professional-Amateur (pro-am) collaboration is enjoying a sort of "golden age" as professionals willingly seek out the assistance of amateurs in their research endeavors. The professionals have the training and the ideas, as well as the funding through grants and contracts, while the amateurs have the time and the equipment that could benefit a professional's project. Lunar meteor astronomy is an excellent example of pro-am collaboration at its finest.

The Lunar Meteoritic Impact Search section of the Association of Lunar and Planetary Observers (referred to as "ALPO-LMIS" in this paper) has been coordinating the activities of interested amateur and professional astronomers since 2000 and has resulted in over 80 impact candidates being documented. A professional group at NASA, at the Marshall Space Flight Center (referred to as "NASA-MSFC" in the paper) Meteoroid Environment Office, coordinated by Dr. Bill Cook, has been regularly monitoring the moon for meteoroid impacts since late 2005 and as of 2011 November, have logged 233 impact candidates, most of which have been confirmed. Both groups have been working together for the last six years on lunar meteor observation and collaboration.

A NASA mission to the moon, to be launched in 2013 July, is the Lunar Atmosphere and Dust Environment Explorer (LADEE), which is expected to

better our understanding of the lunar dust environment and connections between suspended dust and meteoroid impacts. ALPO-LMIS has been asked to collaborate with them during the mission timeframe (late summer to early fall 2013) to observe meteoroid impacts on the moon in order to help correlate increases in dust abundance with meteoroid impacts. This partnership will be an excellent one to further our understanding of the near-moon environment, including the moon's exosphere and changes to it related to impacts.

Anyone who is interested in contributing to the LADEE portion of the campaign, or the general lunar monitoring campaign is encouraged to contact me or visit www.alpo-astronomy.org for more information.

6. Acknowledgements

I want to thank Robert Buchheim for encouraging me to share with the Society of Astronomical Sciences the work I am helping to coordinate. I am thankful for Dr. Premkumar Saganti, my colleague at Prairie View A&M University for his support and encouragement. I also thank Brian Day for providing the opportunity for collaboration between a worthwhile space-based mission and a worthy ground-based observing program. Finally, many thanks go to Mr. Doug Holland for providing the CMOS detector and all the help in its operation.

7. References

Beech, M. and Nikolova, S. (1998). "Leonid flashers-meteoroid impacts on the Moon." *Il Nuovo Cimento, Note Brevi* **21C**, 577-581.

Holland D., *et al.* (2008). U.S. Patent-7411198.

Holland D., *et al.* (2009). U.S. Patent-7521682.

Cudnik, B. M., Saganti, P. B., Erickson, G. M. (2011). "Imaging Detectors in Planetary and Space Science." 42nd Lunar and Planetary Science Conference, 2011 March 7-11 at The Woodlands, Texas. No. **1608**, p. 1543.

Bellot Rubio, L. R., Ortiz, J. L., Sada, P.V. (2000). "Observation and Interpretation of Meteoroid Impact Flashes on the Moon." *Earth Moon and Planets*, **82/83**, 575-598.

First Attempts at Asteroid Shape Modeling

Maurice Clark

Physics Department, Texas Tech University

5200 Broadway Lubbock TX 79411

maurice.clark@ttu.edu

Abstract

Results are presented from initial attempts at asteroid shape-modeling. Three asteroids were chosen in this study: 1708 Polit, 2036 Sheragul and 3015 Candy. Observations used in this study were made by the author, at a variety of locations, most recently at the Preston Gott Observatory at Texas Tech University.

1. Introduction

Having worked on asteroid photometry for some 10 years and built up an archive of more than 100 well-characterized lightcurves, I decided early in 2011 to start re-observing some asteroids with the intention of using the data to model their 3-dimensional shape.

Three asteroids were chosen for this first attempt: 1708 Polit, 2036 Sheragul, and 3015 Candy. All three are main-belt asteroids for which I had very good lightcurve data. 1708 Polit, (Clark, 2011) and 3015 Candy (Clark, 2007) had been observed in 2005 while 2036 Sheragul had been observed in 2003 and 2010 (Clark 2004; Clark, 2011).

Period analysis was also done in MPO *Canopus*, which implements the algorithm developed by Alan Harris (Harris *et al.*, 1989). Differential magnitudes were calculated using reference stars from the USNO-A 2.0 catalog and the UCAC2 catalog. Shape models were derived from the lightcurve data using MPO *LCInvert*.

2. The Observatories

Rosemary Hill Observatory (MPC code 831) is owned by the University of Florida, Gainesville, and is located near Bronson, Florida, at an elevation of 51 m. The main instrument at Rosemary Hill is a 0.76-m Tinsley reflector. For these observations, the instrument was used at its $f/5$ Newtonian focus with an SBIG ST-7E CCD camera.

The Preston Gott Observatory is the main astronomical facility of the Texas Tech University. Located about 20 km north of Lubbock, the main instrument is a 0.5-m $f/6.8$ Dall-Kirkam Cassegrain. An SBIG STL-1001E CCD was used with this telescope.

Bucknell Observatory is located on the campus of Bucknell University in Lewisburg, Pennsylvania. The elevation is 171 m. The telescope used for these observations was a 0.35-m Celestron working at $f/7$ with a focal reducer. The CCD camera was an SBIG ST-9E.

Year	Date Range	Solar Long	Obs	Sess	Per (h)	Err	Amp	Err
2005	Jan 05 - Mar 06	133°-164°	Rosemary Hill	5	7.507	0.001	0.4	0.1
2011	May 06 - Jun 22	224°-240°	Preston Gott	6	7.5085	0.0008	0.35	0.1

Table I. Observational data for 1708 Polit.

Year	Date Range	Solar Long	Obs	Sess	Per (h)	Err	Amp	Err
2003	Jul 29 - Aug 04	232°-238°	Bucknell	5	5.41	0.01	0.58	0.02
2010	Oct 31 - Nov 28	24°-36°	Preston Gott	4	5.413	0.001	0.95	0.02
2012	Jan 18 - Jan 29	54°-67°	Preston Gott	4	5.4120	0.0002	0.60	0.02

Table II. Observational data for 2036 Sheragul.

Year	Date Range	Solar Long	Obs	Sess	Per (h)	Err	Amp	Err
2005	Dec 22 - Dec 29	45°-52°	Rosemary Hill	5	4.6248	0.0003	1.05	0.05
2011	May 06 - Jun 22	209°-225°	Preston Gott	4	4.6249	0.0002	0.85	0.05

Table III. Observational data for 3015 Candy.

3. Observations and Data

Tables I-III summarize the observations used in this study. Included in the tables are the dates over which observations were obtained, the heliocentric longitude of the asteroid, the observatory at which the observations were obtained, the number of observing sessions in which useful data was obtained, the derived period and its estimated uncertainty, and finally the amplitude of the lightcurve and its estimated uncertainty. The resulting lightcurves are shown in Figures 1-7.

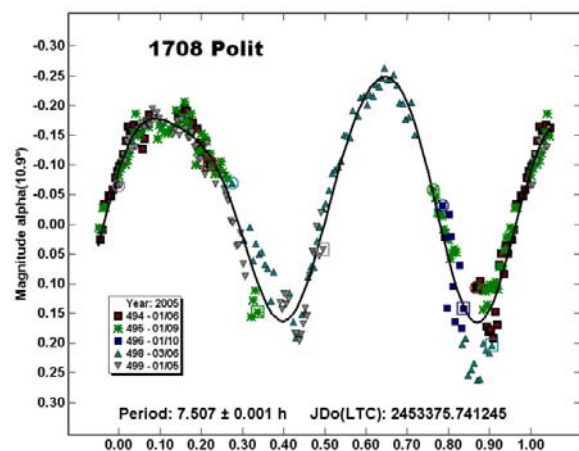


Figure 1. 2005 lightcurve for 1708 Polit

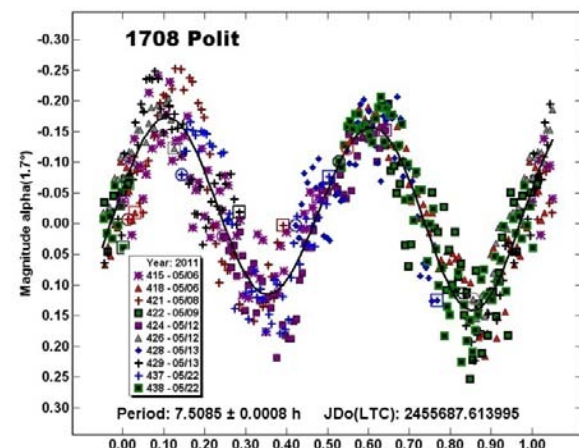


Figure 2. 2011 lightcurve for 1708 Polit

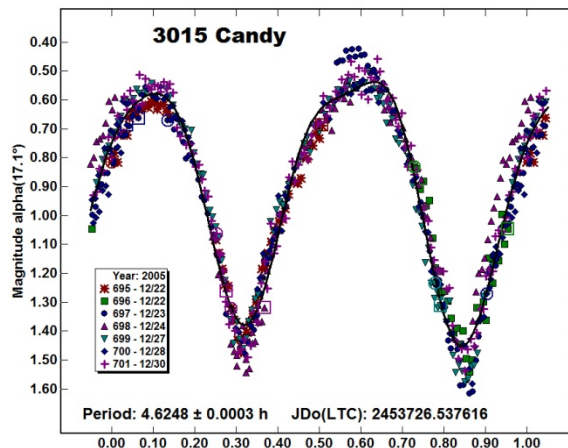


Figure 3. 2005 lightcurve for 3015 Candy

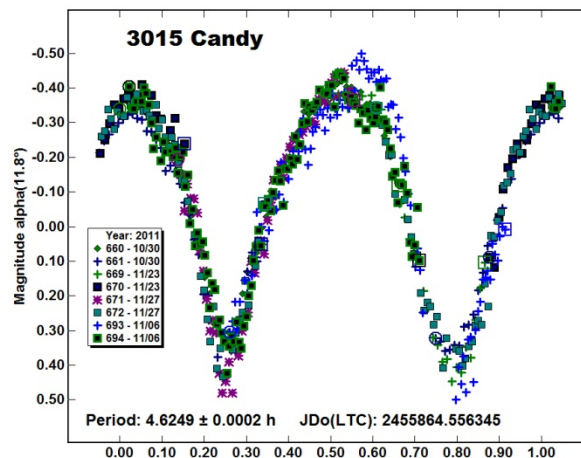


Figure 4. 2011 lightcurve for 3015 Candy

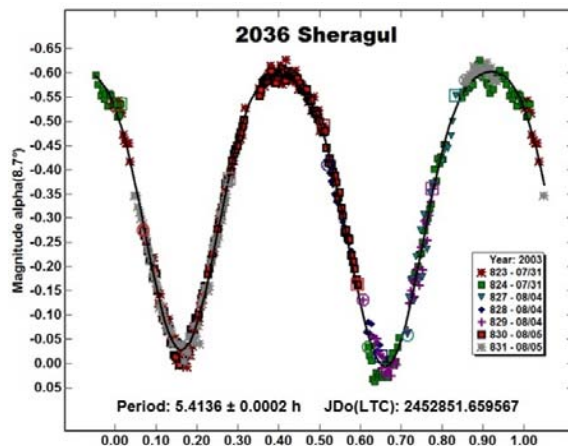


Figure 5. 2010 lightcurve for 2036 Sheragul

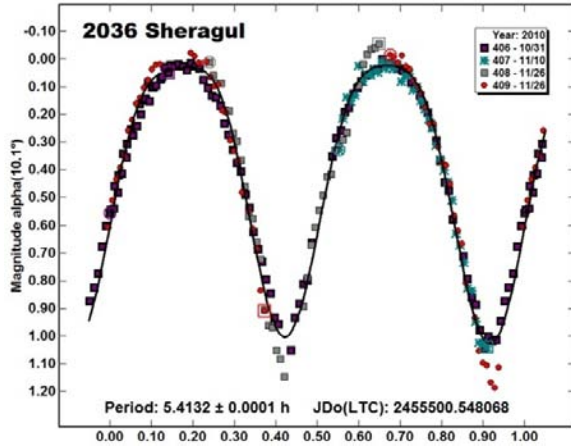


Figure 6. 2010 lightcurve for 2036 Sherugul

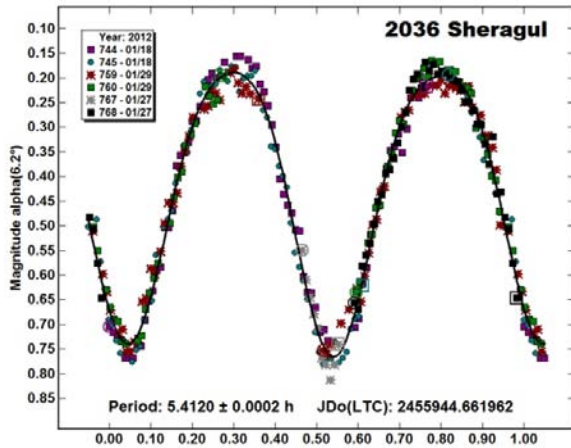


Figure 7. 2012 lightcurve for 2036 Sherugul

4. Analysis

It should be noted that, because of the nature of the lightcurve inversion process, solutions for asteroids that have low-inclination orbits (in reference to the ecliptic plane) usually come in “pairs” where the latitude (b) of the pole, referenced to the ecliptic plane, is nearly the same but the longitudes (λ) of differ by about 180° .

Another possibility is for two solutions where the longitudes differ by about 180° but the latitudes are somewhat mirrored, i.e., one is positive – indicating prograde rotation – while the other is negative – indicating retrograde rotation. In this case, the absolute values of the latitudes are not always similar. In some cases, four solutions are found, combining the two possibilities given above.

4.1 General Procedure

For each asteroid, the lightcurve data outlined in Tables I-III were used in *LCInvert* to find a probable synodic period. A sidereal period was then derived, again using *LCInvert*. This period was applied in a pole search that generated 310 solutions using discrete, fixed longitude-latitude (λ, β) pairs but allowing the sidereal period to “float.”

This produces a “pole search plot” where the log(chi-square) value found in the search for each discrete pair is color-coded to help look for possible solutions. In the plots, deep blue represents the lowest chi-square value and deep red (maroon) represents the highest value. All other values are scaled between dark blue and bright red.

An ideal solution has only one small region of deep blue, a small region of bright red, with the rest of the plot a mix of colors from aqua to yellow. There may be two regions of blue within the sea of mid-colors, indicating the two possible pole solutions discussed above.

If the plot is awash in blues, then the solution is, essentially, meaningless since this means that almost any solution was as good as any other.

Once one or more probable solutions were found, a new search was made using one of the solutions as the starting point, this time allowing the longitude and latitude to float as well as the period. For the final results, the error for the poles is approximately $\pm 10^\circ$ while the period solutions have errors on the order of 2-3 units in the last decimal place.

4.2 1708 Polit

The pole search plot for 1708 Polit is shown in Figure 8. This shows a general solution near $(30^\circ, -10^\circ)$ and a second one near $(210^\circ, +40^\circ)$.

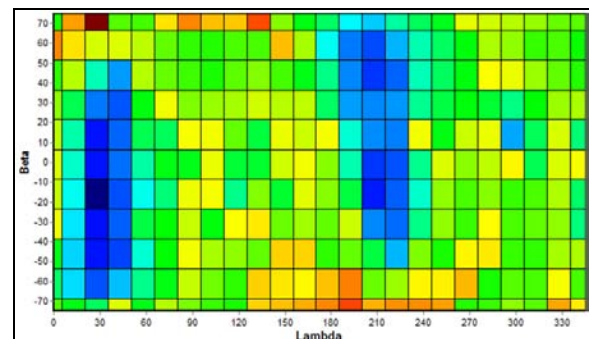


Figure 8. Plot of the log (chi-square) values for 1708 Polit. Dark blue represents the lowest chi-square value.

The final result showed two possible solutions: $(27^\circ, -33^\circ, 7.50837340 \text{ h})$ and $(210^\circ, +47^\circ, 7.50832256 \text{ h})$ The models for these are shown in

Asteroid Shape Modeling - Clark

Figures 9 and 10. The preferred solution is the one at $(210^\circ, +47^\circ)$, or a prograde rotation. Supporting this preference is the derived axis of rotation. As visible in Figures 9 and 10, the spin axis is much more closely aligned with the shortest axis of the asteroid with the $(210^\circ, +47^\circ)$ solution, a much more likely scenario. Also supporting the preferred solution is that the model's lightcurve more closely matches the observed lightcurve, particularly for the 2011 observations. Examples of this are shown in Figures 11-14.

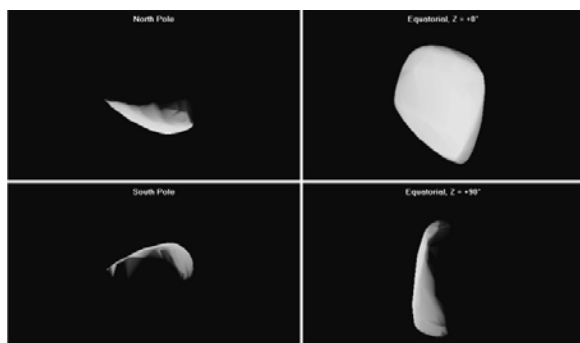


Figure 9. 3-D model of 1708 Polit for solution $(27^\circ, -33^\circ, 7.50837340 \text{ h})$.

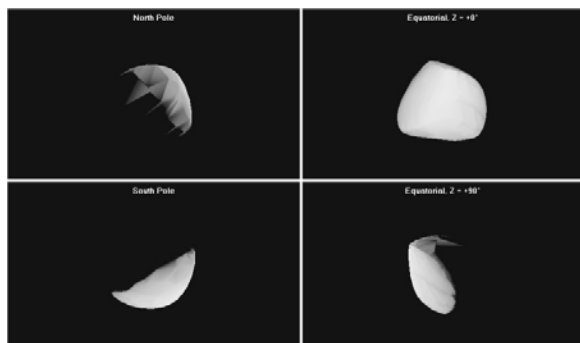


Figure 10. 3-D model of 1708 Polit for solution $(210^\circ, +47^\circ, 7.50832256 \text{ h})$.

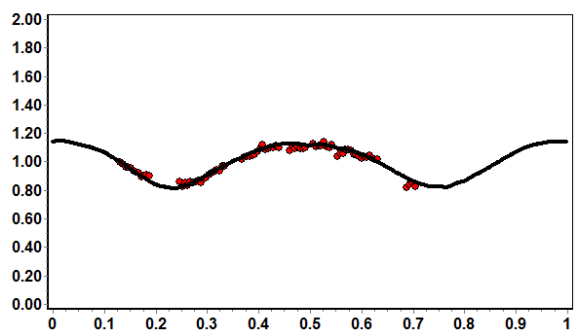


Figure 11. Correspondence between model (black) and observed (red) lightcurves of 1708 Polit for solution $(27^\circ, -33^\circ)$ for 2005 January 9.

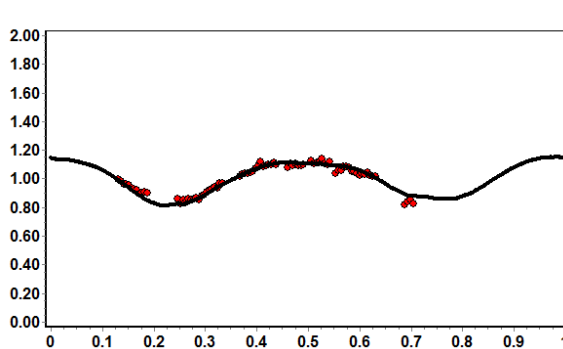


Figure 12. Correspondence between model (black) and observed (red) lightcurve of 1708 Polit for solution $(27^\circ, -33^\circ)$ for 2011 May 6.

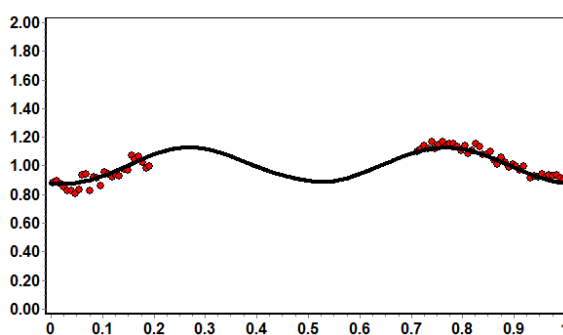


Figure 13. Correspondence between model (black) and observed (red) lightcurve of 1708 Polit for solution $(210^\circ, +47^\circ)$ for 2005 January 9.

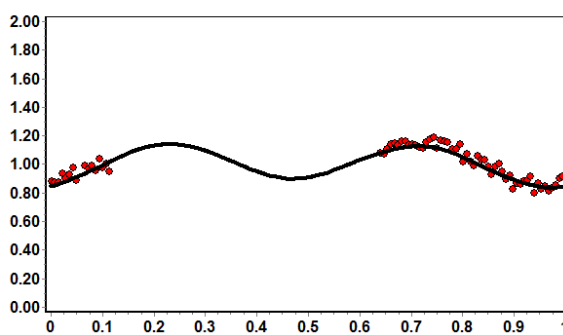


Figure 14. Correspondence between model (black) and observed (red) lightcurve of 1708 Polit for solution $(210^\circ, +47^\circ)$ for 2011 May 6.

4.3 2036 Sheragul

The pole search plot for 2036 Sehragule is shown in Figure 15. This indicates one general solution near $(130^\circ, +50^\circ)$. There is a possible second near $(310^\circ, -30^\circ)$, but it is not very obvious.

The final result showed two possible solutions: $(134^\circ, +38^\circ, 5.41283557 \text{ h})$ and $(314^\circ, -46^\circ,$

5.41282858 h) The models for these are shown in Figures 16 and 17.

The solution at $(134^\circ, 38^\circ)$ is slightly preferred since the model fits the observed lightcurves slightly more closely. However the difference is minimal. Examples of the model fit with observed lightcurves are shown in Figures 18-21. Given the clear ambiguity in the results, more observations at future oppositions are needed.

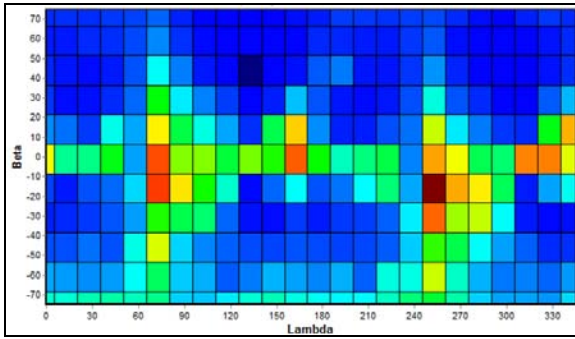


Figure 15. Plot of the log (chi-square) values for 2036 Seheragul. Dark blue represents the lowest chi-square value.

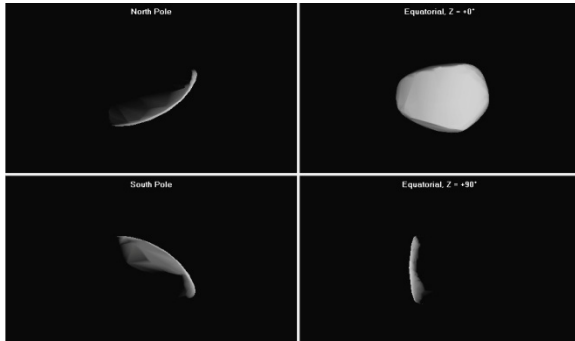


Figure 16. 3-D model of 2036 Seheragul for solution $(134^\circ, +38^\circ, 5.41283557 \text{ h})$.

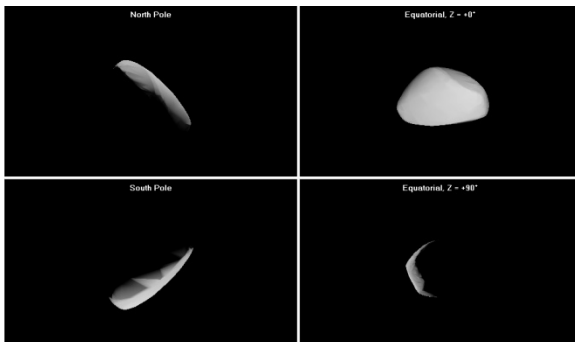


Figure 17. 3-D model of 2036 Seheragul for solution $(314^\circ, -46^\circ, 5.41282858 \text{ h})$.

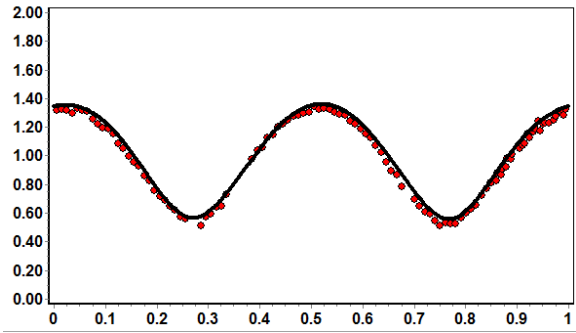


Figure 18. Correspondence between model and observed lightcurve of 2036 Seheragul for solution $(134^\circ, +38^\circ, 5.41283557 \text{ h})$ for 2010 October 31.

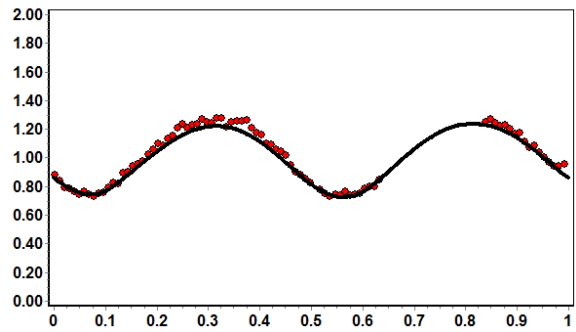


Figure 19. Correspondence between model and observed lightcurve of 2036 Seheragul for solution $(314^\circ, -46^\circ, 5.41282858 \text{ h})$ for 2010 October 31.

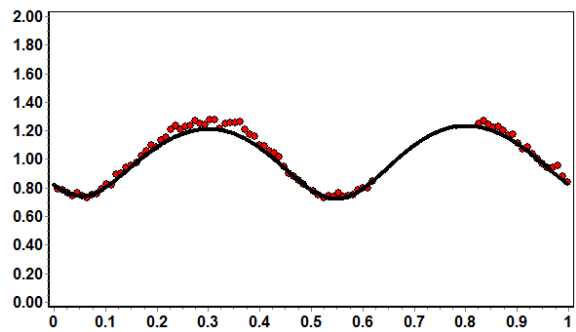


Figure 20. Correspondence between model and observed lightcurve of 2036 Seheragul for solution $(134^\circ, +38^\circ, 5.41283557 \text{ h})$ for 2012 January 18.

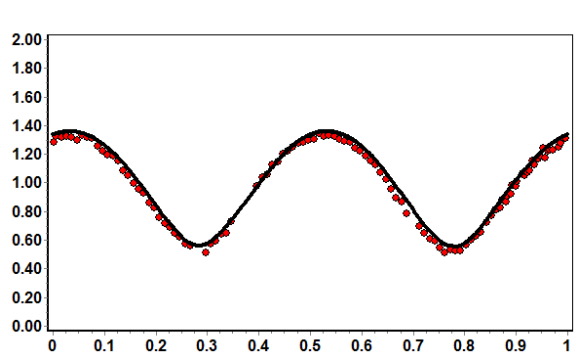


Figure 21. Correspondence between model and observed lightcurve of 2036 Sheragul for solution (314°, -46°, 5.41282858 h) for 2012 January 18.

4.4 3015 Candy

The pole search plot for 3015 Candy is shown in Figure 22. This shows one general solution near (110°, +15°). However there is no strong solution as shown by the large area of blue. This indicates that the pole direction and therefore the shape are poorly constrained.

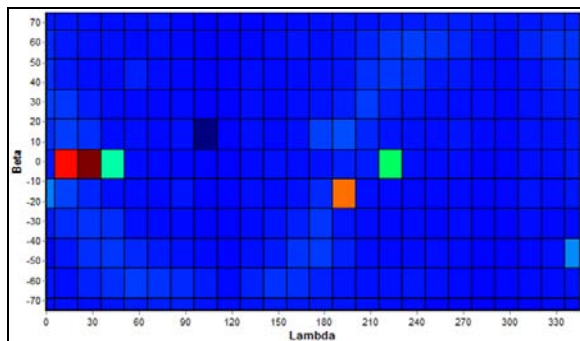


Figure 22. Plot of the log (chi-square) values for 3015 Candy. Dark blue represents the lowest chi-square value.

Two possible solutions were found in the secondary search: (103°, +17°, 4.62500318 h) and (277°, -79°, 4.62498205 h).

Examining the resulting models (Figures 23 and 24), there is little to choose between them. The (103°, +17°) solution slightly more closely matches the observed lightcurve. However, the difference appears minimal. Examples of this correspondence are shown in Figures 25 and 26.

This ambiguity is not surprising given how poorly the pole direction was constrained. As a result, the models presented here have a low confidence. Probably the main cause of this uncertainty is that the observations of the asteroid were made 180° apart in heliocentric longitude. Further observations at future oppositions are required to determine which, if either, of these models reflect reality.

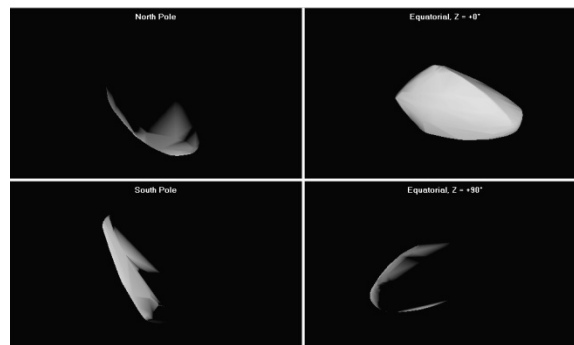


Figure 23. 3-D model of 3015 Candy for solution (103°, +17°, 4.62500318 h).

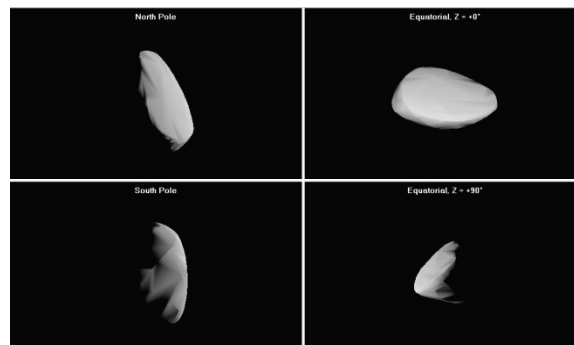


Figure 24. 3-D model of 3015 Candy for solution (277°, -79°, 4.62498205 h).

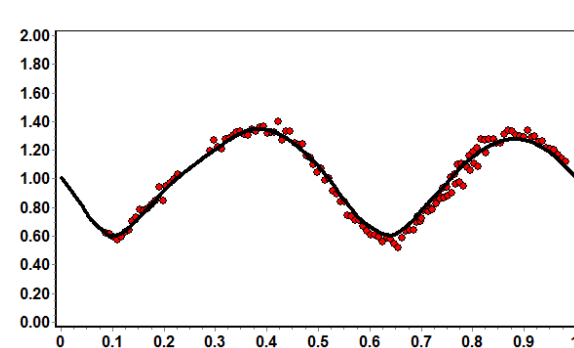


Figure 25. Correspondence between model and observed lightcurve of 3015 Candy for solution (103°, +17°, 4.62500318 h) for 2011 November 6.

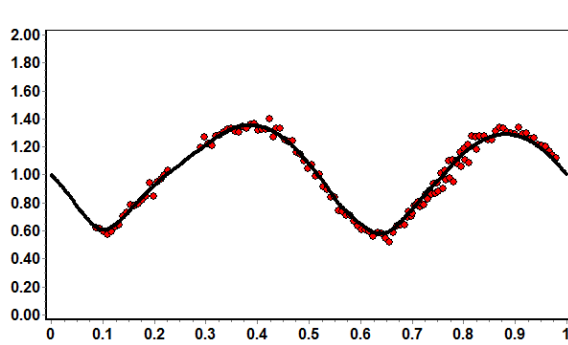


Figure 26. Correspondence between model and observed lightcurve of 3015 Candy for solution (277° , -79° , 4.62498205 h) for 2011 November 6

5. Conclusions

Converting lightcurves into 3-D models of these asteroids has been an interesting experience, despite the steep learning curve. It is certainly a worthwhile endeavor and something I would encourage other asteroid photometrists to become involved in. Of the three asteroids studied in this paper, the results for 1708 Polit have the highest confidence, while those of 3015 Candy are very poorly constrained. Further observations at other heliocentric longitudes are planned to further refine the models presented here.

6. Acknowledgements

I would like to thank Mikko Kaasalainen and Brian Warner for answering all my email questions regarding lightcurve inversion and Brian Warner for all of his work with the program *MPO LCInvert*.

7. References

- Clark, M. L. (2004). "Rosemary Hill Observatory Photometry of Asteroids 2036 Sheragul And (21652) 1999 OQ2." *Minor Planet Bulletin* **31**, 15-16.
- Clark, M. L. (2007). "Lightcurve Results for 1318 Nerina, 2222 Lermontov, 3015 Candy, 3089 Oujianquan, 3155 Lee, 6410 Fujiwara, 6500 Kodaira, (8290) 1992 NP, 9566 Rykhlova, (42923) 1999 SR18, and 2001 FY." *Minor Planet Bulletin* **34**, 19-22.
- Clark, M. L. (2011). "Asteroid Lightcurves from The Preston Gott And Mcdonald Observatories." *Minor Planet Bulletin* **38**, 187-189.

Diurnal Parallax Determinations of Asteroid Distances Using Only Backyard Observations from a Single Station

Eduardo Manuel Alvarez
Observatorio Los Algarrobos, Salto, Uruguay
Costanera Sur 559, Salto 50.000, URUGUAY
olasu@adinet.com.uy

Robert K. Buchheim
Altimira Observatory
Coto de Caza, CA 92679, USA
Bob@RKBuchheim.org

Abstract

A method of using diurnal parallax for determining the distance to asteroids has been developed, which provides excellent accuracy using an amateur-level telescope and CCD, and a surprisingly simple set of observations. Data from two consecutive nights is sufficient, obtained at the beginning of each night, and at each culmination. Just those few data points proved to be enough to allow computing accurately (better than 5%) the distance to the asteroid. Results for several asteroids will be shown.

1. Introduction

The direct comparison of two observations of a relatively near object obtained at exactly the same time from two different stations, where it shows some angular displacement (parallax) with respect to the distant background stars, is a well-known exercise in positional astronomy (astrometry). In fact, as early as 1672 Cassini was able to demonstrate its full validity by achieving quite good results for Mars' parallax – although the extensive travel, and years of preparation and data reduction that this required are testimony to just how difficult a proposition it was!

The advent of photography made this parallax issue far more practical, and the use of CCD cameras made it far more accurate.

Twenty years ago Ratcliff and colleagues reported that they had successfully made parallax observations of two asteroids by this method (Ratcliff et al., 1993). Those pioneering measurements were accomplished after a careful and long preparation, involving the joint and synchronized work of two research observatories. Several years later the measurement of asteroid parallax by means of small telescopes was addressed in detail for Near Earth Objects (NEO) (Smallwood *et al.*, 2004), who exclusively referred to simultaneous measurements obtained from two stations.

In contrast, the method of diurnal parallax requires only a single observing site, and uses a baseline that is provided by the rotation of the Earth. This is also a historically significant and a simpler method

to use (compared to the two-station parallax). It seems to have been first successfully applied to the solar system by Flamsteed in 1672, to measure the parallax of Mars (Forbes, 1976) and later by Lindsay and Gill, when they measured the parallax of Juno in 1874 (Lindsay and Gill, 1877).

The possibility that amateurs could use the diurnal parallax effect for determining Solar System distances from CCD images obtained from just one single observing point has been recently discussed in practical terms by Vanderbei and Belikov (2007) and Buchheim (2011). However, both approaches present drawbacks – the first one requiring precise orbital data which is not obtained by the observer himself; the latter only dealing with a particular case.

The question that we posed was whether a general self-contained practical method for determining asteroid distances via parallax by means of CCD images obtained from just one vantage point could be possible. By “self-contained” we emphasize the condition that all required data for the distance computation must be obtained from direct observations – not from third party data. (If one requires extra technical information for determining an object's distance, the used method seems to us to be a bit handicapped.) The idea was to develop a method that could accurately determine a Solar System object's distance from data gathered by just one observer. The good news is that we confidently think we have succeeded.

2. The Diurnal Parallax Effect

Parallax is a widely-understood and easily demonstrated phenomenon, as well as its derived practical benefit – to allow determining the distance to an object without directly measuring it. In astronomy, this fits like a glove. It has been used to determine the size of the Earth (Eratosthenes), the scale of the Solar System (during Venus’ transits) and the distance to near-by stars (Hipparcos satellite).

In theory, once the parallactic shift of the apparent position of a distant object as observed from the ends of a baseline of known length is measured, then its distance can be readily determined. In practice, taking into account that in most astronomical applications the parallax angle is very small, the only way to improve the accuracy of the distance determination is by means of enlarging the baseline.

As already mentioned, parallactic measures simultaneously performed from two conveniently far away observatories have successfully yielded asteroid distances. The big question here is: can one single observer determine accurate asteroid distances by taking advantage of his relative displacement to the target due to Earth’s rotation?

Placed on the Earth’s surface, any observer is actually moving along a perfectly circular track, several thousand kilometers in radius, making one complete circle in almost 24 hours (sidereal period). At any given time, the observer sees the asteroid from a slightly different perspective compared to a fictitious observer placed at the center of the Earth. Those are the vantage points that play this particular parallax game. This variable parallax effect has nothing to do with the fact that the asteroid is also moving with respect to the Earth – it only refers to the different (and constantly changing) spatial position of the observer relative to the center of the Earth due to the Earth’s rotation.

Assuming the asteroid’s distance is fixed with respect to the Earth’s center – except for NEO asteroids, a general pertinent assumption for time periods as short as half day to a couple of days – the time variability of the parallax angle due to observer location on the rotating Earth can be exclusively attributed to his changing position relative to a fixed direction in the equatorial plane. In other words, the parallax angle relative to the plane that contains the axis of rotation never changes.

This is the basis of the diurnal parallax definition – also called the east-west parallax. As shown in Figure 1, the diurnal parallax effect is the variable parallax due to the observer’s daily rotation with respect to the Earth’s center. It’s clear that at the moment of the target’s culmination (when the target happens to be

on the observer’s Meridian) the diurnal parallax angle becomes null, while achieving its maximum value 6 hours either before or after transit.

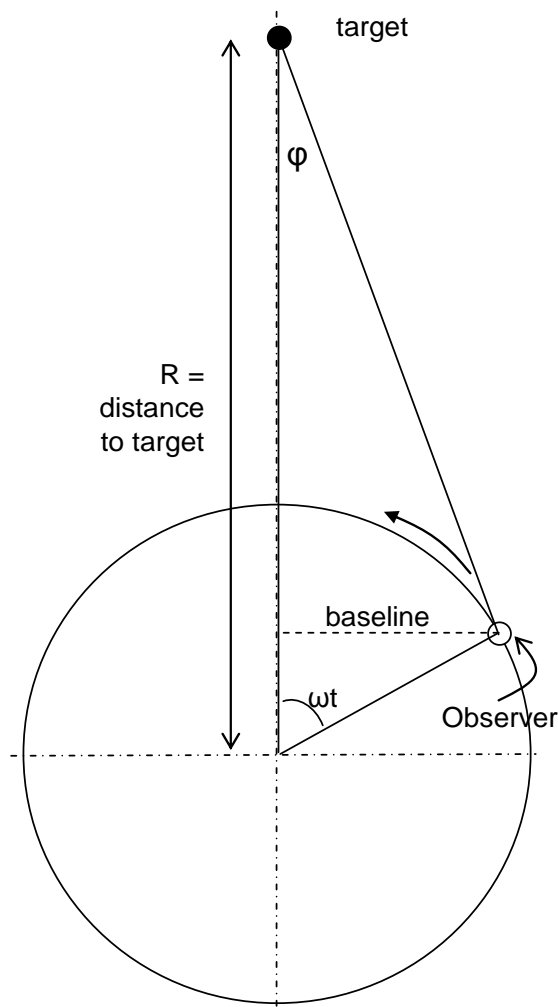


Figure 1 : Geometry of the diurnal parallax effect. As the Earth rotates, any observer on its surface sees the target’s parallactic angle ϕ constantly varying, from a maximum value occurring whenever his Meridian is at right angle to the plane containing the Earth’s rotation axis and the target (some 6 hours prior or after transit time) to a null value whenever the target is placed on his Meridian (target culmination).

The diurnal parallax becomes the angle that at any given moment has the target on its vertex, the observer on one side and the center of the Earth on the other side, projected to the equatorial plane. Therefore, by definition, at any given time t the diurnal parallax angle ϕ becomes

$$\phi(t) = [RA_{topo}(t) - \alpha_{geo}(t)] \cos \delta(t) \quad (1)$$

where RA_{topo} is the object’s topocentric (measured from the observer location) right ascension, α_{geo} is the

object's geocentric (measured from the center of the Earth) right ascension, and δ is the object's declination (assumed to be practically the same as measured either from the observer's place or from the center of the Earth).

Once this angle is determined, and knowing the length of the corresponding projected observational baseline B , the distance to the asteroid R can be readily obtained by making use of the small-angle approximation:

$$R = \frac{B(t)}{\varphi(t)} \quad (2)$$

where B and R are expressed in the same units and the angle φ is in radians. From Figure 1 the projected baseline is

$$B(t) = R_E \cos \lambda \cos(\omega t) \quad (3)$$

where R_E is the radius of the Earth, λ is the latitude of the observer, and ω is the angular sidereal rotation rate of the Earth. Therefore, all that matters now is how to accurately determine the elusive diurnal parallax angle φ .

3. The Model

The geometry of our model is shown in Figure 2. The non-rotating coordinate frame is attached to the center of the Earth (geocentric frame). It is oriented so that the +Z-axis points toward celestial north, and the +X-axis points toward the position where the asteroid is at time $t = 0$. Because of the symmetry of the diurnal parallax effect we strategically select the beginning of the time parameter to coincide with the moment of the asteroid culmination. Hence,

$$t = T - T_0 \quad (4)$$

where T is the "clock" time (this might be civil time or UT, depending on the preference of the observer) and T_0 is the exact time of the asteroid culmination (in the same timing reference).

At any time t , the geocentric position of the asteroid (which does move on the sky) is given by the vector $\mathbf{R}(t)$:

$$\vec{\mathbf{R}}(t) = \begin{bmatrix} x_R(t) \\ y_R(t) \\ z_R(t) \end{bmatrix} = \begin{bmatrix} R \cos \delta \cos \Delta\alpha \\ R \cos \delta \sin \Delta\alpha \\ R \sin \delta \end{bmatrix} \quad (5)$$

where R is the geocentric distance of the asteroid, δ is the geocentric declination of the asteroid, and $\Delta\alpha$ is the angular difference in the geocentric right ascension of the asteroid measured from $t = 0$, thus becoming

$$\Delta\alpha(t) = \alpha_{geo}(t) - \alpha_0 \quad (6)$$

where $\alpha_{geo}(t)$ is the geocentric right ascension of the asteroid at time t , and α_0 is the geocentric right ascension at the moment of the asteroid culmination. R , δ , and $\Delta\alpha$ are functions of time.

Considering that the observer sees the asteroid not from the Earth's center but from a different vantage point (as shown in Figure 2), necessarily the asteroid coordinates that he measures at any given time are (slightly) different from corresponding geocentric coordinates.

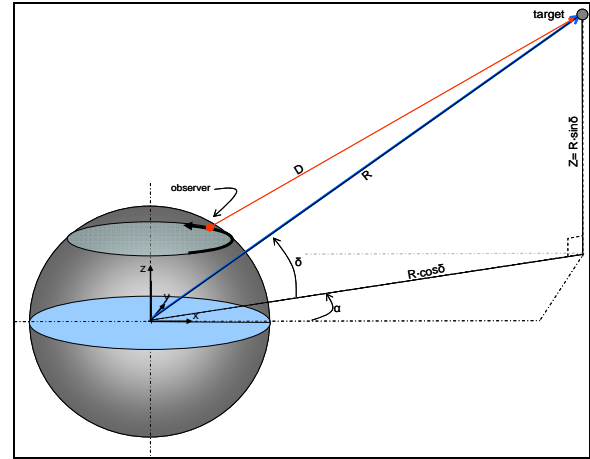


Figure 2: The spatially fixed geocentric frame. It's centered at the Earth center, the Z-axis coinciding with the Earth rotational axis and the X-axis pointing towards the direction that makes the plane XZ to also contain the target at the moment of its culmination.

At any time t , the geocentric position of the observer as he is carried around by the Earth's rotation is given by the vector $\mathbf{r}(t)$ (not shown in Figure 2). Assuming a spherical Earth, the vector $\mathbf{r}(t)$ is:

$$\vec{\mathbf{r}}(t) = \begin{bmatrix} x_r(t) \\ y_r(t) \\ z_r(t) \end{bmatrix} = \begin{bmatrix} R_E \cos \lambda \cos(\omega t) \\ R_E \cos \lambda \sin(\omega t) \\ R_E \sin \lambda \end{bmatrix} \quad (7)$$

where R_E is the radius of the Earth, λ is the latitude of the observer, and ω is the angular sidereal rotation rate of the Earth.

The vector $\mathbf{D}(t)$ from the observer to the asteroid thus becomes:

$$\vec{D}(t) = \vec{R}(t) - \vec{r}(t) \quad (8)$$

so that

$$\vec{D}(t) = \begin{bmatrix} x_D(t) \\ y_D(t) \\ z_D(t) \end{bmatrix} = \begin{bmatrix} R \cos \delta \cos \alpha - R_E \cos \lambda \cos(\omega t) \\ R \cos \delta \sin \alpha - R_E \cos \lambda \sin(\omega t) \\ R \sin \delta - R_E \sin \lambda \end{bmatrix} \quad (9)$$

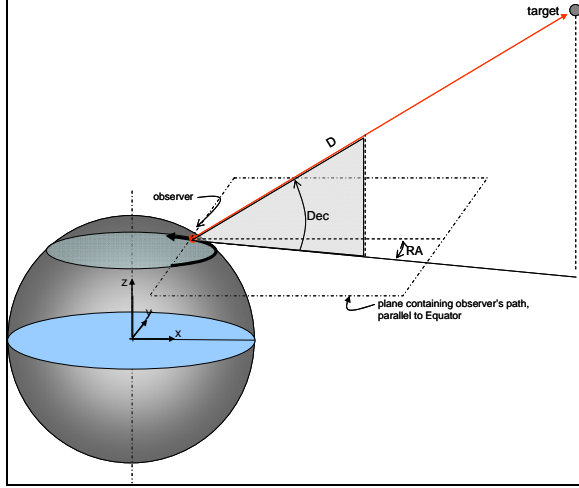


Figure 3: The moving topocentric frame. It's centered at the observer's location on the Earth's surface, but at any time its three axes are parallel to corresponding axes of the geocentric frame. Hence, the XY plane is always parallel to the Equatorial plane, and the XZ plane happens to coincide with the Meridian at the moment of the target's culmination.

Figure 3 shows a non-rotating coordinate frame centered on the observer's location on the surface of the Earth (topocentric frame). It is oriented so that both the +Z-axis and the +X-axis are parallel to corresponding axes in the geocentric frame. Hence, at time $t = 0$ the +X-axis also points toward the position where the asteroid is, which happens to be placed at the Meridian.

At any time t , the topocentric position of the asteroid is given by the vector $D(t)$:

$$\vec{D}(t) = \begin{bmatrix} x_D(t) \\ y_D(t) \\ z_D(t) \end{bmatrix} = \begin{bmatrix} D \cos(Dec) \cos(\Delta RA) \\ D \cos(Dec) \sin(\Delta RA) \\ D \sin(Dec) \end{bmatrix} \quad (10)$$

where D is the topocentric distance to the asteroid, Dec is the topocentric declination of the asteroid, and ΔRA is the angular difference in the topocentric right ascension of the asteroid measured from $t = 0$, thus becoming

$$\Delta RA(t) = RA_{topo}(t) - RA_0 \quad (11)$$

where $RA_{topo}(t)$ is the topocentric right ascension of the asteroid at time t , and RA_0 is the topocentric right ascension at the moment of the asteroid culmination. D , Dec , and ΔRA are functions of time.

From (10), dividing the y_D by the x_D coordinates of the vector $D(t)$ and substituting the corresponding values from (6) it becomes

$$\frac{y_D}{x_D} = \tan(\Delta RA) = \frac{X \cos \delta \sin \Delta \alpha - \sin(\omega t)}{X \cos \delta \cos \Delta \alpha - \cos(\omega t)} \quad (12)$$

where

$$X = \frac{R}{R_E \cos \lambda} \quad (13)$$

Besides the goal distance R , Equation 12 still includes other unknown time-dependent parameters (δ and $\Delta \alpha$) basically related to the actual asteroid motion on the sky. In order to simplify the asteroid distance computation, now we are going to make several important assumptions.

First of all, we assume that the asteroid's geocentric distance R is constant over the interval of a few days during which we make our measurements. Of course this is not true, but it is a pretty good approximation – the geocentric distance to the asteroid does constantly change but slowly, so that over an interval of a couple of nights we can pretend that it is constant.

The next key assumptions relate to the asteroid's orbital motion. They are:

- The geocentric rates in right ascension and declination will be assumed to be constant (linear motion) over an interval of a couple of days.
- We will estimate these orbital rates by using topocentric measurements at the moment of the asteroid culmination (when diurnal parallax is null).
- We will ignore any differences in the asteroid topocentric and geocentric declinations at the moment of transit (in practice, the real difference is usually insignificant).

From these three assumptions, at least in first approximation the asteroid orbital motion (geocentric coordinates) can be determined at any time from topocentric measurements as:

$$\alpha_{geo}(t) \approx \alpha_0 + vt = RA_0 + vt \quad (14)$$

$$\delta_{geo}(t) \approx \delta_0 + \mu t \approx Dec_0 + \mu t \quad (15)$$

where the asteroid right ascension constant rate v is defined as

$$v = \frac{RA_{0_2} - RA_{0_1}}{T_{0_2} - T_{0_1}} \quad (16)$$

and the asteroid declination constant rate μ is defined as

$$\mu = \frac{Dec_{0_2} - Dec_{0_1}}{T_{0_2} - T_{0_1}} \quad (17)$$

where RA_{0_1} and RA_{0_2} are the asteroid topocentric right ascensions respectively at the moment of the first (T_{0_1}) and second (T_{0_2}) transit times, while Dec_{0_1} and Dec_{0_2} are the asteroid topocentric declinations respectively also at the moment of the first (T_{0_1}) and second (T_{0_2}) transit times.

Thus substituting in Equation 12 it becomes

$$\tan(\Delta RA) = \frac{X \cos(Dec_0 + \mu t) \sin(RA_0 + vt) - \sin(\omega t)}{X \cos(Dec_0 + \mu t) \cos(RA_0 + vt) - \cos(\omega t)} \quad (18)$$

This is the fundamental equation of our model. Once the key parameters T_0 and RA_0 become known, the left term is directly measurable by the observer at any given time, while in the right term – except for the geocentric asteroid distance R – all of the remaining parameters are either known a priori (R_E , λ , ω) or are also directly measurable by the observer (Dec_0 , v , μ). In consequence, the asteroid distance can be determined by applying an iterative process to a set of observations as follows:

1. From observed topocentric coordinates the asteroid linear orbital motion is determined, and hence the asteroid geocentric coordinates can be estimated at any given time.
2. Knowing the asteroid orbital motion and assuming a certain (guessed) asteroid distance, the model predicts for any given time what the topocentric right ascension has to be.
3. The distance value that best minimizes all RA residuals (observed minus model predicted

topocentric right ascensions) for the given set of observations becomes the asteroid distance.

4. Determination of the Key Parameters T_0 , RA_0 and Dec_0

The asteroid's exact local transit time T_0 has to be known as precisely as possible. An error of just one second does make difference. This fact imposes a hard restriction on the timing accuracy and therefore the easy shortcut of getting T_0 from published asteroid ephemerides is not an option.

Fortunately, T_0 can be easily determined by the observer at the required accuracy. The way to do this is by taking a set of images while the asteroid is around transit time (preferably from a couple of minutes before up to a couple of minutes after transit time). For each image, the corresponding time has to be accurately known and target astrometry has to be precisely measured. Then, the difference between measured RA of the asteroid to Local Sidereal Time can be determined for each observation time of the set of images. Finally, by using the Intercept function on a spreadsheet the time of transit T_0 and corresponding RA_0 and Dec_0 can be precisely obtained.

Having determined from observations made on two proximate nights (the adjacent, the better) corresponding parameters T_0 , RA_0 and Dec_0 , then the asteroid's geocentric orbital motion in right ascension and declination can be conveniently represented, at least in first approximation, by linear rates v and μ just derived from those six parameters.

5. The RA Geocentric Linear Assumption

The quality of the diurnal parallax angle determination is based on two main subjects: (a) the accuracy of RA topocentric values actually measured, and (b) the accuracy of RA geocentric values estimated for the required parallax computation.

As already discussed, our (self-contained) model uses a linear approximation for the unknown RA geocentric values, so that asteroid distances can be truly determined from just the observer's data. However, replacing a curve by a linear approximation always introduces some error.

In case the time frame we consider is just two consecutive nights and the target asteroid is near opposition, then the asteroid does have an almost linear motion against the background stars and our linear assumption is totally pertinent – even though it's also the time of greatest motion in right ascension. In a more general situation, or for a longer time frame (let's say 3-4 days) the real asteroid trajectory in-

creasingly departs from a linear motion. Could the error derived from the linear simplification still be manageable in a more general context?

The problem to solve is to somehow minimize the error derived by the replacement of the unknown general RA geocentric motion curve by a linear approximation. The linear approximation is the uniform rate v that the observer is able to derive from the only two points (T_{01}, RA_{01}) and (T_{02}, RA_{02}) of the real RA geocentric curve that he can actually measure on just two proximate nights.

Of course, if the observer could be able to observe along several nights he would collect several pairs of (T_0, RA_0) data points, which in turn makes it possible to derive a more accurate variable (time-dependent) rate for the real RA geocentric motion – instead of a simple uniform rate, finding out a first, second or even third order analytical expression for $v(t)$. The same goes in case the observer could know such data from accurate target ephemerides. We are dealing here with the most likely – and easiest – case where the observer dedicates just two (partial) nights to find out the distance to a particular asteroid exclusively by means of his own data.

The graph in Figure 4 poses the question. If the real RA geocentric curve were to be replaced by just a linear approximation, then along one single observing session any “new” RA geocentric values would be either underestimated or overestimated by the simplification (the larger the time apart from the transit time T_0 , the worse). Also for the same observing session, all RA geocentric values prior to the transit time would be replaced in the opposite way as those RA geocentric values after the transit time (if the former became underestimated, the latter resulted overestimated, or vice versa).

It becomes clear that working with a linear RA geocentric rate and using data from just one observing session obtained entirely from one side of the Meridian (either only prior or only after transit time) will achieve the largest error. To minimize diurnal parallax errors derived from the use of data from only one observing session it is necessary to observe the target for a long time both sides of the Meridian.

However, we found out an elegant simplification. Instead of observing the asteroid for a full night from dusk to dawn, and also at transit time on the following day, as shown in Figure 5 basically the same exactitude can be achieved if the target is observed on the two nights just from the same side of the Meridian.

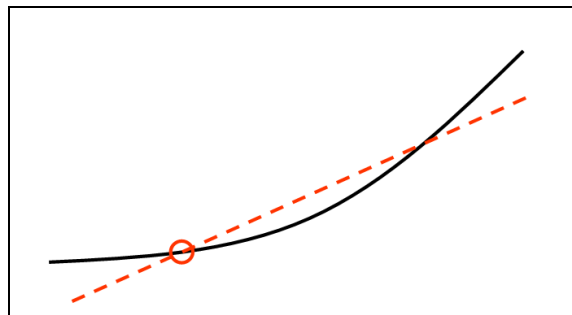


Figure 4: The problem with the linear assumption. Replacing a real curve by a linear approximation introduces errors in a particular direction previous to the point where the segment actually coincides with the curve, and in the opposite direction after such coinciding point.

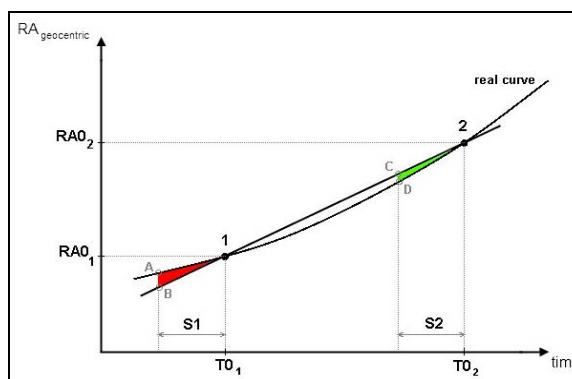


Figure 5: Replacing the real RA geocentric curve by a linear approximation makes the “new” RA values at any time previous to transit time (T_0) to be wrong in one direction for the first session (underestimated as shown in the red area for Session #1) but wrong in the opposite direction for the following session (overestimated as shown in the green area for Session #2).

Therefore, despite the fact that the RA geocentric values for each session necessarily are going to be inexact (the larger the curvature, the greater the error), if the observer only collects data either before or after the transit time, but not simultaneously from both sides, then the error introduced by the linear RA geocentric simplification tends to cancel out.

Using data from just one side of the Meridian not only means the observer does not need to work all night long (not a minor issue for amateurs committed to full-day jobs) but also implies that the asteroid no longer has to be near opposition (it could transit at any time during the night). Of course far from opposition the asteroid will be fainter and may follow a much more complicated trajectory – thus most likely decreasing the properness of the linear rate approximation – but on the other hand (a) the asteroid could be observed for a longer time frame than the 4-5 hours from dusk to midnight, or from midnight to dawn, and consequently (b) the asteroid could also be

observed for longer periods while comparatively at higher altitudes on the sky.

6. The Model At Test

We have applied the model to five different asteroids, trying to cover a wide distance spectrum. One close and fast moving NEO asteroid was observed having a large diurnal parallax angle (greater than 120 arcsec), three asteroids were observed at intermediate distances, and one last asteroid was observed at such a challenging far distance that its diurnal parallax angle (less than 3 arcsec) was as small as the local atmospheric blurring effect (seeing).

All observations were performed from Observatorio Los Algarrobos, Salto, Uruguay (MPC I38) at latitude $-31^{\circ} 23' 33''$, using a 0.3-m telescope and CCD camera yielding an image scale of 1.9 arcsec/pixel. MPO Canopus was the software used for astrometry.

All observed asteroids happened to be relatively close to their opposition date. We observed our five targets at least on one pair of consecutive nights, accumulating 10 pairs of such sessions. Except for one, all individual observing sessions lasted more than 4 hours. For each target we obtained a series of images taken about 15 minutes apart, except at each opening session and close to target culminations – when several images were taken continuously in order to improve derived astrometry accuracy. On some occasions we not only imaged the target for many hours prior to its culmination, but also for many hours after having past the Meridian as well.

6.1 Asteroid 8106 Carpino

This main belt asteroid was our first target, observed on two consecutive nights (2011, April 6 and 7) while exactly at opposition (April 7th) when it appeared with a visual magnitude of 15.5 and a phase angle of 9.9 degrees. Almost all observations of both sessions were made prior to transit time. Figure 6 shows the measured parallax angles assuming a linear RA geocentric motion derived from data collected on those nights.

Technical data for each session and corresponding values are summarized in Table I.

The distance derived from each session data was excellent (better than 4%). As expected, one value was underestimated while the other was overestimated. The found distance derived from the two sessions was remarkably good (2.5%). This proves the full validity of the RA “constant rate” assumption for the asteroid motion at opposition and the predicted

trend for errors to cancel out if working with observations from just one side of the Meridian.

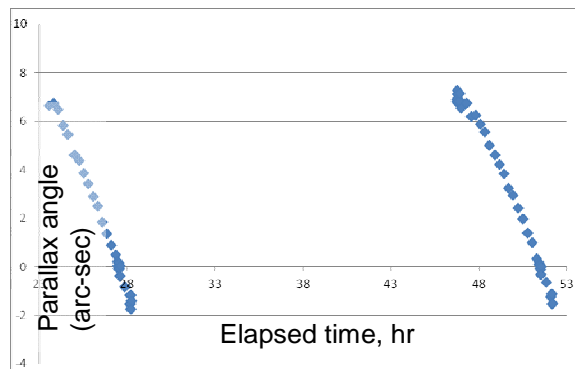


Figure 6: Observed 8106 Carpino’s diurnal parallax by assuming asteroid RA linear motion, from data obtained on two consecutive nights (2011 April 6 and 7), which happened to coincide with its opposition date.

8106 Carpino			
	Session #1	Session #2	Sess. 1&2
Observation date (UT)	2011-04-06	2011-04-07	
Lapse to/from opposit (day)	-1	0	
True Distance (AU)	0.974	0.972	0.973
Phase Angle (deg)	9.94	9.91	
Visual magnitude (mag)	15.53	15.53	
Observed lapse before T0 (h)	4.0	4.8	
Observed lapse after T0 (h)	0.7	0.7	
Used RA rate		Constant: $v = -0.010151$ arcsec/sec	
Found Parallax (arcsec)	7.88	7.41	7.52
Found Distance (AU)	0.951	1.011	0.997
Relative error (%)	-2.4	+4.0	+2.5

Table I: 8106 Carpino Results

6.2 Asteroid 819 Barnardiana

This main belt asteroid was observed on three pairs of consecutive nights (2011, May 29-30, June 1-2, and June 11-12), that is, increasingly apart from opposition (May 19th) when it appeared with a visual magnitude of 13.6 and a phase angle of 5.2 degrees. We tried on this target several different and mixed combinations of prior/after transit observations. Figures 7-9 present the measured parallax angles for each pair of consecutive nights assuming a linear RA geocentric motion derived from data collected on corresponding nights.

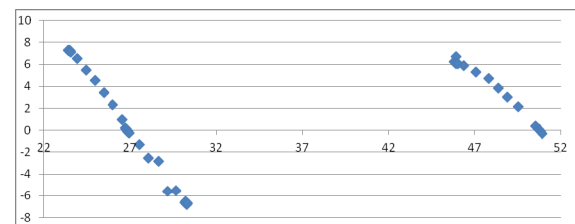


Figure 7: Observed 819 Barnardiana’s diurnal parallax by assuming asteroid RA linear motion, from data obtained on two consecutive nights (2011 May 29 and 30), about ten days past opposition.

Asteroid Distances from Diurnal Parallax – Alvarez et al.

819 Barnardiana									
	Session #1	Session #2	Sess. 1&2	Session #3	Session #4	Sess. 3&4	Session #5	Session #6	Sess. 5&6
Observation date (UT)	2011-05-29	2011-05-30		2011-06-01	2011-06-02		2011-06-11	2011-06-12	
Lapse to/from oposit (day)	+10	+11		+13	+14		+23	+24	
True Distance (AU)	0.939	0.940	0.940	0.943	0.944	0.944	0.967	0.970	0.969
Phase Angle (deg)	7.83	8.24		9.21	9.70		14.32	14.81	
Visual magnitude (mag)	13.75	13.77		13.82	13.84		14.06	14.08	
Observed lapse before T0 (h)	3.5	5.0		4.5	4.7		2.8	3.4	
Observed lapse after T0 (h)	3.5	0.1		1.5	0.7		4.0	5.0	
Used RA rate	Constant: $v = -0.0104803$ arcsec/sec			Constant: $v = -0.0097799$ arcsec/sec			Constant: $v = -0.0064872$ arcsec/sec		
Found Parallax (arcsec)	8.93	6.51	7.81	10.20	6.13	8.22	10.13	4.55	6.60
Found Distance (AU)	0.840	1.152	0.961	0.731	1.223	0.912	0.740	1.644	1.135
Relative error (%)	-10.5	+22.6	+2.2	-22.5	+29.6	-3.4	-23.5	+69.5	+17.1
Used RA rate	Variable (3rd order) rate								
Found Parallax (arcsec)	7.14	7.33	7.23	8.05	7.80	7.93	7.95	8.16	8.08
Found Distance (AU)	1.050	1.023	1.037	0.931	0.961	0.946	0.943	0.919	0.928
Relative error (%)	+11.8	+8.8	+10.3	-1.3	+1.8	+0.2	-2.5	-5.3	-4.2

Table II: Conditions and results for 810 Barnardiana

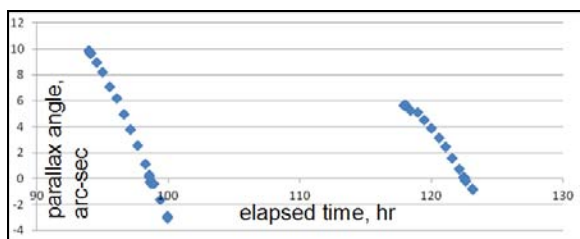


Figure 8: Observed 819 Barnardiana’s diurnal parallax by assuming asteroid RA linear motion, from data obtained on two consecutive nights (2011 June 1 and 2), some 14 days past opposition.

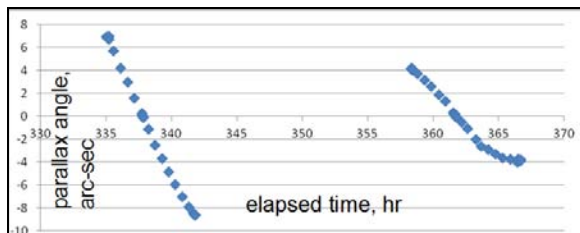


Figure 9: Observed 819 Barnardiana’s diurnal parallax by assuming asteroid RA linear motion, from data obtained on two consecutive nights (2011 June 11 and 12), some 24 days past opposition.

It seems quite evident that for each pair of obtained parallactic curves, the shape of the first compared to the second become increasingly deformed. This is due to the linear RA geocentric assumption, which gradually loses validity as the asteroid moves away from opposition. This is made manifest by observing how the linear rate changed from an almost-similar value for the first pair of nights compared to the last value – respectively, 0.0105, 0.0098 and 0.0065 arcsec/sec, that is, the linear rate for the last pair was only 60% of the first one, thus approaching the highly curved part of its orbital trajectory when the asteroid switches between prograde and retrograde motion. For those sessions that covered a large time on both sides of the Meridian, some deformation of the diurnal parallax curves becomes evident – no-

toriously in Figure 9. Despite the diurnal parallax effect being a totally symmetric phenomenon, the “uniform RA rate” assumption introduces errors that make the angle to appear increased at one side of the Meridian and diminished at the other, so that the shape distortion becomes worse as the asteroid trajectory increases its curvature, i.e., as the asteroid gets farther from opposition.

Having observed this target on six sessions distributed half-month apart, from our own data we were able to find out a much better representation of the actual RA geocentric motion of the asteroid. Figures 10-12 show the same collected data as before, but this time a variable (third order) rate has been used for the RA geocentric trajectory. One glance at Figures 9 and 12, which are based on the same data, is enough for understanding the matter.

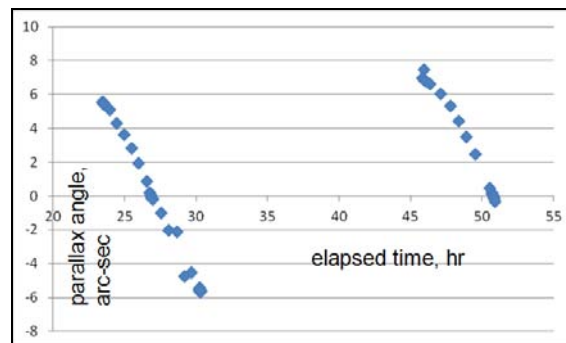


Figure 10: Observed 819 Barnardiana’s diurnal parallax by assuming asteroid RA variable (3rd order) motion, from data obtained on two consecutive nights (2011 May 29 and 30), about ten days past opposition.

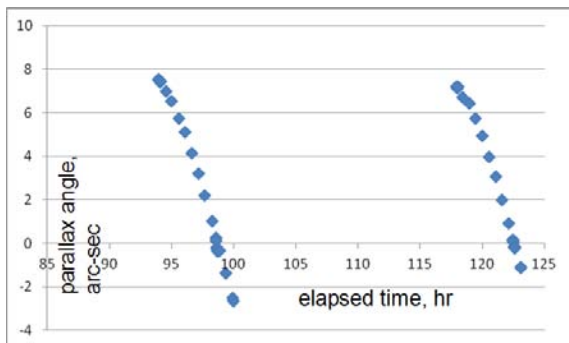


Figure 11: Observed 819 Barnardiana’s diurnal parallax by assuming asteroid RA variable (3rd order) motion, from data obtained on two consecutive nights (2011 June 1 and 2), some 14 days past opposition.

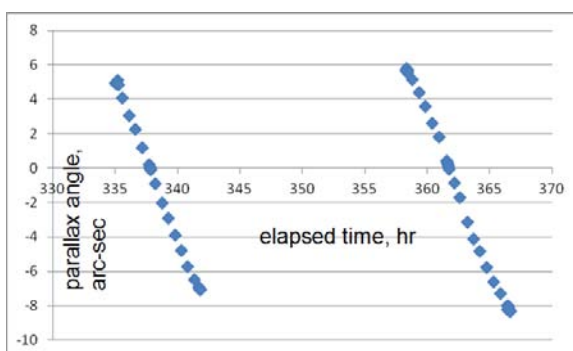


Figure 12: Observed 819 Barnardiana’s diurnal parallax by assuming asteroid RA variable (3rd order) motion, from data obtained on two consecutive nights (2011 June 11 and 12), some 24 days past opposition.

Technical data for each session and corresponding values are summarized in Table II.

Using the linear approximation we obtained mediocre results if considering only data from each night; however, outcomes from considering the joint data of each pair of nights were again excellent (better than 3.5%) for the first and second pairs (those closer to opposition), although poor (17%) for the last

one (24 days past opposition). On the other hand, using a quadratic approximation for the whole considered period we obtained very good results (better than 5%) either for the individual sessions as well as for the pairs, except for the first one (10%). Logically, the variable rate expression rectifies the problem where the trajectory wasn’t uniform, and worsens where the motion was actually practically linear. One last fact worth mentioning is that the two larger errors from combined nights also occurred for those pairs (first and third) when one of the sessions covered a large span on one side of the Meridian not covered by the other.

6.3 The Far Away Asteroid 414 Liriope

This challenging outer main belt asteroid was observed on three pairs of consecutive nights (2011, August 30-31, September 1-2, and September 5-6), that is, increasingly apart from opposition (August 25th) when it appeared with a visual magnitude of 14.5 and a phase angle of 2.5 degrees. We also tried on this target several different and mixed combinations of prior/after transit observations. Unfortunately, the third session was aborted half hour prior transit time due to cloud covering. Figures 13, 14 and 15 present the measured parallax angles for each pair of consecutive nights assuming a linear RA geocentric motion derived from data collected on corresponding nights.

The computation of the exact transit time for the third session (2011-09-01) couldn’t be done as usual (from data collected around asteroid culmination from that session) so that it had to be derived from previous and following observations. The quality of the obtained data is clearly inferior to those from previous targets, something totally expected given the small parallactic angles now in play.

Technical data for each session and corresponding values are summarized in Table III.

414 Liriope	Session #1	Session #2	Sess. 1&2	Session #3	Session #4	Sess. 3&4	Session #5	Session #6	Sess. 5&6
Observation date (UT)	2011-08-30	2011-08-31		2011-09-01	2011-09-02		2011-09-06	2011-09-07	
Lapse to/from opposit (day)	+5	+6		+7	+8		+12	+13	
True Distance (AU)	2.544	2.545	2.545	2.546	2.548	2.547	2.557	2.558	2.558
Phase Angle (deg)	2.92	3.10		3.29	3.51		4.48	4.49	
Visual magnitude (mag)	14.56	14.58		14.59	14.60		14.67	14.67	
Observed lapse before T0 (h)	4.9	5.1		4.6	5.2		4.9	4.7	
Observed lapse after T0 (h)	0.1	0.1		N/A	0.8		0.7	1.0	
Used RA rate	Constant: $v = -0.0070355$ arcsec/sec			Constant: $v = -0.0069983$ arcsec/sec			Constant: $v = -0.0067985$ arcsec/sec		
Found Parallax (arcsec)	2.82	2.79	2.80	3.30	2.91	3.05	2.88	2.56	2.85
Found Distance (AU)	2.660	2.692	2.674	2.273	2.579	2.460	2.604	2.874	2.627
Relative error (%)	+4.6	+5.8	+5.1	-10.7	+1.2	-3.5	+1.8	+12.4	+2.7
Used RA rate	Variable (3rd order) rate								
Found Parallax (arcsec)	2.65	2.97	2.81	2.93	2.89	2.91	2.75	2.98	2.81
Found Distance (AU)	2.830	2.525	2.668	2.559	2.595	2.577	2.727	2.516	2.678
Relative error (%)	+11.2	-0.8	+4.8	+0.5	+1.8	+1.1	+6.6	-1.6	+4.7

Table III: Circumstances and results for 414 Liriope

Asteroid Distances from Diurnal Parallax – Alvarez et al.

Despite the small parallax angle – approaching the frontier where measurement reliability becomes degraded – outcomes from the linear assumption were still very good (around 5%) for the first pair of sessions and even better (better than 3.5%) for the other two pairs.

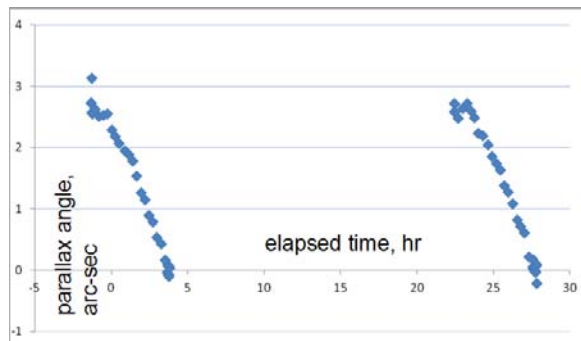


Figure 13: Observed 414 Liriope’s diurnal parallax by assuming asteroid RA linear motion, from data obtained on two consecutive nights (2011 August 30 and 31), some 5 days past opposition.

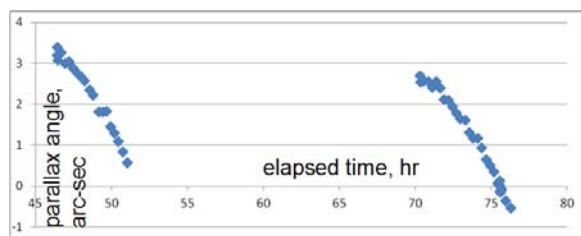


Figure 14: Observed 414 Liriope’s diurnal parallax by assuming asteroid RA linear motion, from data obtained on two consecutive nights (2011 September 1 and 2), some 8 days past opposition.

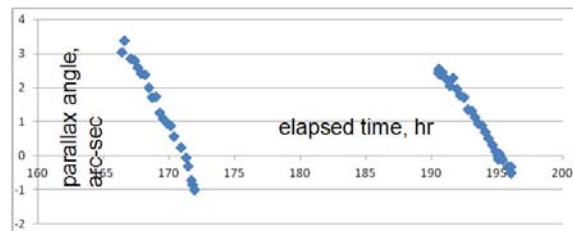


Figure 15: Observed 414 Liriope’s diurnal parallax by assuming asteroid RA linear motion, from data obtained on two consecutive nights (2011 September 6 and 7), some 13 days past opposition.

6.4 Asteroid 1660 Wood

This main belt asteroid was observed on four consecutive nights (2012, January 23-24-25-26) prior to opposition (January 29th) when it appeared with a visual magnitude of 13.4 and a phase angle of 24.6 degrees. Sessions were relatively short (all under 5.5 hours, while the 3.7 hour session from 2012-01-24 was the shortest one for this work). Figures 16 and 17 present the measured parallax angles for each pair of consecutive nights assuming a linear RA geocentric motion derived from data collected on corresponding nights.

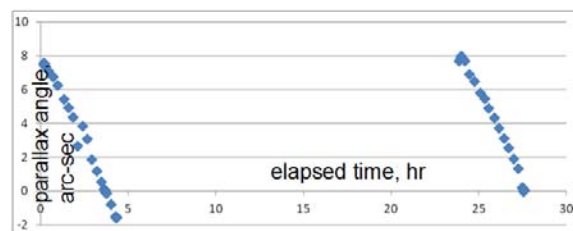


Figure 16: Observed 1660 Wood’s diurnal parallax by assuming asteroid RA linear motion, from data obtained on two consecutive nights (2012 January 23 and 24), some 5 days prior to opposition.

1660 Wood	Session #1	Session #2	Sess. 1&2	Session #3	Session #4	Sess. 3&4
Observation date (UT)	2012-01-23	2012-01-24		2012-01-25	2012-01-26	
Lapse to/from opposit (day)	-6	-5		-4	-3	
True Distance (AU)	0.831	0.830	0.831	0.829	0.828	0.829
Phase Angle (deg)	24.74	24.71		24.64	24.60	
Visual magnitude (mag)	13.76	13.76		13.75	13.75	
Observed lapse before T0 (h)	3.5	3.7		3.8	3.8	
Observed lapse after T0 (h)	0.7	0.0		1.7	1.5	
Used RA rate	Constant: $v = -0.0074036$ arcsec/sec		Constant: $v = -0.0072342$ arcsec/sec			
Found Parallax (arcsec)	9.45	9.70	9.58	9.59	8.32	8.92
Found Distance (AU)	0.793	0.773	0.783	0.782	0.901	0.840
Relative error (%)	-4.6	-6.9	-5.8	-5.7	+8.8	+1.3

Table IV: Circumstances and Results for 1660 Wood

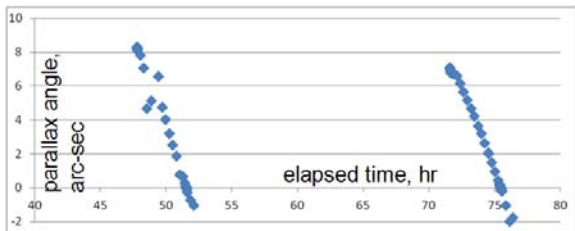


Figure 17: Observed 1660 Wood’s diurnal parallax by assuming asteroid RA linear motion, from data obtained on two consecutive nights (2012 January 25 and 26), some 3 days prior to opposition.

Despite working with short-span data, outcomes for combined sessions were very good (5.8% and 1.3%). The fact that we got (twice) data from three nights in a row allowed us to compare results for the same central night – but derived from two different uniform rates – one applying the linear motion from the adjacent first and central nights, and another from the also adjacent central and last nights of the trio. For the 2012-01-25 session we obtained a distance of 0.885 AU (+6.8%) and 0.781 AU (-5.8%) if we applied the different linear rates measured for each pair of days of the trio (respectively, -0.007404 and -0.007315 arcsec/sec). That is, a mere 1.2% in difference in the assumed uniform RA geocentric rate caused a 12.6% difference in the derived asteroid distance, for data just 4 days away from opposition.

6.5 The Close Asteroid (162421) 2000 ET70

This NEO (Athen) asteroid was observed on two consecutive nights (2012, February 22-23) coinciding with its opposition (February 22nd) when it appeared with a visual magnitude of 13.2 and a phase angle of 40.7 degrees. The rapid sky displacement of this neighbor while visiting us at opposition (-0.2644 arcsec/sec) posed some practical problems (varying star background context from where astrometry was

obtained) not previously dealt with. Figure 18 presents the measured parallax angles for the pair of consecutive nights using the “linear RA geocentric motion” assumption, derived from data collected on these nights.

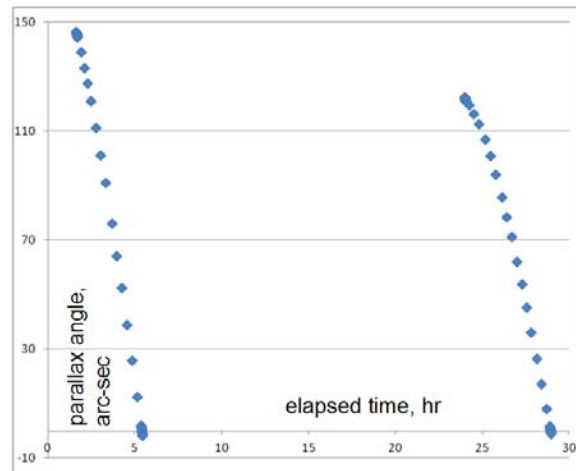


Figure 18: Observed (162421) 2000 ET70’s diurnal parallax by assuming asteroid RA linear motion, from data obtained on two consecutive nights (2012 February 22 and 23), which happened to coincide with its opposition date.

Besides the rapid sky motion, the closeness of the asteroid also implied a large diurnal parallax effect. Hence, absolute measurement errors comparatively became less important, which neatly explains the cleanness of the obtained parallactic curves. Considering that except at the beginning and at transit of each session each data point was obtained at approximately the same intervals, the curves not only show how the parallactic angle actually changed with time, but also its variable rate of change.

The asteroid distance obtained from the combined session was quite good (6%), derived from the two sessions with large individual errors (-10.4 and

(162421) 2000 ET70	Session #1	Session #2	Sess. 1&2
Observation date (UT)	2012-02-22	2012-02-23	
Lapse to/from opposit (day)	0	1	
True Distance (AU)	0.048	0.050	0.049
Phase Angle (deg)	40.80	41.90	
Visual magnitude (mag)	13.27	13.41	
Observed lapse before T0 (h)	3.8	5.0	
Observed lapse after T0 (h)	0.0	0.0	
Used RA rate	Constant: $v = -0.2644330$ arcsec/sec		
Found Parallax (arcsec)	172.6	125.9	145.0
Found Distance (AU)	0.043	0.060	0.052
Relative error (%)	-10.4	+20.0	+6.1

Table V: Circumstances and Results for (162421) 2000 ET70

+20.0%). One important matter for this close flying-by target is that at opposition, its geocentric distance was changing by about 4% per 24-h, which obviously violates the crucial “constant distance” assumption in our model.

6.6 Discussion of Results

Target	RA rate Model	Sess. 1&2	Sess. 3&4	Sess. 5&6
8106 Carpino	uniform	+2.5	-	-
819 Barnardiana	uniform	+2.2	-3.4	+17.1
	variable			
819 Barnardiana	(3rd order)	+10.3	+0.2	-4.2
414 Liriope	uniform	+5.1	-3.5	+2.7
	variable			
414 Liriope	(3rd order)	+4.8	+1.1	+4.7
1660 Wood (162421)	uniform	-5.8	+1.3	-
2000 ET70	uniform	+6.1	-	-

Table VI: Distance percent errors for each one of the combined consecutive sessions

Table VI summarizes final asteroid distances derived from observational data. Distances from combined consecutive nights' data were very good, even for the challenging 2.5 AU far away asteroid. Some measurements for 819 Barnardiana gave the largest errors, due to the fact that observations at first and third pairs of sessions were collected on both sides of the Meridian. The NEA asteroid gave the worst case, but the obtained 6.1% error distance was also surprisingly good, given its rapidly-changing distance.

The adopted asteroid's geocentric rate in RA is critical for an accurate determination of its distance derived from the diurnal parallax effect. Results are very sensitive to the RA geocentric rate that was actually used. Depending on asteroid distance and orbital position, a tiny percent change in the assumed RA rate can change the calculated asteroid distance by far more than ten times such percent.

The linear RA geocentric assumption has been proven useful and effective. Results derived from the more accurate “variable rate” model became marginally superior in the case when 819 Barnardiana was far away from opposition. On this scenario, the a single observer can still accurately determine the distance to an asteroid all by his own by observing the target at transit along a handful of nights, so that he can obtain a good model of the changing RA geocentric rate.

7. A Much Simpler Stratagem

We also applied our data to Equation 1. Assuming that the distance to a far away target remains constant, and that there is almost no variation in declina-

tion for the short considered daily interval, the diurnal parallax angle varies in a sinusoidal way as

$$\varphi(t) \approx A \sin(\omega_T t) \tag{19}$$

where the amplitude A is the maximum diurnal parallax angle (ω_T) is the angular rate of the sine curve and the time variable (t) is selected exactly the same way as before (its beginning coincides with the moment of the asteroid's culmination).

The maximum diurnal parallax angle A corresponds to the parallactic value 6 hours either before or after transit, and becomes the key value for finding out the distance. In theory, it could be possible to directly measure it but it requires the asteroid to be far way from opposition (which poses the problem of the variable RA geocentric rate); in practice, the difficulty of accurately measuring such a small angle (usually less than 10 arcsec) turns the direct attempt almost impossible. However, it is possible to determine it indirectly.

From equations 1 and 19 we have

$$[RA_{topo}(t) - \alpha_{geo}(t)] \cos \delta(t) \approx A \sin(\omega_T t) \tag{20}$$

From our data, at the time of each observation we know the asteroid topocentric coordinates, as well as corresponding RA geocentric value. The angular rate of the sine curve can be readily derived from our observations at two consecutive transit times, becoming

$$\omega_T = \frac{2\pi}{T_{0_2} - T_{0_1}} \tag{21}$$

Therefore, by finding the A value that best minimizes all residuals in Equation 20 for a given set of observations (the same process applied in our previous model to Equation 18, this time trying to determine the sinusoidal curve that best fits the left-side data term in Equation 20) the maximum parallactic angle is determined and yields the distance to the object once the baseline ($R_E \cos \lambda$) is applied to Equation 2.

Asteroid distances obtained by using the simplification of Equation 20 applied to exactly the same observational data already presented were virtually identical to those obtained through our more rigorous model. This wasn't a surprise as both models are basically solving the same geometry, but anyway it was a general validity for Equation 19.

Finally, we tried an even more intrepid bet. Instead of dealing with a large set of observations for

finding the amplitude of the parallactic sine curve, we tried using only four data points: those from the beginning and around transit time for each of two consecutive nights. This ultimate simplification to an already simple method proved to be totally pertinent, as results were only marginally poorer than those obtained from our (much more complex) model. Just four data points strategically selected (those at zero-level parallactic angle and those as large as possible from the same side of the Meridian) are sufficient for accurately finding out the amplitude of the diurnal parallax effect.

In order to improve the quality of the results, in practice the data-points far away from culmination should be obtained as a set of several consecutive images – the same procedure as for accurately determining transit times.

Distance percent errors from combined consecutive sessions, by means of our model, the sine curve simplification, and “the 4-Point shortcut” (as we have named it) are shown in Table VII.

The innovative 4-Point shortcut for determining an asteroid distance is self-contained, extremely simple (only requiring two observations on consecutive nights), and yields very good accuracy (around 5% or better) on condition the asteroid is fairly close to opposition. If that is not the case, some more data is required (observations from a few more nights, but only done at transit times).

8. Range of Distances

By means of a modest 0.30-m telescope we have successfully tested the 4-Point shortcut method for determining asteroid distances up to 2.5 AU – which implied dealing with a parallactic angle about 3 arcsec without any problem. Working with similar sized, good optics telescopes, in principle we don’t see any limitation preventing the detection of a ten times lesser parallactic angle if due care, proper image scale, and favorably seeing conditions are all in play.

From equations 2 and 3, the corresponding distance in AU for a parallactic angle of 0.3 arcsec equals 29.2 times the cosine of the observer’s latitude. Therefore, we think the distance determination of bright enough Solar System objects up to 20-25 AU by means of a backyard telescope applying the 4-POINT shortcut is a feasible task – although a certainly challenging one. We are planning some experiments to see if we can measure the distance to Pluto with this method.

Target	The formal model		
	Sess. 1&2	Sess. 3&4	Sess. 5&6
<i>8106 Carpino</i>	+2.5	-	-
<i>819 Barnardiana</i>	+2.2	-3.4	+17.1
<i>414 Liriope</i>	+5.1	-3.5	+2.7
<i>1660 Wood</i> <i>(162421)</i>	-5.8	+1.3	-
<i>2000 ET70</i>	+6.1	-	-

Target	The sine curve simplification		
	Sess. 1&2	Sess. 3&4	Sess. 5&6
<i>8106 Carpino</i>	+2.5	-	-
<i>819 Barnardiana</i>	+2.1	-3.4	+17.2
<i>414 Liriope</i>	+5.2	-3.5	+2.9
<i>1660 Wood</i> <i>(162421)</i>	-5.8	+1.4	-
<i>2000 ET70</i>	+6.1	-	-

Target	The 4-POINT ultimate simplification		
	Sess. 1&2	Sess. 3&4	Sess. 5&6
<i>8106 Carpino</i>	+1.8	-	-
<i>819 Barnardiana</i>	+4.0	-3.8	+3.7
<i>414 Liriope</i>	+6.4	-	+2.2
<i>1660 Wood</i> <i>(162421)</i>	-5.8	0.0	-
<i>2000 ET70</i>	+4.1	-	-

Table VII: Comparison of Results from Three Methods

9. Stellar Parallax

The distance to nearby stars can be accurately determined by measuring their parallax angle while the Earth orbits around the Sun. The geometry of this situation is exactly the same as drawn in Figure 1, where now the circumference represents the orbit of the Earth. As the Earth orbits around the Sun, any observer on its surface sees the star’s parallactic angle ϕ constantly varying, from a maximum value occurring whenever the Earth is at right angle to the plane perpendicular to the Ecliptic which also contains both the Sun and the star (some 3 months prior or after star due opposition) to a null value whenever the Earth happens to also be placed on such plane (star opposition).

If the beginning of the time parameter is strategically selected to coincide with the moment of the star opposition, then our reasoning for the diurnal parallax effect is completely valid for the star parallax case – and therefore all the equations of our model can be accordingly translated. The former exact time of the asteroid culmination now becomes the exact time of the star opposition; the former unknown geocentric motion of the asteroid now becomes the unknown proper motion of the star.

Therefore, the 4-Point shortcut for the distance determination of a nearby star should work all the same, except this time to collect the four data points will take 15 months instead of just 30 hours.

Considering that the parallax angle of nearby stars is within reach of backyard observers (Sirius has a parallax of about 0.38 arcsec), once again the determination of their distance by means of the 4-Point shortcut should be a challenging but feasible task – although not especially suitable for the impatient observers.

10. Conclusions

For asteroids (or other Solar System objects) our method for determining their diurnal parallax and hence their distance is both simple and sensitive, only requiring two measurements on two proximate nights (the more adjacent, the better) from just one single observing point. On each night one of the measurements must be done around the time of culmination and the other as far from culmination as possible, in order to maximize sensitivity; but on both sets of measurements should be taken from the same side of the Meridian.

Achieving a distance accuracy of 5% for an asteroid close to opposition, derived from nothing other than just backyard observations from a single station during a short time interval – about 30 hours – is remarkable and totally feasible. The cherry on the top is that this goal – a kind of amateur fantasy not so long ago – only demands two sets of asteroid images, each covering not more than ten minutes, taken on two consecutive nights.

11. References

Buchheim, R. K. (2011) “A Modern Incarnation of Tycho’s Diurnal Parallax Method.” in *Proceedings for 31st Annual Symposium on Telescope Science* (Warner et al., eds.) pp. 109-114. Society for Astronomical Sciences, Rancho Cucamonga, CA.

Forbes, E. G. (1976). “Early Astronomical Researches of John Flamsteed.” *Journal for the History of Astronomy* **7**, 124-138.

Lindsay, L., Gill, D. (1877) “Note on the results of heliometer observations of the planet Juno, to determine its diurnal parallax.” *Monthly Notices of the Royal Astronomical Society* **37**, 04/1877, 308.

Ratcliff, S. J., Balonek, T. J., Marschall, L.A., Dupuy, D. L., Pennypacker, C. R., Verma, R., Alexov, A., Bonney, V. (1993). “The measurement of astro-

nomical parallaxes with CCD imaging cameras on small telescopes.” *American Journal of Physics* **61**, 208-216.

Smallwood, L. M., Katz, D. M., Richmond, M. W. (2004). “Near Earth Objects: A Brief Review and A Student Project.” *American Journal of Physics* **72**, 264-279.

Vanderbei, R. J., Belikov, R. (2007). “Measuring the Astronomical Unit.” *Sky and Telescope* January 2007, 91-94.

On the Maximum Amplitude of Harmonics of an Asteroid Lightcurve

Alan Harris
 MoreData!
 La Cañada, CA USA
 harrisaw@att.net

Abstract

Most asteroid lightcurves are dominated by the second harmonic of the rotation period, caused by elongated shape. However, if the shape is not very elongate, other harmonics may dominate, leading to ambiguity of which is the true rotation period. It is argued from geometry that at low phase angle, harmonics other than the second with amplitude exceeding ~ 0.4 are nearly impossible, so lightcurves with larger amplitude than that suggest a unique period dominated by the second harmonic, unless the spin is complex, non-principle axis rotation. On the other hand, lightcurves with amplitude less than 0.2-0.3 magnitudes can be dominated by other harmonics, especially the 4th and 6th, so the period may be ambiguous unless odd harmonics can be found to identify the true rotation period. Examples are presented of each, i.e., low and high amplitude ambiguities.

1. Geometric Rotational Variation Due to Shape

In the limit of geometric scattering at zero phase angle and no albedo variegation, the brightness of an object is just proportional to the projected cross sectional area. Consider various possible shapes as regular polygonal equatorial cross section; either prisms or cones with the same number of sides yield the same rotational variation of cross section. Tables I and II list the maximum range of cross section that comes from each shape, and the amplitude in magnitudes as such a figure rotates, which is just

$$A = -2.5 \log(CS_{min}/CS_{max}) \quad (1)$$

where CS_{min} is the minimum cross section and CS_{max} is the maximum cross section.

Note that concave faces do not increase the variation in cross section, hence amplitude of variation; convex faces reduce it. Thus the polygonal shapes considered represent the maximum variation of cross section as the figure rotates, and hence, subject to the geometric scattering approximation, the maximum amplitude of the primary harmonics due to that shape. Figure 1 illustrates the lightcurves that result from each of the polygonal shapes.

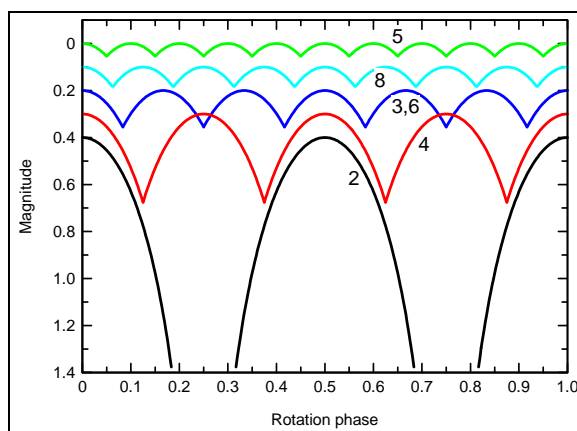


Figure 1. The rotational lightcurve of each of the polygonal figures considered, at zero phase angle and geometric scattering. A “two-sided polygon” is just a flat plate or straight line and has an infinite aspect ratio, hence an infinite amplitude lightcurve. Practically speaking, we see small asteroids of generally prolate form with axis ratios up to around 4:1, yielding lightcurves of 1.5 magnitudes or so. Lightcurves dominated by higher order harmonics (4, 6, 8, 10) have successively lower maximum amplitudes.

We know from symmetry that there are only even harmonics in this approximation. Shapes with odd numbers of sides (3, 5, 7, ...) produce primary harmonics of twice that number, i.e., 6, 10, 14. Figures of even numbers of sides (2, 4, 6, 8, ...) produce primary harmonics equal to the number of sides, i.e., 2, 4, 6, 8. In the left table above, I have calculated the amplitude of variation of the given harmonic that results from these figures. Actually, the amplitudes listed correspond to the maximum vs. minimum cross sectional area of the figure. A Fourier analysis of the

Maximum Amplitudes of Harmonics - Harris







Sides	Shape	Primary harmonic	Min/Max cross section	Maximum amplitude, magnitude	Primary harmonic	Maximum amplitude, magnitude
2		2	∞	∞	2	∞
3		6	$\cos(30^\circ) = 0.866$	0.156	4	0.376
4		4	$\cos(45^\circ) = 0.707$	0.376	6	0.156
5		10	$\cos(18^\circ) = 0.951$	0.054	8	0.086
6		6	$\cos(30^\circ) = 0.866$	0.156	10	0.054
8		8	$\cos(22.5^\circ) = 0.924$	0.086		

Table I. Number of primary harmonics for a shape with a given number of sides, the ratio of the min//max cross section, and the maximum amplitude.

Table II. The maximum amplitude for a given primary harmonic.

cross sectional area under uniform rotation would yield a series of harmonics (e.g., n , $2n$, $3n$, ...); the lowest order harmonic, n (an even number), would have a lower amplitude than listed, but a full composition of the harmonics would yield the amplitude listed, with n pairs of extrema per rotation cycle. The right hand table just re-arranges things by harmonic order. Note that the 3 and 6 sided figures (triangular or hexagonal) both yield maximum amplitudes of the sixth harmonic, and the same value, 0.156 magnitudes. It should also be noted that the above amplitudes are full-range amplitudes, maximum magnitude minus minimum magnitude, which is double what is meant by “amplitude” in harmonic analysis. What is to be noted here is first, the amplitude of the second harmonic has no geometric limit. In practice, it is about equal to the prolate axis ratio of the equator. For a “rubble pile” rotating slow enough that centrifugal force is not a major component, this has a limit of around 4:1 (Harris *et al.*, 2009), corresponding to an amplitude of about 1.5 magnitudes, and indeed that’s about the maximum we see among asteroids at low phase angle. In cases where the equatorial profile is not particularly elongate, that is, where higher shape harmonics dominate, we can consider the maximum amplitude that can result, which is what I have done above. A square profile can result in a 4th harmonic lightcurve of more than 0.3 magnitudes. Either a triangular or hexagonal profile can produce a 6th harmonic amplitude of about 0.15 magnitude. The maximum of still higher harmonics becomes rapidly smaller, such that it is rare to see any

harmonic beyond about order ten with a statistically significant amplitude.

I next examine two examples, one where the amplitude is so low that ambiguity is possible, and the other such a large amplitude that more than two extrema per rotation cycle is essentially impossible. In the latter case, we are forced to conclude that the asteroid is in a state of non-principal axis rotation.

2. 5404 Uemura

The asteroid (5404) Uemura was observed extensively from Modra in 2008 and again in 2009. Figure 1 shows the photometric data from the two apparitions plotted for the half-period of 1.7 hours, and the double-period of 3.4 hours. Even the shorter period shows three pairs of extrema, and the longer period has six. Unfortunately, the longer period contains almost no odd harmonics, and the amplitude is such that the longer period cannot be ruled out on account of its amplitude: the amplitude of ~ 0.12 is possible, even at sixth harmonic. This case was particularly provocative because the shorter period, 1.7 hours, is well shorter than the “spin barrier” for a “rubble pile” of normal rock density, and this object is well larger (~ 8 km diameter) than any other asteroid spinning faster than the “rubble pile” spin barrier (Harris and Pravec, 2006). Thus one is faced with a dilemma: the shorter period is indeed profound, but could not be ruled out based on these observations. When it was re-observed in 2009 (Figure 1c and 1d), essentially the same lightcurve was obtained. There is

just a small hint of asymmetry, that is odd harmonics, which repeats both years, thus leading us to prefer the longer period solution over the shorter period. Nevertheless, it is a cautionary lesson in the difficulty of determining the true period when the amplitude is low. Many other examples exist among larger asteroids, e.g. (53) Kalypso (Pilcher and Pray, 2010), but usually neither the half nor double period is particularly provocative as it is in the case of Uemura, so resolving the ambiguity is not so urgent.

We can further note that ambiguities like this can sometimes be resolved with observations at larger

phase angle. The “geometric” approximation that leads to no odd harmonics is not valid at non-zero phase angle, and in fact odd harmonics often appear enhanced as the phase angle increases. So it can be valuable to break the ambiguity by observing at the largest practical phase angle. Another important factor is to attempt to observe at two or more widely differing viewing geometries. Unfortunately, in the case of (5404) Uemura, the viewing direction in 2009 was almost exactly 180° around from that in 2008, so the projected geometry was nearly the same. Uemura was observed again in early 2011 at an aspect sub-

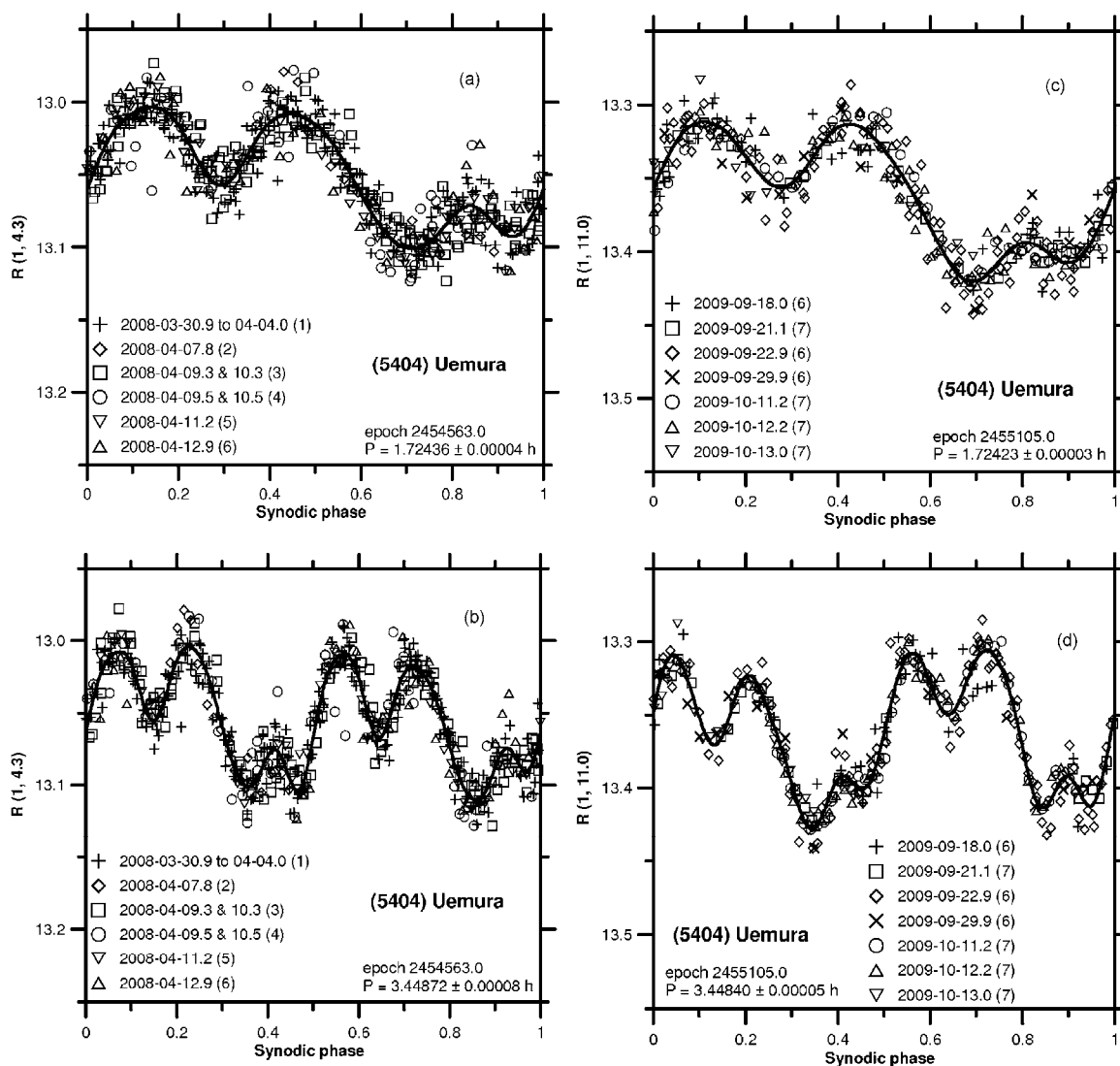


Figure 2. (a) 2008 data plotted with shorter period of 1.7 hours. (b) 2008 data plotted with double period of 3.4 hours. (c) 2009 data plotted with shorter period of 1.7 hours. (d) 2009 data plotted with double period of 3.4 hours. Note in both years, the two closely spaced minima at 0.4 phase in (b) and 0.9 phase in (d) are nearly equal, while the opposite two minima, at 0.9 in (b) and 0.4 in (d), are unequal in the same way. Likewise, the two maxima near 0.2 in (b) and 0.6 in (d) are nearly equal, while the other pair of maxima are slightly unequal, again in the same pattern both years. These subtle differences, well below the noise level of any single night lightcurve but repeating in the two apparitions, lead us to favor the longer period.

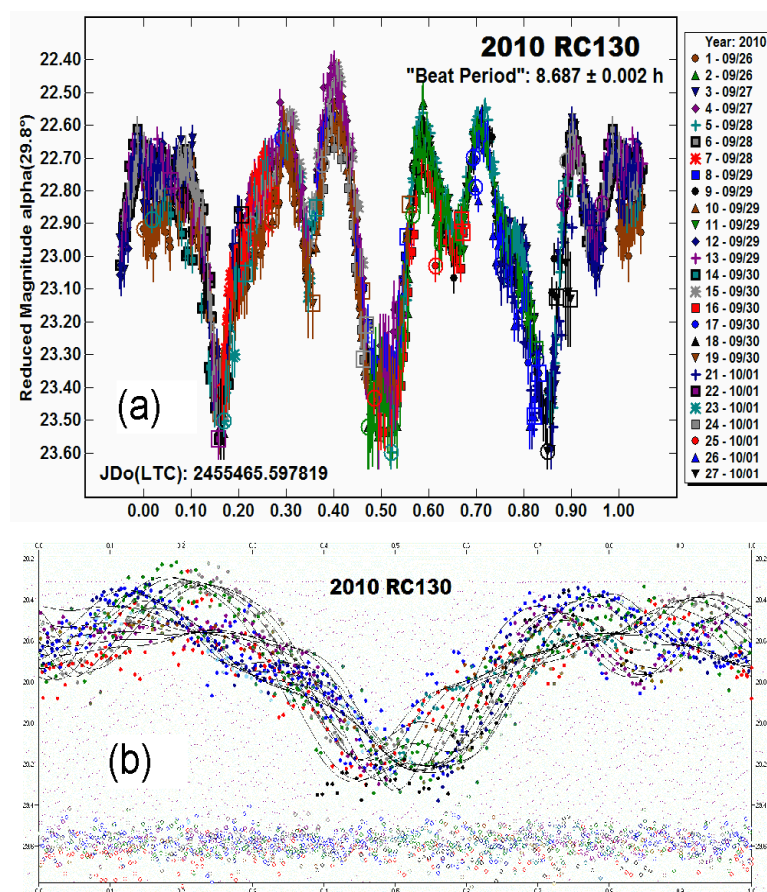


Figure 3. (a) The lightcurve of 2010 RC130 phased for a period of 8.687 hours. The fit is not exact, but mainly has an implausibly large amplitude for more than two minima per rotation cycle. (b) The complex rotation fit, phased to the longer of the two principal periods. The model fit lines show the variation cycle-to-cycle due to the second non-commensurate frequency; the plotted points across the bottom show the fit residuals.

stantially off the line of the 2008 and 2009 aspects, and indeed showed a slightly greater asymmetry, confirming the longer period.

3. 2010 RC130

The second example is the asteroid 2010 RC130, an NEA that is small enough (about 100 m diameter) that super-fast rotation is not unexpected. The lightcurve of this object revealed variations of about one full magnitude, but an apparent repeat period of about 9 hours, featuring three deep minima of about 1 magnitude and several other shallower minima in between. Figure 3(a) displays the data taken at Lowell Observatory phased to a period of 8.687 hours. The fit is not perfect, but more importantly, the large amplitude precludes a rotation period with more than two such deep minima. We therefore suspected a complex “tumbling” rotation state, which a primary

period perhaps about 1/3 of the 8.7 h period, but nearly harmonic with that period such as to produce a “beat” pattern that repeats approximately every 8.7 hours. Pravec ran a dual-frequency fit appropriate for NPA rotation, and indeed found a satisfactory fit with periods of 2.8915 and 1.7378 hours. Figure 3b is that solution, including the Lowell data plus observations from other observers, phased to the longer period. As noted, even if the fundamental rotation period is the shorter one it is not unexpectedly short for an object this small.

4. Conclusions

Deriving correct rotation periods from asteroid lightcurves is often difficult, especially when confronted with the possibility of non-principal axis rotation, super-fast rotation ($P < 2.2$ hours or so), and/or low amplitude of variation. The constraints on ampli-

tude of variation versus harmonic order can help resolve ambiguities. A further complication we have not discussed here is the substantial population of binary asteroids among objects less than ~10 km in diameter, which often show mutual eclipse events, with orbit periods not synchronous with the rotation period(s). All of these complications illustrate the need for extensive sets of high quality data to extract correct results. On the positive side, these complexities can lead to deeper understanding of asteroid structure beyond just measuring the rotation period.

5. Acknowledgements

I want to thank those who contributed data for 5404 Uemera and 2010 RC130: P. Birtwhistle, E. Bowell, A. Carbognani, E. W. R. Cooney, Š. Gajdoš, A. Galád, J. Gross, D. Higgins, K. Hornoch, B. Koehn, P. Kušnirák, B. Skiff, D. Terrell, J. Világi, and B. D. Warner

This work was supported by NASA grant NNX10AL35G and NSF grant AST-1032896.

6. References

Harris, A. W., Pravec, P. (2006). "Rotational properties of asteroids, comets and TNOs." *Proc. IAU Symp.* **229**, 439-447.

Harris, A. W., Fahnestock, E. G., Pravec, P. (2009). "On the shapes and spins of 'rubble pile' asteroids." *Icarus* **199**, 310-318.

Pilcher, F., Pray, D. P. (2010). *Minor Planet Bul.* **37**, 75-76.

PV Cephei and Gyulbudaghian's Variable Nebula

David Boyd

British Astronomical Association, Variable Star Section
5 Silver Lane, West Challow, Wantage, OX12 9TX, United Kingdom
drsboyd@dsl.pipex.com

Abstract

The Herbig Ae star PV Cephei is embedded in a dense molecular cloud which also contains Gyulbudaghian's Variable Nebula. While the variability of PV Cephei has been studied intermittently over the past 35 years, little attention has been paid to measuring the variability of the nebula. We report on photometric observations of both objects over the past two years to investigate if there is a relationship between variations of the star and the nebula.

1. Pre-main-Sequence Stars

Young pre-main-sequence stars are intrinsically variable. They are still in the process of contracting onto the main sequence from dense molecular clouds under the influence of gravity. As a young star contracts, it spins up and material not yet drawn into the star forms an accretion disc around it. Material from the disc falling onto the surface of the embryonic star causes apparently random fluctuations in the star's brightness. At the same time the initially weak magnetic field within the gas cloud is concentrated within the contracting star which often results in an active chromosphere, magnetically channelled accretion from the disc onto the star's surface, and material being ejected along the star's rotational axis in the form of bipolar conical winds and collimated jets (Romanova *et al.*, 2009). The jets may collide at high speed with clumps of gas and dust in the surrounding molecular cloud creating the shock features known as Herbig-Haro objects. Pre-main-sequence stars with mass less than about two solar mass are classified as T Tauri stars, those between two and eight solar mass as Herbig Ae stars.

2. PV Cephei

PV Cephei is a fairly typical Herbig Ae star, spectral type A5e, less than a million years old, ~500pc distant, with ~3.5 solar mass and luminosity at its brightest approaching 100 times that of the Sun. It is still in the process of contracting out of the molecular cloud which surrounds the young star. It has a rather massive circumstellar disc, containing about 20% of the mass of the star (Hamidouche, 2010), with an inclination of about 80 degrees relative to our line of sight so we are looking at the disc almost edge-on (Gomez *et al.*, 1997).

Material from the disc accreting onto the surface of the star causes periods of increased brightness (Lorenzetti *et al.*, 2011). Obscuration by either the edge of the disc or dust close to the star may contribute to occasional fading of the star (Elek and Kun, 2010; Kun *et al.*, 2011).

Measurements of red plates obtained with the Crossley reflector at Lick Observatory in 1977-1979 showed the star brightening to magnitude 11 before fading to magnitude 16 (Cohen *et al.* 1981). Little attention was then paid to the star until 2005 when it was observed at magnitude 12 (Elek and Kun, 2010). Between 2007 and 2010 it varied in the range magnitudes 15 to 18 (Kun *et al.*, 2011, Lorenzetti *et al.*, 2011). A search using adaptive optics failed to reveal a close binary companion to PV Cephei, which could act as a possible cause of variability (Connelley *et al.*, 2009).

PV Cephei is located near the edge of a molecular cloud. Outflow from the star towards the north has cleared a conical cavity in the cloud through which the star's light illuminates the surrounding interstellar medium (Levreault, 1984; Arce and Goodman, 2002). Jets emitted by the star have created several Herbig-Haro objects to the north and south of the star as they plough into the surrounding interstellar medium (Reipurth *et al.*, 1997). The northern jet is blue-shifted and the southern jet red-shifted indicating they are tilted out of the plane of the sky by about 10 degrees. The jets are also precessing in a helical manner with a period of approximately 8300 years (Gomez *et al.*, 1997). From the positions of the Herbig-Haro objects, estimates of the velocity of the jets, and the known distance to the star it is estimated that new Herbig-Haro objects have been produced by major emissions from PV Cephei at approximately 2000 year intervals (Reipurth *et al.*, 1997).

3. Gyulbudaghian's Nebula

Light from PV Cephei shining on the inside of the cavity in the surrounding molecular cloud cleared by the northern outflow creates the variable reflection nebulosity variously known as RNO125, GM29 or Gyulbudaghian's Nebula. The opposing outflow is directed into the molecular cloud and its light is heavily attenuated to the point that it is barely visible.

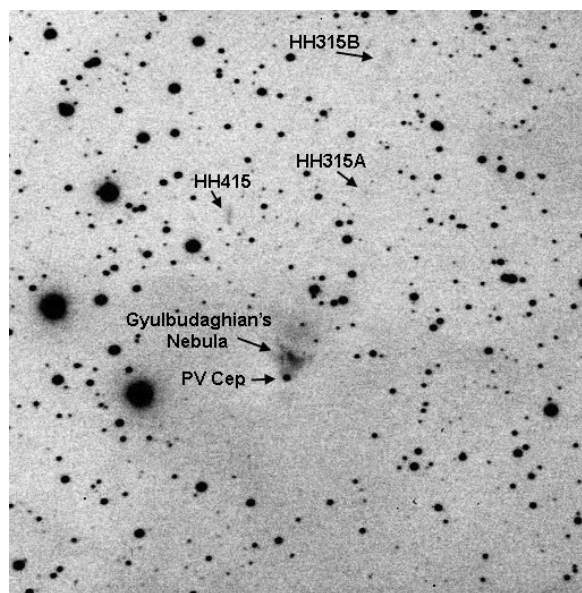


Figure 1. 33 min exposure of the field around PV Cephei.

Figure 1 is a 33-min stacked exposure of the field around PV Cephei taken with a 0.35-m SCT, SXVR-H9 CCD camera, and an R filter on 2011 August 19 when the fan-shaped reflection nebula was relatively bright. It also shows some of the Herbig-Haro objects close to the star.

Although several papers have reported measurements of the variability of PV Cephei, the changing brightness of the nebula has only been commented on qualitatively based on its appearance in photographs and more recently CCD images. For example: “The rapid variability of the nebula indicates that changes in its luminous structure must result from variable illumination.” (Gledhill *et al.*, 1987).

While it has been assumed that the source of this varying illumination is the variability of PV Cephei, no direct evidence has so far been presented to support this assumption. In particular, no one appears to have systematically measured the varying brightness of the nebula and correlated this with the variability of the star.

4. New Observations

The British Astronomical Association's Deep Sky Section has an observing programme to monitor the changing brightness of variable nebulae associated with young stars. As a contribution to this programme, I began monitoring PV Cephei and Gyulbudaghian's Nebula in 2010 March using the equipment listed above. I measured the brightness of PV Cephei by conventional CCD photometry using an R filter because of its predominantly red colour. I took care to measure the sky background outside the area of the nebula. I used a square aperture sufficiently large to encompass the nebula at its brightest to measure the total light intensity from the nebula plus sky background. The level of sky background was estimated by measuring the light intensity in a similar square offset to the east of the star to avoid contamination by the opposing jet hidden within the molecular cloud. The sky background was subtracted from the nebula plus sky background to give a measurement of the light emission from the nebula alone and this was converted to a magnitude using the usual formula. This method has been used consistently throughout the project keeping all aperture sizes constant. The zero point of the nebula magnitude scale was chosen such that the mean magnitudes of the star and the nebula were the same for convenience of graphical representation.

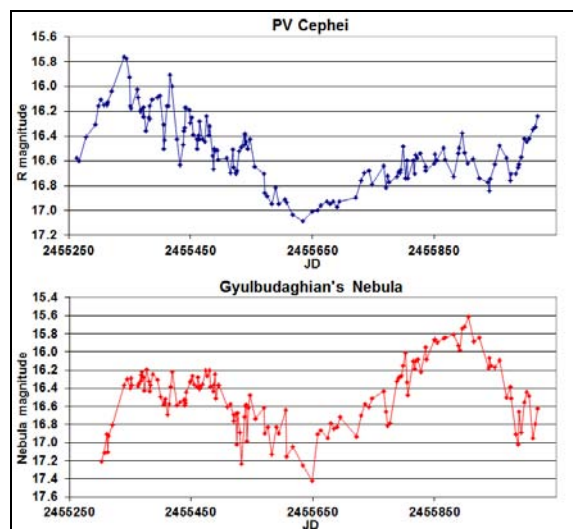


Figure 2. Light curves of PV Cephei and Gyulbudaghian's Nebula.

The star's high declination means it can be followed throughout the year from the UK. During the following two years PV Cephei varied between magnitudes 15.8 and 17.1. Over the same interval, the nebula followed a broadly similar pattern with two bright episodes separated by a deep fade (Fig. 2).

A search for periodic signals in the light curves of PV Cephei and the nebula failed to reveal any significant signals with period between 2 and 200 days.

Figure 3 shows images of the field around PV Cephei taken at various times between 2010 April and 2012 March to illustrate the variability of the nebula. Each image is typically a stack of 25-30 one minute exposures

5. Correlated Variation

To investigate whether there is a relationship in time between these two light curves, a Discrete Correlation Function (Edelson and Krolik, 1988) was computed adding a variable delay to the light from the star. Maximum correlation occurs when the star's light is delayed by 27 ± 2 days relative to that of the nebula. Figure 4 shows the two light curves superimposed with this delay.

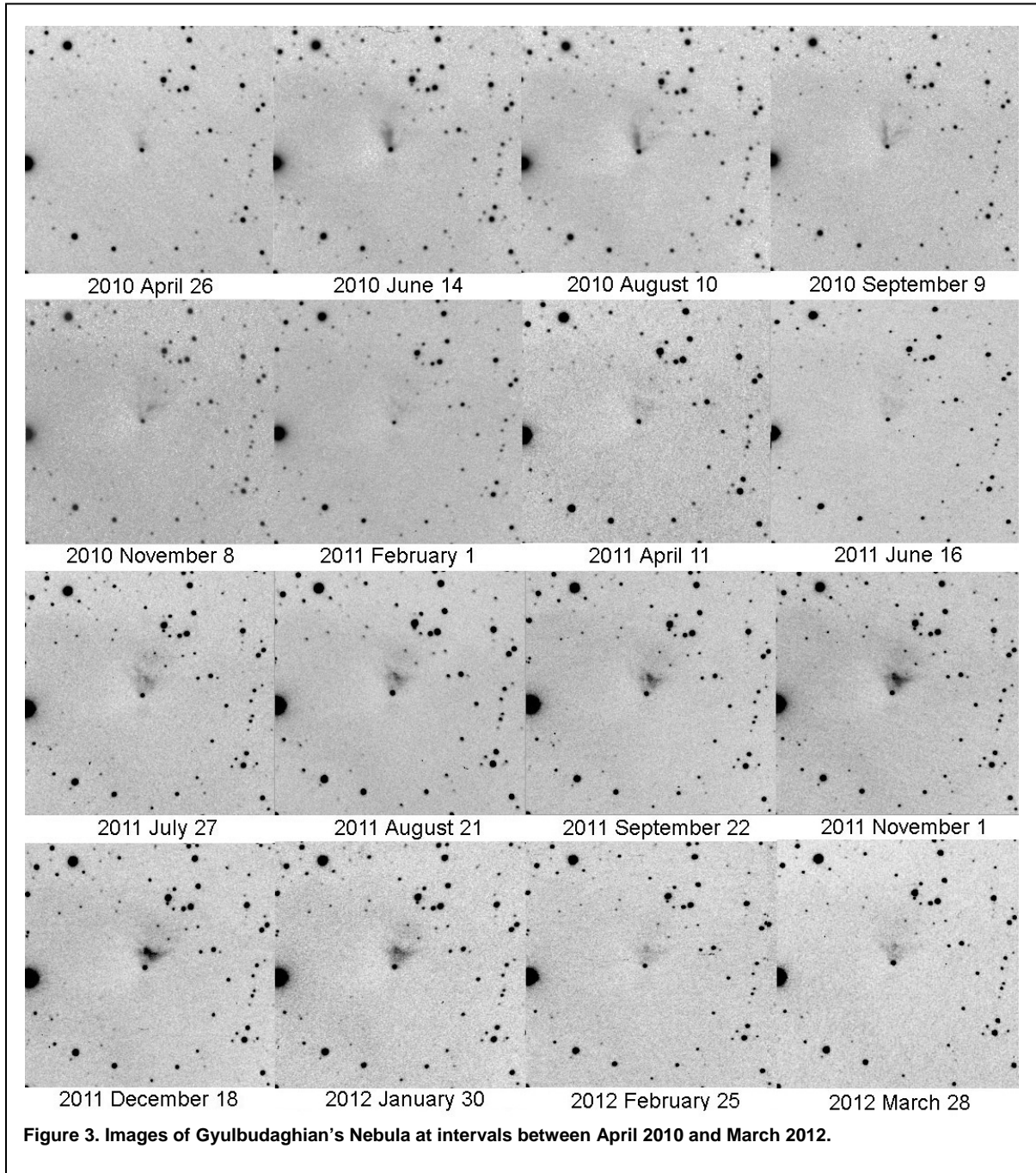


Figure 3. Images of Gyulbudaghian's Nebula at intervals between April 2010 and March 2012.

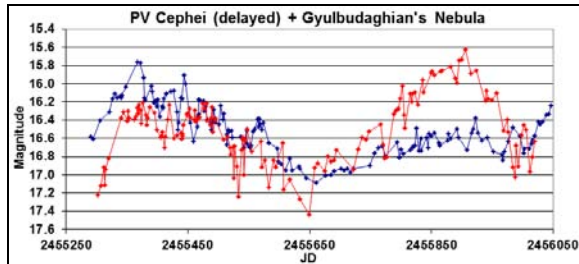


Figure 4. Superimposed light curves of PV Cephei (delayed by 27 days) and Gyulbudaghian's Nebula.

For the first time this provides evidence in support of a direct correlation between changes in the light output of the star and the brightness of the nebula. However, while the major increases and decreases of the two light curves are consistent, the amplitudes of these changes do not follow each other with the same degree of consistency. In particular, the increase in brightness of the star in the latter part of 2011 was considerably less than the corresponding increase in brightness of the nebula.

A possible explanation for this arises from consideration of the mechanisms involved in these changes. It is likely that a steady brightening of the star is caused by a major accretion event. This in turn causes the nebula to brighten. If either the edge of the circumstellar disc or the dust clouds which are in continual movement around the star happen to partially obstruct the light it emits in our direction, this may reduce the apparent increase in the star's brightness. Movement of dust around the star may also create a shadowing effect and lead to the varying pattern of illumination we see in the nebula.

It is interesting to calculate the light travel time from the star to the nebula to see if this is consistent with the observed delay between their respective light curves. Using the published distance to the star, the apparent inclination of the outflow, the distance in images from the star to the nebula and the image plate scale, this light travel time works out at approximately one month.

Only continuing observation will reveal whether this apparent correlation is maintained in the future.

6. Acknowledgements

This research has made use of NASA's Astrophysics Data System Bibliographic Services.

7. References

Arce H. G., Goodman A. A. (2002). *Ap. J.* **575**, 911.
 Cohen M., *et al.* (1981). *Ap. J.* **245**, 920.

Connelley M. S., *et al.* (2009). *Astron. J.* **138**, 1193.
 Edelson, R. A., Krolik, J. H. (1988). *Ap. J.* **333**, 646.
 Elek E., Kun M. (2010). *Journal of Physics Conference Series* **218**, 12021.
 Gledhill T. M., *et al.* (1987). *Monthly Notices of the Royal Astronomical Society* **229**, 643.
 Gomez M., *et al.* (1997). *Astron. J.* **114**, 265.
 Hamidouche, M. (2010). *Ap. J.* **722**, 204.
 Kun M., *et al.* (2011). *Monthly Notices of the Royal Astronomical Society* **413**, 2689.
 Levreault R. M. (1984). *Ap. J.* **277**, 634.
 Lorenzetti D., *et al.* (2011). *Ap. J.* **732**, 69.
 Reipurth B., *et al.* (1997). *Astron. J.* **114**, 2708.
 Romanova, M. M., *et al.* (2009). *Monthly Notices of the Royal Astronomical Society* **399**, 1802.

Why Visual Observations of Mu Cephei are Important

David G. Turner
 Saint Mary's University
 Halifax, Nova Scotia, B3H 3C3, Canada
 turner@ap.smu.ca

Abstract

Our understanding of Type C (M supergiant) semiregular variables such as Mu Cep, Betelgeuse, S Per, BC Cyg, etc. is limited to some extent by a lack of regular and accurate observations for the stars. Bright objects like Mu Cep, in particular, are frustrating to observe because of their long periods of variability, almost two and a half years for Mu Cep, a lack of reference standards lying in close proximity, and red colors, which affect visual perceptions of brightness and/or photometric reductions. Yet such observations are essential for proper phasing of spectroscopic studies, which are beginning to reveal intriguing insights into the nature of their variability.

1. Introduction



Figure 1. The SRC variable S Persei according to the Digitized Sky Survey (Moncrieff 2011).

Variable M-type supergiants such as S Per (Fig. 1) belong to a small group of long-period variables, referred to as Type C semiregulars (SRCs), that are intrinsically interesting for several reasons. They are identified as likely precursors to core collapse supernovae, typically Type II (possibly within our lifetimes), and have been identified (Pierce *et al.*, 2000; Jurcevic *et al.*, 2000) as potentially valuable extragalactic distance indicators because of their high luminosities, brighter than that of Cepheids, and the fact that, like Cepheids, they appear to obey their own period-luminosity relation (Stothers, 1969; Moncrieff, 2011). They have actually been used as distance indicators for Local Group galaxies for several

decades. Yet as a group they are also relatively understudied, for obvious reasons: periods of variability spanning anywhere from 100 to 900 days, low amplitudes of variability (for most), complex spectra dominated by TiO molecular bands, and photometric brightnesses that are a challenge to calibrate reliably on a common system. That is where simple eye estimates may play an important role.

2. Current Knowledge

So few researchers specialize in and actively observe Type C semiregulars that even the description of their particulars given in the *General Catalogue of Variable Stars* is misleading. Photographic light curves for CL Car and IX Car presented in Figs. 2 and 3 illustrate some of the main characteristics. True Type C semiregulars, unlike their M supergiant cousins, the LC irregular variables, display highly regular light variations, which can be attributed to pulsation (Stothers, 1969; Turner *et al.*, 2012). They often display superposed long-term variations in mean brightness of unknown origin. Perhaps starspot cycles occur as well? The light amplitudes depend upon the effective temperature of the stellar photosphere and the luminosity of the star, with the cool, luminous supergiant variables displaying the largest light amplitudes (Moncrieff, 2011). The SRC variable IX Car is a most curious case, since its light amplitude appears to increase as the star brightens.

The periods of variability attributed to individual objects vary from source to source in the literature, and probably depend upon the method adopted to measure them. Fourier techniques do not always work well for SRC variables. For the regular light variations of the intriguing SRC variable BC Cyg (Fig. 4), for example, the author developed a variant of existing techniques in which measured times of

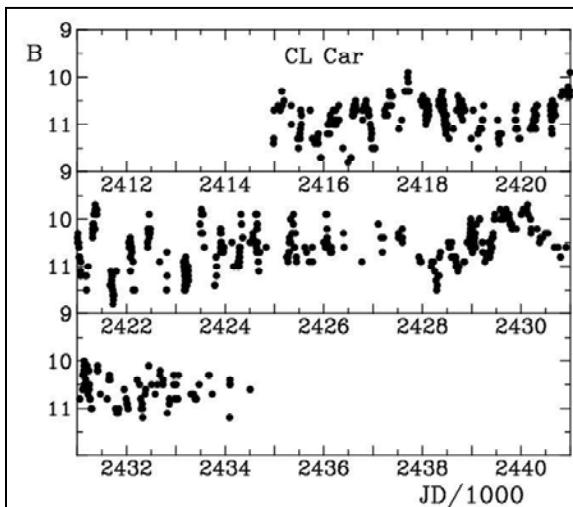


Figure 2. Eye estimates for CL Car (spectral type M5 Ia) from photographic plates in the Harvard collection. The blue light variability has a dominant period of 512 days superposed upon gradual changes in mean brightness.

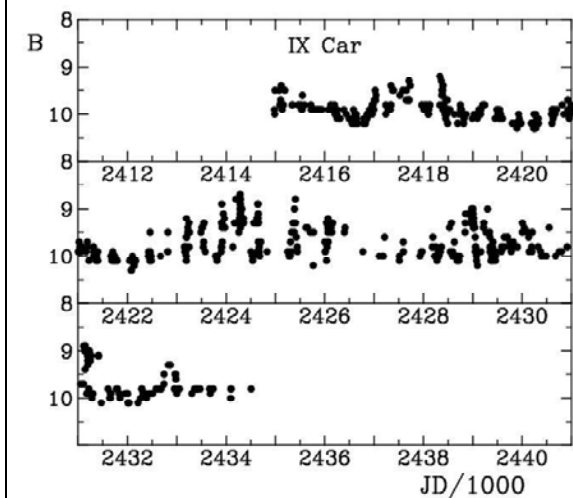


Figure 3. Eye estimates for IX Car (spectral type M2 Iab) from photographic plates in the Harvard collection. The blue light variability has a dominant period of 357 days, with the amplitude appearing to increase as the star brightens.

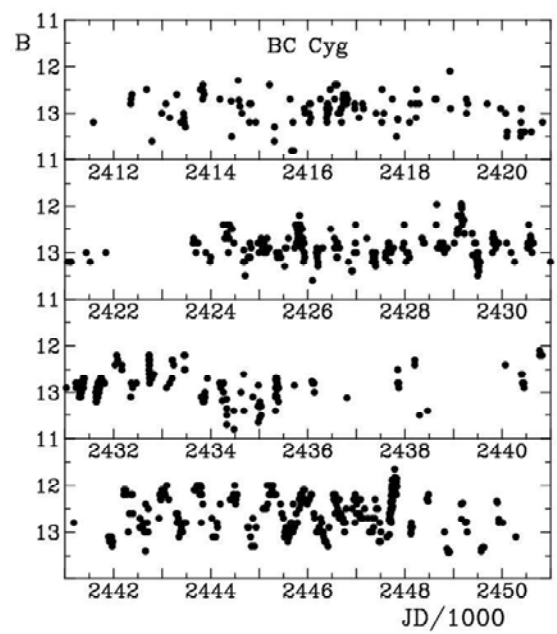


Figure 4. Eye estimates for BC Cyg (spectral type M3-5 Ia) from photographic plates in the Harvard and Sternberg collections. The blue light variability has a dominant period of 692.8 days established from observed times of light maximum.

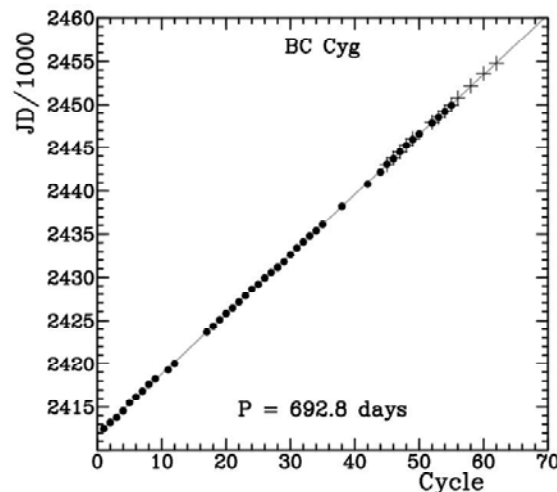


Figure 5. Estimated times of light maximum as a function of cycle count for BC Cyg, where points represent maxima measured photographically and plus signs from AAVSO visual estimates.

light maximum are correlated with cycle number to establish the mean period (Turner *et al.*, 2012), as in Fig. 5. BC Cyg varies with a mean period of 692.8 days, but individual times of light maximum appear to deviate from the predicted times by as much as 100 days on average (Fig. 6). Much of the scatter is probably caused by deviant observations used in the analysis (see recent AAVSO visual observations in Fig. 7), but a small proportion of the scatter is consis-

tent with what is observed for random fluctuations in period for pulsating variables (Turner *et al.*, 2009).

The establishment of an accurate period of variability for BC Cyg was an essential step towards understanding the physics of the variability in the star. A reliable ephemeris for BC Cyg permitted an accurate phasing of older and more recent spectroscopic and spectrophotometric observations of the star (White and Wing, 1978; Turner *et al.*, 2012).

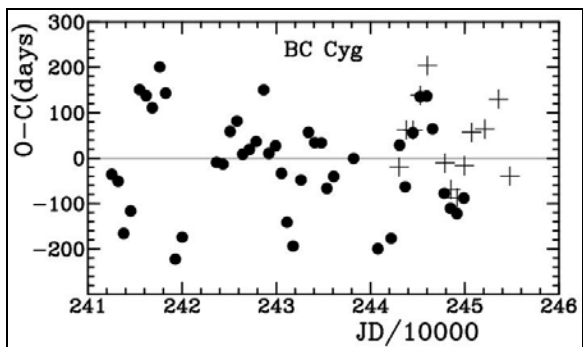


Figure 6. O-C residuals for BC Cyg from measured times of light maximum, with symbols as in Fig. 5.

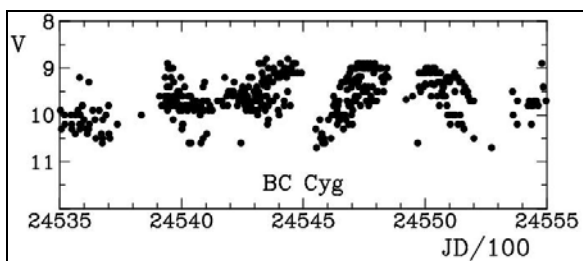


Figure 7. Recent visual estimates for BC Cyg from the AAVSO database. The large scatter makes it difficult to establish the periodicity of the star and times of light maximum reliably.

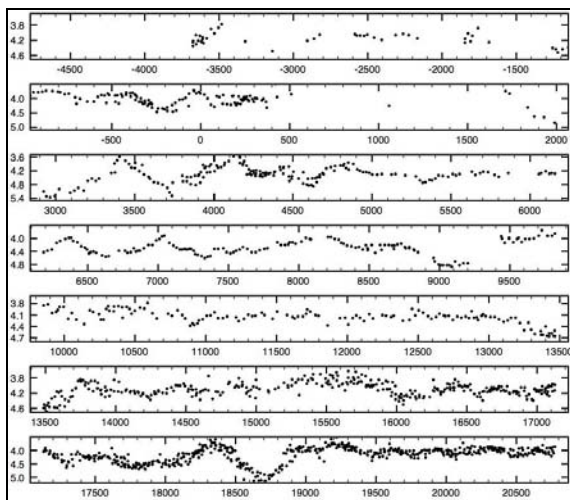


Figure 8. Older visual brightness estimates for Mu Cep from the AAVSO database for dates normalized to HJD 2400000.

That in turn revealed that the systemic velocity of the star as well as its temperature and luminosity class variations are correlated directly with its brightness variations, in much the same fashion as in pulsating classical Cepheids (Turner *et al.*, 2012). Apparently the dominant variability in such stars is the result of radial pulsation, as argued years ago by Stothers (1969).

Many Type C semiregulars are members of open clusters. S Per and several SRC variables around it are members of the young cluster Chi Persei (NGC 884), for example, BC Cyg is an outlying member of the extremely young cluster Berkeley 87, and Mu Cep is a member of the young cluster Trumpler 37. At least 17 of the known SRCs, about a third of the existing sample, are identified as belonging to Galactic clusters (Moncrieff, 2011).

The location of the stars in their cluster H-R diagrams implies masses for them of order 15-20 solar masses, with indications of higher turnoff point masses for the associated clusters. It appears that the stars have undergone considerable mass loss since the main-sequence stage prior to reaching their current state. The final stages of nuclear energy generation in the cores of these stars involve fusion of heavy elements through alpha particle capture, and are predicted to occur fairly quickly, in some cases over intervals shorter than the pulsation periods of the stars. The possibility that a known Type C semiregular variable might soon explode as a supernova cannot be discounted, in which case all information about its light signature prior to the event would be of significant scientific value.

It is here that visual observations of SRC variables become important. The literature contains very few photoelectric or CCD observations of such stars. A long-term photoelectric monitoring of the Type C semiregulars Alpha Ori and TV Gem by Wasatonic *et al.* (2011) is an exception, although future and current ground-based surveys should fill the void. However, all estimates of reddening and luminosity for known SRC variables must currently rely upon visual estimates, since high precision light curves are simply unavailable in most cases. A particularly challenging case is that of Mu Cephei.

3. Mu Cephei

Mu Cephei is one of the brighter SRC variables, and is bright enough and close enough spatially to the Cepheid Delta Cephei that both can be observed simultaneously, either through binoculars or without optical aid. The star exhibits a relatively small light amplitude, however, which means that the collection of AAVSO observations for the variable (Figs. 8 and 9) is particularly difficult to analyze either for periodicity or mean brightness. Moncrieff (2011) used Fourier techniques to find a range of best-fitting periods for the star covering values from 747 days to 1116 days, with an optimum value of 844 days for all AAVSO estimates. The resulting phasing of available spectroscopic and spectrophotometric measures (radial velocities, spectral types) with that period was

particularly troublesome (Moncrieff *et al.*, 2010; Moncrieff, 2011), implying that a different period is needed to match all available observations.

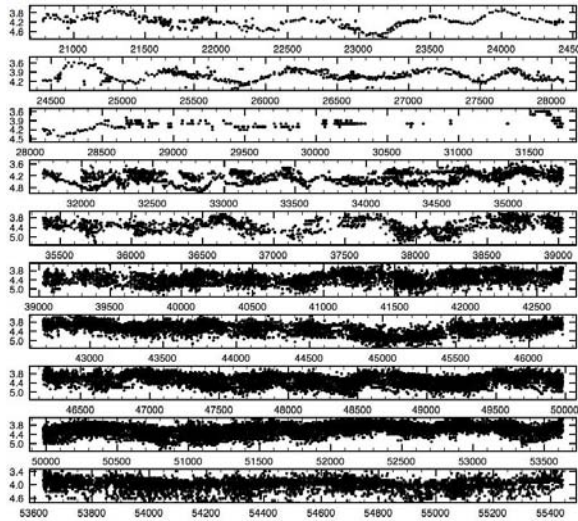


Figure 9. More recent visual brightness estimates for Mu Cep from the AAVSO database for dates normalized to HJD 2400000.

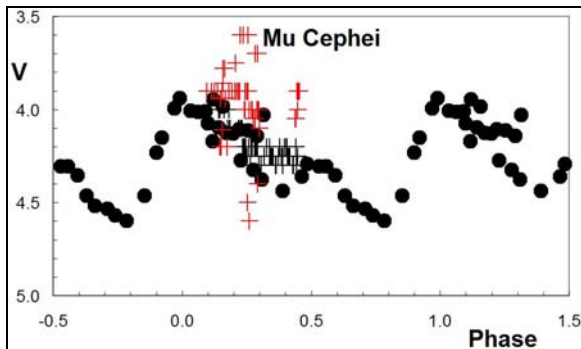


Figure 10. Recent visual brightness estimates for Mu Cep by the author (black plus signs) and from the AAVSO database (red plus signs) relative to older photoelectric and *Hipparcos* data (filled circles) phased to a period of 787 days.

There are a few photoelectric observations for the star available in the literature, as well as more than three years of monitoring from space by *Hipparcos*. Those observations were combined with recent visual observations of the star by the author to infer a possible best-fit period of 787 days for the star, with considerable uncertainty. The data phased to that period are plotted in Fig. 10, and include some recent visual estimates from the AAVSO database.

The light curve is probably less well defined than indicated by the observations, although the recent steady drop in brightness is real. At least another year or two of monitoring is needed to establish the period accurately. It may even be undergoing irregular changes. It seems like such a minor parameter, the

period of variability for Mu Cephei, but the membership of the star in the cluster Trumpler 37 implies that this variable M supergiant is a valuable calibrator for the SRC period-luminosity relation, particularly since it is the longest period Type C semiregular defining the relationship. It is at long pulsation periods that extragalactic SRC variables are most easily detected and reliably observed photometrically. Nailing down an accurate value for the pulsation period of Mu Cep could have implications for our knowledge of the extragalactic distance scale, which, at present, is essential for understanding the nature of the universe on large scales.

4. Future Observations

While it is true that observations of all Type C semiregular variables are valuable, a strong case can be made for the current need of observations for Mu Cephei. The period of variability for the star is still very uncertain, and the scatter in recent AAVSO observations for it (Fig. 10) suggests a need for improving the accuracy of observers worldwide. The great visual observer Johann Friedrich Julius Schmidt got practical assistance from Argelander in the 1800s at the start of his long-term program of monitoring the brightness of Polaris (Schmidt, 1857), and such mentoring would seem to be of particular value in observations of red variables like the SRCs.

Most observers are aware of the Purkinje effect when observing red stars at low light levels, since the stars may appear fainter than they actually are because of the changing color sensitivity of the eye at different light levels. Such effects may be present in some older AAVSO estimates for the brightness of BC Cyg, for example (Turner *et al.*, 2006), since it was often observed to be about 0.5 magnitude fainter than expected several decades ago. In the case of Mu Cep an opposite effect may be present (Fig. 10), since some observers appear to overestimate the brightness of the star, perhaps through overcompensation for the Purkinje effect. The red variables have long been a major component of AAVSO programs (Williams and Saladyga, 2011), but the method of averaging observations by individual observers into mean light curves of higher precision may need improvement in the case of M supergiant variables. A concerted program to recalibrate observers of SRC variables onto a common, accurate system linked to the Johnson *UBV* system may be needed if we are to advance our understanding of what is truly an intriguing and valuable class of variable star.

All observations of Mu Cephei would be welcomed by this researcher, who is willing to provide advice on different techniques to try. The precision of

eye estimates is best when the object being observed is near the limit of vision (Turner, 2000), and the author has found that observing bright stars through binoculars that have been defocused enough to place either the program star or the comparison star at the limit of detectability provides more reliable magnitude estimates than is the case for in-focus images. Experience in making eye estimates of brightness for stars on out-of-focus plates in the collection of the Harvard College Observatory is sufficient to confirm the validity of such an approach. Perhaps more experienced visual observers have their own tricks to share?

5. Acknowledgements

The author is grateful to Kathleen Moncrieff for permission to use some of her thesis work in this study, and acknowledges with thanks the variable star observations from the AAVSO International Database that were contributed by observers worldwide and used in this research.

6. References

- Jurcevic, J. S., Pierce, M. J., Jacoby, G. H. (2000). "Period-Luminosity Relations for Red Supergiant Variables, I. The Distance to M101." *Mon. Not. Roy. Astron. Soc.* **313**, 868.
- Moncrieff, K. E. (2011). "Improving Our Understanding of SRC Variable Stars." Ph.D. Thesis, Saint Mary's University.
- Moncrieff, K. E., Turner, D. G., Short, C. I., Bennett, P. D. (2010). "Spectral Type and Radial Velocity Variations in Three SRC Variables." *Odessa Astron. Publ.* **23**, 86.
- Pierce, M. J., Jurcevic, J. S., Crabtree, D. (2000). "Period-Luminosity Relations for Red Supergiant Variables, I. The Calibration." *Mon. Not. Roy. Astron. Soc.* **313**, 271.
- Schmidt, J. F. J. (1857). "Über veränderliche Sterne." *Astron. Nachr.* **46**, 293.
- Stothers, R. (1969). "On the Pulsation Hypothesis for Massive Red Supergiants." *Astrophys. J.* **156**, 541.
- Turner, D. G. (2000). "Observing Bright Cepheids without Optical Aid." *J.A.A.V.S.O.* **28**, 116.
- Turner, D. G., Rohanizadegan, M., Berdnikov, L. N., Pastukhova, E. N. (2006). "The Long Term Behavior of the Semiregular M Supergiant Variable BC Cygni." *Publ. Astron. Soc. Pacific* **118**, 1533.
- Turner, D. G., Percy, J. R., Colivas, T., Berdnikov, L. N., Abdel-Sabour Abdel-Latif, M. (2009). "Stochastic Processes in Yellow and Red Pulsating Variables. In Stellar Pulsation: Challenges for Theory and Observation." *AIP Conference Series 1170* (J. A. Guzik, P. A. Bradley, eds.). p. 167.
- Turner, D. G., Moncrieff, K. E., Short, C. I., Wing, R. W. (2012). "The Nature of Variability in M Supergiants: The Forgotten Type C Semiregulars." *Astrophys. Space Sci. Proceedings*, in press.
- Wasatonic, R. P., Guinan, E., Engle, S. (2011). "Red-Eye Astronomy: 15 Years of V-band and Near-IR TiO Photometry of the Red Supergiants Alpha Orionis And TV Geminorum." *Bull. Am. Astron. Soc.* **43**, AAS 218, #322.05.
- White, N. M., Wing, R. F. (1978). "Photoelectric Two-Dimensional Spectral Classification of M Supergiants." *Astrophys. J.* **222**, 209.
- Williams, T. R., Saladyga, M. (2011). *Advancing Variable Star Astronomy: The Centennial History of the American Association of Variable Star Observers*. Cambridge University Press, Cambridge.

ROAD (Remote Observatory Atacama Desert): Intensive Observations of Variable Stars

*Franz-Josef Hamsch
VVS, AAVSO, BAV, GEOS
Oude Bleken 12, B- 2400 Mol, Belgium
M31@telenet.be*

Abstract

The author discusses his new remote observatory under pristine skies and the intensive observations of variable stars he is accomplishing. The stars under investigations are mainly cataclysmic variables in request of AAVSO, CBA and VSNET alerts as well as other type of stars like RR Lyrae stars. Examples of dense observations of different cataclysmic variables as well as a RR Lyrae star are presented. The focus goes to the first bright outburst of SV Ari (Nova Ari 1905) since its discovery as well as the first outburst of UGWZ candidate BW Scl. Also results for VW Hyi, another cataclysmic variable will be shown. Furthermore an intensively observed RR Lyrae star will be highlighted.

1. Introduction

It is an amateur astronomer's dream to observe under pristine dark and clear skies nearly every night like at the sites where the professional astronomical observatories are located. Such a dream normally never comes true. However, modern techniques and infrastructures in most countries make it possible nowadays to observe from remote sites using off the shelf technology. The author installed a remote observatory under the dark skies of the Atacama Desert close to the town of San Pedro de Atacama. The telescope is housed at SPACE (San Pedro de Atacama Celestial Exploration; <http://www.spaceobs.com/index.html>). The owner is an amateur astronomer, too who formerly worked at ESO at the big telescope sites in Chile. In 2003 he started SPACE, which has been extended to telescope hosting since a couple of years.

I got in contact with him in 2009 and decided to put my observatory at his place.

Unfortunately, delivery of the telescope took much longer than anticipated and only in 2011 July, the dome, mount and telescope could be installed. Since 2011 August 1, the remote observatory is producing data every clear night. So far in the less than 8.5 month of operation this amounted to about 220 data taking nights. Not bad, is it not?

I am collaborating with J. Patterson from the Center of Backyard Astrophysics (CBA) and T. Kato from the VSNET email alerts on the observation of cataclysmic variable stars.

Furthermore I am interested in observing RR Lyrae stars. Here, I collaborate with the Groupe Européen d'Observations Stellaires (GEOS). In Belgium I am member of the Werkgroep Veranderlijke

Sterren (WVS) on High Amplitude Delta Scuti (HADS) stars. I am also member of AAVSO and the German Bundesdeutsche Arbeitsgemeinschaft für Veränderliche Sterne (BAV).

During the many clear nights a lot of data is being gathered on many stars. Since the space here is limited I restrict myself to some highlights, the outburst of SV Ari, BW Scl and VW Hyi. Also a RR Lyrae type star with a strong Blazhko effect will be mentioned.

2. Observatory

The remote observatory in Chile houses a 40-cm f/6.8 Optimized Dall-Kirkham (ODK) from Orion Optics, England. The CCD camera is from FLI and contains a Kodak 16803 CCD chip with 4kx4k pixels of 9 μm size. The filter wheel is also from FLI and contains photometric BVI filters from Astrodon.

In Belgium, where I live, I have a roll-off-roof observatory in my backyard, housing three scopes for variable star observations if it ever gets clear. Belgium is neither famous about its weather nor its light pollution, nevertheless there is still some room for interesting observations. Those telescopes are a Celestron C14 and C11 and a Meade ACF14. The telescopes are equipped with two SBIG ST8XME and an STL-11kXM CCD camera using BVRI photometric filters.

To make the telescope park complete I also collaborate with AAVSO in sharing an AAVSONet telescope (a Meade 30-cm SCT) with an SBIG ST9-XME CCD.



Fig. 1 Photo of the remote telescope installation in Chile.

Fig. 1 shows an image of the remote telescope in Chile. It is housed in a clamshell dome, making easy movement of the telescope possible without the need to follow with a shutter of a normal dome.

Images of a night's session are either acquired with ACP or CCDCommander automation software. Further analysis in terms of determination of the brightness of the stars is done using a program developed by P. de Ponthierre (2010). The data are then finally submitted to the AAVSO.

3. SV Aries (Nova Aries 1905)

As a first example, I show the results of the campaign on SV Ari. SV Ari was discovered on 1905 Nov. 6 by M. and G. Wolf in Heidelberg, Germany, at a photographic magnitude of 12.0. It was reported that it had brightened from mag 22.1. Kimpel and Jansch reported a possible sighting in 1943 September at a magnitude of 15.7, but this was not confirmed. No brightness increase has been observed for this star ever since.

Then on 2011 August 2.788 UT, R. Stubbings observed the field of SV Ari and saw an object at magnitude 15.0. He sent an alert via the mailing list cvnet-outburst around to ask for confirmation. Also via the VSNET mailing list the information of the outburst of SV Ari was spread. This led to confirmation by G. Masi (2011) and R. Fidirich (2011). I saw those alerts via VSNET and since G. Masi immediately took a time series and observed superhumps, I also decided to go after this star and started a time series at Aug., 2.844 UT just 1.34 h after the initial discovery. A first analysis of the data of G. Masi by the Kyoto team (Ohshima *et al.*, 2011) showed that the star is probably an SU UMa type dwarf nova with a superhump period of about 1.54 h. The present outburst seems also not as bright as the one during the discovery of magnitude 12. However, another mail from T. Kato (2011) on VSNET reported that probably the original brightness estimate was too optimis-

tic as it seems that many brightness determinations of M. Wolf were about 2 magnitudes too bright.

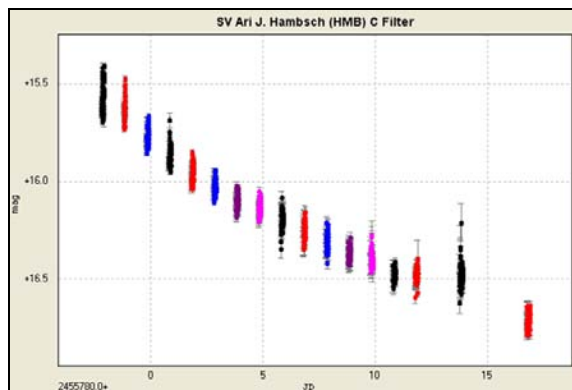


Fig. 2 Light curve of the observations of SV Ari over a period of more than two weeks.

Fig. 2 shows the observations I took of this star during a period of more than two weeks. During this period the star dropped more than one magnitude in brightness. It is also clearly visible from this figure that individual nights show brightness variations of about 0.3 magnitudes.

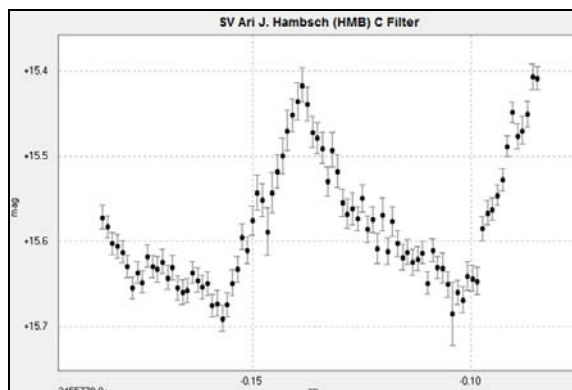


Fig. 3 Light curve of the observations of SV Ari over a period of more than two weeks.

Fig. 3 shows the time series observation during the first night. Clearly a superhump of 0.3 magnitudes is visible. The magnitude of the superhumps reduced to about 0.15 magnitudes after a couple of days.

Based on the analysis by the Kyoto team, there have been distinct stages in the evolution of superhumps in SV Ari. The mean period before Aug. 4 was 0.05574(18) d, which has since shortened to 0.05519(5) d. Later data also showed that SV Ari was gradually declining (~ 0.05 mag / day). This seemed very slow for an ordinary SU UMa type dwarf nova. Thus probably this object may be a WZ Sge type dwarf nova. This information is based on e-mail exchanges via VSNET. Towards the end of 2011 August, SV Ari had dimmed towards magnitude 18.

4. BW Sculptoris

Another example of an intensively followed star is BW Sculptoris, which went in its first ever observed outburst on October 21. BW Scl is also a cataclysmic variable star. The AAVSO published on the same day a special notice #261 mentioning the outburst of BW Scl. It was visually observed by M. Linolt on Oct. 21.3146 at a magnitude of 9.6 (vis). The outburst was confirmed by A. Plummer at mag. 9.4 (vis). The star has conflicting classifications in literature and is probably a WZ Sge-type dwarf nova. On Oct. 25 AAVSO issued an Alert Notice 449 concerning this outburst.

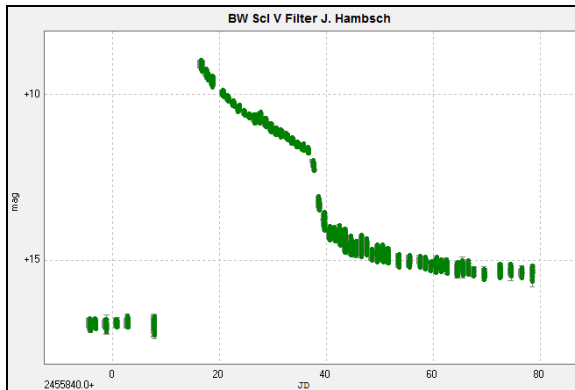


Fig. 4 Light curve of the observations of BW Scl over a period of nearly three month..

The star was followed by me already in the pre-outburst phase. However, I missed the outburst as I thought the star is not doing much so stopped observations on Oct. 14, just a week before the outburst took place. Of course I restarted observations immediately after the news was spread and followed the star over a period of 2.5 month. Fig. 4 shows the development of the brightness over the full observing period.

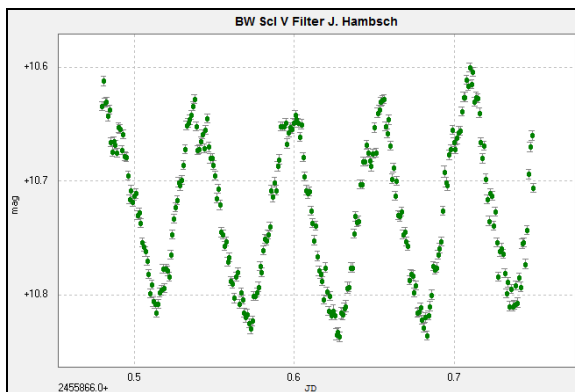


Fig. 5 Light curve of the observations of BW Scl over a period of nearly three month.

After a few days nice superhumps developed of about 0.25 mag as can be seen in Fig. 5. After a week into the outburst the early superhump period was determined to be 0.054308(3) by Ohshima *et al.* (2011a). After a rapid declining phase from mag. 11.7 to about mag. 14 starting at about JD 2455877 again nice superhumps of 0.3 mag developed.

5. VW Hydri

On request by professional astronomers, I started observations of VW Hyi just as it went into superoutburst, although that was a surprise to the pros as the superoutburst was not expected yet. My observations triggered satellite observations of the star

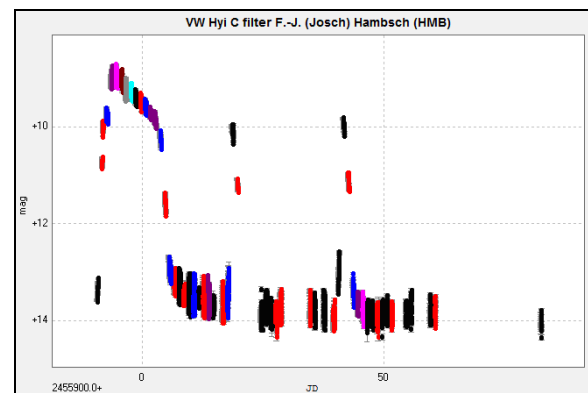


Fig. 6 Observations of VW Hyi during superoutburst and normal outburst.

VW Hyi is a popular cataclysmic variable in the Southern sky. Many studies have been performed about this star; see e.g. AAVSO (2010). During quiescence the star is at magnitude 14.4. Normal outbursts happen on average every 27.3 d and last about 1.4 d. The superoutburst happens on average every 179 d and lasts for about 12.6 d. Fig. 6 shows impressively this behavior of VW Hyi with one superoutburst and two normal outbursts.

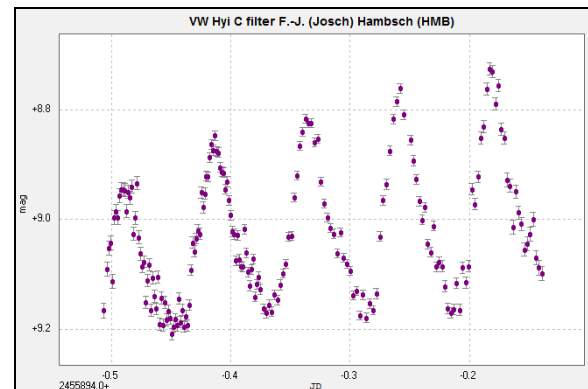


Fig. 7 Observations during one night at the top of the superoutburst.

The star develops strong superhumps during its outburst as can be seen in Fig. 7. The variation of those humps reaches 0.5 magnitudes.

6. Example of an RR Lyr Star: V1820 Ori

This type of variable is named after the prototype, the variable star RR Lyrae in the constellation Lyra. RR Lyr stars are pulsating horizontal branch stars with a mass of around half of our Sun's. Their period is short, typically less than one day.

My interest in observing RR Lyr stars is on one hand due to the short period of those stars. So within one night you can see already quite a change in brightness. On the other hand the stars also show some brightness modulations which is known as the Blazhko effect. Back in 1907, S. Blazhko observed this effect for the first time on the star RW Dra (Smith, 2004). The Blazhko effect is to date not really understood and needs further observational campaigns. Recently due to the Kepler and CoRoT satellite missions more insight into this phenomenon has been gained as the satellites can of course observe the stars continuously, which is impossible for Earth-bound observations. Nevertheless observations from Earth are also very valuable as can be seen in many publications on this subject in the astronomical literature. Fig. 8 shows the phase diagram of the RR Lyr star V1820 Ori, which has been observed from Chile over a full season (more than 3 month). It is obvious from the figure that the light curve is not regular, the maximum brightness is changing over more than 0.5 mag. And also the moment of maximum time is changing. So a rather complex light curve is the result. Presently the data are under analysis and the results are intended to be published.

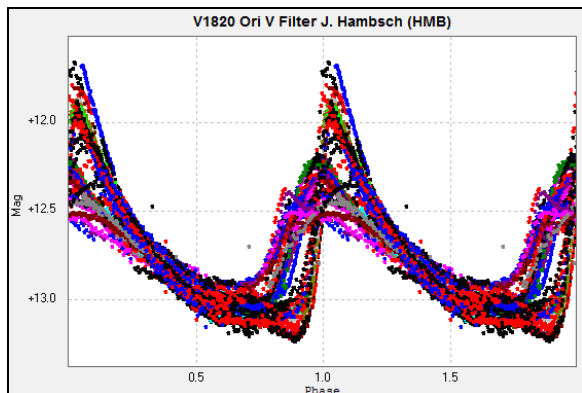


Fig. 8 Light curve of the observations of BW Scl over a period of nearly three month.

7. Conclusion

The remote observatory under pristine skies in the Atacama Desert opens up great possibilities to observe variable stars. Intensive follow-up observations over many days, weeks or even months are possible due to the stable weather conditions. The given examples show impressively what is possible. Collaborations are searched for in order to contribute to scientific research of common interest.

8. References

- AAVSO (2010) "Variable Star of the Month." http://www.aavso.org/vsots_vwhyi
- de Ponthierre, P. (2010) LesvePhotometry software at <http://www.dppobservatory.net/AstroPrograms/Software4VSObservers.php>
- Fridrich, R. (2011). e-mail to cvnet-outburst.
- Kato, T. (2011). vsnet-alert e-mail message 13544.
- Masi, G. (2011). vsnet-alert e-mail message 13538.
- Ohshima, T. (2011). vsnet-alert e-mail message 13543.
- Ohshima, T. (2011a) vsnet-alert e-mail message 13799.
- Smith, H. A. (2004). *RR Lyrae Stars*. Cambridge University Press. p. 103. ISBN 0521548179.

ER Ursae Majoris: A dwarf nova with surprises

Enrique de Miguel

*CBA (Huelva), Observatorio del CIECEM, Matalascañas, 21076 Almonte, Huelva, Spain
Departamento de Física Aplicada, Universidad de Huelva, 21071 Huelva, Spain
edmiguel63@gmail.com*

Joe Patterson

*Department of Astronomy, Columbia University, 550 West 120th Street, New York, NY 10027
jop@astro.columbia.edu*

Jonathan Kemp

*Gemini Observatory, Hilo, HI 96720
jk@155west.org*

William Stein

AAVSO and CBA, Las Cruces, NM

George Roberts

CBA (Tennessee), 2007 Cedarfont Dr., Franklin, TN 37067

T. Campbell

CBA (Arkansas), 7021 Whispering Pine, Harrison, AR 72601

Franz-J. Hambsch

CBA (Mol), Oude Bleken 12,B-2400 Mol, Belgium

Tom Krajci

CBA (New Mexico), PO Box 1351 Cloudcroft, NM 88317

Shawn Dvorak

AAVSO, 1643 Nightfall Dr., Clermont, FL 34711

Robert A. Koff

CBA (Colorado), Antelope Hills Observatory, 980 Antelope Drive West, Bennett, CO 80102

Etienne Morelle

CBA (France), Sirene ObservatoryLagarde d'Apt, France

Michael Potter

CBA (Baltimore), 3206 Overland Ave., Baltimore, MD 21214

David Cejudo

CBA (Madrid), Observatorio El Gallinero, El Berrueco, Madrid, Spain

Steve Brady

AAVSO, 49 Bay State Rd, Cambridge, MA 02138

Kenneth Menzies

Tigh Speuran Observatory, Framingham, MA

Abstract

ER Ursae Majoris is a relatively bright member of the SU UMa-type dwarf novae that undergoes frequent eruptions of amplitude ~ 2 mag every ~ 4 d. In addition to these ordinary dwarf-nova outbursts, ER UMa shows brighter eruptions (superoutbursts) lasting ~ 20 d with a recurrence time of ~ 44 d. As other members of the SU UMa class, ER UMa displays a characteristic periodic modulation (superhumps) in its light curve during the course of a superoutburst, the period being a few percent longer than the orbital period of the underlying binary system. A routine photometric patrol of ER UMa during its January 2011 superoutburst became much more interesting after noticing the presence of an additional modulation in its light curve, with a period slightly shorter than the orbital period. Similar photometric waves (known as negative superhumps) have already been observed in other cataclysmic variables, mainly in nova-like systems, but only in a small handful of SU UMa-type stars during quiescence, and never before during a superoutburst. We report in this communication the results of a worldwide photometric campaign that was orchestrated right after the discovery of negative superhumps in ER UMa, and provide a thorough analysis of the data obtained from more than 10 stations of the Center of Backyard Astrophysics (CBA) network, which include more than 1000 hours of photometric data over a 4-month baseline on 2011, and a similar (still in progress) dense coverage in 2012.

1. Introduction

On 2011 January 19, an e-mail sent by the VSNET network (vsnet-alert 12671) reported that ER Ursae Majoris (ER UMa) was likely undergoing a superoutburst, as the visual estimate of $V = 12.6$ from Gary Poyner seemed to suggest. As cataclysmic variable devotees probably know, this is not the type of news that calls for immediate change of observing plan in the middle of the night: after all, ER UMa is known to be a very active dwarf nova that pays short visits (~ 3 d) to its low state before resuming its eruptive activity with outbursts of amplitude ~ 2.5 – 3 mag. Such a state of frenetic activity is characteristic of a handful of dwarf novae that are collectively known as ER UMa stars.¹ These stars constitute a small group of the broader SU UMa class of dwarf novae. Most SU UMa stars have orbital periods shorter than ~ 2.2 hr. They all exhibit two distinct types of eruptions: short normal outbursts lasting a few days; and longer, less frequent, and slightly brighter superoutbursts with typical duration of ~ 15 – 20 d.

All SU UMa stars show distinctive periodic oscillations in brightness during superoutburst, with periods a few percent *longer* than the orbital period. These characteristic light modulations have been given the name of ordinary (also known as common, apsidal, or positive) superhumps. As a general rule, ordinary superhumps in SU UMa stars are exclusively observed during superoutburst, and are extinguished once the superoutburst ends and the system returns to its quiescent state.

Superoutbursts recur in time at a rather regular pace – usually, even more regularly than the se-

quence of normal outbursts occurring between consecutive superoutbursts. In usual SU UMa stars, the recurrence time (supercycle) is normally in the range 150–1000 d. But there are outliers. Stars of the WZ Sge subclass undergo very infrequent superoutbursts at intervals of decades. ER UMa is also an outlier but exactly for the opposite reason.

ER Ursae Majoris (PG 0943+521) was discovered in the Palomar Green survey for blue objects (Green *et al.*, 1986), and later identified as a cataclysmic variable (Robertson *et al.*, 1995, R95 hereafter; Misselt and Shafter, 1995; Kato and Kunjaya, 1995; Zhao *et al.*, 2006). Based on a photometric study consisting on 454 exposures on 145 nights during the interval 1993 October 6 to 1995 January 5, R95 concluded that ER UMa exhibited eruptions with the typical long (and brighter) and short (and slightly fainter) dichotomy of SU UMa systems. This identification was confirmed by the detection of superhumps with periodicity $P_{sh} = 94.41(3)$ min (Kato *et al.*, 2003). This is just 3% longer than the orbital period $P_{orb} = 91.67(4)$ min (Thorstensen *et al.*, 1997), an excess value typical for SU UMa stars. However, with a supercycle period of 42.95(6) d and normal eruptions taking place every 4.4(1) d (R95), ER UMa cannot be simply considered as a typical SU UMa dwarf nova. This high outburst frequency is the main observational hallmark of ER UMa stars, all having short supercycles (19–50 d), which testifies to a very large accretion rate and high intrinsic luminosity.

Our observational program was initially conceived as a long-term project aiming to investigate possible minor differences between superoutbursts on the same object. ER UMa, being bright enough, and having long-lasting and frequent superoutbursts, seemed to be a good choice; and that alert on 2011 Jan 19, the right excuse to start the observations. The data obtained that night confirmed that ER UMa was in superoutburst, exhibiting the usual superhump-like

¹ Sometimes, also known as RZ LMi stars. Accredited members of this subgroup are, in addition to ER UMa, DI UMa (Kato *et al.*, 1996), RZ LMi (R95, Nogami *et al.*, 1995), V1159 Ori (R95, Patterson *et al.*, 1995), and IX Dra (Ishioaka *et al.*, 2001; Olech *et al.*, 2004)

modulations, but with a period of ~ 89.6 min, definitely *shorter* than P_{orb} . In the cataclysmic variable jargon, photometric waves with periods slightly less than P_{orb} are known as *negative superhumps*.² They are definitely less common than ordinary superhumps, and are almost exclusively observed in nova-like cataclysmic variables.

The campaign that was subsequently launched is still in progress, and from the very beginning, ER UMa has been gifting us with daily negative superhumps. Here we report on a preliminary analysis of the main features found after more than 2000 hr of photometric coverage, paying particular attention to: (1) the global light curve; and (2) the characterization of the negative superhump in ER UMa and its stability.

2. Observations

All observations reported here were performed by contributors to the Center of Backyard Astrophysics (CBA), a worldwide network of observing stations equipped with small telescopes in the 0.25–0.40 m range.³ A total of 12 CBA stations contributed to this campaign: 4 in Europe (2 in Spain, 1 in Belgium, and 1 in France), and 8 in America (7 in the USA, and 1 in Chile).

The 2011 season included time-resolved photometry on 97 nights over a 131 day baseline, from January 19 to May 30, totaling 1190 (~ 900 non-overlapping) hours. The 2012 campaign was started on 2011 December 4 and is still in progress. By the time of writing, time-resolved photometry has been performed on 91 nights over a 123 day baseline, this amounting to more than 1200 hours of photometric data.

Most of the observations were carried out unfiltered, with integration times in the range 40–60 s. Raw images were dark-subtracted and flat-fielded before performing differential photometry relative to a nearby star. There was no unique choice of comparison star, but GSC 3493–00920, with $V = 14.203(2)$ and $B = 14.833(4)$ according to a photometric calibration by Henden (2010), was the most commonly used. The dense coverage in both seasons ensured temporal overlapping data sets, which allowed us to bring all data under a common magnitude scale by adding appropriate offsets. This procedure is not expected to introduce errors larger than 0.03–0.04 magnitudes. All magnitudes reported here are formed

from adding the V magnitude of the comparison star to our differential magnitudes.⁴ Heliocentric corrections were applied to all observation times. Hereafter, time will be referred to in the truncated form $HJD \equiv HJD(\text{true}) - 2455000$ and, similarly, dates in truncated JD format.

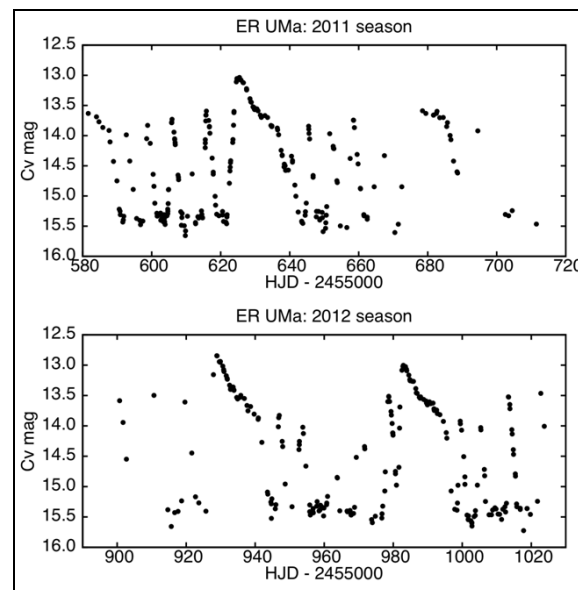


Figure 1. Light curves of ER UMa from 2011 January 19 to May 30 (2011 season) and from 2011 December 4 to 2012 April 4 (2012 season). Data points are mean values of nightly time series.

3. Global Light Curve

We show in Fig. 1 the overall light curves obtained in the 2011 and 2012 seasons. Data points included in this figure correspond to the averages over each individual time series. As more than 90% of the data sets consisted on series spanning more than 3 hr, each data point in the figure is expected to be unaffected by variations at short timescales. Except for the last segment of the 2011 season and the early stages of the 2012 season, ER UMa was followed essentially on a daily basis. The supercycle was sampled uniformly in both seasons, with $\approx 40\%$ of the data collected during superoutbursts. This is consistent with the expected time ER UMa spends in each of the different stages along a supercycle. Inspection of Fig. 1 shows that ER UMa exhibits the expected sequence of long-lasting, bright eruptions, followed by a series of much shorter, slightly fainter normal outbursts. We now turn to discuss these features in more detail.

² A plausible explanation of the negative superhump clock is the retrograde precession of a tilted accretion disk (Patterson et al., 1993, 1997).

³ More details relative to the CBA can be found at <http://cbastro.org>

⁴ For enthusiasts of standard magnitudes, we have estimated that V magnitudes follow from our magnitudes by adding -0.22 .

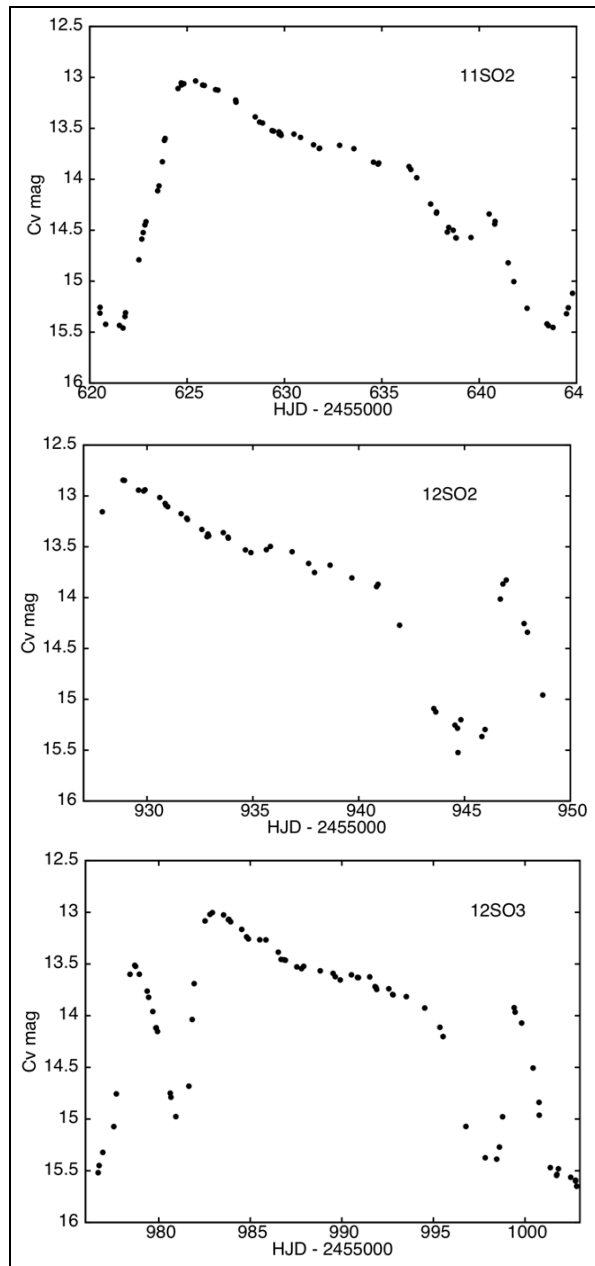


Figure 2. Expanded portions of Fig. 1 showing superoutbursts in ER UMa.

As can be seen in Fig. 1, our data are able to capture three superoutbursts in their entirety, one in 2011 (11SO2), and two in 2012 (12SO2, and 12SO3). These are shown in Fig. 2 on an expanded scale. For two additional superoutbursts (11SO1 and 11SO3), we missed the initial stages, but we managed to cover most of the plateau and fading stages of the eruption. For the purpose of discussion, let us take the JD 925–944 superoutburst (12SO2, middle panel of Fig. 2) as reference: it starts from quiescence at 15.44 mag; reaches supermaximum in 3.2(2) d while

brightening 2.5(1) mag; enters a smooth, non-linear fading stage, where the brightness decreases by 1.02(8) mag over the subsequent 12.1(3) d; and drops rapidly toward quiescence, the brightness decreasing by 1.47(8) mag on the following 3.7(2) d. The eruption has been alive for 18.9(1) d, a value that is consistent with the estimate of 20 d quoted by Kato and Kunjaya (1995). The overall shape of the light curve remains very similar from one superoutburst to the next. The rise to maximum brightness spans ~ 3.5 d, and seems to occur at a non-constant rate –much faster over the first 1–2 d. On average, the brightness at supermaximum is 12.94(4) mag. The duration of the plateau stage of all superoutbursts is remarkably similar, 11.4(3) and 12.0(2) d for 11SO2 (top panel of Fig. 2) and 12SO3 (lower panel of Fig. 2), respectively. These values are to be compared with the duration of 13 days reported by R95. The difference is small and probably of no physical significance. Assuming 11.4 d for the duration of the two partially covered superoutbursts in 2011, we can estimate that supermaxima occurred around JD 576.1 (for 11SO1) and JD 674.2 (for 11SO3) to within 0.5 d. This will be useful for later discussion in the next section.

A closer inspection of Fig. 2 shows two subtle differences among the fully covered superoutbursts. Firstly, a normal outburst seems to interrupt the rapid fading branch of 11SO2; secondly, 12SO3 is not triggered from quiescence, but before the preceding normal outburst had relaxed to the quiescent state. As a result, both superoutbursts are slightly shorter than our reference superoutburst by 1–2 d.

The main eruption is followed by a sequence of 5 normal outbursts. This is definitely at variance with the sequence of 7 outbursts at intervals of 4.4(1) d reported by R95. We find no definite recurrence time for the normal outbursts in our data. Times between consecutive outbursts tend to be clustered around 6 d, but we find values anywhere in the range 5.5–10 d. It is noteworthy that the interval between outbursts seems to stretch over a supercycle. This is not at the cost of the duration of individual outbursts –which almost invariably involve 4 days– but is seemingly due to the tendency of the system to remain in its faint state slightly longer as the supercycle proceeds and the system approaches the next superoutburst.⁵

⁵ This being said, we should note that ER UMa probably does not have a truly state of quiescence, but short periods -- typically 1-3 d, and rarely as long as 6-7 d-- where it wanders around a mean magnitude of 15.55. Something qualitatively similar is found for the other ER UMa stars.

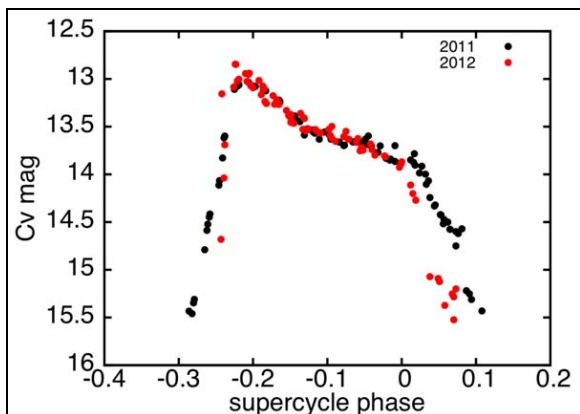


Figure 3. Phased light curves of the superoutbursts in the 2011 and 2012 seasons folded on $P = 49.3$ d (2011) and $P = 53.8$ d (2012).

What about the supercycle period? The data in Fig. 1 suggest a value of ~ 50 d between consecutive superoutbursts in 2011 and of ~ 55 d between the only two main eruptions registered in 2012. These values are significantly longer than those reported previously (R95, Kato and Kunjaya, 1995), and call for a more detailed analysis. A power spectrum of the data pertaining to superoutburst stages shows a strong peak at 49.3(3) d in 2011 and at 53.8(1.3) d in 2012. When folding the data from each season on the corresponding period the resulting phased light curves show little dispersion, as can be appreciated in Fig. 3. As one may anticipate, no single period can bring superoutbursts in both seasons into a neat, phased light curve. Further insight into the time variations of the supercycle period can be obtained from an O-C analysis. As a fiducial marker, we choose the time at which the plateau stage ends (or, equivalently, the time at which the ensuing rapid decay to quiescence takes place). The choice follows from practical reasons: this feature is observed in all superoutbursts, and can be timed with a precision of ~ 0.2 d. The linear ephemeris is

$$2455585.5(1.5) + 51.0(3) E \quad (1)$$

The O-C deviations from this ephemeris are shown in Fig. 4. Assuming a parabolic O-C diagram, we find $dP/dt = 1.5(2) \times 10^{-2}$, to be contrasted with the value of 4×10^{-3} reported by R95. Although consistent with our data, this period change must certainly be non monotonic. We may conclude at this point that the supercycle seems to be stretching in ER UMa at a rate yet to be convincingly determined. One would be tempted to conclude that ER UMa is telling us that it is becoming an SU UMa star, but the baseline of our observations is insufficient to draw any definite conclusion.

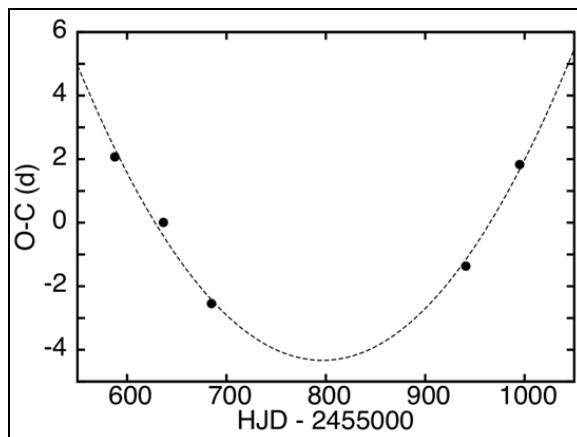


Figure 4. O-C deviations of the times of superoutbursts in ER UMa using the linear ephemeris given in Eq. (1).

4. Periodic Signals

As stated in the Introduction, the ultimate reason that triggered this extensive campaign on ER UMa was the discovery of a strong periodic signal slightly, but clearly shorter than the 91.67 min orbital signal. We turn next to characterize this signal and its stability throughout the 2011 and 2012 seasons. In the process, we also analyze the existence of other possible periodic signals.

A common feature to all light curves is the presence of prominent oscillations of varying amplitude at all phases of the supercycle, sometimes as large as 0.8 mag. This has been a daily constant during 2011 and 2012 with no exceptions. Not even one single night. Some light curves were seen to exhibit a seemingly simple pattern, as it is the case at supermaximum and 2–3 d thereafter (top frame in Fig. 5). But in most instances, nightly light curves were complex, without a visually clear regular pattern, and largely changeable from night to night (see lower frame in Fig. 5). In general, amplitudes (in magnitude units) were larger as the system was fainter.

4.1 Frequency analysis

We performed a Fourier analysis using the `Period04` (Lenz and Breger, 2005) program. This package allows identification of frequencies and sequential prewhitening of selected frequencies by a least-square technique. In order to emphasize the actual changes in signal strength, we normally make use of intensity units rather than magnitudes in the analysis. Relative intensities, I/I_0 are formed from magnitudes, m , according to

$$m - m_0 = -2.5 \log(I/I_0) \quad (2)$$

where $m_0 = 16$ mag is arbitrarily chosen here to set the unit of intensity. The mean intensity was removed from each nightly light curve, as it was any obvious trend.

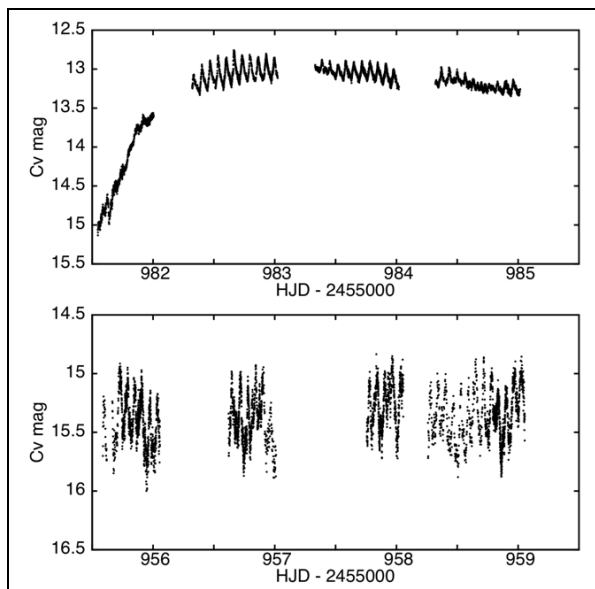


Figure 5. Upper frame: 2012 February superoutburst, dominated by positive superhumps. Lower frame: ER UMa at quiescence. The apparent modulation corresponds to negative superhumps.

In order to gain in frequency resolution, we formed sets of long light curves over different intervals of evolution. The sets corresponding to superoutbursts included photometry obtained over all stages (whenever observed), and therefore contain data pertaining to the rise and decay stages in addition to data along the main plateau. With the convention introduced before, these data sets are labeled 11SO $_n$, and 12SO $_n$, with $n = 1, 2, 3$ representing each of the supercycles observed in 2011, and 2012, respectively. We also formed light curves for each individual normal outburst. In this case, each light curve included all data from the start of a given outburst to the start of the next, thus including photometric data obtained while ER UMa was at quiescence. These data sets are referred to as 11NO $_n$ - m , with $m = 1, 2, \dots$ labeling the outburst during supercycle n in 2011, and similarly for normal outbursts in the 2012 season. We refer to tables 2 and 3 for further details. As a useful reference, we recall that the orbital frequency is $\Omega = 15.708$ cycles/day (abbreviated in the following as c/d), the orbital period being $P_{orb} = 91.67$ min (Thorstensen *et al.*, 1997).

4.2 The 2011 season

The frequencies of the periodic signals found in each data set over the 2011 season have been included in Table I, along with the amplitude of the corresponding signal. Amplitudes are in units of intensity, I_0 , as defined in Eq. 2, and represent half of the full variation of the signal (sometimes, called "semi-amplitude"). These values follow from a least-square optimization procedure implemented within the Period04 package. Occasionally, the output amplitudes were found to be unreliable. This happened particularly nearby supermaxima, where the oscillations in the photometric wave (in intensity units) are of large amplitude and the least-square procedure converged poorly. In these cases, we simply give in Tables I and II an estimate from the light curves.

The power spectrum of the 2011 January superoutburst (11SO1) is dominated by a strong peak at 16.07(2) c/d, (associated period of 89.6(1) min). A peak at 32.13(3) c/d, corresponding to the first harmonic of the fundamental signal, is also visible in the spectrum at higher frequencies. No other peak of physical significance is observed in the spectrum. This is surprising, as the period of ordinary superhumps in ER UMa is known to be significantly longer (≈ 94.4 min; Kato *et al.*, 2009). Having a periodicity about 2.1% shorter than the orbital period, the detected signal must correspond to negative superhumps. Negative superhumps had been detected before in some SU UMa stars (Patterson *et al.*, 1995), but they had never before been observed during the course of a superoutburst. The amplitude of negative superhumps (in intensity units) was seen to remain essentially constant along the superoutburst.

Also seemingly intriguing is the complete absence of positive superhumps during the 2011 January superoutburst. Even more striking is the fact that negative superhumps survived the superoutburst and were detected at all phases of the supercycle. The peak-to-through amplitude of these oscillations was as large as 0.8 mag when ER UMa was in its low state, but the amplitude was not seen to change appreciably when expressed in intensity units (see values included in Tables I and II). Also the mean frequency of negative superhumps remained nearly constant after the superoutburst, with values wandering in the range 16.01–16.10 c/d.

The fundamental signal in the power spectrum during the following superoutburst in March 2011 (11SO2) occurs at 16.05(1) c/d, and corresponds once again to negative superhumps. A second peak is also found at 15.23(2) c/d, fully consistent with the frequency of positive superhumps. When the power spectra of individual nights are analyzed, we con-

label	JDi-JDf	nights	hours	ω -, A-	ω +, A+
11SO1	581-590	8/10	56.52	16.07(2), 0.363	
11NO1-1	591-597	7/7	52.45	16.01(2), 0.389	
11NO1-2	598-603	6/6	76.94	16.03(2), 0.345	
11NO1-3	604-409	6/6	65.28	16.06(2), 0.358	
11NO1-4	610-614	5/5	34.25	16.04(2), 0.365	
11NO1-5	615-621	7/7	103.17	16.10(2), 0.307	
11SC1	581-621	39/41	388.61	16.051(9), 0.271	
11SO2	622-638	16/17	208.14	16.08(2), 0.349	15.23(2), ~2.5
11NO2-1	639-643	5/5	47.60	16.02(2), 0.412	
11NO2-2	644-650	7/7	73.29	16.03(2), 0.324	
11NO2-3	651-656	5/6	26.94	16.05(3), 0.380	
11NO2-4	657-661	5/5	39.17	16.08(2), 0.456	
11NO2-5	662-671	5/10	31.89	16.08(3), 0.256	
11SC2	622-671	43/50	427.03	16.052(12), 0.238	15.253(12), ~2.5
11SO3	672-688	11/17	69.69	16.07(2), 0.291	15.16(2), 0.114
11NO3	689-711	5/23	21.29	16.04(3), 0.381	
11SC3	672-711	16/40	90.98	16.057(20), 0.226	15.137(20), 0.182

Table I: The frequencies and amplitudes (in intensity units) of the photometric signals exhibited by ER UMa on 2011 over different intervals of evolution.

clude that positive superhumps developed only when the supermaximum was reached, the amplitude being ~5–10 times as large as those of their negative counterparts. The amplitude decreased nearly exponentially, and 4 days after supermaximum, no trace of positive superhumps was found in the power spectra. By contrast, negative superhumps were persistently observed all nights.⁶ Incidentally, we note that this may explain why positive superhumps were not detected during the previous superoutburst. As argued in the previous section, the supermaximum of the 2011 January superoutburst is estimated to have occurred around JD 576, 5 days before our first observation (on JD 581).

The power spectrum during the 2011 April superoutburst (11SO3) showed, once again, two main peaks at 16.07(2) c/d (negative superhumps) and 15.16(2) c/d (positive superhumps), with negative superhumps being again the winner.

4.3 The 2012 season

A similar frequency analysis was implemented for the 2012 season. Frequencies and amplitudes of the periodic signals have been collected in Table II. The season was started early in 2011 December and ER UMa underwent the first superoutburst of the season on 2012 January 1. Data collected during

label	JDi-JDf	nights	hours	ω -, A-	ω +, A+
12SC1	900-926	14/27	67.59	16.07(2), 0.256	
12SO2	927-944	17/18	172.74	16.08(2), 0.340	15.24(2), ~3.2
12NO2-1	945-950	5/5	34.82	16.02(2), 0.303	
12NO2-2	951-960	9/10	96.12	16.04(2), 0.312	
12NO2-3	961-968	5/8	65.86	16.06(3), 0.340	
12NO2-4	969-976	5/8	38.88	16.09(2), 0.256	
12NO2-5	977-980	5/5	48.18	16.16(3), 0.315	
12SC2	927-980	46/54	456.60	16.075(14), 0.260	15.281(14), ~3.2
12SO3	981-997	17/17	216.43	16.06(2), 0.292	15.25(2), ~3.5
12NO3-1	998-1003	6/6	96.41	16.02(2), 0.268	
12NO3-2	1004-1012	9/9	94.77	16.02(2), 0.293	
12NO3-3	1013-1019	7/7	69.92	16.05(3), 0.328	
12SC3	981-1019	38/38	477.53	16.040(13), 0.260	15.226(13), ~3.5

Table II: As in table I, but for the 2012 season.

2011 December have been grouped into a single light curve (12SC1) for frequency analysis. The spectrum during that time segment is dominated by a peak at 16.07(1) c/d: negative superhumps did not seem to have disappeared.

The power spectra during the 2012 January (12SO2) and 2012 February (12SO3) superoutbursts are essentially the same as those corresponding to superoutbursts 11SO2 and 11SO3: two main signals at 16.08(1) c/d and 15.24(2) c/d associated to negative and positive superhumps, respectively. A conspicuous peak at or near frequency 16.07 c/d was the norm in all power spectra.

5. Stability of Negative Superhumps

Up to this point, we have provided strong evidence of the presence of negative superhumps in ER UMa at all phases of the supercycle. While positive superhumps are only excited during superoutburst, the essentially constant amplitude of the negative superhumps testifies to a weak dependence, if any, with the particular outburst state of the system.

What about their stability? During superoutbursts, the period of positive superhumps in SU UMa stars is known to be unstable, with characteristic times in the range $|dP/dt| \approx 5\text{--}25 \times 10^{-5}$ (Kato *et al.*, 2009). This wandering is usually manifested in the power spectrum of a superoutburst in the form of peaks close to the fundamental signal, typically to within a distance of ± 0.15 c/d, and they show up in the spectrum if the resolution is sufficiently high (otherwise, the result is a broadening of the fundamental peak). Side peaks around the frequency of negative superhumps, ω_- , were seen in most of the spectra analyzed in the previous section, which points to a likely variation of ω_- with time. Inspection of the values of ω_- included in Tables 2 and 3 seems to suggest that some wandering do exist, but also that the mean ω_- does not change from one superoutburst to the next. If we stopped at this point, we would be allowed to conclude that the period of negative superhumps remains essentially constant (at least, during superoutbursts), and varies slightly afterwards. We decided, however, to investigate this point further.

Time variations of ω_- were analyzed using an O–C analysis of the times of maxima of the negative superhump waves. In principle, timing these maxima poses no major problem when the oscillations are well defined. In the case of ER UMa, most nightly light curves show secondary peaks at all sort of fre-

quencies.⁷ Rather than timing individual maxima, we proceeded to extract one timing per night. For this purpose, we first identified all relevant frequencies of each nightly curve, fitted the light curve to a sin-Fourier series using the least-square technique embedded in the Period04 package, and determined one epoch of maximum associated with the nightly value of ω_- . In total, we extracted 93 and 88 timings from the 2011 and 2012 campaigns, respectively. A linear regression yields

$$2455581.503(2) + 0.062269(2) E \quad (3)$$

for the 2011 season, and

$$2455900.661(4) + 0.062282(3) E \quad (4)$$

for the 2012 season, the corresponding frequencies being $\omega_- = 16.0594(5)$ c/d and $\omega_- = 16.0560(8)$ c/d, for each season. Thus the negative superhump in ER UMa is very stable, with a characteristic period change of $dP/dt = (4 \pm 1) \times 10^{-8}$. This is equivalent to an increase of 1.3 seconds per year, certainly a very stable clock.

The tenacious reader may still wonder how the apparent wandering of ω_- can be reconciled with the alleged stability of negative superhumps in ER UMa. The clue is provided in Fig. 6. We plot in that figure the O–C deviations from the ephemeris given in Eqs. (3) and (4). According to the figure, the period of the negative superhump varies at shorter time-scales, but these variations are cyclical (almost sinusoidal), and so they essentially vanish when averaged over each season. But what we find most striking is the fact that *the frequency of these cyclic variations coincides with the frequency of the supercycle*. Assuming a sinusoidal variation of the O–C deviations shown in Fig. 6, the best fits are achieved with periods 48(4) d and 55(8) d for the 2011 and 2012 seasons, in full consistency with the supercycle length found in each season. It is noteworthy that the minima in the O–C diagrams correspond to superoutburst stages. Also, we note that this modulation keeps coherence from season to season, which provides further evidence of the intimate interplay between period modulations of the negative superhump and supercycle.

⁷ They resemble low-energy fluctuations -thus becoming more apparent when ER UMa is in its low state- but show no coherence. They are definitely non periodic and probably related with flickering.

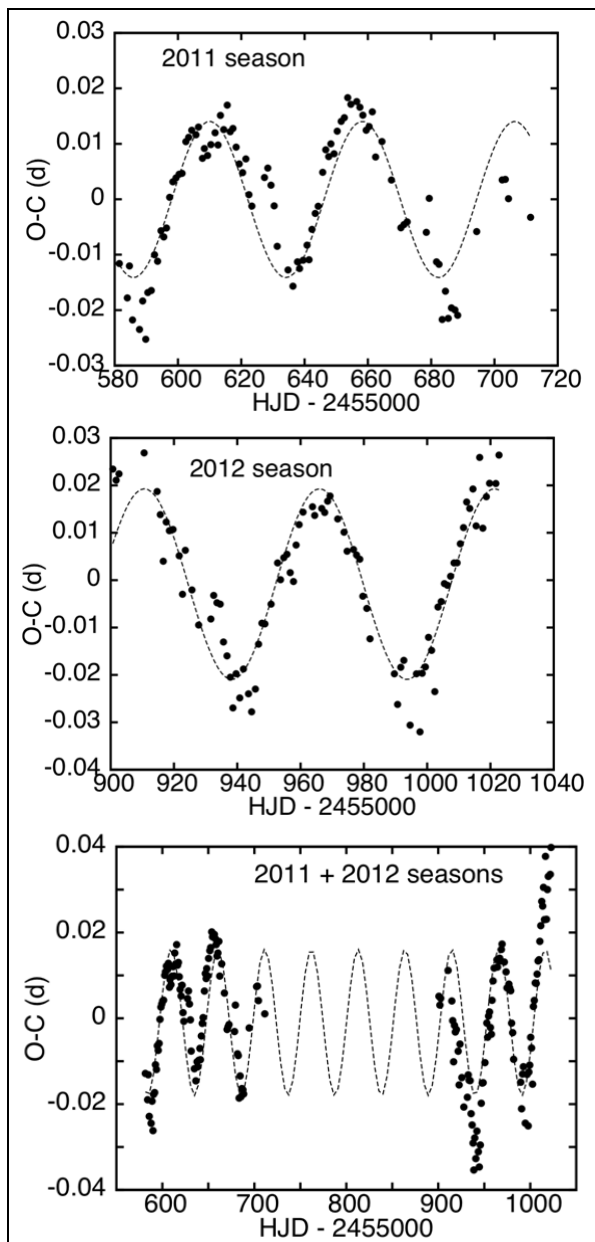


Figure 6. O-C deviations of the times of maxima of negative superhumps.

6. Summary

1. We report extensive time-resolved photometry of ER UMa carried out on 2010 and 2011. The global light curve shows the sequence of superoutbursts and interspersed outbursts expected for a highly active cataclysmic variable.
2. In all cases, ER UMa was seen to display 5 normal outbursts before a new superoutburst was triggered, with no clearly defined regularity. This is at variance with the reported se-

quence of 7 outbursts at regular intervals of 4.4(1) d reported for ER UMa during 1993-1995. These outbursts tend to be increasingly brighter as the supercycle proceeds, and have a rather constant duration of 4 d.

3. All observed superoutbursts had a similar pattern. The amplitude of the eruption is 2.60 mag (in white light), with the system rising from 15.55 to 12.95 mag (in white light) in ~ 3.5 d. The brightness increases at a lower rate than in the case of normal eruptions. After supermaximum, the brightness decreases slowly and non-linearly over the next 11.8(4) d at a mean rate of 0.085 mag/day. Afterwards, the system returns to quiescence in ~ 3.8 d at a rate of ~ 0.4 mag/day. The mean duration of the eruption is 19.1(5) d.
4. Our data are consistent with a lengthening of the supercycle. It was found to be 49.3(3) d in 2011, and 53.8(1.3) d on 2012. The supercycle was of 44 d in the 1993-1995 photometric study reported by R95. If this is a secular variation, we may be witnessing a transition of ER UMa to a SU UMa-like star, with much lower accretion rates and, subsequently, longer waiting times between superoutbursts. However, the current information at our disposal is limited and the above conclusion is not fully warranted. Probably, a simpler explanation is that the supercycle in ER UMa stars is not very stable, but subject to cyclic (or irregular) variations.
5. For reasons yet to be known, ER UMa is systematically exhibiting since 2011 a highly stable signal with a period shorter than the orbital period. We ascribe this modulation to negative superhumps. The seasonal value of the period has increased from 89.667(3) min in 2011 to 89.686(4) min in 2012. This negative superhump is present at all phases of the supercycle, and its amplitude in intensity units is essentially constant. The period of the negative superhump exhibits cyclic variations modulated by the supercycle.

7. Acknowledgements

We welcome this opportunity to acknowledge the work of observers of the Center of Backyard Astrophysics (CBA) who contributed to this and related campaigns.

8. References

- Gao, W., Li, Z., Wu, X., Zhang, Z., Li, Y. (1999). *AP* **527**, L55.
- Green, R. F., Schmidt, M., Liebert, J. E., (1986). *ApJS* **61**, 305.
- Henden, A. (2010). AAVSO Database.
- Ishioka, R., Kato, T., Uemura, M., Iwamatsu, H., Matsumoto, K., Martin, B. E., Billings, G. W., Novak, R. (2001). *PASJ* **53**, L51.
- Kato, T., Kunjaya, C. (1995). *PASJ* **47**, 163.
- Kato, T., Masuda, S., Nogami, D. (1995). *IBVS* **4233**.
- Kato, T., Nogami, D., Baba, H. (1996). *PASJ* **48**, L93.
- Kato, T., Nogami, D., Masuda, S. (2003). *PASJ* **55**, L7.
- Kato, T., *et al.* (2009). *PASJ* **61**, S395.
- Lenz, P., Breger, M. (2005). *Commun. Asteroseismol.* **146**, 53.
- Misselt, K.A., Shafter, A.W. (1995). *Astron. J.* **109**, 1757.
- Nogami, D., Kato, T., Masuda, S., Hirata, R., Matsumoto, K., Tanabe, K., Yokoo, T. (1995). *PASJ* **47**, 897.
- Olech, A., Zloczewski, K., Mularczyk, K., Kedzierski, P., Wisniewski, M., Stachowski, G. (2004). *Acta Astron.* **54**, 57.
- Patterson, J., Thomas, G., Skillman, D.R., Diaz, M. (1993). *ApJS* **86**, 235.
- Patterson, J., Jablonski, F., Koen, C., O'Donoghue, D., Skillman, D. R. (1995). *PASP* **107**, 1183.
- Patterson, J., Kemp, J., Saad, J., Skillman, D. R., Harvey, D., Fried, R., Thorstensen, J. R., Ashely, R. (1997). *PASP* **109**, 468.
- Robertson, J. W., Honeycutt, R. K., Turner, G. W. (1995). *PASP* **107**, 443.
- Thorstensen, J. R., Taylor, C. J., Becker, C. M., Remillard, R. A. (1997). *PASP* **109**, 477.
- Zhao, Y., Li, Z., Wu, X., Peng, Q., Zhang, Z., Li, Z. (2006). *PASJ* **58**, 367.

Small Telescope Spectroscopy of Epsilon Aurigae

*Jeffrey L. Hopkins
Hopkins Phoenix Observatory
7812 West Clayton Drive
Phoenix, Arizona USA 85033-2439
phxjeff@hposoft.com*

Abstract

With the availability of professional quality and reasonably priced spectrographs such as the Star Analyser, for low-resolution work, and the Lhires III with a 2400 l/mm grating, for high-resolution work, along with easy to learn and use spectral processing software such as RSpec, what was once well beyond the backyard astronomer is now well within the means of the advanced amateur astronomer allowing them to do serious astronomical spectroscopic work. The 27-year eclipse of Epsilon Aurigae is over until 2036, but there is still much going on out-of-eclipse that warrants continued observations. This paper will describe low and high-resolution spectroscopy of Epsilon Aurigae done at the Hopkins Phoenix Observatory. In particular five prominent hydrogen Balmer and sodium D lines will be examined.

1. Introduction

The purpose of this paper is to explore the hydrogen Balmer lines and sodium D lines of Epsilon Aurigae. Both low and high-resolution spectroscopy is used.

The exploration of these spectroscopic lines is an excellent learning exercise as well as a chance to discover some interesting features and changes. The low-resolution spectroscopy provides a complete visible spectrum picture. High-resolution spectroscopy provides a detailed look at each spectral region of interest.

While the recent eclipse of Epsilon Aurigae is over, the star system is constantly changing. The hydrogen alpha ($H\alpha$) line has been studied in detail and has provided tantalizing spectra of an emission line horn dance. The hydrogen Balmer lines $H\beta$, $H\gamma$, $H\delta$, and $H\epsilon$ have been neglected. The $H\alpha$ and sodium D lines have ample telluric and neon lines for wavelength calibration. The shorter wavelength lines are much more challenging and require a considerable changing of techniques.

2. Low-Resolution Spectroscopy

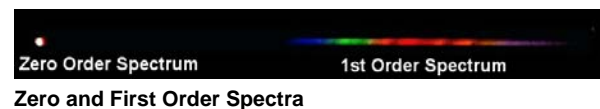
2.1 Introduction

For low resolution spectroscopy four things are sought

1. A low-resolution zero and first order spectrum image of epsilon Aurigae.
2. A low-resolution first order spectrum image of Epsilon Aurigae.

3. A trimmed and calibrated line profile of the first order spectrum.
4. An instrument wavelength response calibrated line profile.

2.2 Low-Resolution Equipment



Star Analyser Spectrograph (Shelyak Instruments)

A Star Analyser spectrograph was used for the low-resolution work. This unit is the size of an eyepiece filter and screws into the nosepiece of a CCD camera for zero order spectra and the front of a star diagonal for just first order spectra imaging. The spectra should be horizontal with the zero order spectrum to the left and the first order spectrum with the shorter wavelength (blue part) to the left and the

Epsilon Aurigae Spectroscopy - Hopkins

longer wavelength red part to the right. The Star Analyser must be rotated relative to the camera's CCD chip to obtain the correct orientation.

A Meade 8" LX90 telescope was used along with a Meade DSI Pro II monochrome CCD camera to image the spectra.



Meade 8" LX90 Telescope and DSI Pro II Camera

2.3 Wavelength Calibration

There are multiple techniques for the wavelength calibration. For low resolution the zero order spectrum and one identifiable first order spectrum line can be used. For a first order spectrum image, two lines identified lines can be used.

3. High-Resolution Spectroscopy

3.1 Introduction

For high-resolution spectroscopy five things are sought

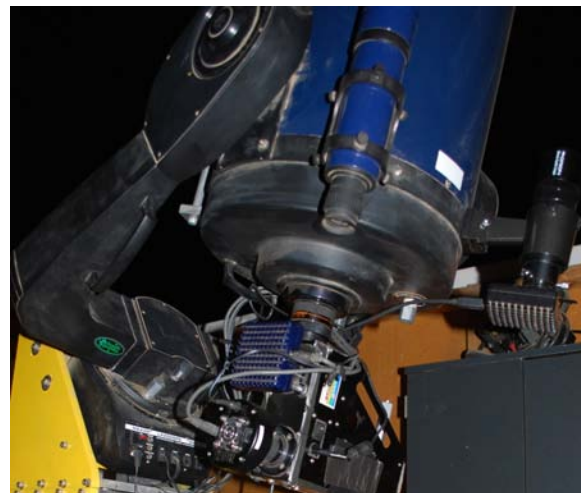
1. High-resolution spectrum images of the H α , H β , H γ , H δ , H ϵ and sodium D lines of epsilon Aurigae.

2. A trimmed and wavelength-calibrated (including heliocentric correction) line profile of each spectrum.
3. A normalized line profile for each spectrum.
4. Precise measurements of the wavelength of each line.
5. Precise measurements of the equivalent width of each line of interest.

3.2 High-Resolution Equipment



Lhires III Spectrograph (Shelyak Instruments)



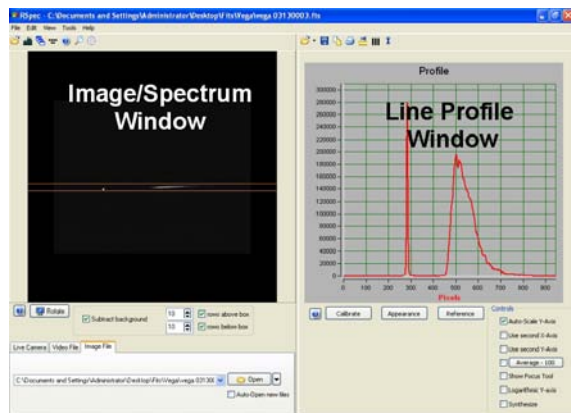
Meade 12" LX200 Telescope, Lhires III Spectrograph and CCD Cameras

For high-resolution work the built-in neon calibrator of the Lhires III provides the easiest set of reference neon lines. The disadvantage is for high-

precision work just flipping the calibrator in and out of the light path can introduce slight physical stress to the spectrograph and thereby introduce slight changes in the wavelength relationship. An alternate approach is to use an external neon ring on the front of the telescope to add the neon lines to the same spectrum image as the main object. For the spectral areas where there are telluric lines, these can be used to precisely calibrate wavelengths. A final method is to use various elemental gas discharge tubes on the bench to provide calibration lines. This is particularly important in the shorter wavelength Balmer lines. In some cases the neon lamps provide lines, but are not neon lines. These lines can be calibrated and used, however.

4. Spectrum Processing Software

4.1 Introduction



RSpec Initial Screen

Spectral images are first processed like regular astronomical images. Exposures are set to stay within the camera's linearity range. Dark frames are subtracted for exposures greater than 1.0 second. The image is then loaded into a spectrum processing software application. Because of its ease of use for this project the commercial program RSpec was chosen. Upon opening RSpec two windows are presented, the Image/Spectrum window and the Profile window. The spectrum image will be in the Image window. The sky background can be subtracted and the image orientation adjusted if needed. Two orange horizontal lines bracket the spectrum. These can be dragged up or down to precisely bracket the image. Whatever is between these lines has its pixel columns summed and a line profile created and displayed in the Profile window. A calibrated line profile of a spectrum is needed if empirical data are to be produced from it. Once a line profile has been created

the Profile window can be dragged top the left to expand it.

4.2 Low Resolution

4.2.1. Wavelength Calibration

There are several methods for calibrating low-resolution line profiles. These include two points, zero order and one point, one point and known dispersion and multi point non-linear calibration.

4.2.2. Instrument Response

While it is not required for wavelength determination or element identification, for the line profile to look anything like a standard star's profile, the profile must be corrected for the instrument's spectral response.

4.3 High Resolution

4.3.1. Wavelength Calibration

There are no zero order spectra seen with a high-resolution spectrum. Calibration of high-resolution line profiles is limited to two points and multi point calibration. The dispersion method is not recommended. Because resolution in the tenths of an angstrom can be achieved, it is very important to correct for the Earth's motion relative to the object of interest. This is known as heliocentric correction. As the Earth travels in its orbit around the Sun, the radial velocity relative to a stationary astronomical object outside the solar system can vary from +67,000 MPH to -67,000 MPH. In addition, the Earth's rotation can contribute an additional velocity of up to $\pm 1,042$ MPH. The heliocentric correction compensates for this motion by calculating a wavelength shift that is added or subtracted from a line's wavelength. RSpec does not have this capability so the French Freeware program VSpec was used for this calculation.

4.3.2. Normalization

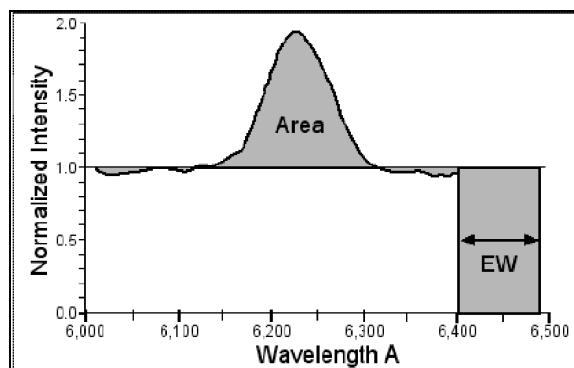
To calculate the equivalent width of a line, the line profile must be normalized. To normalize a line profile an average value for the continuum in the area of the line of interest must be determined. That value is then divided into the line profile causing the continuum to be centered on a value of 1.0.

4.3.3. Equivalent Width

Once a line profile has been normalized the equivalent width of a line can be determined. The

Epsilon Aurigae Spectroscopy - Hopkins

equivalent width is an indication of the power of the line. It's the line's area. The equivalent width is the width in angstroms for the area of a rectangle from the 1.0 level to the zero level equivalent to the line's area. Studying the equivalent width of a line as it changes over time can give insights as to what is going on in a star system.

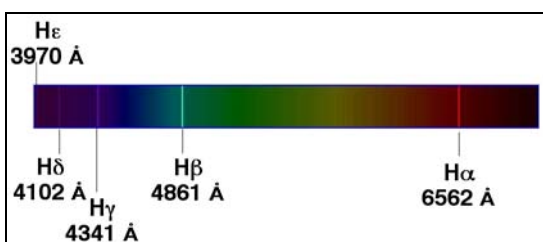


Equivalent Width Calculation

5. Observations

5.1 Introduction

Spectral observations of Epsilon Aurigae were done with both low and high-resolution equipment. All the hydrogen Balmer lines can be seen in the low-resolution spectra. For high-resolution spectra there are images for each of the first 5 lines and Na D lines.



Hydrogen Balmer Lines

Observatory Log (General)

Observer: Jeff Hopkins
Observatory: Hopkins Phoenix Observatory
Latitude: 33d 30' 06'
 +33.5017 decimal
Longitude: +112d 13' 23"
 112.229 decimal
Object: Epsilon Aurigae
RA (2000): 5h 01m 58.1s
Dec (2000): +43d 49' 24"

5.2 Low-Resolution Spectroscopy

For low-resolution work images of Epsilon Aurigae's spectra were taken to include the zero and first order spectra and also just the expanded first order spectra.

Equipment:

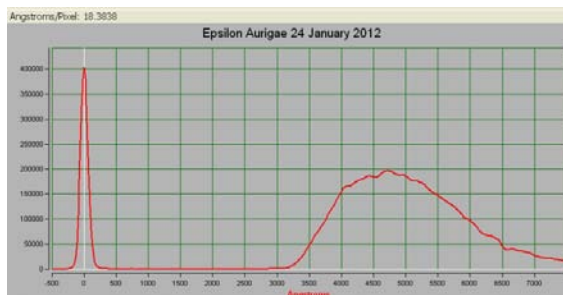
Telescope: 8" LX90, f/10
Spectrograph: Star Analyser
Slit: N/A
Grating: 100 l/mm
Detector: DSI Pro II

Observation

Double Date: 24/25 January 2012
Local Time: 18:53 MST
Universal Time: 01:53
Decimal UT Day: 25.07847
JD: 2,455,951.5785
Spectral Region: Visible Spectrum
Exposure: 1.0 Second
Fits File: Eaurnz.fts

Results

Air Mass: 1.1478
Rv: -19.89 k/s



Zero and First Order Spectra Line Profile



First Order Spectrum Calibrated Line Profile

RSpec has the capability of generating a color pseudo spectrum of a calibrated line profile.



Epsilon Aurigae Pseudo Spectrum

5.3 High-Resolution Spectroscopy

For high-resolution work, the five most prominent hydrogen Balmer lines ($H\alpha$, $H\beta$, $H\gamma$, $H\delta$ and $H\epsilon$) and sodium D lines of Epsilon Aurigae were observed. All Exposures were 480 seconds (8 minutes) with dark frames subtracted

Equipment:

Telescope: 12" LX200 GPS
Spectrograph: Lhires III (2400 l/mm)
Slit: 22 μm
Grating: 2400 l/mm
Imaging CCD: Orion StarShoot G3 mono
Guiding Camera: DSI Pro II

5.3.1. Epsilon Aurigae Hydrogen alpha

Observation

Double Date: 17/18 February 2012
Local Time: 19:47 MST
Universal Time: 02:47
Decimal UT: 18.11597
JD: 2,455,975.6160

Spectral Region: $H\alpha$ 6563 \AA
Reference Wavelength: 6562.81 \AA
Micrometer Setting: 2010

Fits File: EaurHalpfa.fts

Results

Wavelength Center:

$\lambda_b = 6560.98 \text{\AA}$
 $\lambda_a = 6562.84 \text{\AA}$
 $\lambda_r = 6564.91 \text{\AA}$

Heliocentric Correction: -0.576\AA

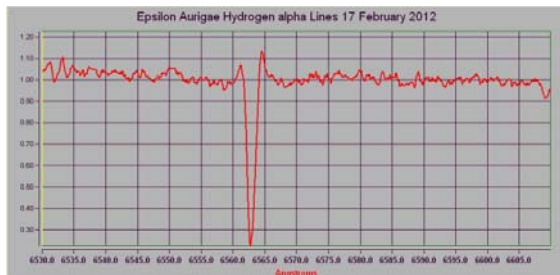
RV (km/s): -26.33 k/s

Air Mass: 1.0166

Equivalent Width:

$\lambda_b = 0.006 \text{\AA}$
 $\lambda_a = -0.484 \text{\AA}$
 $\lambda_r = 0.036 \text{\AA}$

VR (If applicable): 0.167



Epsilon Aurigae $H\alpha$ Calibrated Line Profile

5.3.2. Epsilon Aurigae Hydrogen beta

The $H\beta$ region was a bit more difficult to work with. The neon lines must be used for the wavelength calibration here.

Observation

Double Date: 18/19 February 2012

Local Time: 19:16 MST

Universal Time: 02:16

Decimal UT Day: 19.09444

JD: 2,455,976.5944

Spectral Region: $H\beta$ 4861 \AA

Reference Wavelength: 4861.350 \AA

Micrometer Setting: 1466

Fits File: Eaur Hbeta.fits

Results

Wavelength Center: 4862.10 \AA

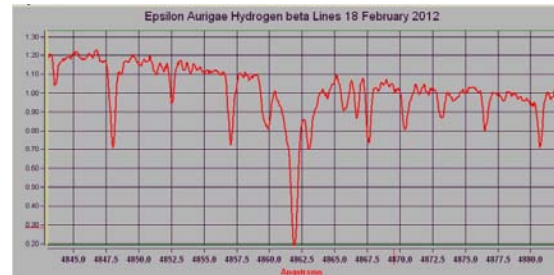
Heliocentric Correction: -0.429\AA

RV (km/s): -26.45 k/s

Air Mass: 1.019

Equivalent Width: -0.868\AA

VR (If applicable): N/A



Epsilon Aurigae $H\beta$ Calibrated Line Profile

5.3.3. Epsilon Aurigae Hydrogen gamma

As with the $H\beta$ line the $H\gamma$ line must also rely on the neon reference lines for the wavelength calibration.

Observation

Double Date: 21/22 February 2012

Local Time: 19:32 MST

Universal Time: 02:32

Decimal UT Day: 22.10556

JD: 2,455,979.6056

Spectral Region: $H\gamma$ 4340 \AA

Reference Wavelength: 4340.470 \AA

Micrometer Setting: 1320

Fits File: EaurHgamma.fts

Results

Wavelength Center: 4343.62 \AA

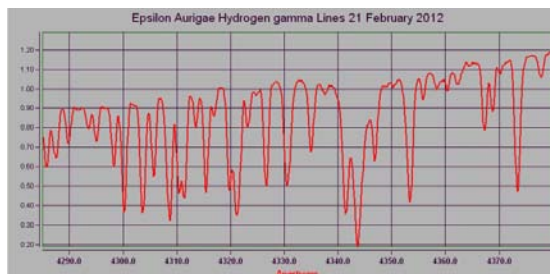
Heliocentric Correction: -0.39\AA

RV (km/s): -26.93 k/s

Air Mass: 1.0167

Epsilon Aurigae Spectroscopy - Hopkins

Equivalent Width: -3.022 \AA
 VR (If applicable): N/A



Epsilon Aurigae H γ Calibrated Line Profile

5.3.4. Epsilon Aurigae Hydrogen delta

As with the H β and H γ lines the H δ line must also rely on neon line spectra for wavelength calibration. The problem is that there are no usable neon lines in the area of the H δ line. It turns out that the neon lamps have contamination in them. As a result if a neon lamp, either the built-in neon calibrator or an external neon ring, is used lines will be seen that are not neon lines, but if calibrated can still be used. These may be mercury and/or argon lines. If the H δ line is moved to the far left of the computer window three lines at the far right can be used for the wavelength calibration. The reference wavelengths are 4149.42 \AA , 4144.55, 4132.08 \AA .

Observation

Double Date: 15/16 February 2012
 Local Time: 20:28 MST
 Universal Time: 03:07
 Decimal UT Day: 16.14444
 JD: 2,455,973.6299

Spectral Region: H δ 4102 \AA

Reference Wavelength: 4101.740 \AA

Micrometer Setting: 1250

Fits File: EaurHdelta.fits

Results

Wavelength Center: 4102.05 \AA

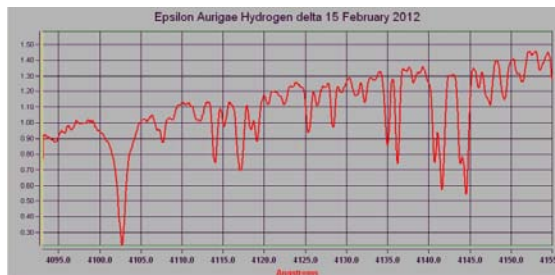
Heliocentric Correction: -0.356 \AA

RV (km/s): -26.02 k/s

Air Mass: 1.0256

Equivalent Width: -1.285 \AA

VR (If applicable): N/A



Epsilon Aurigae H δ Calibrated Line Profile

5.3.5. Epsilon Aurigae Hydrogen epsilon

Again the problem is that there are no usable neon lines in the area of the H ϵ line. Again it turns out that the neon lamp contamination provides some useful reference lines. If a neon lamp is used, either the built-in neon calibrator or an external neon ring, the contamination will produce reference lines that can be calibrated and used for the wavelength calibration.

Observation

Double Date: 12/13 February 2012

Local Time: 21:07 MST

Universal Time: 04:07

Decimal UT Day: 13.12986

JD: 2,455,970.6715

Spectral Region: H ϵ 3970 \AA

Reference Wavelength: 3970.07 \AA

Micrometer Setting: 1215

Fits File: EaurHepsilon.fits

Results

Wavelength Center: 3970.05 \AA

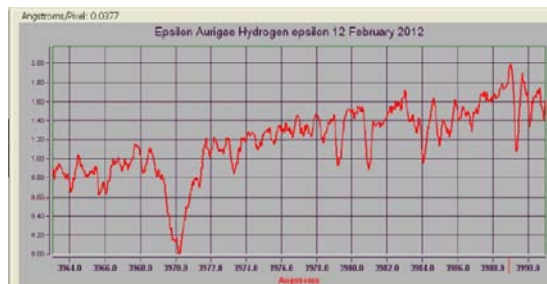
Heliocentric Correction: -0.336 \AA

RV (km/s): -25.39 k/s

Air Mass: 1.0167

Equivalent Width: -1.271 \AA

VR (If applicable): N/A



Epsilon Aurigae H ϵ Calibrated Line Profile

5.3.6. Epsilon Aurigae Sodium D Lines

The second spectral area of most interest, behind the hydrogen alpha region is the sodium D line region. The two sodium D lines are very prominent.

Observation

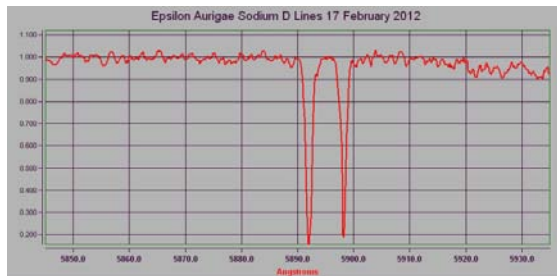
Double Date: 17/18 February 2012
Local Time: 19:30 MST
Universal Time: 02:30
Decimal UT Day: 18.10417
JD: 2,455,975.6042

Spectral Region: Na D Lines 5892 Å
Reference Wavelength: 5889.950/5895.929 Å
Micrometer Setting: 1782

Fits File: Eaur NaD.fts

Results

Wavelength Center: D1 5892.41 Å
 D2 5898.29 Å
Heliocentric Correction: -0.516 Å
RV (km/s): -26.30 k/s
Air Mass: 1.0171
Equivalent Width: D1 -1.106 Å
 D2 -0.821 Å
VR (If applicable): N/A



Epsilon Aurigae Na D Calibrated Line Profile

6. High-Resolution Data Summary

RJD	Micro	Region	λc	EW
5,975.6178	2010	Hαv	6560.98	0.01
5,975.6178	2010	Hαa	6562.84	-0.48
5,975.6178	2010	Hαr	6564.94	0.04
5,976.5962	1466	Hβ	4862.10	-0.43
5,979.6070	1320	Hγ	4343.62	-3.02
5,973.6464	1250	Hδ	4102.05	-1.29
5,970.6321	1215	Hε	3970.05	-1.27
5,975.6060	1782	NaD1	5892.41	-1.11
5,975.6060	1782	NaD2	5898.29	-0.82

Note: Reduced Julian Date RJD = JD - 2,450,000

Micro is the Lhires III Micrometer setting

Hαv is the Hα violet emission line

Hαa is the Hα absorption line

Hαr is Hα the red emission line

λc is line center wavelength

EW is Equivalent Width

7. Conclusions

It has been demonstrated that with even very simple and inexpensive equipment and software an observer can get started into the world of small telescope astronomical spectroscopy. By adding a high-resolution spectrograph, e.g., the Lhires III with a 2400 l/mm grating, high quality and high-precision spectroscopy can be done. Scientifically useful data can be produced e.g., wavelength calibrated line profiles. Equivalent widths of various lines can be determined and plotted over time to see changes in the star system. Knowing calibration lines in various areas of the visible spectrum can help wavelength calibration. The built-in neon calibrator of the Lhires III helps, but some areas are void of neon lines. Sometimes fluorescent lights can be used with the mercury lines. For the sodium D lines an inexpensive low-pressure sodium light can provide a very accurate wavelength calibration. A set of gas discharge tubes for various elements can also enhance the bag of tricks for wavelength calibration.

During the observation of the Balmer line regions of the spectrum of Epsilon Aurigae, other unknown lines were seen. Some of these are very strong and worth further investigation. It may require the use of a lower resolution spectrograph so more of the spectrum can be viewed. This would help in identifying the unknown lines. Once identified high-resolution spectroscopy could be done to examine those lines in detail. Continued observations out-of-eclipse may help in unraveling the mystery of Epsilon Aurigae. Not all the action is limited to the main eclipse. There is still a lot of action going on right now.

8. Acknowledgements

I wish to thank the following people:

Dr. Douglas Walker, Estrella Community College, for his encouragement.

Tom Field for providing the excellent, easy to learn and use spectroscopy processing software RSpec.

Olivier Thizy, of Shelyak Instruments, for making excellent spectroscopic equipment available and for his enthusiasm, which is contagious.

Dr. Robert Stencel (Dr. Bob), University of Denver, for his encouragement, inspiration and for being patient with all my questions. Our December 2010 observing session on Mt. Hopkins with the infrared spectroscopy using the MIRAC4 mid-infrared spectrograph and 8-meter telescope was inspirational.

Dr. William F. Ketzbeck, Apache Point Observatory, New Mexico, for his spectroscopic work on Epsilon Aurigae and his kind assistance in answering my questions about the sodium D line changes.

9. References

Hopkins, J.L. Stencel, R.E. (2009). "Epsilon Aurigae Hydrogen Alpha Emission Line Variation Horn Dance." *Proceedings for the 28th Proceedings for the 28th Annual Conference of the Society for Astronomical Sciences*. (Warner et al., eds). Society for Astronomical Sciences, Rancho Cucamonga, CA.

Hopkins, J. L. (2012). *Small Telescope Astronomical Spectroscopy*. HPOSoft. Phoenix, AZ.
<http://www.hposoft.com/SB/SpectroBook.html>

Observations Using a Bespoke Medium Resolution Fast Spectrograph

*John Menke
22500 Old Hundred Rd
Barnesville, MD 20838
john@menkescientific.com*

Abstract

Designing and building a medium resolution ($R = 3000$) spectrograph was the relatively easy part. The really challenging part is learning how to use it: learning the characteristics of the spectrograph, choosing the right kind of astronomical problems, learning the best methods of taking data, and figuring out how to analyze the results. I have used several observing projects to “commission” this system, including measuring the Doppler shifts in several WUMa type stars. I will briefly describe the spectrograph but discuss in more detail the early experiences of using it.

1. Introduction

After four years of using a low resolution $R=100$ SBIG DSS7 spectrograph, I am still in awe of what it can do. But in this paper I describe exploratory work with a new bespoke (custom) Fast Spectrograph (FS1) of $R = 3000$ – some 30x greater than the DSS7.

The price of high resolution is low signal level! A spectrometer resolution of $R = 3000$ implies roughly a $\times 3000$ reduction in s/n at each pixel, so a five minute exposure of say 16 mag now only reaches about 7 mag., and probably only 6 mag with real optical elements!

RGB and similar filter combinations do allow some ability to distinguish among the colors in the light from an astronomical object. RGB filters have a wavelength resolution of about 10 or so—at about 5000Å the bandwidth is about 500Å, but already we begin to sacrifice s/n for information. But for greater resolution, we move to ever higher resolution spectroscopy: We always want “more, more, more”, whether it is light gathering or resolution, ice cream, or Scotch.

The design and construction of the FS1 is given in detail in a paper on our website (Menke, 2012) and in a brief poster at this conference. After completing construction and “first light” with the new FS1, I embarked on a series of observations designed to explore the capability of the instrument and to help me learn how to use it. Of course, identifying and conducting useful research opportunities is the real next step.

2. DSS7 Experience

Some may believe that the “low” resolution of the DSS7 prevents useful work. However, in past years, I have used it to learn spectroscopy observational and analytic techniques. Observations included performing coarse stellar classification from the shape of the spectrum, observing a variety of objects including planets, comets, planetary nebula, and novae. The most notable of these were observations of nova U Scorpii as reported at SAS in 2010.

In previous papers and on our website, I have detailed some of the limitations of the DSS7 and effective ways to overcome them (Menke, 2011). One of the limitations of the DSS7 is (as with most spectrometers) that it is designed for an $f/10$ optical system. However, my 18-inch Newtonian is $f/3.5$, thus requiring a properly matched Barlow lens. This extends the optical train, and of course, enlarges the stellar image on the slit, thus usually requiring use of a larger slit with reduced resolution and very tight tracking because there is no real time guiding in the DSS7. The second limitation is, of course, the low resolution. .

3. Fast Spectrometer FS1

After several years of using the DSS7—and by no means exhausting its possibilities—I decided to obtain a higher resolution unit in the $R = 2-6000$ range and suitable for my $f/3.5$ Newtonian. A particular attraction of higher resolution is the possibility of measuring astronomical Doppler shifts. While some galactic and nova Doppler shifts can be observed with the DSS7, velocities of planets are in the 10s of km/s, semidetached binaries are in the low 100s of km/s.

Using a Bespoke Spectrograph - Menke

100 km/s corresponds to about a Doppler shift of about 1:3000 or 2 Å at 6000 Å. To accomplish a 10% precision implies the ability to measure to about 0.2 Å.

After searching the market, and finding that nearly all units were designed for f/7-f/10 and had other features I did not like, I decided to “roll my own” (plus I like building things). The design goals included:

- Native f/3.5 design (but will easily accept slower telescopes)
- Physically compact, and well balanced
- Inexpensive (approx \$500)
- Construction requiring only basic machining skills
- Adaptable, easy to modify
- Accept almost any CCD camera (I use an SBIG ST1603)
- R = 3000 with possibility to go higher, and with high stability
- Built-in calibration (e.g., neon bulb or other)
- Built-in guiding, including offset guiding (i.e., not using the target) using Starlight Express Lodestar or SBIG SGI

Fig. 1 shows the FS1, while Fig. 2 shows the Littrow design (in which the light comes back off the grating at the same nominal angle as incoming) that allows for a single collimating lens that is more compact. The many design considerations are detailed in our website paper (Menke, 2012a). Construction and alignment was relatively straightforward using several red lasers to trace rays through the unit and neon bulb and sodium flame sources to measure resolution as described in the reference.

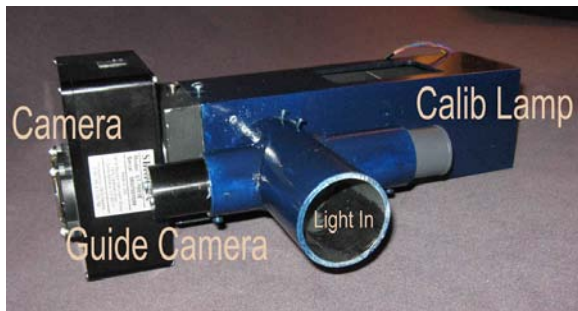


Fig. 1. Picture of FS1 Spectrograph

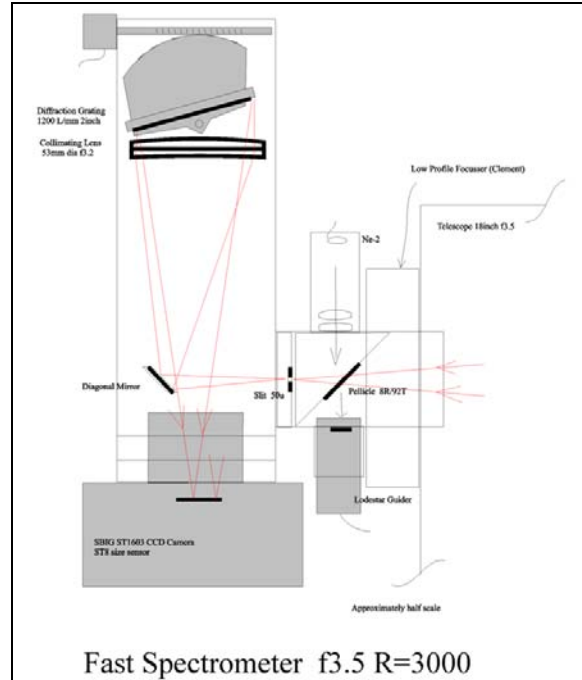


Fig. 2. Schematic Diagram of FS1

Once turned on the sky, it was obvious that this was a very different instrument from the DSS7! The integral real time guiding meant that keeping the star on the slit, or even precisely in the middle of the slit, was now easy-no custom software needed. The very first night showed lots of solar lines from the moon, splitting sodium D-lines, and even (incorrectly) seemed to show the rotation of Jupiter. And it showed that the expected mag 8 was indeed about the practical limit with good S/N.

After the first night euphoria, the challenges were to measure the characteristics of the FS1 (and making any necessary modifications) while performing “real” observations that would help me learn how to use it and how to interpret the data.

4. Studies of FS1 Performance

The first “real world” task was to determine how well the tracking worked, not only for short data runs, but also for long runs while the telescope shifted in direction. In general, the guider kept the target within the slit to a few tenths of a 8-µ pixel: guiding was a cinch. Another question was whether there were special demands for the focus of the telescope. Due to a fault in the design of the telescope, its focus shifts when low in the sky, especially toward E/W; however, this did not affect the spectrograph more than expected and defocus could be easily detected and compensated.

There were many questions about wavelength measurement: resolution, dispersion, stability, repeatability, etc. Measurements quickly using the ST1603 camera (ST8 size chip) showed that the wavelength span is approximately 600Å at ~ 0.4 Å per 9- μ pixel dispersion. The remote stepping motor controlled operation of the grating sets the coarse energy scale. When setting the energy scale using the stepping motor drive, the repeatability is about 10Å (corresponding to approximately 1 arcminute of grating rotation). While the spectrometer has a resolution of about 2 Å, it is important that the stability exceed this so that wavelength changes can be accurately followed. Studies discussed below showed that the stability over a data run is normally about 0.2 Å, thus allowing Doppler shift and related work more than 10 times finer than the resolution.

As I expected, it is essential to establish the wavelength scale using either the internal calibrator (usually Neon, fluorescent, or other source) or a spectral feature. One limitation of using the calibrator is that it does require a special exposure, i.e., during long data runs, the sequence must be interrupted either manually or via special software to obtain a calibration image. Calibrating on a feature of the spectrum being taken is often feasible, depending on the wavelength range being used and the object being observed. In some cases sky background can provide a line; however, the most useful for many of my observations in the 6200-6800 Å band has been use of the O2 absorption at 6283 Å which I used to measure the wavelength stability of the spectrometer.

A particular concern was to measure the stability of the wavelength calibration, especially over long observing runs. The most obvious potential problem is mechanical shifts are due to orientation changes as the telescope tracks the star, temperature, etc. However, there a more subtle issue is the stability of the target position in the slit.

Depending on the target, the slit of the spectrograph has two major purposes. If the target is a star (point source) focused at the plane where the slit would go, and if the star image is placed and held on precisely that spot, then the spectrum will be formed even though the slit is not present and the wavelength scale will be set and stable. If the star is faint, then the sky background light may contaminate the spectrum, but providing a slit reduces this. If the target cannot be kept stable in position, the wavelength scale will change but a slit at least limits this change. Of course, a slit also allows a spectrum to be formed from a diffuse target.

The point of this discussion is that good guiding stability allows a stability of the wavelength calibration that can be substantially tighter than the resolution calculated from the slit width, and indeed, tighter

even than the FWHM of the target image would indicate.

To test wavelength stability, Fig. 3 shows the result of a long run of taking neon calibrator spectra every ten minutes. The graph shows a variation of nearly 5 Å, which of course, should not happen. I traced this instability to a minor slop in the grating holder that was cured with a 5-cent spring.

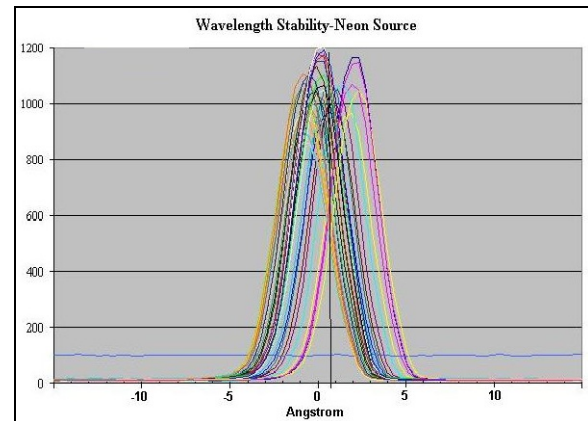


Fig. 3. Wavelength Stability Test (Neon)

Just as challenging as learning how the spectrograph operated was learning how to analyze and interpret the spectral. To accomplish these goals, I undertook two major observational programs as discussed below:

- Measuring the Doppler shift from a pulsating star. The star chosen was Beta Cephei, the namesake of this class. It is bright and hot: 3.3 mag and B spectral class, so there is plenty of light. The pulsations will cause the lines to swing back and forth over a few tenths of Angstrom.
- Measuring the Doppler shift for several semi-detached eclipsing binaries (including WUMa 7.8mag) having Doppler shifts of 1-200 km/s (about 2 Å). With an 8-hr period, WUMa would show splitting of the lines every four hours.

5. Data Processing Methods

I will describe the observing and data analysis used for the Beta Cephei project, and later the modifications needed for the WUMa observations.

The FS1 operates with automatic guiding using the internal beam splitter (pellicle) and Starlight Xpress Lodestar guide camera that has an electronic shutter system. In general, guide exposures can be 10 sec or longer if needed, however, this bright target star allowed <1 sec exposures to avoid saturation.

The guider easily kept the target on the slit to within the desired 0.1-0.2 pixel rms.

Spectral images were five minutes duration, for Beta Cephei typically reaching about 1/3 of saturation, and were taken using the MaximDL in sequence mode.

Each morning, after a night of automated data collection, the archived images were downloaded from the observatory (about 400 ft away). I use Maxim and Visual Basic for the image manipulation and reading the images, then Excel for analysis. This allows me to easily tailor the spreadsheet to perform the analysis I need and the graphic or other outputs I desire. Plus, the spreadsheet itself records all the arithmetical steps so that I can later review and verify what was done. As you will see later in the WUMa analysis, this process also allows easy simulation of data so that one can explore alternative analytic schemes with “known” data.

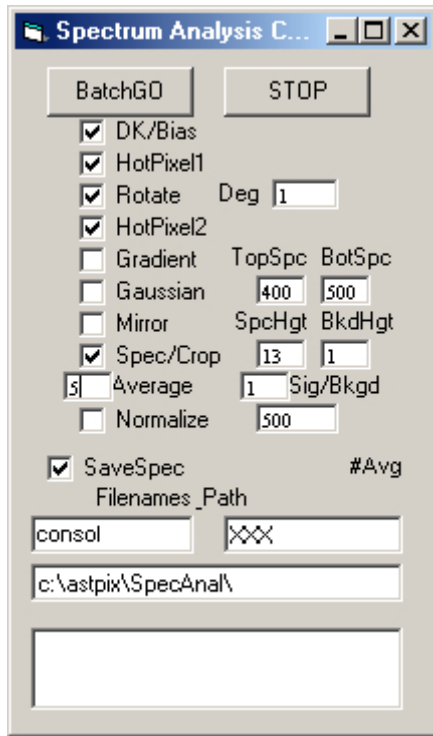


Fig. 4. Spectrum Processing Control Window

As noted, image manipulation was done in MaximDL. Due to the volume of data, I wrote a VB program (Fig. 4) to control Maxim that would allow processing scores of images at a time using simple checkboxes to set the manipulations needed. In this case, the spectral image manipulation included dark and bias calibration and rotation of the image to align the spectral band. The program measures the vertical center of the spectral band in the image, averages the value at each wavelength interval (horizontal pixel),

and subtracts the associated background. The program also automatically averages a specified number of successive images, and has the ability to reject images with poor s/n while maintaining a uniform cadence (timing) of the averaged images. The resulting averaged images (typically 10-30) in the batch are written into a single numerical array. I call the entire array the dataset for the night, while each averaged spectral image is a data subset.

Each array is copied into a spreadsheet for that night’s run where the array is displayed as “n” spectral image columns. By using a standardized spreadsheet, the data automatically display into the desired graphs. The standard spreadsheet then repeats the array to the right to allow an adjustable wavelength calibration for each data subset. Pasting the data into the sheet takes about 20 sec, and all the results are available immediately. Fig 5 shows a typical result of an observing run, with each data subset vertically offset for easy viewing.

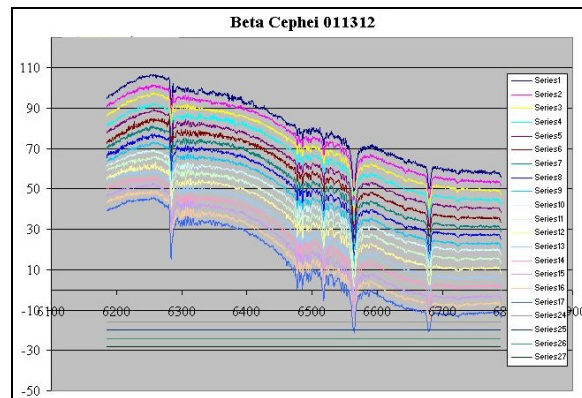


Fig. 5. Typical Spectra Display (Beta Cephei)

6. Beta Cephei Observations

The BCep program data became vital data for verifying FS1 operation and for developing the analytic process.

Beta Cephei pulsates in brightness with a period of 4.57 hr and an amplitude of about 0.02 mag. The pulsation is driven by internal processes that result in expansion/contraction of the star’s outer surface whose Doppler shifts can be detected. The line of sight velocity of the oscillation is only about 20-30km/s, corresponding to a total wavelength shift of 0.4-0.6 Å, which is much smaller than the 2 Å resolution of the spectrometer. The brightness of the star provides plenty of light, however, so that exposures of only five minutes still have sufficient s/n to allow precise determination of the wavelengths of the absorption lines. Thus, if the instrument calibration is stable, or if each exposure can be calibrated, then this

instrument would be able to measure the Doppler signal.

Fig. 6 shows the Telluric O₂ line at 6283 Å from a Beta Cephei observing run. One can see that the lines are unchanged in wavelength during the run to better than 0.2 Å. And as expected, the relative depth of the 6183 line does vary during the run as the light travels through differing thickness of atmosphere, while the lines of astronomical sources do not. The stability results show that long runs with only occasional calibrations with the Neon (or other) calibrator are feasible.

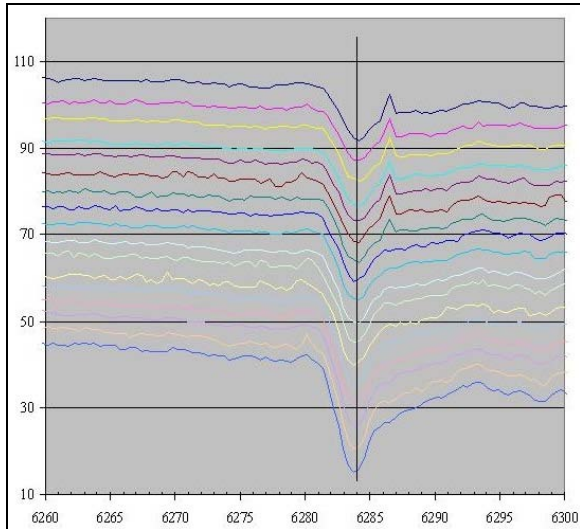


Fig. 6. Stability Verification (Beta Cephei)

So, is the Doppler oscillation of Beta Cephei visible with this spectrograph? Fig 7 and Fig. 8 show the 6563 H α and 6683 He lines from the same data set. The spectra are vertically offset for easy visibility, and represent 15 minute averages (period of the pulsation is 4.5 hrs). Clearly, the H α line shows a wavelength shift during the run of about 0.6 Å. However, the HeII line at 6283 Å shows a more complex behavior as both shape and apparent wavelength change hour to hour. Examining the data makes one suspect not only similar wavelength changes as with H α , but also the strengthening and weakening of nearby absorption lines as the star pulsates. In fact, there are additional HeII lines nearby, at 6678 and 6681, that appear to be varying in strength as the star pulsates.

These changes in line shapes have been studied since the 1950s as giving insights into the internal process of this class of stars. What is gratifying is that homemade equipment can allow its study by an amateur in 2012! If tracking these or similar variations would be useful to a Pro, this Am would be happy to track this for many nights!

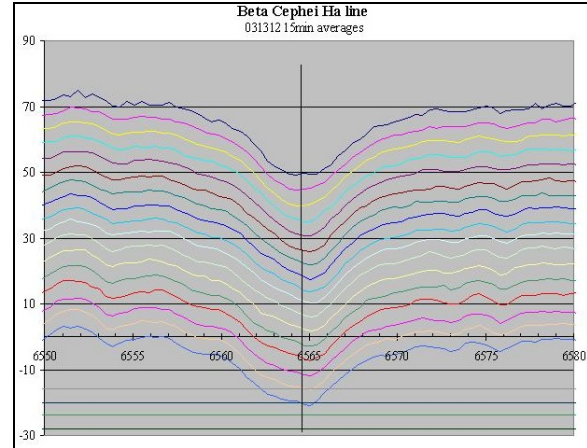


Fig. 7. Beta Cephei H α Oscillation

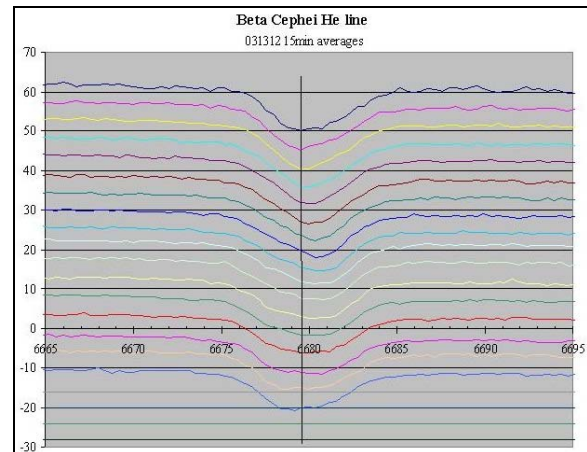


Fig. 8. Beta Cephei He Oscillation

7. WUMa Observations

WUMa is a semi-detached eclipsing binary with an 8.00 hr period. The variable nature of the star was discovered in 1903 and its binary nature in 1919 when the first Doppler measurements were published. However, the measurements are surprisingly difficult to make accurately and have been refined ever since.

As the stars orbit one another, they almost totally eclipse one another. During the eclipses, first one, then the second star is the only one seen. At such times, the single star spectrum will show only the system Doppler shift due to the Sun-WUMa relative velocities and the line of sight movement of the front star relative to the system barymetric center: Both of these shifts are relatively small. At quadrature, however, one will see the spectra of the two stars, but with each displaced in wavelength relative to the eclipsed wavelengths. Observing this split sounds easy but turns out to be not so, especially not with marginal 2 Å resolution on a relatively faint star.

While the 7.7 mag of the star greatly restricts the available signal, it proved to be a good test for learning how to handle poor s/n while seeking to measure small effects! Although there are more absorption lines available in bluer wavelength bands, for most of this work I chose to continue in the 6100-6800 band due to the availability of the Ha line from the source and the 6183 telluric line.

Given the full 8 hr cycle of the WUMa, one can combine about 6 five minute images without introducing more than 10% error in the Doppler velocity. Obviously, it is desirable to perform the averaging so that the averages are centered on the orbit quadratures, thus requiring accurate knowledge of the ephemeris. Caution: many standard tables of ephemeris are outdated: not only are some periods in error, but also the periods change over years and decades. For most of the interesting binary stars, Bob Nelson and AAVSO maintain a valuable updated catalog on the web (Nelson). I also found it sometimes useful and reassuring to verify the timings by performing the necessary photometry.

Even with 30 min averaging, the WUMa data were rather noisy. In some runs (depending on the quality of focus, night clarity, etc.), the deep Ha line shows the splitting very clearly, as shown in Fig 9 along with a double Gaussian fitted to the points.

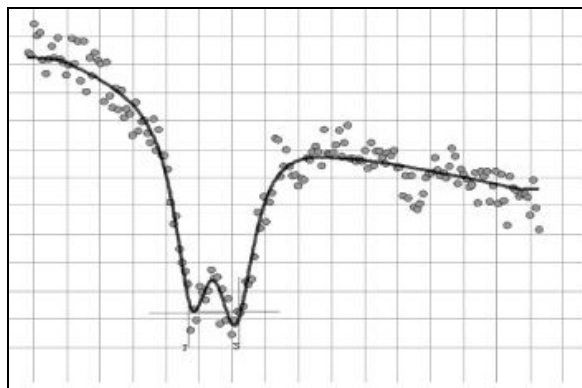


Fig. 9. WUMa Line Split

Using only Ha lines wavelength measurements from quadrature data averaged over three nights, calculations yielded WUMa star velocities of 260 and 77 km/sec. This result may be compared with other measurements from the literature such as those of Worden (Worden, 1977) that showed 243 and 131 km/s. The relatively impressive agreement may be fortuitous, given the data noise levels and the early stage of this analysis.

However, because most of my data were not as good as these sets, there is need for a better approach that takes advantage of all the lines in the spectrum even though affected by noise. One answer is to obtain a reference spectrum of a similar class star with

undisplaced. Then using the target spectrum, one computes the correlation coefficient (CC) between the two, thus measuring the relative similarity of the two. If one then calculates the CC for a range of displacements (e.g., $\pm 15 \text{ \AA}$) between the two spectra and graphs the result, the value of the CC vs. displacement wavelength will actually be an accurate graph of the shape of the split spectral lines!

Professional astronomers have spent much effort refining this general approach and developing similar analytic methods; however, this one is easy to implement in Excel.

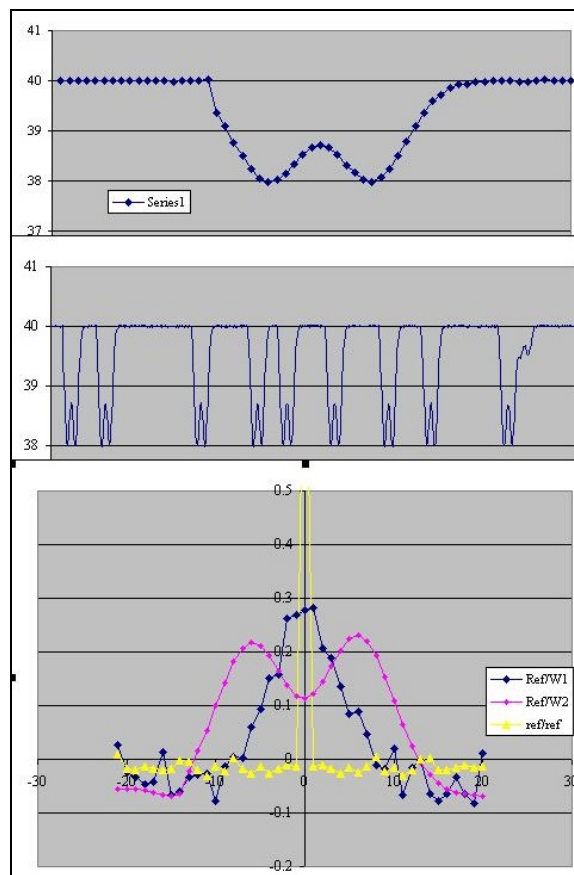


Fig. 10. Synthesized Spectra-Low Noise

It was fairly easy to prove that the method was workable by generating a synthetic spectrum in Excel. The spectrum included Gaussian noise and Gaussian shaped lines of adjustable width and spacing. Fig. 10 and 11 show low and high noise spectra, and the CC results. This test shows the ability of the method to pull data out of noise and the feasibility of spreadsheet implementation.

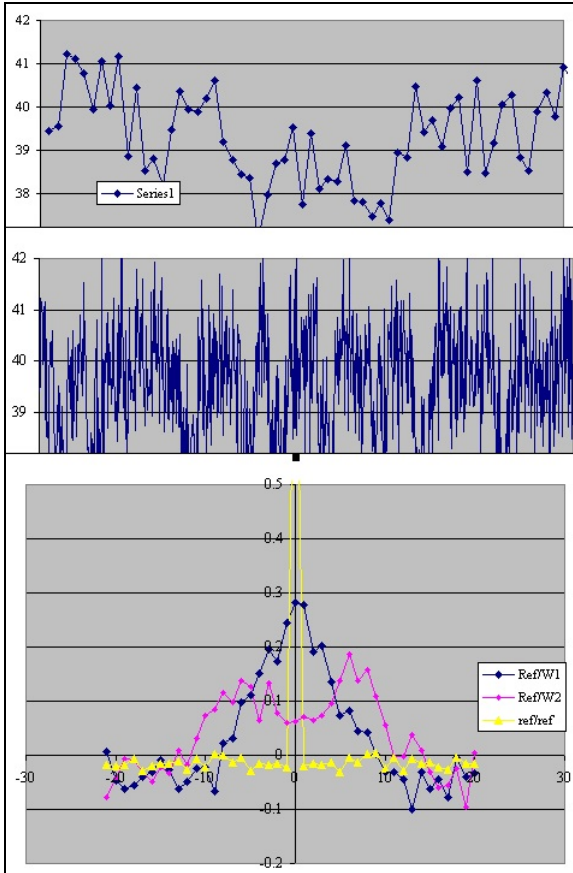


Fig. 11. Synthesized Spectra-High Noise

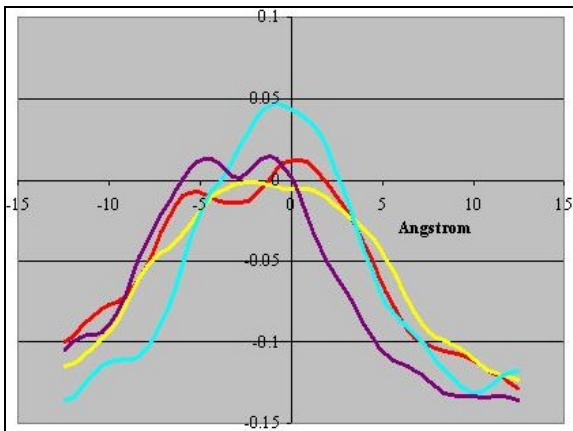


Fig. 12. Example Correlation Coefficient Results

The reference spectrum must of course have the same dispersion as the observed spectrum. Thus, I have used as reference spectra my own measures of stars or the sun; however, the reference spectrum that was most effective was generated from the website of R.O.Gray (Gray). Using the SPECTRUM program from that site, one can manufacture a digital reference spectrum of desired line widths and dispersion.

Using such a reference, and using quadrature data from a noisy WUMa observing session, Fig 12 shows a typical set of promising CC results for the four quadratures from early tests of this method.

With hundreds of data sets from many nights of data covering the entire orbital period (not just quadratures), one is tempted to massage it forever, or until one is exhausted or the computer crashes. While it is clear that substantial refinement of the methods are needed, the results already show that the general approach is correct and that this work is feasible for amateur equipment and skills.

8. Conclusions and Implications for SAS Members

This work has already shown that a shop-built spectrometer can be used for many advanced observing projects requiring rather stringent instrument stability. The initial observing projects have been a challenge to analyze, but the results already show the validity of the FS1 design and the promising work that can be performed.

There are many additional targets for this spectrometer including the planets, nebulae, novae, and following the shape changes in particular spectral lines. As an example of the latter, Christian Buil has led a major effort in this area, mostly following Be stars (these are hot B-stars with hydrogen emission features). Because we amateurs can spend as much time on a subject as we wish, time series spectroscopy would appear to be a very fruitful area for us. However, it will likely take a substantial expansion of the Pro-Am programs to identify research areas suitable for amateurs with this type of equipment and this level of skill.

When Dale Mais several years ago gave several talks on his spectroscopic work, he wowed me. And intimidated me with his encyclopedic knowledge of astrophysics, of this and that spectral line, and of the significance to astrophysics. But if one is not in a university setting, then even with the Internet, how does an amateur—even one with some knowledge of the physics of instruments and stars and research—ever get started? The Internet helps, but many papers of interest are essentially unavailable to the individual, thus making self-education in advanced spectroscopy difficult. In contrast, there are many websites and other resources that help one learn advanced photometric techniques, develop Pro-Am contacts, submit and publish data, etc.

That may be changing. As more of us move into spectroscopy, there will be more cross-fertilization among amateurs. And we are seeing an increase in organized Pro-Am work – witness AAVSO and espe-

cially the Lowell initiative that I hope will develop programs to build advance skills in spectroscopy. In the long run, these programs should help increase the ease of establishing Pro-Am collaborations and encourage amateur driven research (i.e., non-Pro-Am) as well.

So let me leave you with a dual challenge

- To the Pros: Seek out amateurs who can contribute to spectroscopic astronomical research, both in support of your particular study area or to broader research objectives. It would seem that amateurs might be particularly helpful in long time series spectroscopy.
- To the Ams: Seek out the new challenges of spectroscopic research, and to learn how to do it—it is, after all, *The Dark Side*...

9. References

Gray, R. O. (2012).

<http://www1.appstate.edu/dept/physics/spectrum/spectrum.html>

Menke, J. L. (2011). “Spectroscopy Techniques I and II” and others.

Menke, J. L. (2012). “Construction of a Fast f/3.5 Medium Resolution Spectrometer.”

<http://www.Menkescientific.com>

Nelson (2012). Updated O-C files for eclipsing binaries. <http://www.aavso.org/bob-nelsons-o-c-files>

Worden, S. P., Whelan, J. (1977). “W Ursae Majoris: The parameters of a Contact Binary”. *Mon. Not. R. Ast. Soc.* **163**, 391-400.

High Resolution Spectroscopy for the Amateur: Experiences with the LHIRES III Spectrograph

*Stanley A. Gorodenski
Blue Hills Observatory
9440 E. Newtown Avenue
Dewey, Arizona 86327
stanlep@commspeed.net*

Abstract

This paper describes the author's experience with the high resolution LHIRES III spectrograph and other equipment used. It discusses mechanical improvements made that may have increased the calibration accuracy of the spectrograph, problems with guiding, and the need to take flat fields. It also briefly mentions the freeware software used and the types of computer programs written by the author to aid in the reduction and analysis of the spectra. An assessment is made of the method for determining equivalent width the author described in the 2011 issue of the SAS News. It finishes by illustrating the ability to study binary stars, such as V1143 Cyg, with the LHIRES III, and discusses some interesting results that were obtained on Epsilon Aurigae. The evolution of a split line centered at around 5853 Angstroms is mentioned, as well as other aspects of the Sodium D Lines region, such as the constancy of separation between the two lines.

1. Introduction

I have a two story 16'x16' observatory in Dewey, Arizona, about 7 miles from Prescott, Arizona in a straight line, at an elevation of 5,140 ft. The observatory and dome are my own designs and I constructed them completely by myself (except for the concrete and block work). For a long time all I had in it was a 12.5" Dall-Kirkham made by a machinist friend in the 1970's (see <http://users.commspeed.net/stanlep/homepagens.html> for more information about the observatory and the Dall-Kirkham). Although an excellent telescope for visual observing, to use it for serious science would have required some major retrofitting. Instead of doing this I purchased a 16" Meade LX200R in 2006 (see SAS Newsletter Vol 5, No 2 for more information about the Meade and its installation in the observatory).

For many years I wanted to get into photometry. However, building the observatory and dome was a major project taking many years that prevented me from doing this at the same time. With good intentions I had purchased a used Starlight-1 photometer but it would have been too difficult to do photometry with the Dall-Kirkham. I have always had an interest in spectroscopy and the 2005 issue of the SAS Newsletter, Vol 3, No 3, had an ad for the newly introduced LHIRES III spectrograph as a knock down kit. It had a good introductory price and so I purchased and assembled it. Shortly after this I purchased the Meade 16". Now I was ready to do some science.

2. Equipping the Observatory

To attach the spectrograph to the telescope, I attempted to use the Meade electronic focuser that came with the Meade 16" but it had a number of problems: 1) It was not strong enough to lift the weight (about seventy pounds) of the instrument package consistently at all times, 2) the 2" diameter nose of the spectrograph could not be tightened down enough in the draw tube to prevent wobble, and 3) the draw tube wobbled inside its housing.

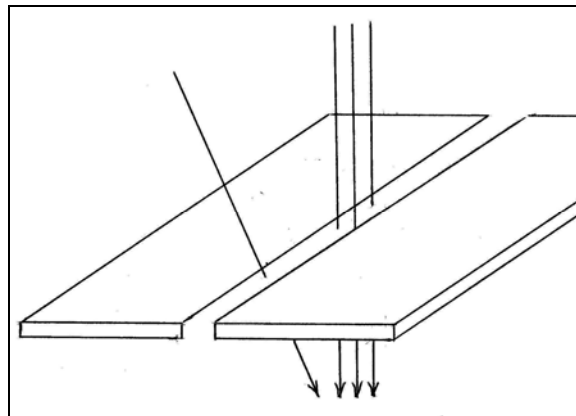


Figure 1.

I felt wobble could be a potential problem for the following reason. Figure 1 is a diagram of a slit with four incident light rays. If guiding is not perfect and the target star drifts parallel to the slit (the 2nd and 4th light ray from the front), all it will do is spread the image of the spectrum over a larger area on the CCD

chip. Instead of it being a narrow bright line it will be wider with a reduced intensity peak. This will result in having to increase integration time to reach the ideal saturation level. If the star drifts in declination (i.e., in a direction perpendicular to the slit, the 3rd light ray from the front), all it will do is result in light loss, again resulting in having to increase integration time. However, a wobble, I think, changes the angular direction of the light ray through the spectrograph (the first light ray in Figure 1) and I think this could cause problems with getting a high quality spectrum. I do not know if this is a significant concern or if it has any detrimental effect at all, but even if there is no effect I like things to be rigidly attached. I replaced the Meade focuser with a v-grooved adapter I machined (see Figure 2).



Figure 1.

The spectrograph nose slides over it as shown in Figure 3. This design completely eliminated all wobble (note the four stainless steel allen head screws. These screws have tapered ends to match the v-grooves of the adapter). In Figure 3 is also shown the ST-8XME imaging camera, and the Meade DSI I guiding camera.

With this setup I had to use the telescope manual focus to focus the target star for guiding. With increased use, manual focus (the long bottom knob at the back of the OTA in Figure 3) started feeling rough in one direction. Consequently, I felt I needed an electronic focuser to eliminate having to use manual focus. This would avoid further wear and possible future problems. However, I also wanted an electronic focuser so that I could lock the primary mirror of the 16" telescope and thereby eliminate mirror movement as a possible source of spectral error. For those who are not familiar with this (poor?) design feature of the Meade telescope, the mirror lock is the upper knob at the back of the OTA in Figure 3.

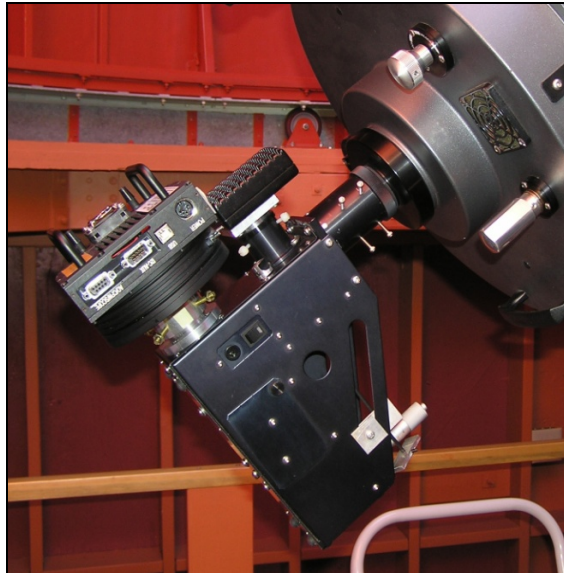


Figure 3.

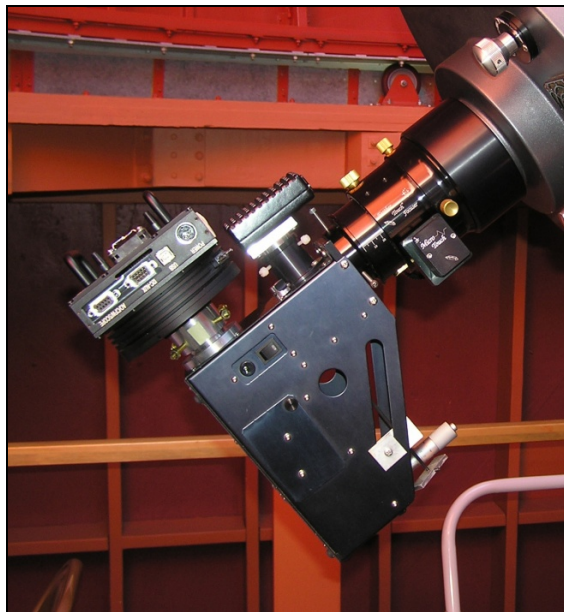


Figure 4.

Some of the focusers I found on the internet that could handle a heavy load were Crayford types. These were fairly expensive but aside from the cost, I do not like the Crayford design because not only is there still the possibility of slippage even though they are designed to handle a heavy load (the manufacturers of the Crayfords admit this), the intense pressure the roller(s) has(have) to be under does not appeal to me. I came across Starlight Instruments which makes one that is relatively inexpensive and uses a helical gear. A helical gear will not slip and it is not under intense pressure. I bought the Feathertouch FTF

3015-B-A, and the add on developed by Starizona which gives it the electronic focus capability. The electronic focus developed by Starizona works great. Figure 4 shows what the focuser looks like with the instrument package attached.

The Starlight focuser is a real work of art, but I discovered a number of problems. One is that the spectrograph still wobbled in the draw tube eyepiece holder, like it did in the Meade focuser, even though I tightened down the spectrograph nose as much as I dared. To correct this problem I removed the compression ring from the draw tube eyepiece holder and replaced the thumb screws with tapered allen head stainless steel screws. Then I drilled three tapered holes near the base of the nose of the spectrograph. These tapered holes are offset so that when the screws are tightened the front plate of the spectrograph is pulled against the back surface of the focuser, thereby, eliminating all wobble. Figure 5 shows the modification I made to the nose of the spectrograph.

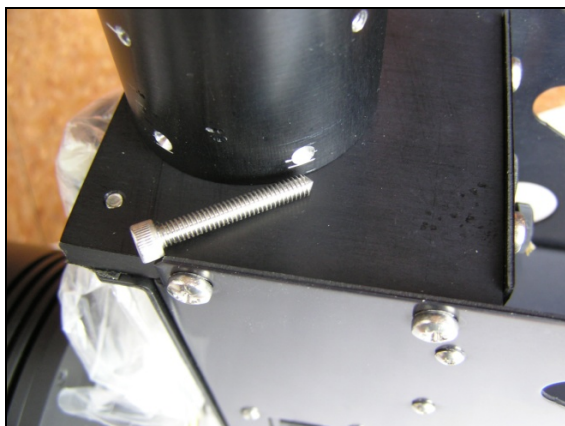


Figure 5.

After eliminating this problem, I discovered that, just as with the Meade focuser, the draw tube wobbles in its housing. However, this wobble can be eliminated by tightening a (one) brass knob (the 2nd brass knob from the back of the telescope in Figure 4). I thought I would have to loosen this knob each time I focus, but according to Starlight I can tighten the knob to the point where it just eliminates wobble without damaging the focuser, or the Starizona focus motor.

Another problem is the mechanism to lock the focuser in a desired rotational position around the optical axis. It is fixed in place by finger tightening three large brass knobs (two of them can be seen in Figure 4). However, because the brass knobs are nylon tipped, accidentally bumping the spectrograph can cause the rotational setting to shift. When this

happens I have to again reset the rotational orientation of the spectrograph.

Finally, I am not happy about weight of the Starlight focuser. The aluminum adapter I machined (Figure 2) to replace the Meade electronic focuser weighs only 2/3 of a lb. The Starlight focuser weighs an additional four lbs, a 7-fold increase in weight. To make matters even worse, the focuser adds another 3" or so to the back of the OTA and this increases the moment of the instrument package. This means more counterbalance weight is needed. The adapter I machined is the best solution to the wobble, but, of course, it doesn't have electronic focus.

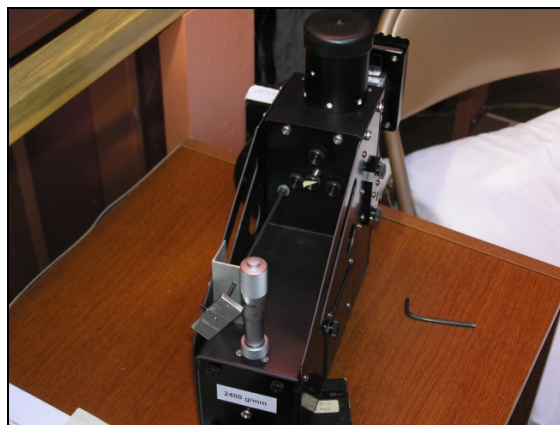


Figure 6.

There are a few modifications I made which may have improved the calibration accuracy of the target spectrum. To calibrate the target spectrum, one needs a calibration spectrum immediately before and after the acquisition of the target spectrum. The calibration spectrum in the LHIRES III is obtained from a neon lamp built into the spectrograph. To get a calibration spectrum requires manually positioning the neon lamp over the slit by turning a knob at the front of the spectrograph. This mechanical act can upset the mechanical stability of the spectrograph and result in a shift of the calibration spectrum relative to the target spectrum. To reduce this potential affect, some owners of the LHIRES have added a stepper motor to turn the knob. I do not have the electronics capability to do this, but I noticed that I could more easily move the lamp from the back of the spectrograph with an allen wrench. Figure 6 shows a permanently mounted allen wrench for this purpose.

Another change I made was replacing the adapters that attach the ST-8 camera to the spectrograph. I felt the ones that came with the unit were too light duty with too many treaded parts and so I machined my own. The machined adapters are the bare (non-anodized) aluminum parts in Figure 7.

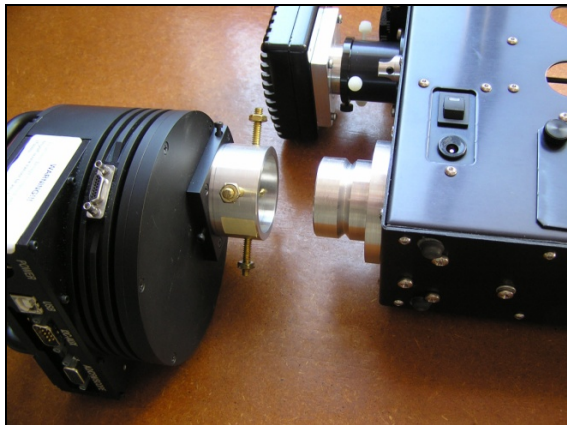


Figure 7.

Figure 7 shows the camera is attached to the spectrograph with four tapered #10 brass screws. The v-groove was offset a small amount so that when the brass screws are tightened they push the male adapter (the adapter attached to the spectrograph) against the back of the female adapter (the adapter attached to the camera), thus eliminating any possibility of movement.

I do not know if the changes I made improved calibration accuracy but I think they have. It has been stated in the Spectro-L discussion group (Spectro-L@yahoo.com) that one can at best expect no more than a 0.1 of an Angstrom accuracy using the internal neon lamp. I am getting better than this. Out

of a sample of 51 spectra only 9 were off by more 0.05 A, and 33 were only off by no more than 0.03A, the rest falling in between 0.03A and 0.05A.

3. Software

I use CCDSOFT to image the spectrum and do the dark subtraction. Currently, I am using an old version of IRIS, ver 5.57, to reduce the spectra. This includes flipping the spectra so the blue is on the left side, making tilt and slant corrections, removing the sky background, and optimizing the final spectrum for input into VSPEC. These reductions in IRIS involve much more than the quick description just given. I use Audela to get the Gaussian line center estimates of the neon spectral lines (the calibration lines). I use VSPEC to calibrate the target spectrum (usually a multiline, i.e., at least three neon lines, calibration using the neon line center estimates from Audela), correcting the spectrum for instrumental response, fine tuning the calibration with telluric lines, removing the telluric lines after fine tuning, and performing a heliocentric correction. I keep a record in an EXCEL spreadsheet (Figure 8) of all my steps in reducing a spectrum so that I can reproduce a reduction if needed. The final step in VSPEC is to create a TXT file of the fully processed, i.e., reduced, spectrum. The .txt file is input into SPSS programs I write for analysis, graphing, computing equivalent widths, and other statistics. SPSS has very good pro-

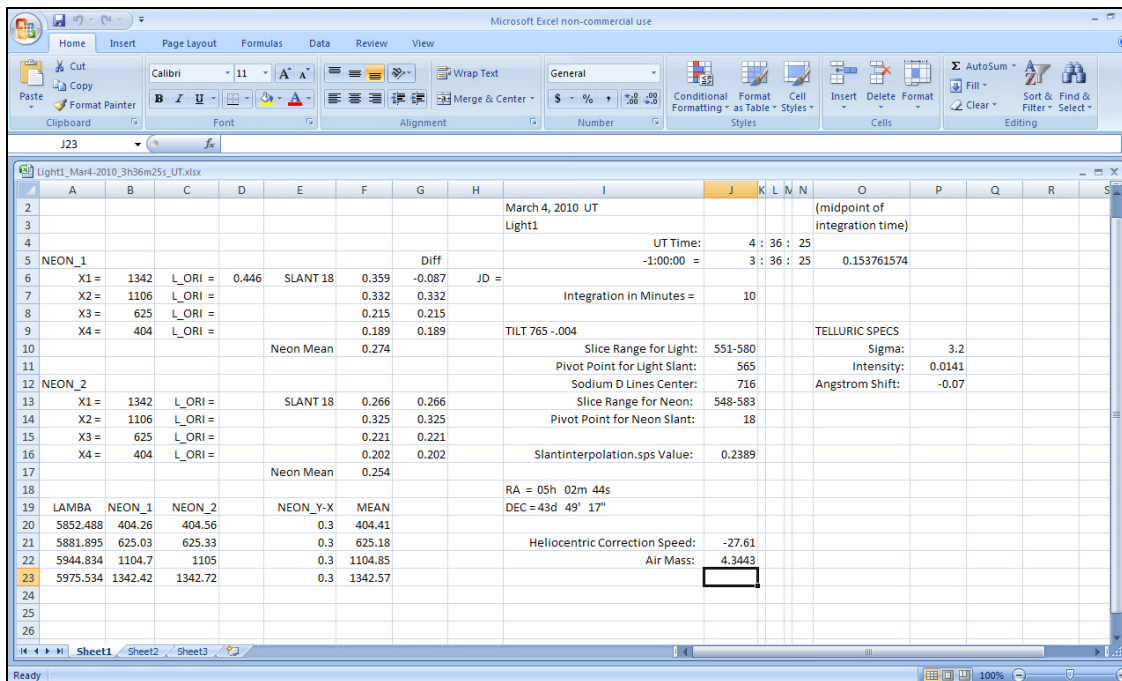


Figure 8.

gramming and statistical capabilities. I have been using SPSS for over 25 years and so I am knowledgeable of its capabilities. IRIS and VSPEC are freeware. SPSS is not but I purchased it at a good price years ago.

4. Data Analysis

I use an SPSS computer program I wrote to estimate equivalent width (EW). The EW estimation method I use is the one I developed as described in the SAS Newsletter Vol 9, No 2. To briefly describe it, the first step is to identify those parts of the spectrum that are obviously not noise (such as absorption and emission lines). Once these are identified their intensity values are set to system missing in the SPSS program. What is left is considered to be noise for estimating a continuum.

The second step is to select a range of noise values around the line (whose EW is being estimated) to estimate a continuum with a polynomial least squares regression model. Generally, I have found it is not a good idea to use a large range on either side of a line. Why it is not a good idea is shown in Figure 9.

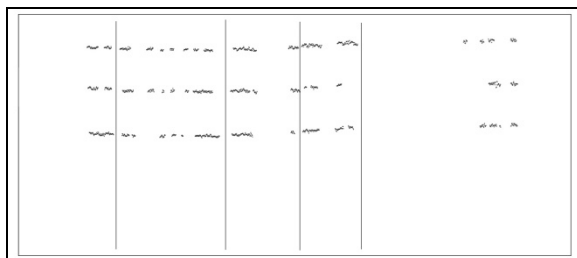


Figure 9.

Figure 9 are plots of what were deemed to be noise for three spectra. The spectra were taken within a half hour of each other, all had the same integration time and camera cooling, and each one was integrated on a different area of the CCD chip. To estimate the continuum for the Sodium D lines (the vacant area between the 2nd and 3rd lines from the left) one could use the entire range of the spectrum. However, upon a study of the graph it can be seen minor differences exist in the noise levels prior to the first line, and the noise values are quite variable between the third and fourth lines (from the left) in intensity and shape. Also, the group of noise values at the ex-

treme right end of the graph could potentially have a large regression model leveraging effect and, thereby, result in a poor estimate of a Sodium D lines continuum. Consequently, for estimating a continuum for the Sodium D lines in this example, I would use the noise values between the 2nd and 3rd lines. By extension, it should be apparent that, generally, it would not be a good idea to use the same range of data to estimate one continuum for two or more lines (one exception being the Sodium D lines).

Once a continuum is estimated I determine the beginning and end points of a line (from an overlay graph of the estimated continuum and actual data points) and then run the complete SPSS program to get an output of equivalent widths and 95% confidence limits.

As can be seen from an example output titled "Equivalent Width Data for Epsilon Aurigae", my SPSS program can estimate the EW for up to four lines (the 5853A line, the two Na D lines, and the 5978A line) at a time. I could modify my program to do more lines if the need ever arises.

I like this method for computing EW because it gives me greater flexibility than exists in some spectroscopic software, it has greater statistical validity, and it can be better defended than some of the other simpler methods. However, all these presumed advantages may be swamped out by a small degree of subjectivity in telluric line removal, the somewhat subjective determination of the beginning and end of a line, other random effects near a line that can affect continuum estimation, improper (or no) flat fielding, the resolution of the LHIREs, and the fact that the continuum estimate, at the non-professional level, is usually somewhat a guess to begin with. It may be some of the simpler and quicker methods to compute equivalent width may produce equally good estimates. This is something I have not looked into.

I have looked at many spectra for the same star taken on the same night on different parts of the CCD chip (with equal integration times and cooling temperatures) and for the most part the shapes of the spectral profiles agree very close with one another. At times there are some minor disagreements. I am not sure what the causes of these are, but it could reflect the need to take flat fields. Currently, I have the slit on my spectrograph set at 22 microns, which is very narrow. Because of this small size I was not

Line	yyyy	m	d	Time	Min	EW	Max	Start	End	Å/pix	S.D.	All	Miss
5853A	2010	3	4	03:36:25	0.0422	0.0560	0.0698	416	432	0.132	2325.54	360	152
Na D1	2010	3	4	03:36:25	1.2957	1.3247	1.3536	684	715	0.132	2418.27	336	176
Na D2	2010	3	4	03:36:25	1.2032	1.2331	1.2631	729	761	0.132	2418.27	336	176
5978A	2010	3	4	03:36:25	0.0679	0.0836	0.0993	1364	1381	0.132	2291.98	84	46

Table I. Equivalent width data for epsilon Aurigae. The *Min/Max* values are the lower and upper limits for EW. *Start/End* are the line start/end values. *All* gives the number of all cases while *Miss* gives the number of missing cases.

able to get enough light through the spectrograph, in a reasonable integration time, for a flat with two 90 watt Halogen lamps illuminating a white surface. However, even without a flat correction nearly all spectra taken on the same night are generally in very good agreement with each other and I am getting good results. I will continue to work on getting a flat but it seems there is some contention, at least among some of the non-professional spectroscopists, as to whether a flat is necessary and whether a flat could introduce unwanted effects by subtracting an effect that is not present under the actual conditions of getting a star spectrum.

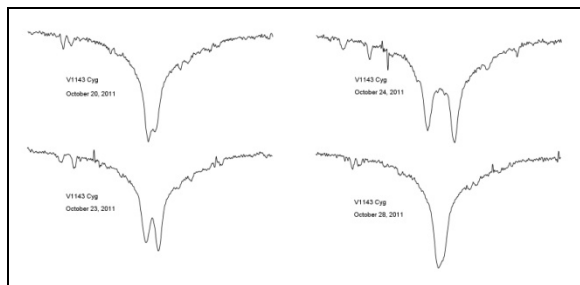


Figure 10.

A big problem is guiding on faint stars, but even on brighter stars it is hard for me to guide accurately enough to get a tight bright line. I have tried a number of guiding software that support the Meade DSI I camera. Meade's Envisage software is unstable and frequently crashes. MaximDL worked good but I could not justify spending \$565 for a package that will only be used for guiding. I tried Astroart but I was unable to center the guide star (which is also the target star) over the slit. I am currently using PHD and it seems to work okay but on a faint star I frequently get a message saying the signal to noise is low. A lot of times when this happens I lose guiding. I am restricted to guiding software that support the Meade DSI cameras which is a problem. At some time in the future I will have to break down and get another, and better, guiding camera.

Now I would like to show some of the things that can be done with the LHIREs. Figure 10 are spectra I took of the binary V1143 Cyg. Because it is a 5.9 magnitude star, I had to integrate an hour with the 22 micron slit width, but even with an hour's integration time the peak intensity of the spectrum was still only about 5% of saturation. I was not happy with the spectra because I could see more noise in their profiles than I am used to seeing on much brighter stars like Epsilon Aurigae. However, Dr. Dirk Terrell analyzed them, came up with a velocity estimate of 131 km/sec, and said this shows I can do pretty good work with the system I have. This favorable assess-

ment amazed me, because, as I said, I was only reaching about 5% of saturation.

Figure 11 is the classic P Cygni profile of P Cyni itself. The noise in this profile is unbelievably low. I think this is partly the result of a scale effect caused by the emission line being over four times the magnitude of the continuum level.

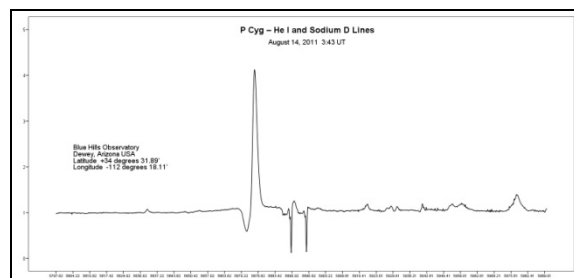


Figure 11.

Figures 12 and 13 are two graphs in press for the special edition the JAAVSO on the Epsilon Aurigae campaign.

In Figure 12, a graph of equivalent widths of the Na D1 line, a number of things can be seen. First, the equivalent widths are at a low point at mid-eclipse. This is expected because there is less disk material at this point that contributes to the absorption line. After mid-eclipse the EW's gradually increase until a high point is reached at 3rd contact. This again is expected. After 3rd contact there is a decline, and this is expected since the disk is now on its way to clearing the primary star. Far after 4th contact, when the primary star should be clear of the disk, the EW's are still significantly non-zero. This indicates the disk material does not end at fourth contact, but continues significantly further.

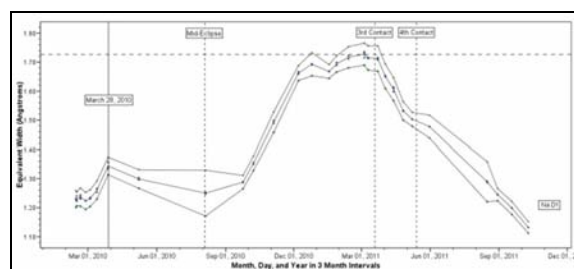


Figure 12.

The low point prior to March 28, 2010 is hypothesized to be either the result of a void in the disk, or a ring structure. Evidence for the latter has been seen by some astronomers (Leadbeater *et al.*, 2010, Seebode *et al.*, 2011). The sharp downturn in radial velocities in Figure 13 also confirms this interpretation.

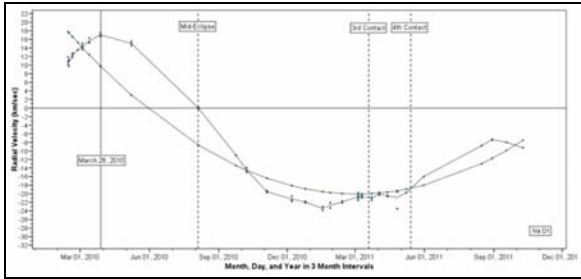


Figure 13.

The shape of the radial velocity (Figure 13) curve from about May 6, 2010 to about November 1, 2010 is what is expected of a disk with a central clearing around a primary object. The predicted date of mid-eclipse was August 4, 2010, although this will probably change as more data comes in. Based on the two Sodium D lines and taking into account that the Epsilon Aurigae system is moving toward Earth at about 2.5 km/sec, I came up with a mid-eclipse date of August 17, 2010. Finally, the continuation of a significant non-zero radial velocity after 4th contact supports the equivalent width interpretation that the disk continues well after 4th contact.

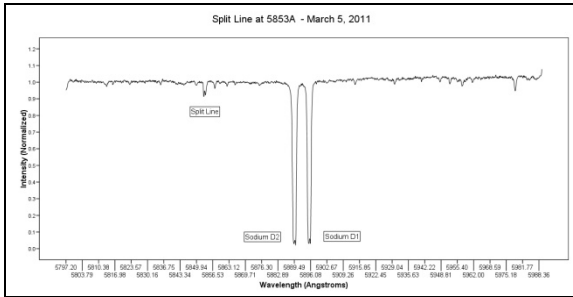


Figure 14.

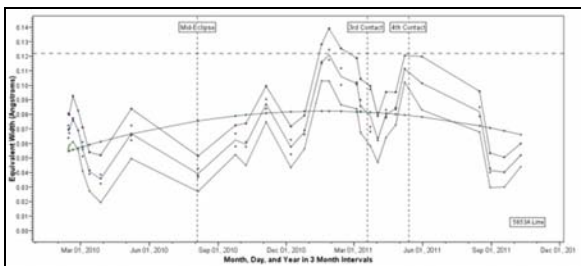


Figure 15.

One thing I observed during my participation in the Epsilon Aurigae campaign was a split line at about 5853 Angstroms that can be seen in Figure 14. Figure 15 is an equivalent width graph of the 5853A line. From Figure 15 the split line event is estimated to start on January 27, 2011 and end on May 8, 2011 which gives a duration of 101 days.

Now I want to show some stuff that is not in the JAAVSO paper. I came up with four different methods to estimate line centers for the D2 and D1 lines. There were two categories. One was based on the beginning and end points of the line that were used to compute equivalent width. The other was a visual estimate in VSPEC of the beginning and end of a line. Within each category there were two line estimation methods: the wavelength center of the line barycenter, and the wavelength center of the VSPEC Gaussian fit to a line. Figure 16 contains four graphs, one for each of the four different methods of estimating line center, of the wavelength difference between the D1 and D2 lines vs. time.

Based on my understanding of quantum mechanics (which is very little), I would expect the separation between the two Sodium D lines to be constant. However, it can be seen that a second order polynomial model fits both Gaussian estimates, and a linear trend fits the visual-barycenter estimate. This indicates the separation between D2 and D1 is not constant but changes over time. However, a statistically significant curve could not be fit to the EW-barycenter estimate. This indicates the D lines separation is constant. Maybe some kind of line measurement bias is present in the other three estimates that result in a false change over time. The

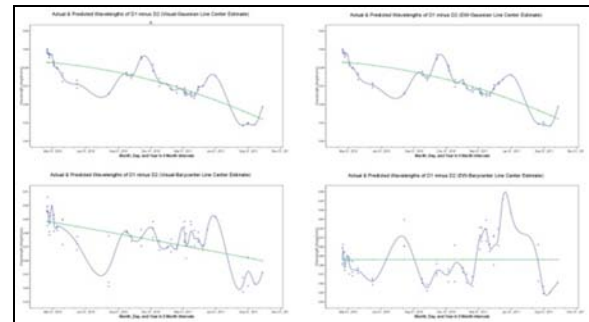


Figure 16.

Line	Method	Mean	Std Dev
Na D2	EW Barycenter	5889.79	0.3152
	EW Gaussian	5889.82	0.3033
	Visual Barycenter	5889.80	0.3028
	Visual Gaussian	5889.82	0.3032
Na D1	Barycenter	5895.77	0.3093
	EW Gaussian	5895.79	0.3084
	Visual Barycenter	5895.78	0.3072
	Visual Gaussian	5895.79	0.3085

Table II. Standard deviations of the line estimation methods.

EW-barycenter estimation method could be unbiased and be giving the correct relation, which is no relation, but it has the highest variance among all the methods. This higher variability could mean the EW-

barycenter estimate was just too variable to detect a small linear relation or for a bias to be seen.

I wanted to show this to demonstrate the care one has to exercise in interpreting results. More than likely the change over time shown in three of the methods is the result of a bias in line center estimation, but wouldn't it be something if I, with an LHIRES III spectrograph and a relatively inexpensive Meade telescope, discovered a major flaw in Quantum Mechanics? On the other hand, maybe there is a quantum mechanical explanation.

5. Conclusion

In conclusion, I have had a very good experience using the LHIRES III high resolution spectrograph. I think this may in part be because the seeing is pretty good at my observatory resulting in low spectral noise, I am in a desert area and so I do not have a major problem with telluric lines, my introduction to spectrometry was on a bright star (Epsilon Aurigae), because my introduction was on a bright star I was able to set the slit width near the Nyquist minimum to give me maximal resolution without adversely affecting integration time, and I have a good imaging camera, a Class I ST-8XME. Generally, it seems deviations from ideal seeing, ideal mechanical aspects, and ideal guiding has been very forgiving. If one reads all the very technical advice and very technical solutions to problems given in the Spectro-L discussion group one could quickly become overwhelmed and conclude spectroscopy is not for them. Maybe the best advice is to get good equipment (especially the imaging camera), just do it, and, at least at first, concentrate on the brighter stars.

6. References

Leadbeater, Robin; Stencel, Robert E. (2010). "Structure of the Disc of Epsilon Aurigae: Spectroscopic Observations of neutral Potassium during Eclipse Ingress." *arXiv:1003.3617v2* [astro-ph.SR].

Seebode, *et al.* (2011) "Ring-like Structures around Epsilon Aurigae Companion." 217th AAS Meeting, Poster Paper **257.08**.

Extremely Low-Cost Point-Source Spectrophotometry (ELCPSS)

John Beaver

*University of Wisconsin – Fox Valley
1478 Midway Rd.
Menasha, WI 54952
john.beaver@uwc.edu*

Charles Conger

*University of Wisconsin – Platteville
1478 Midway Rd
Menasha, WI 54952
congerc@uwplatt.edu*

Abstract

We describe preliminary tests of a low-cost method for obtaining, reducing and calibrating stellar spectra. Instead of a post-focus spectrometer, we use an inexpensive, low-dispersion objective grating made by printing onto acetate with a laser printer, coupled with a low-end digital SLR camera as the detector. Although originally intended for educational use, we consider the possibility of using this technique to obtain accurately-transformed B and V magnitudes of stars without the need of an expensive photometric filter and filter wheel system. The results of two nights of observations of several bright stars are presented. Future plans are presented for more tests using a wider range of gratings, telescopes and detectors, and more advanced observing techniques that are likely to produce higher-quality data. But we show that even the crude observing techniques used for the test data can produce calibrated B and V magnitudes. General methods for reducing and calibrating the data are described, and some of the educational uses for ELCPS are also considered.

1. Introduction

The usual method for taking spectra of stars and other astronomical objects is to use a telescope to gather and focus the light, and then allow the light to pass into a spectrograph attached to the eyepiece end of the telescope. The focused light passes through a slit, where it is dispersed by a diffraction grating into different wavelengths and then detected by a CCD array digital detector. A spectrograph such as this, even a relatively low-cost one, can be quite expensive for an individual amateur astronomer or even a high school or small-college astronomy program.

Extremely Low-Cost, Point-Source Spectrophotometry (ELCPSS) is an attempt to bring stellar spectrophotometry to those who otherwise would have little opportunity. We do this by using a simple low-dispersion diffraction grating, produced for almost nothing by printing a pattern of lines onto acetate with an ordinary laser printer. This grating is placed over the objective of a typical small amateur telescope and an ordinary low-end commercial digital SLR camera (DSLR) is used as the detector. Thus the entire telescope becomes the spectrograph, and all of the equipment is of the sort a typical small college,

high school or amateur astronomer may already own (Beaver and Robert, 2011a).

These slitless spectra produced by ELCPS are of rather low resolution, since the spectral resolution is limited by the observed size of the star image, and this is degraded by the acetate base of the objective grating itself. The point of ELCPS is not to produce research-quality spectra in and of themselves. Rather, we hope to inexpensively obtain low-resolution spectra that are nonetheless fully wavelength and flux-calibrated, and using much of the same procedure as at any major observatory. This means ELCPS has a fairly clear educational use. But we also show that ELCPS may be useful as a roundabout but inexpensive method for obtaining calibrated BV (and perhaps BVR) stellar magnitudes.

Here we present the results of two nights of ELCPS data. We demonstrate proof of concept regarding using it as a back door to stellar broadband photometry, and we consider its potential as an educational tool. We also lay out a strategy for making the rather complex data reduction and calibration process more accessible to the uninitiated. Future work to be done is outlined, and collaborations are solicited.

2. Useful Numerical Relations for Objective-Grating Spectroscopy

For objective-grating spectroscopy, the scale of the spectrum on the detector (in angstroms per pixel, for example) is set only by the line spacing of the grating, the focal length of the telescope and the physical size of the detector pixels. These data, combined with the number of pixels on the detector in the dispersion direction, then fix the possible range of wavelengths that can be imaged for a particular combination of grating, telescope and detector. We define the following quantities, with units chosen to give typical values near unity:

- d grating spacing, in hundredths of an inch.
- m order number of the spectrum.
- p pixel size on the detector, in microns.
- f focal length of the telescope, in meters.

With these definitions, a given number, N , of pixels in the dispersion direction, corresponds to a given range of wavelength in Angstroms, $\Delta\lambda$, given by:

$$\Delta\lambda = 2.540 \frac{d p N}{m F} \quad (1)$$

As an example, for the instrumentation used in this paper the pixel size was 7.88 micron, the grating was 200 lines/inch ($d = 0.5$) and the focal length of the telescope was 2.0 m. And so for this case $\Delta\lambda N = 5.0$ Angstroms/pixel for the first order spectrum ($m = 1$). As another example, to get everything from the direct image of the star ($m = 0$) to 7000 Angstroms in the first order onto the detector, solving Equation 1 for N shows that about 1400 pixels are needed for this combination of grating, detector and telescope.

The lack of a slit ties the spectral resolution directly to the angular resolution. For a given angular resolution element, θ_R , in arcseconds, the corresponding wavelength resolution element, λ_R , in Angstroms, is given by:

$$\lambda_R = 12.3 \frac{d \theta_R}{m} \quad (2)$$

Since θ_R is set by the seeing, tracking, and especially the degrading of the image by the acetate grating, this means that one would want the smallest value of d possible, so as to maximize the wavelength resolution (i.e. minimize the size of the resolution element), even if this means the data is oversampled. But of course we also want d chosen such that the combination of telescope focal length and detector size puts the desired wavelength range onto the de-

tor. For the data presented here, we estimate the size of the direct star image through the grating to have been about 10 arcsecond, and this corresponds to a spectral resolution element of about 60 Angstrom for our grating ($d = 0.5$).

3. Observations

The observations presented here were carried out on two nights, 2010 June 7 (Night 1) and 2010 October 1 (Night 2). All observations were made from Appleton, Wisconsin, with moderately light-polluted skies (naked-eye limit $m = 4.5$). Both nights were judged to be photometric. The observing log for the observations is given in Table I. For reasons discussed below, multiple short exposures were combined to give the total exposure times listed in Table I. The individual exposures were all between 1 and 30 seconds. Preliminary results from Night 1 were previously published (Beaver and Robert, 2011a; Beaver and Robert, 2011b), but errors in the reduction and calibration process have been corrected for the results presented here.

Star	Night	X	Exp. (s)
α Lyr	1	1.49	12
γ UMa	1	1.10	20
γ Dra	1	1.22	68
α Lyr	2	1.09	20
α Lyr	2	1.17	22
58 Aql	2	1.44	210
β Cyg	2	1.10	60
ζ Her	2	1.67	105

Table I. The observing log for the stars observed for this paper.

For a post-focus slit spectrograph the spectrum automatically appears at the same location on the detector each time. But with an objective-grating, the spectrum could in principal appear anywhere on the detector, depending on the pointing of the telescope. And so if one is to be able to relate a given position in the observed spectrum to wavelength, either there must be a reference for wavelength in the image itself or there must be a way to exactly repeat the positioning of the star image in the telescope (and thus the location of the spectrum) from frame to frame.

Thus there are two obvious approaches. For what we call zero-order referenced (ZOR) spectra, we use the zero-order spectrum (the same as the direct image of the star) as a wavelength reference for each frame

separately. Thus, for ZOR spectra, both the zero and first orders must be present on each frame, but there is no need to ensure that each exposure is taken with the same positioning of the object. Since the zero-order, direct image of the star is much more intense than the first-order spectrum, short exposures must be used so as to not overly saturate the zero-order spectrum. With proper guiding, however, one could in principal take a series of exposures for each object – long exposures to record the first-order spectrum, and short exposures to accurately determine the location of the zero-order spectrum (although one would still need to worry about scattered light and blooming from the saturated pixels).

The other approach, zero-order guided (ZOG), is to guide directly on the zero-order spectrum during the exposure, perhaps with an off-axis guider or by using the separate guide chip included with some astronomical CCD cameras. The ZOG technique would seem to have a big advantage over ZOR spectra, as the much brighter zero-order spectrum is out of the frame. But ZOG gives fewer choices of dispersion, given a particular off-axis guiding arrangement. For example, if one is using a fixed-prism off-axis guider, then the correct grating to put the desired maximum wavelength at the far edge of the detector will not necessarily put the desired minimum wavelength at the near edge. Put another way, a choice of grating that places the desired wavelength range across the detector may not at the same time put the direct image of the star in the guiding field.

For the spectra presented here, we have used the ZOR technique, in part to first test the efficacy of the crudest and lowest-cost observing techniques. A Celestron 8 (with uncoated corrector plate) was used with a 200 line/inch objective grating and a Nikon D40 SLR shooting in RAW mode (with noise reduction on) at ISO 1600. Exposure times were limited by the tracking of the (unguided) telescope and the fact that we could not too-badly saturate the zero-order spectra, as they are needed as a reference for the wavelength calibration.

We took the standard array of basic CCD reduction frames, including bias, dark and flat field. Flat fielding was accomplished by means of observations of a white screen illuminated by an old slide projector. We also used twilight sky flats to produce a final illumination correction. These frames were all taken with the objective grating in place. Since the sources of light for the flat field frames were diffuse over the entire field, so too was the spectrum produced, the zero and first order spectra mixing over the entirety of the image so as to produce images very much as if the grating were not present at all. Dark frames were taken implicitly for the longer exposures, as it is a property of the “noise reduction” feature of this par-

ticular DSLR to take a dark frame immediately after the exposure and to automatically subtract it. This feature can be turned off, but it was left on for these data. The built-in noise reduction also performs some median filtering, and this would have been a concern except that the spectral data is grossly oversampled in wavelength, and so this could not have removed “real” features of the spectra.

In addition to these basic CCD imaging calibration frames, we have taken others related directly to the calibration of the spectra. For wavelength calibration we observed a low-pressure sodium light, occluded by a screen except for a small pinhole, placed about 30 m from the telescope. A similar arrangement was used to make an artificial point source of a 300-W, 3100-K color-temperature quartz lamp. This was needed to flatten the spectra somewhat in order to better accomplish the final flux calibration.

4. Data Reduction and Calibration

The RAW Nikon images were extracted to FITS format (Wells *et al.*, 1981) with the low-cost proprietary software package ImageTOOLSca (<http://arnholm.org/astro/software/ImageTOOLSca/>). This program effectively converts many consumer digital RAW formats to FITS, and writes a proper header with standard fields such as exposure time and date and time of observation. The data were extracted summing the three separate RGB mask images to single-band, 16-bit FITS images.

We used IRAF (Tody *et al.*, 1986; Tody *et al.*, 1993) to reduce and calibrate the data. The basic image reductions, incorporating bad-pixel repair, bias subtraction, flat-fielding (using the white-screen flats), and illumination correction (using twilight flats), were carried out in the usual way with the IRAF task CCDPROC.

The 1-d spectra were extracted from each 2-d image using the APEXTRACT package of IRAF, which fits a function to a trace of the spectrum on the 2-d image. Care was taken to use an aperture large enough to account for differences in tracking and focus, except for the extractions of the double star β Cyg, which required a smaller extraction aperture than we would have liked.

A dispersion in Angstrom/pixel was determined by measuring the separation in pixels of the zero and first order spectrum of the sole line in the observed sodium spectrum. This dispersion was then applied to the extracted 1-d spectra by directly editing the image headers. The zero-point for the wavelength calibration was determined separately for each spectrum using the interactive IRAF task SPLOT. Only a simple linear dispersion relation was applied, since for

ZOR spectra nothing else would be meaningful given the fact that the individual spectra were at different locations on the detector.

A multi-order cubic spline was fit to the quartz lamp spectrum and all of the stellar spectra were divided by this spectrum in order to remove medium-scale variations before attempting flux calibration. This greatly facilitates the process of flux calibration because the instrumentation introduces medium-scale features in the spectrum due to, for example, the RGB pixel mask and interference coatings on the intervening optics (for example, the IR and UV blocking filter Nikon places over the CCD).

Flux calibration was performed with the IRAF tasks STANDARD, SENSFUNC and CALBRATE, using α Lyr as the sole spectrophotometric standard. For the second night, only the second observation of α Lyr was used for the calibration, as the first observation was inconsistent in overall scaling. This was the first observation of the night and the observing log noted that dewing may have been a problem for that observation (and this is consistent with the measured flux level being too low for that observation). No extinction curve was determined from the data; instead the mean extinction curve for KPNO was applied.

5. Results

We compare our observed, calibrated spectra to catalog spectra from the STScI HST Calibration Database Systems (CDBS) Stellar Spectral Atlases (STScI, 2012a). Figure 1 shows, plotted along with a Kurucz model-atmosphere α Lyr spectrum (Colina, 1995), the three α Lyr observations and the observations of γ Uma, also an A0V star. Figure 2 shows the observed spectrum of 58 Aql, along with a comparison spectrum of that star from the Bruzual-Persson-Gunn-Stryker (BPGS) Atlas of the CDBS. Figure 3 shows the observed spectra of β Cyg A and B, along with CDBS spectra of stars of similar spectral type. Figure 4 shows the observed spectrum of ζ Her, along with a spectrum of that star from the Wisconsin Halfwave Polarimeter (HPOL), retrieved from <http://archive.stsci.edu>, and Figure 5 shows the observed spectrum of γ Dra, compared to a BPGS catalog spectrum of a star of similar spectral type. The CDBS spectra were all obtained via the STScI Specview software package (STScI, 2012b). Finally, Figure 6 shows the flux-calibrated spectrum of the observed quartz lamp, compared to a 2900 K blackbody, in rough agreement with the rated color temperature of 3100 K for the bulb used.

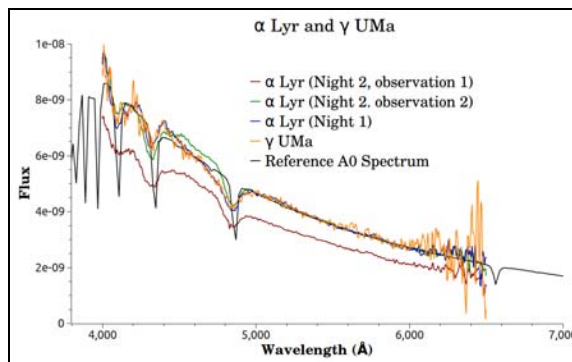


Figure 1: A Kurucz model atmosphere of α Lyr, along with our three α Lyr observations and the A0V star γ UMa.

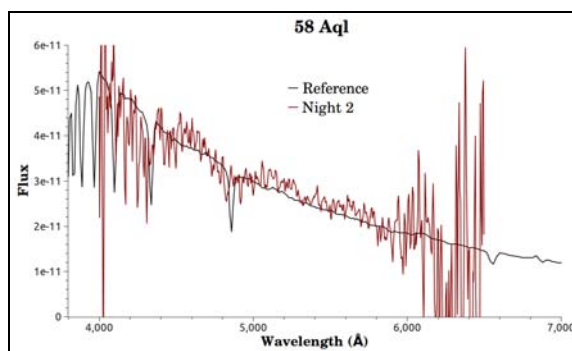


Figure 2: Our observed spectrum of 58 Aql, along with a comparison spectrum of that star from the BPGS atlas.

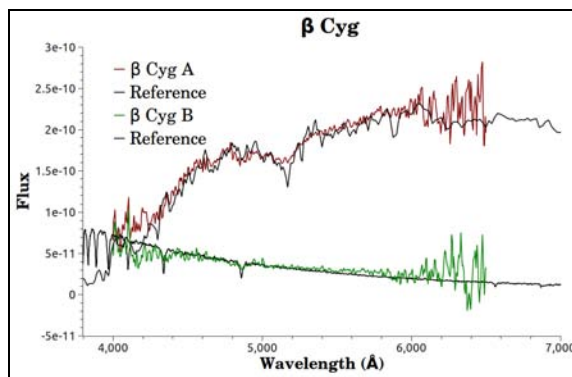


Figure 3: Our observed spectra of β Cyg A and B, along with CDBS spectra of stars of similar spectral type.

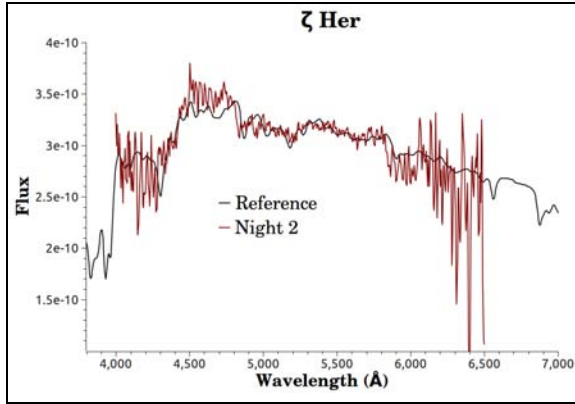


Figure 4: Our observed spectrum of ζ Her along with a spectrum of that star from the Wisconsin Halfwave Polarimeter.

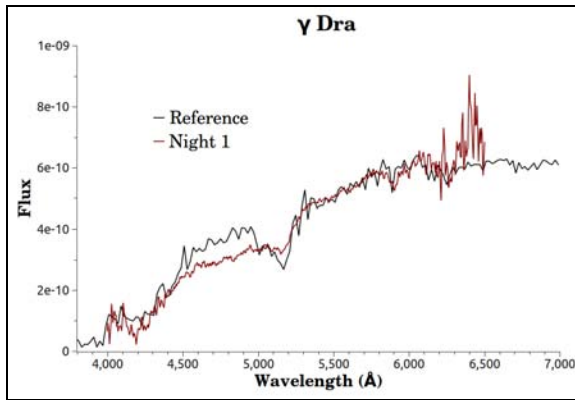


Figure 5: Our observed spectrum of γ Dra, compared to a BPGS catalog spectrum of a star of similar spectral type.

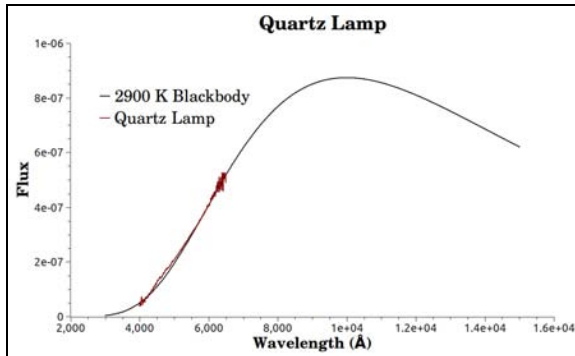


Figure 6: The flux-calibrated spectrum of the observed quartz lamp, compared to a 2900 K blackbody.

We note that α Lyr was used as the spectrophotometric standard for both nights, and so the agreement between these spectra and the catalog spectrum is unremarkable. The first α Lyr spectrum from Night 1, however, was not used for the flux calibration, and so its agreement (or lack thereof) is meaningful. This spectrum shows good relative flux calibration, but a

noticeable error in absolute calibration, appearing too faint by the equivalent of a few tenths of a magnitude. This is not surprising as the observing log for that particular observation reports “dewing problem?” The rest of the observed spectra agree well with the comparison spectra, with the exception of β Cyg B, which shows a noticeable error in relative flux calibration, appearing too red. We suspect this may be due to the difficulty in extracting this spectrum without contamination from its much brighter close neighbor, β Cyg A.

With the exception of α Lyr, the comparison spectra presented in these graphs have all had a scale factor applied to best match the observed spectra. This is because the comparison spectra we found had only relative flux calibration, and in some cases we could only find comparison spectra of the same spectral class (but not the same star). We will see in the next section, however, that we have good reason to believe the absolute flux calibrations of the spectra are reasonable, with the exceptions of β Cyg B and the first Night-2 α Lyr spectrum, as previously noted.

6. ELCPSS as a Back-Door to Broad-Band Photometry

Broad-band B and V filter photometry takes complex spectral information over a range of nearly 3000 Angstrom, and compresses it into just two numbers. The success of broad-band filter photometry depends on the spectral response of the instrument-detector system, and the spectrum of the observed source, being similar enough to that which set up the standard system. If not, then a one-to-one correspondence between the instrumental and standard magnitudes may not be obtainable.

Even a low-resolution spectrum contains far more information than a set of broad-band photometric measurements. In particular, the problems of flux calibration and extinction correction for spectra are in many ways simpler than the corresponding problems of transforming instrumental broad-band magnitudes to standard magnitudes.

Thus once a spectrum is accurately wavelength and flux calibrated, a standard magnitude can be extracted simply by convolving the appropriate magnitude bandpass function with the spectrum.

We have done this for the spectra here presented using the IRAF task SBANDS, and the filter profiles for B and V from Ažusienis and Straižys (1969). These profiles are normalized, and so we used the filter extractions of our standard star (α Lyr) to set the zero points for the magnitudes. Table II shows the results of these extracted magnitudes, as well as the values from SIMBAD for comparison. As can be

seen, even with only one observation of a single standard star and the use of a mean extinction curve for a different site, the values are all to within 0.2 magnitude in V and 0.13 in B-V, except for β Cyg B and the first α Lyr spectrum from Night 2, as already noted.

Star	X	V	V'	B-V	B'-V'
α Lyr	1.09	0.27	0.03	0.01	0.00
58 Aql	1.44	5.45	5.63	0.18	0.08
ζ Her	1.67	2.71	2.80	0.69	0.63
γ Dra	1.22	2.23	2.23	1.65	1.52
γ UMa	1.10	2.38	2.43	0.01	0.04
β Cyg A	1.10	3.20	3.09	1.19	1.09
β Cyg B	1.10	5.23	5.09	0.16	-0.06

Table II. The extracted V and B-V magnitudes for the program stars, compared to the values from SIMBAD (the primed columns).

In principal, one should be able to do much better by adopting a hybrid technique. Instead of treating these extracted magnitudes as the final values, think of them instead as raw instrumental magnitudes for a program of broad-band photometry that includes observations of broad-band photometric standards as well as the spectrophotometric standards used for the spectroscopic flux calibrations.

Even using one spectrophotometric standard star and a generic mean extinction curve to establish the calibration, the extracted magnitudes should still be closer to the standard system than many detector-filter-instrument combinations in use. Thus one could in principal use ELCPSS to observe a regular program of photometric standards in order to determine accurate standard magnitudes from these almost-calibrated extractions. The extracted magnitudes should transform very smoothly to the standard system since they are almost there to begin with.

This would also solve the problem of a relative lack of bright spectrophotometric standards (as compared to broad-band photometric standards), thus allowing ELCPSS to be useful for differential photometry.

7. Educational Uses of ECLPSS

Both the process of carrying out ELCPSS and the calibrated spectra that result can be of educational use. We choose to illustrate this with an example. Although we present this as a hypothetical case, we are attempting to actually carry out much of this at the University of Wisconsin – Fox Valley, a small two-year campus with a primary mission of transfer

to one of the four-year campuses of the University of Wisconsin system.

A beginning astronomy major starts a project to record and calibrate ECLPSS spectra, with the goal of compiling an atlas of stellar spectra. Some of the spectral types have already been recorded by a student from the previous year. The current student adds to the previous work, getting spectra of multiple stars for some spectral types. In the process, she has to plan and execute an observing run, and then reduce and calibrate the data with IRAF using a pre-configured virtual machine environment set up especially for this purpose (see Section 8). Although all of this is done with modest equipment, the basic observing and data reduction techniques and the software used are all likely to be similar to what she will eventually use in graduate school.

Although the data themselves may not contribute directly to basic research, the results still have a purpose beyond that of a mere student exercise. This is because the spectra are to be used for introducing the concept of spectral classification to the beginning Survey of Astronomy courses for non-science majors. Instead of the students learning about stellar spectra from examples in a textbook or on the Internet, obtained by a process to which the students have no direct connection, they are presented with data obtained locally by one or more of their peers.

In fact, the astronomy major makes a presentation to the class, explaining how the spectra were taken, and the actual telescope used is set up for the students. The Survey of Astronomy students gain a learning experience that has a visible and immediate connection to their experience, and the astronomy major is motivated by contributing to their learning with data she gathered herself. This is “service learning” in the true sense of the term.

8. Facilitating the Reduction and Calibration Process

Since the goal of ELCPSS is to make spectrophotometry more accessible, the complex process of reducing and calibrating the spectra is a concern. To address this, we have developed a virtual machine (VM) with an open-source operating system (Ubuntu), with all of the necessary software (also free and open-source) pre-configured and including documentation and tutorials, for reducing and calibrating ELCPSS spectra, along with other common astronomical research projects (Beaver, 2012). The goal is to provide a self-contained research-computing environment that can be shared between users, thus sidestepping for beginners the difficult

process of establishing such a computing environment from scratch.

Since the virtual machines can be portable and cross-platform, individual VMs can be customized for particular combinations of projects and users. We see this, then as a key component to making ELCPSS practical and useful. For example, the coauthor of this paper had no prior training in astronomy before beginning this project, and he learned much of the process via a virtual machine specifically developed for this task.

9. Extending the Wavelength Range

The usable wavelength range for the current set of observations is from 4000-6500 Angstrom. The short wavelength cutoff is mostly from the small amount of light output at short wavelengths by the spectral flat-fielding lamp used (see above), but also from absorption by the corrector plate and the band-pass filter built into the CCD camera.

The long wavelength cutoff is mostly due to the IR blocking properties of the CCD bandpass filter, and it is possible to have this filter removed and replaced with a broad-spectrum window, extending the spectral response out to much longer wavelengths. This would possibly allow for extraction of the R-band as well as B and V.

The traditional complication of near-IR spectroscopy is that a diffraction grating produces a second-order short-wavelength spectrum that overlaps the first-order, long-wavelength spectrum. The usual method of dealing with this is to take a second spectrum through an order-separating filter that blocks the short-wavelength first-order spectrum. Since the point of ELCPSS is that it is simple and low-cost, the introduction of a filter-wheel mechanism and a specialized order-separating filter is counter to the goals of the project.

There may be another approach however. Since the spacing of the lines in the grating is relatively large compared to a traditional grating, it may be possible to execute control not only over the spacing of the lines, but also over their actual transmission profile. This raises the possibility of making a grating that produces no significant second-order spectrum in the first place, thus eliminating the need for an order-separating filter and allowing for one to record a spectrum from 3500-1050 Angstrom in one exposure. Thus one could in principal obtain BVR magnitudes with a single spectrum.

The correct transmission profile for a grating that produces only odd orders (and thus no second-order spectrum) is that of equally-sized adjacent dark and clear bands (Jenkins and White, 1950). Indeed, the

100 line/inch grating we produced already approximates this, as it was printed from a digital file with this pattern, and the 600 dpi laser printer was able to approximate this pattern. We believe that with a high-end inkjet printer, it may be possible to produce gratings that effectively suppress the second-order spectrum. Thus ELCPSS could perhaps be used as a roundabout means for extremely low-cost BVR photometry (ELCBVR).

10. Conclusions

We find that the use of a low-cost objective grating on a small telescope, coupled with a low-end consumer DSLR camera, can yield wavelength and flux-calibrated spectra. Standard B and V magnitudes can be extracted from the spectra, and our early results suggest this may be a useful way in some circumstances to obtain accurate B and V stellar magnitudes at very little cost in equipment.

Although the process itself has clear educational uses, much work remains to be done to determine whether ELCPSS could find practical use as a tool for extending broad-band photometry to users who otherwise would be limited to visual magnitude estimates. Further tests need to be done using ZOG techniques, and the practical limits in magnitude and precision need to be determined, for both absolute spectrophotometric calibration and for “hybrid” techniques that use ELCPSS to obtain nearly-calibrated “instrumental” magnitudes with broad-band photometric standards providing the final calibration. Experiments should be carried out with other grating materials and printing methods, and a wider array of telescopes and detectors should be tested. Individuals wishing to collaborate on the ELCPSS project should contact the authors.

11. Acknowledgements

We engaged in many helpful discussions with Doug Fowler. This work was supported in part by the following grants:

- UW - Fox Valley Foundation Grant, 2010
- UW - Fox Valley Professional Development Grants, 2010, 2012
- UW Colleges Department of Computer Science, Engineering and Physics Professional Development Grants 2010, 2012

12. References

Ažusienis, A., Straižys, V. (1969). *Soviet Astronomy* **13**, 316.

Beaver, J. E. (2012). “A Virtual Astronomical Research Machine in No Time (VARMiNT)” in *Proceedings for the 31st Annual Symposium on Telescope Science* (Warner et al., eds.), pp. 203-208. Society for Astronomical Sciences, Rancho Cucamonga, CA.

Beaver, J. E, Robert, D. M. (2011a). “A CCD Spectrograph for One Dollar.” in *Earth and Space Science: Making Connections in Education and Public Outreach*, ASP Conference Series, **433**, 425.

Beaver, J. E., Robert, D. M. (2011b). “A CCD Spectrometer for One Dollar.” in *Cosmos in the Classroom 2010: A Hands-on Symposium on Teaching Introductory Astronomy*. (A. Fraknoi, ed.). C1. Astronomical Society of the Pacific.

Colina, L. (1995). “CDBS Kurucz Stellar Atmosphere Atlas.” *STScI OSG# Instrument Science Report SCS CAL-006*.

Jenkins, F. A., White, H. E., (1950). *Fundamentals of Optics*. p. 310, 327. McGraw Hill, New York.

Space Telescope Science Institute (2012a). Calibration Database System (CDBS). http://www.stsci.edu/hst/observatory/cdb/astronomical_catalogs.html. Retrieved, 11 April 2012.

Space Telescope Science Institute (2012b). Specview. www.stsci.edu/institute/software_hardware/specview. Retrieved, 11 April 2012.

Tody, D. (1986). “The IRAF Data Reduction and Analysis System.” in *Proc. SPIE Instrumentation in Astronomy VI*. (D. L. Crawford, ed.). **627**, 733.

Tody, D. (1993). “IRAF in the Nineties.” in *Astronomical Data Analysis Software and Systems II*, A.S.P. Conference Ser. (R. J. Hanisch, R. J. V. Brissenden, J. Barnes, eds.) **52**, 173.

Wells, D. C., Griesen, E. W., Harten, R. H. (1981). “FITS - a Flexible Image Transport System.” *Astronomy and Astrophysics Supp. Series* **44**, 363–370.

Spectroscopic Analysis of Algol during Eclipse Cycle

*Jonathan Boyd, Kodiak Darling, Elise Sparks, Lajeana West
Students*

Estrella Mountain Community College, Phoenix, Arizona

Douglas Walker

Adjunct Faculty

Estrella Mountain Community College, Phoenix, Arizona

Douglas.Walker@estrellamountain.edu

Abstract

Algol, within the Perseus constellation, is referred to as the Winking Demon Star due to its varying apparent magnitude and its representation of the Gorgon Medusa. Every 68.75 hours its light dims suddenly, and brightens again over a ten-hour period. Further observation shows a small dip in light output halfway in between the large dips, indicating that Algol is an eclipsing binary star system. Detailed inspection of the spectrum indicates that Algol is also a spectroscopic binary. Algol consists of a 3 solar diameter B8V star and a 3.5 solar diameter K0IV in very close orbit around each other. This project investigated the spectral characteristics of Algol A and B during the primary eclipse cycle. Low-resolution spectroscopy of the eclipse cycle was imaged over several nights in order to investigate any changes in the emission line profile of the star system. This work lays the foundation for future studies in low-resolution spectroscopy of the Algol and Algol-type systems.

1. Introduction

1.1 Background

Since the fall of 2010, Estrella Mountain Community College (EMCC) has offered a series of special mathematics project courses focused on applied research for the undergraduate student. The first series of courses, offered in the fall 2010 and spring 2011 semesters, engaged the students in observing and recording visual measurements of double stars, selected from the US Naval Observatory maintained Washington Double Star Catalog. This research oriented course was extended in the fall 2011 semester, in a learning community which combined an introductory astronomy course with the special mathematics projects course. This approach was intended to extend the student's exposure to observational astronomy and data collection and analysis. The success of this sequence resulted in a special astronomy projects course being offered for spring 2012, focusing on spectroscopy. The objective of this course was to introduce the student to spectroscopy and its applications to stellar observation and analysis. The intent of this course offering was to give students the opportunity to conduct original astronomical research with the application of mathematics to data collections and analysis.

1.2 Special Projects Course Structure

Estrella Mountain Community College is part of the Maricopa County Community College System. This system consists of ten colleges, two skill centers, and numerous education centers, all dedicated to educational excellence, and to meeting the needs of businesses and the citizens of Maricopa County. Each college is individually accredited, yet part of a larger system – the Maricopa County Community College District, which is one of the largest providers of higher education in the United States.

EMCC's special mathematics course, designated MAT298AC, is a student driven research course focused on the application of learned techniques in the fields of astronomy, applied mathematics, and statistics. Students study with a large array of goals in mind; a common goal amongst the student body is to gain the knowledge necessary for work in a gamut of fields and professions. MAT298AC offered a unique opportunity within this environment to gain a particularly advantageous amount of experience in primary research and data analysis. The class, having been reclassified as AST298A, now has a greater focus on the techniques and skills needed for astronomy specific activities. At the start of the semester the class had a wide variety of possible research projects to choose from, each with its own unique obstacles and avenues of experience. The field of study chosen, spectroscopic analysis of the Algol system during its primary eclipse, was both within the capabilities of EMCC equipment and the classes' experience in the

astronomical sciences. This study resumes work in the field of binary star research, further augmenting EMCC's fledgling contributions to this field. With this in mind, the students of AST298A began their research project with the following objectives:

- to gain further knowledge of the nature of the individual stars within the Algol system
- to use the knowledge gained to make inferences about the Algol system
- to provide data for more accurate models of binary stars
- to establish a foundation for further Algol research
- to expand upon individual knowledge of research processes and analysis
- to provide an avenue for the students to attempt publication of their work in a recognized journal

1.3 Algol System

Algol, also known as Beta Persei, is the most famous eclipsing binary star system, because it can be distinguished with the naked eye. It is found in the constellation of Perseus, named for the ancient hero who killed the gorgon Medusa. Because of the stars' dramatic eclipse cycle and the star's position on the disembodied "head" of Medusa, it has been nicknamed the Winking Demon star.

Algol is an eclipsing trinary star system, determined to be 93 light years from Sol. It is one of the first eclipsing variable stars to ever be discovered. The main star (Algol A) is a spectral class B8V main sequence star with a mass 3.5 times greater, a diameter 3 times greater, and an absolute brightness 100 times brighter than our Sun. The secondary star (Algol B) is a spectral class K2IV type subgiant that measures about 0.8 solar masses, 3.5 solar diameters, and an absolute brightness 3 times brighter than our Sun. Algol A and B are a close binary pair, about 8 solar diameters apart, with a period of 2.87 days. The primary eclipse happens when the less massive Algol B passes in front of the more massive Algol A. The eclipse cycle lasts for a period of about 10 hours. At the eclipse's minima, the luminosity changes from an apparent magnitude of 2.1 to an apparent magnitude of 3.4. There is a faint third star (Algol C) in the Algol system, which is a spectral class F1 main sequence star. Algol C measures 1.7 solar masses, with a diameter slightly smaller than our Sun and an absolute brightness of about 4 times that of our Sun. Algol C orbits the inner two stars at a distance of about 2.69 AU with a period of about 1.86 years. Due to the

difficulty of resolving Algol C as an individual star, it is often overlooked and incorporated with light emitted from Algol B.

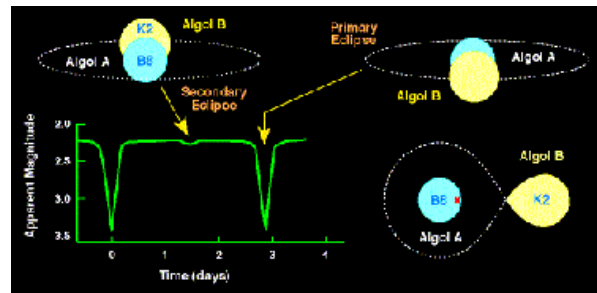


Figure 1. Diagram of Algol's eclipse cycle.

2. Equipment & Resources

2.1 Telescope

Equipment for observing sessions consisted of a Celestron 11-inch Schmidt-Cassegrain telescope with a 2800mm focal length. The telescope was used in conjunction with a Meade DSIPro CCD camera fitted with a diffraction grating to image the Algol system. The telescope was kept on target through the use of a heavy-duty (CG-5GT) computerized German Equatorial Mount.

The Celestron 11-inch Schmidt-Cassegrain telescope is equipped on a mobile tripod base which made transport to and from a remote location observing site relatively quick and easy.



Figure 2. Celestron Schmidt-Cassegrain telescope and student, Jonathan Boyd.

2.2 Star Analyzer

The Paton Hawksley Star Analyser 100 was used to provide the spectra of the Algol system. The Star Analyser 100 was designed specifically for amateur astronomical spectroscopy. It can be mounted on the telescope similarly to other 1.25-inch filters and will

work with most cameras. It can image dim objects and display the zero-order (star) along with the spectrum. This makes it easy for spectra to be calculated. The Star Analyser was mounted on the end of the CCD camera.



Figure 3 Hawksley Star Analyser 100

2.3 Meade DSIpro CCD Camera

The Meade DSIpro CCD camera is designed to help novice and amateur astronomers capture the images of a variety of objects throughout the night sky. By attaching the Star Analyser to the camera, the spectral images created were captured for later analysis.



Figure 4. Meade DSIpro CCD Camera

2.4 RSpec Real-Time Spectroscopy Software

RSpec is a new form of software that allows astronomers to take raw spectrum images and create a calibrated profile in real time. The software allows the user to analyze the composition of various stellar objects ranging from stars, to nebula emission lines, to detecting the red shift of a receding quasar. It also provides a library of reference series including profiles for all star spectral types and a small variety of

line profiles, for identifying the compounds that correspond to the spectral features within the calibrated graph.

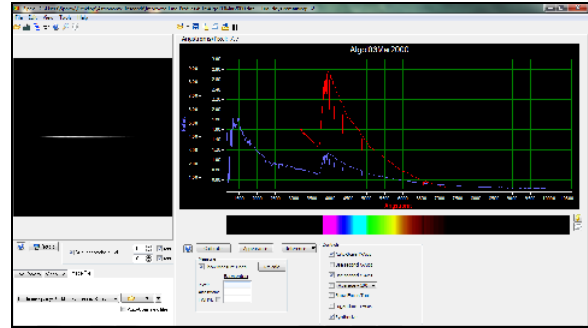


Figure 5. Screenshot of RSpec software in use.

2.5 Observing Site



Figure 6. Student Jonathan Boyd, guest Melissa Boyd, and instructor Doug Walker at Litchfield Park location.



Figure 7. Students Elise Sparks, Lajeana West, and Kodiak Darling at Buckeye location.

Observations were taken at two separate coordinates. The first quarter of the eclipse cycle was imaged at 33.503049° N, 112.363466° W, in Litchfield Park, Arizona, with medium levels of light pollution. The other part of the eclipse cycle was imaged at

33.365849° N, 112.577612° W in Buckeye Arizona, with low levels of light pollution. Ambient temperature at ground level was between 14-25 degrees Celsius.

Reduction and analysis of raw images was accomplished through the use of RSpec v1.5. The library of reference spectra for B8V and KOIV stars included in RSpec 1.5 was used as a calibration and analysis tool throughout the research process. Adobe Photoshop CS5 was used as an aid in the analysis of changing spectral features as the eclipse cycle progressed.

3. Observations

3.1 Observation Procedure

Imaging of the eclipse cycle was broken into two segments due to the Algol system setting on the horizon during the latter portion of the eclipse cycle. The first imaging session took place on 2012 February 28. The second imaging session took place on 2012 March 2 with the third and final imaging session taking place on 2012 March 3.

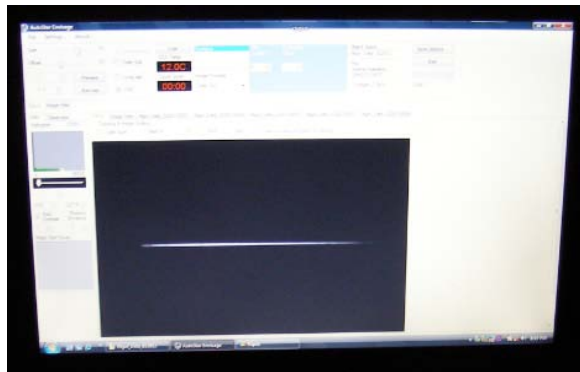


Figure 8. Laptop image of spectrum of Algol

The telescope was set to track on the Algol system, and the CCD camera mounted on the view-piece; the CCD camera was connected to its accompanying computer software, which was used to set image parameters and capture images. Images were taken at 15 minute intervals, beginning immediately before Algol B began its eclipse of Algol A, and ending directly after the conclusion of the eclipse cycle. Images were taken through the use of the CCD camera and diffraction filter described above. The Images were saved as FTS files and analyzed in their raw format with the RSpec computer program.

3.2 Observing Session 1

The first night of observation encompassed the evening February 28 to the morning of February 29. The minimum of the eclipse was scheduled for 01:46 on February 29, which meant the eclipse would begin at 20:46. The first image was taken at 20:00 then further images were taken at 15 minute intervals. This allowed for a couple images outside of the eclipse to be considered as a baseline image.

February 28-29 had been chosen for its ideal time frame. The eclipse would begin shortly after sunset and finish approximately at sunrise. However, at the beginning of the eclipse cycle, the star was almost directly overhead. Therefore, due to the star's movement across the sky, the images became unclear as the star approached the horizon. Images were captured until 23:30, approximately 30% completion of the eclipse. The star was no longer within view after 23:37.

3.3 Observing Session 2

To continue with the eclipse cycle, another night of observation would be required. The evening of March 2 to the morning of March 3 was chosen because the minimum would be at 22:36. The eclipse would begin at 17:36, but by the time images could be captured, beginning at 19:30, the star would be at approximately 25% completion. This allowed for overlap with the previous session of observation.

In the hopes of keeping view of the star system for a longer time frame, the location had been changed from Litchfield Park to Buckeye, in order to lower light pollution and the number of ground level obstructions. Images were collected through the minimum and until 00:30, approximately 70% completion of the eclipse cycle.

3.4 Observing Session 3

Observation 3 was conducted outside of the primary eclipse, in order to establish a set of data against which spectra changes during the primary eclipse could be compared to. Observations were undertaken at the original Litchfield Park location, initiating at 19:45 on March 3rd and ending at 22:15 the same night.

4. Data Collection and Reduction

4.1 Measurement Data

During observing sessions, imagery was captured at 15 minute intervals on the quarter hour. Each

set of observation data was archived in separate folders that were organized according to date of observation. The raw profile line image is shown in Figure 12. During the early part of the observing run, the line profile was relatively clean, but as Algol began to approach the horizon, atmospheric extinction began to take its toll: the line profile became very noisy, as shown in Figure 10.

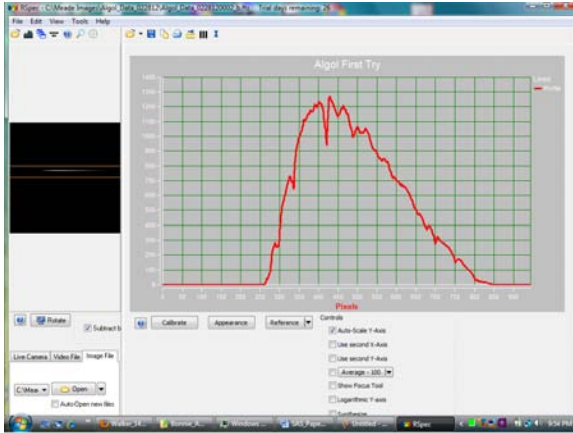


Figure 9. Algol line profile during early part of observing session.

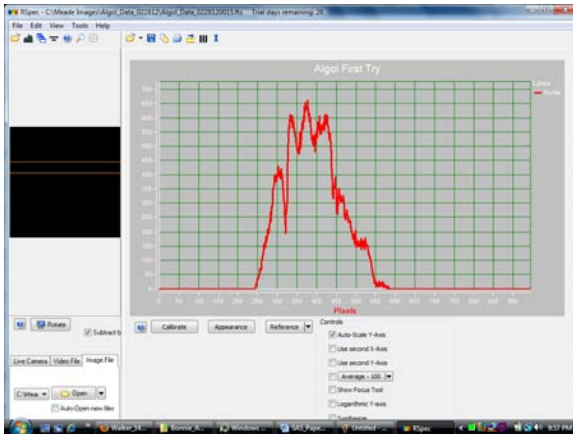


Figure 10. Algol profile during latter part of observing session.

The data reduction process consisted of reviewing the quality of the line profiles and producing instrument response curves for all good profiles.

5. Data Analysis

5.1 Analysis of Observing Session 1 (Feb 28)

Data from observing session 1 consists of 17 individual profiles spanning the time from 20:00 until 23:30. The Hydrogen Balmer absorption lines were the primary focus of the analysis.

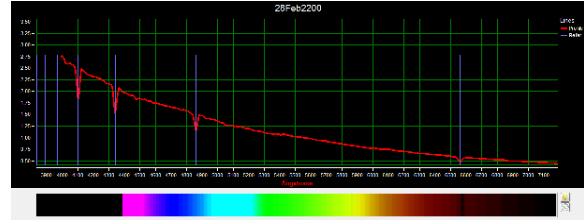


Figure 11. Instrumented corrected profile on February 28 at 22:00, includes Hydrogen Balmer lines.

5.2 Analysis Observing Session 2 (Mar 2)

Data from observing session 2 consists of 49 individual profiles spanning the time from 20:00 until 00:15. In order to validate the quality of the data being collected, the response curve during the same portion of the eclipse cycle for observing session 1 and 2 were compared. As shown in Figure

5.3 Analysis Observing Session 3 (Mar 3)

Data from observing session 3 consists of 11 individual profiles spanning the time from 19:45 until 22:15. This observing run was conducted to obtain additional baseline data outside of the eclipse cycle.

5.4 Summary Analysis of Eclipse

To establish a baseline of instrumentation stability throughout the eclipse, two profiles were taken at the same time within the eclipse cycle. The first profile was from February 28 and the second one was from March 2 at 25% completion within the eclipse cycle. As shown in Figure 12, the profiles from both lines align, establishing stability within the data collection between the two separate nights



Figure 12. Line profiles from March 2 at 20:00 and February 28 at 11:15: 25% completion of the eclipse cycle.

A comparison of line profiles covering the pre-eclipse from observing session 1 with line profiles during the first quarter, last quarter from sessions 1 and 2, and from outside the eclipse from session 3 shows the changes in the Hydrogen Alpha, Beta, Gamma and Delta absorption lines as shown in Table I and Figures 13, 14, 15, and 16 respectively.

Date	Time	Halpha EW	Halpha Cont.	Hbeta EW	Hbeta cont.	Hgamma EW	Hgamma Cont	Hdelta EW	Hdelta Cont.
02/28/12	07:58:00 PM	4.67	0.38	5.41	0.71	6.19	0.83	6.44	2.55
02/28/12	11:15:00 PM	4.64	0.38	5.35	0.71	5.92	0.83 no data	6.44	2.51
03/02/12	08:01:00 PM	4.2	0.38	5.42	0.71	5.83	0.83	6.07	2.51
03/02/12	10:30:00 PM	4.52	0.38	5.61	0.72	6.88	0.83	6.35	2.5
03/03/12	12:15:00 AM	4.77	0.38	5.51	0.71	6.09	0.83	6.12	2.53
03/03/12	08:45:00 PM	4.66	0.38	5.34	0.71	6.04	0.83	7.24	2.53

Table I. Measurement Data Spreadsheet.

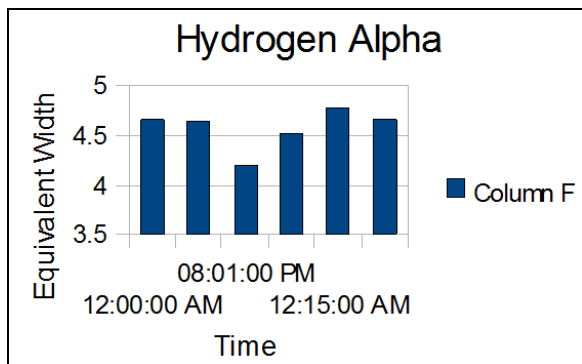


Figure 13. Hydrogen Alpha.

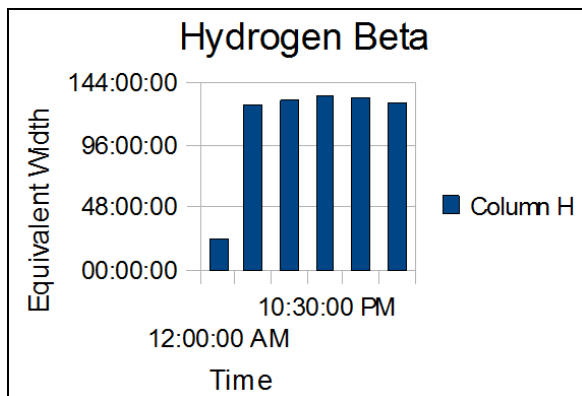


Figure 14. Hydrogen Beta.

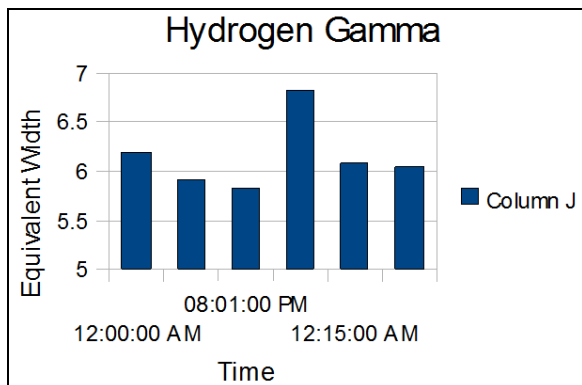


Figure 15. Hydrogen Gamma.

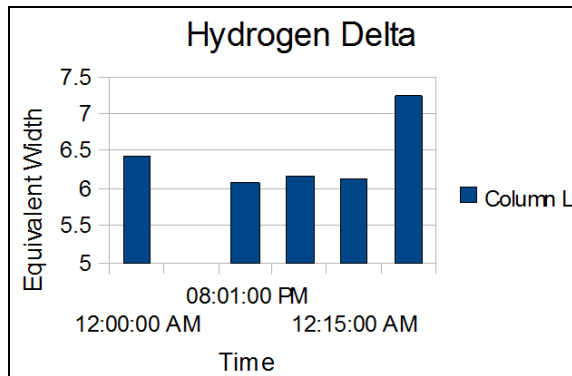


Figure 16. Hydrogen Delta.

6. Conclusion

Variations in spectral features at this point may be attributed to several possible factors, which are currently under further investigation. Additional data and updated conclusions are available upon request.

Throughout the data analysis process, student familiarity with the RSpec program and associated equipment has increased to a point which will allow for more thorough and complex research initiatives in the future. Using the data of this paper as a launching point for future lines of inquiry, EMCC special projects courses may be able to contribute to the current available body of data on the Algol system in a significant way.

7. Acknowledgments

The authors thank Tom Fields for his guidance and assistance with the use and acquisition of the RSpec program; to Doug Walker for the use of his equipment, expertise, and guidance. A very special thanks goes to Jeff Hopkins of the Hopkins Phoenix Observatory for his guidance and assistance at every step of the way. Finally, we thank the Estrella Mountain Community College administration for their enthusiastic support.

8. References

- Rspec reference libraries
- NASA.gov
- The SAO/NASA Astrophysics Data System
- Sky and Telescope Magazine star charts

A Fresh Look at the Algol-like Eclipsing Binary, AO Ser

Kevin B. Alton
UnderOak Observatory
70 Summit Ave., Cedar Knolls, NJ 07927
mail@underoakobservatory.com

Andrej Prša
Dept. of Astronomy & Astrophysics
800 Lancaster Ave, Villanova University, Villanova, PA 19085
aprsa@villanova.edu

Abstract

CCD images acquired in B, V, and I_c passbands between July and August 2008 and from June to August 2010 were used to revise the ephemeris and update the orbital period for AO Ser. Analysis of the O-C diagram using all available time-of-minima data revealed a continually increasing orbital period for at least 68 years. Thereafter, a sudden decrease in orbital period (~ 0.84 sec) most likely occurred during the first few months of 1998; potential causes for this abrupt jump and other alternating changes in period are discussed. Although the spectral classification of the primary star has been long considered A2V ($T_{\text{eff}} \sim 8800$ K), B-V data from this study as well as color index estimates from several other recent survey catalogs suggest a significantly cooler A7V ($T_{\text{eff}} \sim 7800$ K) primary. A semi-detached Roche model of the binary produced theoretical fits matching light curve data in all passbands. AO Ser is reported to be an oscillating Algol-type variable star referred to as an oEA system. Using Fourier methods, lightcurve analysis in this study did not convincingly reveal any underlying periodicity other than that expected from the dominant orbital period.

1. Introduction

AO Ser is a short period (< 1 day) and bright Algol-type binary suitable for study by amateur and professional astronomers alike. After its discovery in 1935 by the prolific observer Cuno Hoffmeister, the publication record for AO Ser was very sporadic with only a handful of times-of-minima (ToM) available for each of the next three decades. These mostly included photographic as well as visual timings. Only since 1969 has a steady flow of ToM values been available but no full light curve had been published until Zavros *et al.* (2008). AO Ser not only varies extrinsically by mutual eclipses but evidence is mounting that it also varies intrinsically by δ Sct-type pulsation of its primary component (Kim *et al.*, 2004; Zavros *et al.*, 2008). This new class of oscillating Algol-type variable stars is now designated as an oEA variable (Mkrichian *et al.*, 2004). More recently, the multiband (V and R) photometric properties and period variations of AO Ser were published by Yang *et al.* (2010).

AO Ser (BD+17°2943) varies in magnitude (V) between 10.8 and 12.2; the first modern orbital period (0.87934745 d) was reported by Koch (1961). This target is favorably positioned ($\alpha_{J2000} = 15^{\text{h}}58^{\text{m}}18^{\text{s}}.408$, $\delta_{J2000} = +17^{\circ}16'9.96''$) for mid latitude backyard observers in the Northern Hemisphere with a clear view of Serpens Caput. Its

spectral type (A2) reported by Brancewicz and Dworak (1980) is consistent with what would be expected for an Algol-like binary system, however, evidence from this study and several survey catalogs (eg. Tycho-2, USNO-A2.0, USNO-B1.0, and 2MASS) suggest a much cooler A7 system. This difference from all other published reports on this binary system will be discussed herein.

2. Methods, Observations and Data Reduction

2.1 Astrometry

Images of AO Ser were matched against the UCAC3-based standard star fields provided in MPO Canopus (V10.3.0.2 Bdw Publishing, Inc.). This “automatch” feature generates a star chart centered on the putative center of the image and then matches the chart’s center, rotation, and scaling to the image. Plate constants are internally calculated which convert X/Y coordinates of a detected object to a corresponding RA and declination.

2.2 Photometry

CCD observations at UnderOak Observatory span from 2008 July 25 to August 22 and then again from 2010 June 19 to August 31. Equipment included

a 0.2-m catadioptric telescope with an SBIG ST 402ME CCD camera mounted at the primary focus. The KAF 0402ME camera array (765×510) comprised of square pixels (9 μm) produces a ~9×14 arcmin field-of-view (FOV) with an image scale of ~1 arcsec/pixel with this optical assembly. The CCD camera was maintained at 0°C with thermoelectric cooling. Automated multi-bandwidth (B, V, and I_c) imaging was performed with SBIG photometric filters manufactured to match the Bessell prescription. During each 2008 session, an image in each bandpass was sequentially collected every 45 s; data acquisition and reduction (raw lights, darks, and flats) for this camera system has been described elsewhere (Alton, 2010). The other campaign which started in 2010 employed essentially the same equipment except that the acquisition time for each filter was increased to 60 s. Instrumental readings were reduced to catalog-based magnitudes using the MPOSC3 reference star fields built into MPO Canopus. The MPO Star Catalog (MPOSC3) is a hybrid assemblage which includes a large subset of the Carlsberg Meridian Catalog (CMC-14) as well as from the Sloan Digital Sky Survey (SDSS). Almost all stars in MPOSC3 also have BVRI magnitudes derived from 2MASS J-K magnitudes; these have an internal consistency of ±0.05 mag for V, ±0.08 mag for B, ±0.03 mag for I_c, and ±0.05 mag for B-V (Warner, 2007).

2.3 Lightcurve Analyses

Light curve modeling was performed using Binary Maker 3 (Bradstreet and Steelman, 2002), PHOEBE 0.31a (Prša and Zwitter, 2005), and Wdwind Version 5.6a (Nelson, 2009), all of which employ the Wilson-Devinney (W-D) code (Wilson and Devinney, 1971; Wilson, 1979). Geometric renderings were produced by Binary Maker 3 (Bradstreet and Steelman, 2002).

3. Results and Discussion

3.1 Ensemble Photometry

Five comparison stars in the same field of view with AO Ser were used to calculate the relative change in flux and standard magnitudes (Table I). Over the duration of each session, comparison stars did not exhibit any variable behavior so Comp Cavg values remained constant over each observation period (Figure 1). The mean standard magnitude for each comparison star varied between ±0.015 (V and I_c) and ±0.03 (B) mag. During the entire campaign the airmass for all observations was kept under 2 to

minimize error due to differential refraction and color extinction.

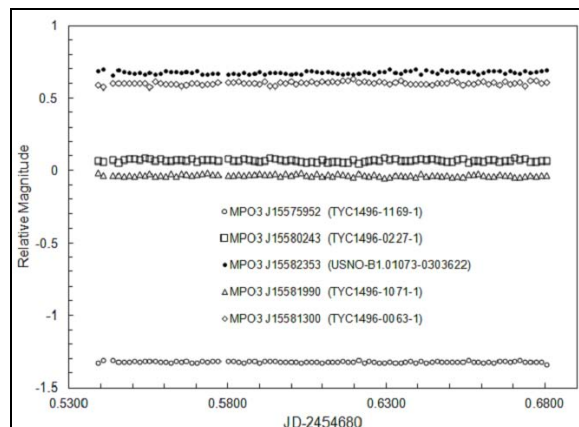


Figure 1. Constant relative magnitude (I_c-band) exhibited by comparison stars during a typical AO Ser photometric session (2008 Aug 02).

3.2 Folded Light Curves and Ephemerides

Individual photometric values in B ($n = 1573$), V ($n = 1598$), and I_c ($n = 1580$) were combined by filter to produce light curves that spanned 4 weeks of imaging in 2008 and 10 weeks in 2010. A period solution from all folded 2008 and 2010 datasets was calculated by MPO Canopus. Accordingly, the linear ephemeris (Eq. 1) for the heliocentric primary minimum was initially determined to be:

$$\text{Min I} = \text{HJD } 2454664.54963 + 0.8793429 (\pm 0.0000013) \cdot E \quad (1)$$

This result is in general agreement with the orbital period reported over the past 5 decades from other investigators. The period determination was confirmed with periodograms produced (Peranso v 2.1, CBA Belgium Observatory) by applying periodic orthogonals (Schwarzenberg-Czerny, 1996) to fit observation and analysis of variance (ANOVA) which was used to evaluate fit quality.

ToM values were estimated by Minima (V24b, Nelson, 2007) using a simple mean from a suite of six different methods including parabolic fit, tracing paper, bisecting chords, Kwee and van Woerden (1956), Fourier fit, and sliding integrations (Ghedini, 1981). Four new secondary (s) and two new primary (p) minima were detected during this investigation. Since no obvious color dependencies emerged, the timings from all three filters were averaged for each newly determined ToM. Residual values (O-C) were estimated from a complete set of visual (vis), photographic (pg), photoelectric (pe) and CCD timings reported over the past 80 years. Calculations were

MPOSC3 ¹ Star Identification	RA	DEC	B mag	V mag	I _c mag	(B-V)
MPO3 J15575952	15 ^h 57 ^m 59 ^s .52	+17°19'26.3"	10.843	10.41	9.889	0.433
MPO3 J15580243	15 ^h 58 ^m 02 ^s .43	+17°21'13.4"	11.985	11.547	11.021	0.438
MPO3 J15581300	15 ^h 58 ^m 13 ^s .00	+17°16'42.5"	12.852	12.158	11.391	0.694
MPO3 J15581841	15 ^h 58 ^m 18 ^s .41	+17°16'10.0"	11.667	11.208	10.661	0.459
MPO3 J15581990	15 ^h 58 ^m 19 ^s .90	+17°19'45.4"	12.518	11.50	10.445	1.018
MPO3 J15582353	15 ^h 58 ^m 23 ^s .53	+17°18'39.8"	12.876	12.214	11.474	0.662

¹MPOSC3 is a hybrid assemblage which includes a large subset of the Carlsberg Meridian Catalog (CMC-14), the Sloan Digital Sky Survey (SDSS), and 2MASS Catalog.

Table I. Astrometric Coordinates and Estimated Color of AO Ser (MPO3 J15581841) and Five Comparison Stars in Same Field of View

initially based upon the linear elements (Eq. 2) defined by Kreiner (2004):

$$\text{Min I} = \text{HJD } 2452500.3991 (\pm 0.0007) + 0.8793410 (\pm 0.0000004) \cdot E \quad (2)$$

The O-C diagram (Figure 2) for AO Ser is complex and characterized by parabolic and possibly alternating changes exhibited by many other late type Algol-like binary systems such as U Cep (Manzoori, 2008), Y Leo (Pop, 2005), TY Peg (Qian, 2002), and X Tri (Qian, 2002). Regression analysis using a scaled Levenberg-Marquardt algorithm (Press et al., 1992) as implemented in QtiPlot (v0.9.8 2010) revealed that the O-C data from the initial timing in 1930 until the last twelve years could be fit ($r^2 > 0.99$) by a quadratic expression (Eq. 3) modulated with a sinusoidal term:

$$c + a_1x + a_2x^2 + a_3\sin(a_4x + a_5) \quad (3)$$

Accordingly, the coefficients (\pm error) for each solved term in the above (Eq. 3) are provided in Table II. From the parabolic component ($c + a_1x + a_2x^2$) it is apparent that the orbital period has been slowly

increasing linearly with time as suggested by the positive coefficient (a_2) for the quadratic term, x^2 . Algol-type binaries typically consist of a hot main-sequence massive primary well within its Roche lobe and a less-massive subgiant companion filling its Roche lobe. Gas streams from the secondary to the primary result in mass exchange and barring any other competing phenomena, the net effect is a change in the orbital period. In this case, the orbital period rate of increase ($\Delta p/p = 2a_2 = 1.25 \times 10^{-10}$) of this system, which is equivalent to a period increase rate of $dp/dt = +0.004479 \text{ sec yr}^{-1}$, lasted for at least 68 years but suddenly slowed to a standstill as judged by the break in O-C residuals (Figure 2) around cycle -1855. The intersection of Q+S and L1 suggests this change which is centered at the beginning of 1998 probably occurred sometime between mid 1996 and mid-1999. This cannot be attributed to the shift from vis-pg to ccd-pe recordings since instrument-derived ToMs regularly reported after cycle 118.5 continue in a similar fashion until another break is observed near cycle 2000. This characterization of AO Ser is in contrast to that described by Yang et al. (2010) who only report a period decrease since 1981. This obvious difference from our findings is dis-

Curve	c	a ₁	a ₂	a ₃	a ₄	a ₅
L1a	1.593×10 ⁻³ (±0.290×10 ⁻³)	-8.679×10 ⁻⁷ (±0.228)	-	-	-	-
L2a	-6.503×10 ⁻³ (±1.088×10 ⁻³)	3.046×10 ⁻⁶ (±0.4189×10 ⁻⁶)	-	-	-	-
Q+Sb	1.667×10 ⁻² (±0.136×10 ⁻²)	+8.911×10 ⁻⁶ (±0.237×10 ⁻⁶)	+6.240×10 ⁻¹¹ (±0.760×10 ⁻¹¹)			
Q+S _c	1.667×10 ⁻² (±0.136×10 ⁻²)	+8.911×10 ⁻⁶ (±0.237×10 ⁻⁶)	+6.240×10 ⁻¹¹ (±0.760×10 ⁻¹¹)	+3.748×10 ⁻³ (±0.593×10 ⁻³)	4.249×10 ⁻⁴ (±0.206×10 ⁻⁴)	3.209 (±0.244)

a: Linear least squares fit: (O-C) = c + a₁x
b: Non-linear regression fit (O-C) = c + a₁x + a₂x²
c: Non-linear regression fit (O-C) = c + a₁x + a₂x² + a₃sin(a₄x + a₅)

Table II. Coefficients (\pm error) From Regression Analysis of O-C vs Cycle Number Data for AO Ser

cussed further on in this section along with the potential for a light time effect which they also had proposed.

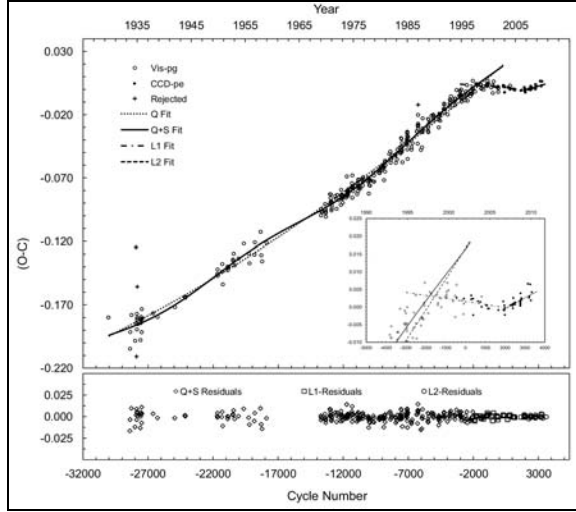


Figure 2. Nonlinear quadratic+sine term fit (Q+S) of residuals (O-C) vs cycle number for AO Ser observed from 1930 March to 1998 June 17. The inset figure shows a breakpoint centered near cycle -1855 (1998 Feb-March) and the straight line linear fit of data (L1) through cycle 1983.5 (mid-2007). Near term data (L2) were also fit using simple linear least squares analysis. The bottom panel represents a composite plot of all (O-C)₂ residuals from fitting Q+S, L1, and L2. All ToM values and references used to prepare this figure can be obtained by request (mail@underoakobservatory.com).

Calculations based on linear coefficients from the quadratic + sine term (Eq. 4) and simple least squares (Eq. 5) fits resulted in the following ephemerides, respectively:

$$\text{Min I} = \text{HJD } 2455666.9548 (\pm 0.0013) + 0.8793499 (\pm 0.0000002) \cdot E \quad (4)$$

$$\text{Min I} = \text{HJD } 2455666.9045 (\pm 0.0003) + 0.8793401 (\pm 0.0000002) \cdot E \quad (5)$$

The orbital period difference (-9.7788×10^{-6} days) between equations (Eq. 4) and (Eq. 5) corresponds to a rather large decrease (0.844 sec) over a relatively short period of time. The two most likely causes for a decrease in period are mass exchange between the components and/or angular momentum loss from the binary system. A rate of conservative mass transfer can be predicted (Eq. 6) as follows from Kwee (1958):

$$dm/dt = m \left[\frac{q}{3P(1-q^2)} \right] dP/dt \quad (6)$$

where

$$m = M_1 + M_2 \text{ and } q = M_2/M_1$$

The abrupt change in orbital period likely took place within a 3 year window as suggested by the O-C diagram (Figure 2). Assuming the solar mass of a putative A7V primary approximates $1.82 M_{\odot}$ (Harmanec, 1988), then from the mass ratio ($q_{\text{ph}}=0.235$) determined herein, the calculated mass loss is $6.851 \times 10^{-7} M_{\odot} \text{ y}^{-1}$. Averaged over three years this translates into nearly two-thirds of the Earth's mass. Alternatively from Mikuž *et al.* (2002), the associated change in angular momentum can also be estimated from the equations for total angular momentum (L) and Kepler's law:

$$\frac{dL}{L} = \left[\frac{2}{3} + \frac{q}{3(1+q)} \right] dm_1/m_1 + \left[1 - \frac{q}{3(1+q)} \right] dm_2/m_2 + \frac{1}{3} dP/P,$$

where $q = m_2/m_1$ and P is the period of AO Ser.

Assuming that the angular momentum change dL can only be zero or a negative value, then in order to produce a period change of $dP/P = 1.11 \times 10^{-5}$ the total mass lost from the system had to be at least 3.23×10^{24} kg or slightly more than one half (~54%) of Earth's mass. The corresponding magnitude of mass loss estimated by either equation 6 or 7 is significant but nonetheless not unprecedented (1.626×10^{-4} to $9.5 \times 10^{-8} M_{\odot} \text{ y}^{-1}$) for semi-detached binaries (van Rensbergen *et al.*, 2011).

Due to the continually changing nature of the O-C diagram, a new ephemeris equation (Eq. 8) based upon a linear least squares fit (L2) of near-term data (Table III) collected over the past four years (cycle 1905 to 3601) was calculated:

$$\text{Min I} = \text{HJD } 2455,666.9105 (\pm 0.0011) + 0.8793441 (\pm 0.0000004) \cdot E \quad (8)$$

As such, if the complex O-C behavior of this system continues unabated, revised ephemerides for AO Ser will need to be calculated on a more regular basis. The composite residuals from the quadratic + sine term fit (Q+S) and simple least squares fit (L1 and L2) are shown in the bottom panel of Figure 2. No additional underlying periodicity in the (O-C)₂ diagram was uncovered with Peranso using Fourier (Lomb-Scargle) and statistical (ANOVA) methods.

In a recent publication, Yang *et al.* (2010) attempted to make a case for decreasing period and a third body with an incomplete set of data which ex-

cluded all pg and visual ($n = 300$) plus other CCD readings ($n = 10$) published from 1941 through the middle of 2008. It is unfortunate that this rich set of

Time of Minimum (– 2,400,000)	Type	Cycle Number	(O-C) ₁	(O-C) ₂	Reference
54175.5429	p	1905	-0.000805	-0.000700	3
54186.5371	s	1917.5	0.001632	-0.000662	3
54201.4835	s	1934.5	-0.000765	-0.000610	3
54211.5959	p	1946	-0.000786	-0.000575	3
54213.3545	p	1948	-0.000868	-0.000569	3
54220.3893	p	1956	-0.000826	-0.000545	2
54220.3906	p	1956	0.000494	-0.000545	2
54224.7859	p	1961	-0.000901	-0.000529	1
54242.3741	p	1981	0.000459	-0.000469	2
54244.5717	s	1983.5	-0.000274	-0.000461	3
54491.6646	s	2264.5	-0.002195	0.000395	4
54574.7651	p	2359	0.000581	0.000683	5
54581.3604	s	2366.5	0.000823	0.000706	6
54599.3865	p	2387	0.000433	0.000768	7
54610.8172	p	2400	-0.000300	0.000808	5
54612.5770	p	2402	0.000818	0.000814	8
54614.3375	p	2404	0.002636	0.000820	8
54628.4051	p	2420	0.000780	0.000869	8
54685.5625	p	2485	0.001015	0.001067	9
54696.5546	s	2497.5	0.001353	0.001105	9
54926.5017	p	2759	0.000781	0.001901	10
54928.2612	p	2761	0.001599	0.001907	11
54928.2614	p	2761	0.001799	0.001907	11
54929.1397	p	2762	0.000758	0.001911	11
54929.1400	p	2762	0.001058	0.001911	11
54932.2170	s	2765.5	0.000364	0.001921	11
54932.2181	s	2765.5	0.001464	0.001921	11
54939.6925	p	2774	0.001466	0.001947	12
54952.8851	p	2789	0.003951	0.001993	13
54968.7113	p	2807	0.002013	0.002048	12
54974.4272	s	2813.5	0.002196	0.002067	9
55259.7737	p	3138	0.002542	0.003056	14
55316.4953	s	3202.5	0.006647	0.003252	15
55327.4831	p	3215	0.002685	0.003290	15
55366.6142	s	3259.5	0.003157	0.003426	9
55395.6358	s	3292.5	0.006504	0.003526	9
55436.5206	p	3339	0.001938	0.003668	9
55666.9103	p	3601	0.004259	0.004466	16

(1) Baldwin and Samolyk, 2007 (2) Brát *et al.*, 2007 (3) Borkovits *et al.*, 2008 (4) Parimucha *et al.*, 2009 (5) Samolyk, 2008 (6) Brát *et al.*, 2008 (7) Hübscher *et al.*, 2010 (8) Lampens *et al.*, 2010 (9) Present study (10) Doğru *et al.*, 2009 (11) Yang *et al.*, 2010 (12) Samolyk, 2010 (13) Diethelm, 2009 (14) Samolyk, 2011 (15) Doğru *et al.*, 2011 (16) Diethelm, 2011.

Table III. Near Term Recalculated Residuals (O-C)₂ for AO Ser Following Simple Linear Least Squares Fit of (O-C)₁ and Cycle Number Between 2007March16 and 2011April15.

data was not considered since out of 300 additional visual and pg observations, we found that only four values needed to be rejected as spurious. In contrast when all data are evaluated, residuals for the first seven decades clearly describe an upwardly turned parabola (Q), namely behavior consistent with conservative mass transfer and a continually increasing period. Additionally on this quadratic curve, there is evidence for underlying cyclical changes based upon non-linear regression analysis (Eq. 3). The amplitude (0.003748 ± 0.000593 d) of the periodic oscillation is defined by a_3 , the coefficient of the sine term. Assuming for the moment that this behavior is associated with a third body, then according to the relationship:

$$P_3 = 2\pi P/\omega,$$

where the angular frequency, ω , corresponding to $a_4 = 4.249 (\pm 0.206) \times 10^{-4}$, its Keplerian orbital period would be ~ 36 y. This estimate is more than twice as long as the periodic value (~ 17 y) reported by Yang *et al.* (2010) using an incomplete dataset covering the time span between 1981 and 2009.

Analysis of the complete set O-C residuals available between 1930 and 2011 paints a very different behavioral picture for this binary system. We agree there is a modicum of evidence that suggests cyclic, if not sinusoidal behavior in the O-C diagram but only up to 1998. Thereafter, between 1998 and 2011 the O-C trace is curvilinear but not necessarily sinusoidal for this system. It is possible that the event(s) responsible for the sudden change in orbital period in 1998 have masked our ability to tease out the putative 36 year periodicity observed during prior epochs.

Nonetheless, since the gravitational influence of a third body cannot be simply turned off, we believe that evidence for the presence of a third body in this system is inconclusive. Moreover, during attempts to fit light curve data to a Roche type model with our data, neither the orbital eccentricity (e) nor third light (l_3) rose above a level different than zero when included as variable parameters.

This begs the question as to what other phenomena might lead to cyclic, but not necessarily, persistent sinusoidal behavior. Hall (1989) noted that Algol-like systems which exhibit alternating variability in their O-C diagrams are almost exclusively those possessing a late-type secondary which to a high degree of certainty are chromospherically active. Furthermore, earlier type Algols composed of two radiative-envelope companions yield much simpler O-C diagrams rarely demonstrating cyclic behavior (Budding and Demircan, 2007). The secondary in AO Ser is likely a rapidly rotating late type subgiant and

therefore possesses a dynamically active lobe-filling convection envelope.

A plausible alternative to the light travel time effect (LITE) from additional unseen mass involves cyclic variability arising from magnetic activity of the secondary (Applegate, 1992). In addition, Biermann and Hall (1973) proposed a model where the secondary experiences abrupt episodes of mass transfer which orbits the primary as a disk. This leads to a temporary reservoir of orbital angular momentum where P decreases but at later time, angular momentum is returned by accretion during which P increases.

This scenario may have played out with AO Ser starting with the sudden break observed in the O-C diagram in early 1998 followed by a period decrease which begins to reverse direction around cycle 2000 (mid-2007). At this time in the absence of any supporting data from a spectroscopic study or speckle interferometry it would be speculative to assign any single reason or combination of phenomena that would unequivocally include LITE as an explanation to this very complex O-C diagram for AO Ser.

3.3 Light Curve Synthesis

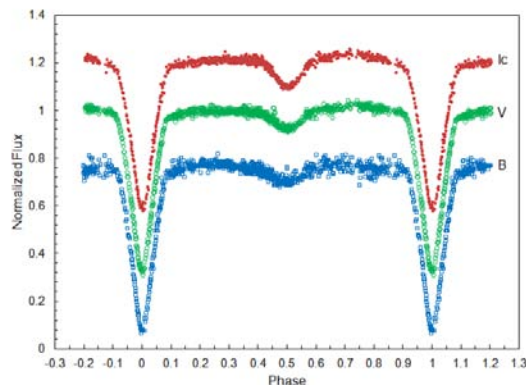


Figure 3. Folded (2008 July-August and 2010 June-August) CCD light curves for AO Ser captured in B, V, and I_c bandpasses.

Folded light curves (Figure 3) comprised of all observations (relative magnitude) in B, V, and I_c , show that minima are separated by 0.5 phase. Collectively, mode 5 (semi-detached; secondary fills Roche lobe), synchronous rotation and circular orbits were selected for modeling by PHOEBE. Each model fit incorporated individual observations assigned an equal weight of 1. Bolometric albedo ($A_1 = 1$) and gravity darkening coefficients ($g_1 = 1$) for the primary component were based on theoretical considerations for radiative stars reported by Eddington (1926) and von Zeipel (1924), respectively. As mentioned previously, third light (l_3) did not rise above a value differ-

ent than zero when adjusted. Bolometric albedo ($A_2=0.5$) and gravity darkening coefficients ($g_2 = 0.32$) for cooler stars with convective envelopes were assigned as determined by Rucinski (1969) and Lucy (1967), respectively. After any change in T_{eff} , logarithmic limb darkening coefficients (x_1, x_2, y_1, y_2) for both stars were interpolated from PHOEBE (Van Hamme, 1993). Once an approximate fit was obtained, differential corrections (DC) were applied simultaneously to photometric data in all filters.

3.3.1. Binary Model

As mentioned earlier the spectral type reported by Brancewicz and Dworak (1980) was A2 while the color index ($B-V = -0.1$) listed by Kreiner *et al.* (2004) suggests an even hotter primary star. Yet, evidence from this study which is the first to simultaneously acquire AO Ser light curves in B and V passbands, as well as data from multiple survey catalogs point to a much cooler system (Table IV).

The B-V value (0.247) observed in this study was taken during Min II when spectral contamination by the secondary was least likely to bias the result. In addition, maximum galactic reddening ($E_{(B-V)} = 0.0381$) in this region of the sky (Schlegel *et al.*, 1998) is unremarkable and therefore no adjustment has been made to obtain the associated intrinsic color index for AO Ser.

On balance, we adopted an A7 spectral classification for AO Ser which is considerably cooler than that reported by all previous investigators; the effective temperature of the primary was estimated to be 7800 K based on the tables from Flower (1996). Values for q , Ω_1 , Ω_2 , and i reported by Zavros *et al.* (2008) were used as a starting point for an unspotted fit (V bandpass) using Binary Maker 3. A_1 , A_2 , g_1 , g_2 , q , and T_1 were fixed parameters whereas Ω_1 , T_2 , phase shift, x_1 , x_2 , and i were iteratively adjusted until a reasonable fit of the observed relative flux by the model was obtained.

Thereafter, the model fit was refined with PHOEBE while using DC to achieve a simultaneous minimum residual fit of all (B, V, and I_c) photometric observations. In mode 5, Ω_2 is constrained and as

such is automatically calculated with any change to this parameter. The initial W-D model fit was marginally acceptable in all passbands which led to further adjustment of variable parameters. Early investigators of this Algol like system had used a mass ratio ($q = m_2/m_1$) of 0.45, presumably based on a tabulation of computed parameters for eclipsing binaries published by Brancewicz and Dworak (1980). However, in the absence of any radial velocity data for this binary system, it was deemed appropriate to allow this physical element to also vary freely.

An improved solution quickly emerged at a significantly different value, so it was decided to carefully examine this parameter under more controlled conditions. Mass ratio (q) was fixed over a range of 0.1 to 0.8 and a series of fits allowed to converge. The curve generated by plotting χ^2 as a function of the putative mass ratio showed a shallow minimum between $q = 0.220$ and 0.260 (Figure 4). The mid-point (0.240) was nominally assigned as the starting q -value during Roche modeling.

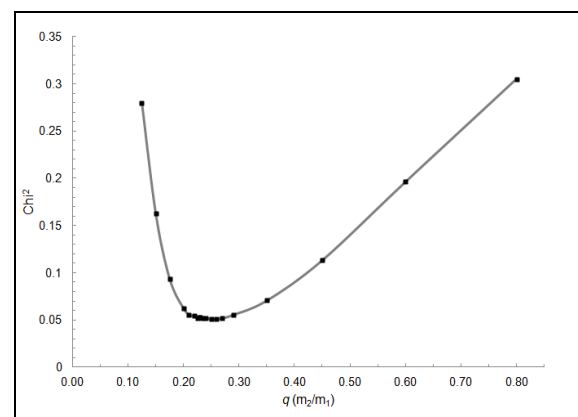


Figure 4. Search for mass ratio (q) providing the best simultaneous light curve fit (χ^2) using data from all passbands (B, V, and I_c). The shallow minimum is essentially the same between 0.22 and 0.26 q .

Elements for AO Ser obtained using PHOEBE are provided in Table V while light curve fits for each filter band (B, V, and I_c) are respectively illustrated in Figures 5, 6, and 7. A 3-dimensional rendering produced using Binary Maker 3 depicts a spatial

Survey	Tycho-2	USNO-B1.0	USNO-A2.0	2MASS	ASCC-2.5 V3	Present Study
(B-V) ^a	0.219	0.195	0.235	0.459	0.266	0.247
Spectral Class ^b	A7	A7	A7	F5	A8	A7

a: Not corrected for galactic reddening – $E_{(B-V)} \sim 0.0381$
b: Estimated from Fitzgerald (1970)

Table IV. AO Ser Color Index (B-V) From Several Survey Catalogs and the Present Study

Parameter	Present Study	Zavros <i>et al.</i> 2008	Yang <i>et al.</i> 2010
T_1 (K) ^a	7800	8770	9480
T_2 (K) ^b	4412 (33)	4858–5137 ^c	4786 (11)
q (M_2/M_1) ^b	0.235 (3)	0.45	0.220 (2)
A_1 ^a	1.0	1.0	1.0
A_2 ^a	0.5	0.5	0.5
g_1 ^a	1.0	1.0	1.0
g_2 ^a	0.32	0.32	0.32
Ω_1 ^b	3.56 (3)	4.625–4.936 ^c	2.597 (11)
Ω_2	2.318	2.778	2.282
i ^o ^b	86.8 (4)	80.12–81.18 ^c	87.62 (17)

a: Fixed elements during DC
 b: Error estimated from heuristic scanning of the $\Delta\chi^2$ surface (Prša and Zwitter, 2005)
 c: Range since V, R, and I not simultaneously fit during W-D modeling

Table V. A Comparison of Selected Photometric Elements for AO Ser Obtained Following Roche Model Curve Fitting

model for AO Ser (Figure 8). As might be expected from adopting an A7 primary for AO Ser instead of a hotter A2, most of the physical and geometric elements determined in this study are quite different from those most recently reported by Yang *et al.* (2010) and Zavros *et al.* (2008). One other revealing difference is related to using a theoretical q value (0.45) from the literature (Zavros *et al.* 2008), as opposed to empirically determining a photometric q . As such, our value ($q_{ph} = 0.235$) agrees reasonably well with the value reported by Yang *et al.* (2010) of $q_{ph} = 0.220$). Based upon a compilation of absolute dimensions of eclipsing binaries (Harmanec, 1988), the mean stellar mass for an A7 main sequence binary star ($1.82 M_{\odot}$) was used to estimate the mass of the secondary and the semi-major axis ($a = 5.055$) in solar units. The associated mass ($0.428 M_{\odot}$) of the secondary and best fit temperature for T_2 (4412 K; $\log 3.645$) of the putative sub-giant suggested a spectral type between K1 and K3 (Harmanec, 1988; İbanoğlu *et al.*, 2006; Surkova and Svechnikov, 2004). Clearly, further spectroscopic analyses will be necessary to solidify the spectral classification of this Algol-like system.

3.3.2. Oscillating Frequencies of the Primary Star

Recent evidence suggests that AO Ser not only varies extrinsically by mutual eclipses but also intrinsically by δ Sct-type pulsation of its primary component (Kim *et al.*, 2004; Zavros *et al.*, 2008). To this end, we investigated the possibility that such oscillation could be detected in our data. Frequency analysis by classical Fourier methods with Period04 (Lenz and Breger, 2005) and Peranso did not convincingly expose any underlying periodicity other than that expected from the dominant orbital period. The spectral window (Figure 9) exhibits strong side-bands

offset by 1 cycle per day and likely result from daily sampling aliases; results are shown for B-band, however, similar findings were observed in V and I_c . Data subsets intentionally stripped of measurements around the primary minimum or residuals remaining after Roche modeling were no more revealing of any underlying pulsations. Successive pre-whitening did not expose any other statistically meaningful ($s/n > 4$) oscillations in the frequency range ($5\text{--}80 \text{ d}^{-1}$) expected for δ Sct-type pulsations (Breger, 2000) according to the criterion proposed by Breger *et al.* (1993). It is entirely possible, however, that intrinsic oscillations were not detected due to insufficient precision during photometric sampling given that low amplitude δ Sct-type pulsations may not exceed 0.06 mag (Christiansen, 2007).

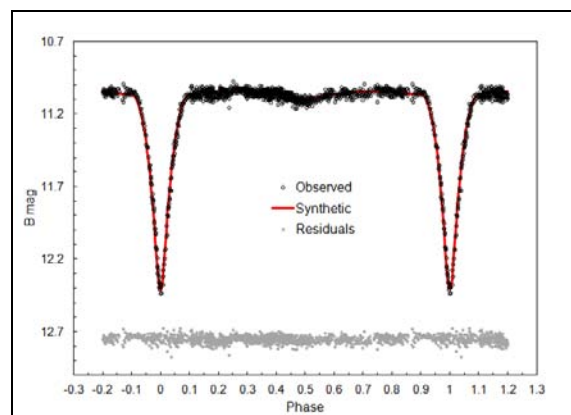


Figure 5. AO Ser light curve (B-band) synthesis determined by PHOEBE after simultaneous fit of all photometric data from three passbands (B, V, and I_c). Roche model residuals are adjusted by a fixed amount to display them in the same chart.

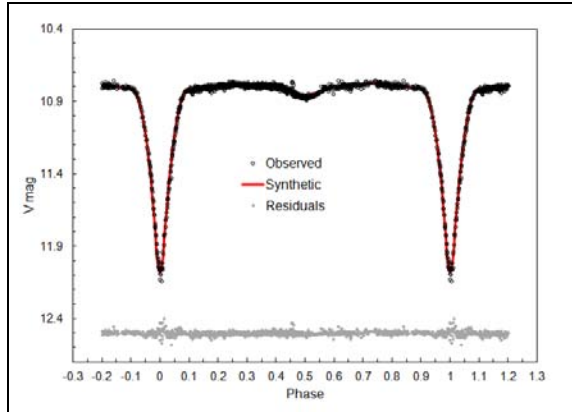


Figure 6. AO Ser light curve (V-band) synthesis determined by PHOEBE after simultaneous fit of all photometric data from three passbands (B, V, and I_c). Roche model residuals are adjusted by a fixed amount to display them in the same chart.

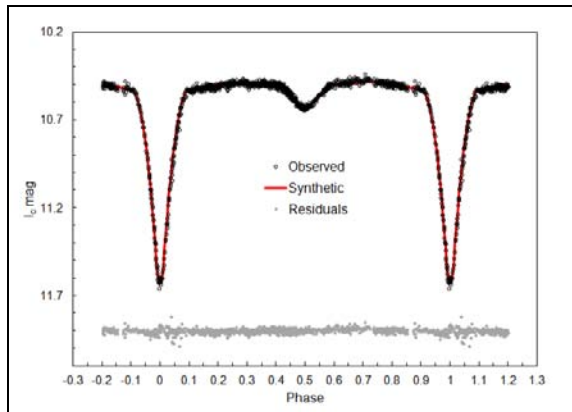


Figure 7. AO Ser light curve (I_c -band) synthesis determined by PHOEBE after simultaneous fit of all photometric data from three passbands (B, V, and I_c). Roche model residuals are adjusted by a fixed amount to display them in the same chart.

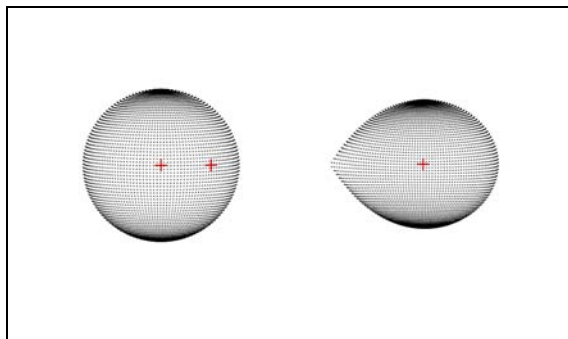


Figure 8. Three-dimensional rendering of the AO Ser binary system at phase 0.25.

4. Conclusions

CCD (B, V, and I_c filters) photometric readings were used to revise the orbital period for AO Ser and calculate an updated ephemeris. A detailed period analysis using O-C residuals generated from observations spanning 80 years revealed a very complex pattern of changes. Following at least seven decades of a constantly increasing orbital period, a sudden decrease (0.844 s) probably occurred around the beginning of 1998. Assuming no mass loss from the system and conservation of angular momentum, on average the minimum amount of stellar material transferred during that period exceeded 50% the mass of Earth.

Since then, the O-C residuals suggest that AO Ser is presently undergoing further changes caused by a yet to be determined phenomena or combination of effects. Evidence points to cyclic, if not sinusoidal behavior in the O-C diagram but only up to 1998; however, this same cyclic periodicity (~ 36 y) is not obvious within subsequent O-C residuals available for this system between 1998 and 2011.

At this time in the absence of any supporting data from a spectroscopic study or speckle interferometry it would be too early to assign any single reason or combination of phenomena that would unequivocally include the light travel time effect as an explanation to this very complex O-C diagram for AO Ser.

A Roche model based on the W-D code provided a simultaneous theoretical fit of light curve data in three colors (B, V, and I_c). The photometric mass ratio estimated ($q = 0.235$) from W-D analyses is at odds with a theoretically computed value (0.45) published in 1980 (Brancewicz and Dworak), but consistent with that recently published by Yang *et al.* (2010). Despite lacking critical spectroscopic or radial velocity data for this binary system, the light curve analysis herein based on a revised B-V color-index value for AO Ser provide strong evidence for an Algol-type binary system composed of an A7V main-sequence primary and K1 to K3 subgiant secondary. This classification is much cooler than previously considered by all other investigators. Finally, Fourier analysis did not convincingly reveal any underlying periodicity other than that expected from the dominant orbital period. However, it is possible that the magnitude of any putative δ Sct-type pulsation is below the limits of detection for the equipment used in this investigation.

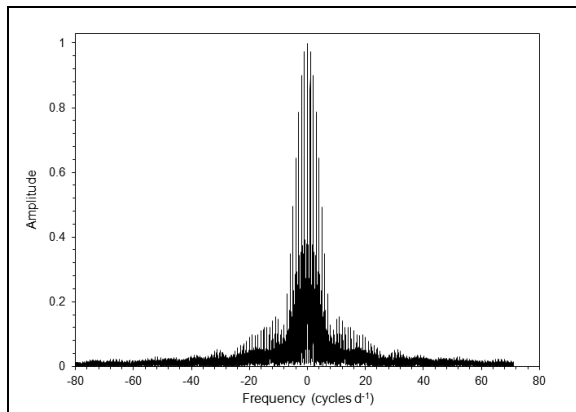


Figure 9. Spectral window for AO Ser exhibits strong side-bands offset by 1 cycle per day resulting from daily sampling aliases; results are shown for B-band residuals following Roche modeling, however, similar findings were observed in V and I_c.

5. Acknowledgements

Special thanks are due to the NASA Astrophysics Data System hosted by the Computation Facility at the Harvard-Smithsonian Center for Astrophysics for providing convenient access to published literature. This research has also made use of the NASA/IPAC Infrared Science Archive, which is operated by the Jet Propulsion Laboratory, California Institute of Technology, under contract with the National Aeronautics and Space Administration. The contribution of all the dedicated folks contributing to or managing the variable star time-of-minima data housed at the AAVSO, B.R.N.O., BBSAG, VSOLJ, and IBVS websites is gratefully acknowledged. This investigation has also made use of the SIMBAD database, operated at CDS, Strasbourg, France and the Bundesdeutsche Arbeitsgemeinschaft für Veränderliche Sterne (BAV) website in Berlin, Germany.

6. References

Alton, K. B. (2010). “A Unified Roche-Model Light Curve Solution for the W UMa Binary AC Bootis.” *JAASO* **38**.

Applegate, J. H. (1992). “A mechanism for orbital period modulation in close binaries.” *Ap. J.* **385**, 621.

Baldwin, M., Samolyk, G. (2007). “Observed Minima Timings of Eclipsing Binaries No. 12.” AAVSO, Cambridge, MA.

Biermann, P., Hall, D. S. (1973). *Astron. Astrophys.* **27**, 249.

Borkovits, T., Van Cauteren, P., Lampens, P., et al. (2008). “New and Archive Times of Minima of Eclipsing Binary Systems.” *IBVS* **5835**, 3.

Bradstreet, D. H., Steelman D. P. (2002). “Binary Maker 3.0 – An Interactive Graphics-Based Light Curve Synthesis Program Written in Java.” *Bull. A.A.S.* **34**, 1224.

Brancewicz, H. K., Dworak, T. Z. (1980). “A catalogue of parameters for eclipsing binaries.” *Acta Astron.* **30**, 501.

Brát, L., Zejda, M., Svoboda, P. (2007). “B.R.N.O. Contributions #34.” *Open Eur. J. Var. Stars* **74**, 65.

Brát, L., Šmelcer, L., Kučáková, H., et al. (2008). “B.R.N.O. Times of minima.” *Open Eur. J. Var. Stars* **94**.

Breger, M. (2000). “Asteroseismology of Delta Scuti Stars.” *Balt. Astron.* **9**, 149.

Breger, M., Stich, J., Garrido, R., et al. (1993). “Non-radial Pulsation of the Delta-Scuti Star BU Cancri in the Praesepe Cluster.” *Astron. Astrophys.* **271**, 482.

Budding, E., Demircan O. (2007). *Introduction to Astronomical Photometry*. Cambridge University Press, New York.

Christiansen, J. L., Derekas, A., Ashley, M. C. B., et al. (2007). “The first high-amplitude δ Scuti star in an eclipsing binary system.” *MNRAS* **382**, 239.

Diethelm, R. (2009). “Timings of Minima of Eclipsing Binaries.” *IBVS* **5894**, 7.

Diethelm, R. (2011). “Timings of Minima of Eclipsing Binaries.” *IBVS* **5992**, 16.

Doğru, S. S., Erdem, A., Dönmez, A., et al. (2009). “New Times of Minima of Some Eclipsing Binary Stars.” *IBVS* **5893**, 2.

Doğru, S. S., Erdem, A., Aliçavuş, F., et al. (2011). “CCD Times of Minima of Some Eclipsing Variables.” *IBVS* **5988**, 2.

Eddington, A.S. (1926). “The reflection effect in eclipsing variables.” *MNRAS* **86**, 320.

Fitzgerald, M. P. (1970). “The Intrinsic Colours of Stars and Two-Colour Reddening Lines.” *Astron. Astrophys.* **4**, 234.

- Flower, P. J. (1996). “Transformations from Theoretical Hertzsprung-Russell Diagrams to Color-Magnitude Diagrams: Effective Temperatures, B-V Colors, and Bolometric Corrections.” *ApJ*, 469, 355.
- Ghedini, S. (1981). “A method for evaluating the epoch of minimum of an eclipsing variable - the sliding integrations.” *Societa Astronomica Italiana* **52**, 633.
- Hall, D. S. (1989) “The relation between RS CVn and Algol.” *Space Science Reviews* **50**, 219.
- Harmanec, P. (1988). “Stellar masses and radii based on modern binary data.” *Bull. Astron. Inst. Czechosl.* **39**, 329.
- Hoffmeister, C. (1935). “162 neue Veränderliche.” *Astron. Nachr.* **255**, 401.
- Hübscher, J., Lehmann, P. B., Monninger, G., et al. (2010). “BAV-Results of Observations – Photoelectric Minima of Selected Eclipsing Binaries and Maxima of Pulsating Stars.” *IBVS* **5918**, 10.
- İbanoğlu, C., Soyduğan, F., Soyduğan, E., Dervişoğlu, A. (2006). “Angular momentum evolution of Algol binaries.” *MNRAS* **373**, 435.
- Koch, R. H. (1961) “Times of minimum light for several eclipsing binaries.” *Astron. J.* **66**, 35.
- Kim, S.-L., Kang, Y. B., Koo, J.-R., et al. (2004). “Discovery of a short-periodic pulsating component in the Algol-type eclipsing binary system AO Ser.” *IBVS* **5538**, 1.
- Kreiner, J. M. (2004). “Up-to-Date Linear Elements of Eclipsing Binaries.” *Acta Astron.* **54**, 207.
- Kwee, K. K. and van Woerden, H. (1956). “A method for computing accurately the epoch of minimum of an eclipsing variable.” *B.A.N.* **12**, 327.
- Kwee, K. K. (1958). “Investigation of variations in the period of sixteen bright short-period eclipsing binary stars.” *B.A.N.* **14**, 131.
- Lampens, P., Kleidis, S., Van Cauteren, P., et al. (2010). “New Times of Minima of 36 Eclipsing Binary Systems.” *IBVS* **5933**, 3.
- Lenz, P., Breger, M. (2005). “Period04 User Guide.” *Commun. Asteroseismol.* **146**, 53.
- Lucy, L. B. (1967). “Gravity-Darkening for Stars with Convective Envelopes.” *Z. Astrophys.* **65**, 89.
- Manzoori, D. (2008). “The O-C curve analysis and simultaneous light curve solutions of classical Algol system U Cephei.” *Ap&SS* **318**, 57.
- Mikuž, H., Dintinjana, B., Prša, A., et al. (2002). “Period Change and Surface Activity of the Eclipsing Binary UV Leonis.” *IBVS* **5338**.
- Mkrtychian, D. E., Kusakin, A. V., Rodriguez, E., et al. (2004). “Frequency spectrum of the rapidly-oscillating mass-accreting component of the Algol-type system AS Eri.” *Astron. Astrophys.* **419**, 1015.
- MPO Canopus ©1996-2008. *MPO Canopus and PhotoRed Installation Guide and Reference Manual*. Bdw Publishing, Colorado Springs, CO 80908.
- Nelson, R. H. (2007). “Minima©2002, 2006: “Astronomy Software by Bob Nelson” URL: <http://members.shaw.ca/bob.nelson/software1.htm>.
- Nelson, R. H. 2009, “WDwint Version5.6a: “Astronomy Software by Bob Nelson” URL: <http://members.shaw.ca/bob.nelson/software1.htm>.
- Parimucha, Š., Dubovský, P., Baludanský, D., et al. (2009). “Minima Times of Selected Eclipsing Binaries.” *IBVS* **5898**, 8.
- Pop, A. (2005). “On the Orbital Period Modulation of the Eclipsing Binary System Y Leonis.” *Proceedings of ASP Conference Series* **335**, 263.
- Press, W., Teukolsky, S. A., Flannery, B. P., Vetterling, W. T. (1992). “Numerical Recipes in FORTRAN.” Cambridge Univ. Press. Cambridge.
- Prša, A., Zwitter, T. (2005). “A Computational Guide to Physics of Eclipsing Binaries. I. Demonstrations and Perspectives.” *Ap. J.* **628**, 426.
- Qian, S. (2002). “Orbital Period Studies of Two Algol-Type Eclipsing Binary Systems: TY Pegasi and X Trianguli.” *PASP* **114**, 650.
- Rensbergen, W. van De Greve, J. P., Mennekens, N., et al. (2011). “Mass loss out of close binaries. II.” *Astron. Astrophys.* **528**, A16.
- Rucinski, S. M. (1969). “The Proximity Effects in Close Binary Systems. II. The Bolometric Reflection Effect for Stars with Deep Convective Envelopes.” *Acta Astron.* **19**, 245.

Samolyk, G. (2008). “Recent Minima of 184 Eclipsing Binary Stars.” *JAAVSO* **36**, 186.

Samolyk, G. (2010). “Recent Minima of 161 Eclipsing Binary Stars.” *JAAVSO* **38**, 85.

Samolyk, G. (2011). “Recent Minima of 144 Eclipsing Binary Stars.” *JAAVSO* **39**, 94.

Schlegel, D., Finkbeiner, D., Davis, M. (1998). “Application of SFD Dust Maps to Galaxy Counts and CMB Experiments.” *Wide Field Surveys in Cosmology*. 14th IAP Meeting, May 26-30, Paris.

Schwarzenberg-Czerny, A. (1996). “Fast and Statistically Optimal Period Search in Uneven Sampled Observations.” *Ap. J.* **460**, L107.

Surkova, L. P., Svechnikov, M. A. (2004). “Semi-detached eclipsing binaries (Surkova+, 2004).” *VizieR On-line Data Catalog*: V/115.

van Hamme, W. (1993). “New limb-darkening coefficients for modeling binary star light curves.” *Ap. J.* **106**, 2096.

von Zeipel, H. (1924). “Radiative equilibrium of a double-star system with nearly spherical components.” *MNRAS* **84**, 702.

Warner, B. D. (2007). “Initial Results of a Dedicated H-G Project.” *Minor Planet Bulletin* **34**, 113.

Wilson, R. E., Devinney, E. J. (1971). “Realization of Accurate Close-Binary Light Curves: Application to MR Cygni.” *Ap. J.* **166**, 605.

Wilson, R. E. (1979). “Eccentric orbit generalization and simultaneous solution of binary star light and velocity curves.” *Ap. J.* **234**, 1054.

Yang, Y.-G., Hu, S.-M., Guo, D.-F., Wei, J.-Y., Dai, H.-F. (2010). “Photometric Properties for Selected Algol-type Binaries. II. AO Serpentis and V338 Herculis.” *Astron. J.* **139**, 1360.

Zavros, P., Tstantilas, S., Rovithis-Livaniou, E. (2008). “AO Serpentis: Observations and Interpretations.” *Romanian Astronomical Journal Suppl.* **18**, 113.

The Light at Night Mapping Project: LAN MAP 1, the Tucson Basin

E.R. Craine

*Western Research Company, Inc. and STEM Laboratory, Inc.
3275 West Ina Road, Suite 217, Tucson, AZ 85741
ercraine@stemlab.org*

B.L. Craine

*Western Research Company, Inc. and STEM Laboratory, Inc.
3275 West Ina Road, Suite 217, Tucson, AZ 85741
blcraine@wrc-inc.com*

P.R. Craine

*STEM Laboratory, Inc.
Tucson, AZ 85741
prcraine@gmail.com*

E.M. Craine

*STEM Laboratory, Inc.
Tucson, AZ 85741
ecraine@dakotacom.net*

Abstract

Tucson, Arizona, once billed as the Astronomical Capital of the World, has long been home to at least ten major astronomical institutions and facilities. The region also hosts numerous productive amateur observatories and professional-amateur astronomical collaborations. In spite of the implementation of progressive night time lighting codes, the continued growth of the region has arguably deprived Tucson of its title, and threatens the future of some if not all of these facilities. It has become apparent that there are several difficulties in regulating this lighting environment. It is not easy to model the actual effects of new or changed lighting fixtures, there are compelling economic conflicts that must be considered, and adherence to various guidelines is often ignored. Perhaps the most fundamental problem is that there have historically been no comprehensive measures of either light at night or sky brightness over the extended growth areas. What measurements do exist are inhomogeneous and poorly accessible spot measurements at some observatory sites. These have little to tell us about the actual light distributions in the overall region, and rarely are informative of the specific light sources that offend the observatory sites. Tucson remains, for the time, an important astronomical resource. Because of its astronomical and lighting code circumstances, it is an interesting and valuable laboratory for studying these issues. In this paper we introduce an innovative new 5-year project to comprehensively map both sky brightness and associated artificial lighting over extended areas of development in the vicinity of important astronomical institutions. We discuss the various vectors employed in data collection; we outline the protocols used for each methodology, give examples of the data collected, and discuss data analysis and conclusions. This program has been underway since January 2012, and has already produced results of interest to professional and amateur astronomers alike.

1. Introduction

During the past 15-20 years there has been a steady increase in collective sensitivity to issues surrounding the quality of artificial light at night. Prior to this time, relatively little thought was given to these issues, but now whole communities are enacting lighting codes directed at requiring efficient, effective, and non-intrusive artificial lighting. In many cases the net results of these codes are not well un-

derstood, nor is it clear how to measure compliance, or identify and verify mitigation procedures. A common approach to planning is to implement unverified computer models as a best guess at the resultant impact of lighting projects, but systematic, high resolution measurements of real effects are rare or non-existent.

The Light at Night Mapping Project (LAN MAP) is a unique program to address this problem. The prototype LAN MAP project is focused on the

Tucson, AZ urban area as a demonstration of the utility of actual measurement of community wide lighting output, and is known as LAN MAP 1.

An approximately 1,000 square mile area, centered roughly on Davis Monthan AFB, will be mapped from the air by collecting sky brightness data in the survey. These data will be collected using STEM Laboratory, Inc. (STEM) Sky Brightness Meter (SBM) and LAN Monitor (LANM), single channel and multispectral photometers. The data collection will be targeted on multiple clear, moonless, nights and the airborne data will be both up- and down-looking measurements.

The LAN MAP 1 survey region is shown in Figure 1. The data collection from aircraft will be at an altitude of 8,000 ft MSL. This will allow safe clearance of the mountains in the flight operations area, and will provide data also relevant to many astronomical observatories in the surrounding area. The airborne data will be supplemented by both mobile and static ground-based data. These data can be used to scale the airborne observations to comparable ground intensities and allow for future comparisons from ground based measurements.

Each survey session will be repeated periodically for the projected five year duration of the project resulting in the most detailed and comprehensive LAN survey analysis yet undertaken.

We will also obtain limited ground based photography of some of the encompassed light installations, both to illustrate the good and bad installations and to show the changes in lighting over the project time line.

2. Background

Tucson, Arizona is a southwestern desert community that grew from a population of 120,000 in 1950 to 220,000 in 1960, by which time Kitt Peak National Observatory had been installed west of the town. In 2010 the city population was about 546,000 and the urban metropolitan area was over 1.02 million, with a current annual growth rate of about 4%.

This is now a sprawling community encompassing numerous suburban areas and adjacent cities. City lights, once confined to a few square miles, now spread over an area well in excess of 1,000 square miles.

The city is largely situated on the floor of a desert basin (about 2,600 ft MSL), nearly completely ringed by mountain ranges of up to about 7,000 – 8,000 ft MSL. Many of these mountain peaks host facilities and multiple telescopes, of approximately a dozen major astronomical observatories.

In addition to the professional facilities, there are numerous privately owned observatories, many engaged in productive astronomical research, scattered throughout the region. Some of these reside close to the several National Forest, State Park, and wildlife preserve lands in the region. All are concerned with increases in LAN that accompany the population growth and expanded areas of development.



Figure 1. FAA Aeronautical Chart, Phoenix Sectional, Tucson, AZ surroundings, showing the LAN MAP 1 flight grid throughout the Tucson basin.

The LAN MAP 1 project is using multiple mobile photometers to provide the first comprehensive, quantitative monitoring of LAN in the Tucson Basin area that impacts all of these light sensitive activities.

3. SBM and LANM Photometers

Mobile, temporal sky brightness measurements benefit from access to an integrated photosensor, Global Positioning System (GPS) receiver, data logger, microcontroller and power source. Such a system has further value if it can operate in an automatic autonomous mode. Compact size and light weight are additional advantages. With this specification in hand the design and construction of a family of such units was undertaken by STEM Laboratory (Tucson, AZ). We briefly summarize three members of the family in

this section: SBM Model 4, LANM Model 5, and LANM Model 6.

3.1 SBM Model 4

The SBM Model 4 is the first of the photometers that STEM completed beyond the prototype stage, and used in a variety of mobile ground and air based sky brightness data collection projects. This unit uses a single light-to-frequency silicon photodiode detector. In its stock form it is optically filtered with an IRC-20 infrared cut filter (Sunex), as shown in Figure 2. The unit operates with an integrated GPS module which is polled every two seconds to yield date, time, geographic coordinates, and altitude. The GPS output is a standard National Marine Electronics Association (NMEA) GPS data suite; c.f. SIRF (2005) and NMEA (2011). Simultaneously, the photodiode is sampled for light intensity ($\text{mag}/\text{arcsec}^2$ and cd/m^2). These quantities are coordinated in the onboard microcontroller and written to an onboard micro-SD card writer, from which they can be transferred to a project data analysis computer upon completion of the data collection flight.

3.2 LANM Model 5

The Light at Night Monitor, LANM Model 5, is built on the same platform as the SBM Model 4, but has two of the silicon photodiode detectors that are read simultaneously. The GPS data polled are the same as the SBM Model 4, with the exception of the inclusion of the speed of the vehicle carrying the LANM Model 5. Also, there are two channels of photometric data rather than just one. The optical filtration is generally an IRC-20 infrared cut filter; otherwise the spectral response is that of the silicon photodiode. Another distinguishing feature of the LANM Model 5 is that the two photodiodes are aligned with a separation of 180° on the optical axis, ensuring that they are looking in opposite directions. For purposes of airborne operations, this ideally results in one detector looking at the zenith and the other simultaneously observing the nadir. Thus, the LANM Model 5, operated in airborne mode, provides a good contrast between sky brightness overhead, and the distribution of light intensity on the ground that is scattered upward to contribute to sky brightness.

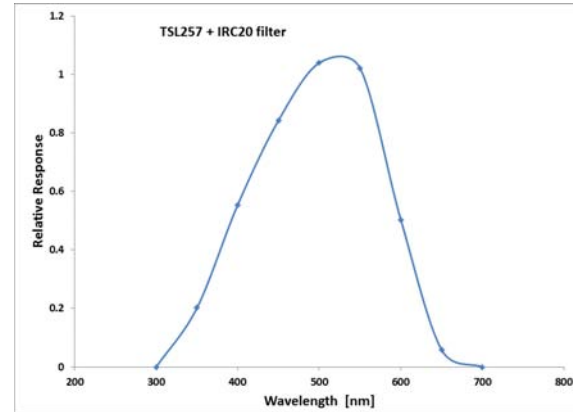


Figure 2. The spectral response curve of the SBM Model 4 Sky Brightness Meter and the LANM Model 5 photometer.

3.3 LANM Model 6

The LANM Model 6 is electronically identical to the LANM Model 5. The distinguishing feature of the LANM Model 6 is that the two detectors are aligned to look simultaneously at the same target field, and the optical filtration is different from the other units. We are using the LANM Model 6 somewhat as a custom system where we can insert specific optical filters of interest. Our early work involves two filter combinations: 1) IRC-21 infrared cut + Wratten 47 and 2) IRC-21 infrared cut + Wratten 58; yielding blue (B) and visual (V) band data for each scene, as shown in Figure 3. The LANM Model 6 is thus most useful for defining a color (such as B-V) for a relatively bright area (since the introduction of additional optical filters reduces the sensitivity of the photometric system).

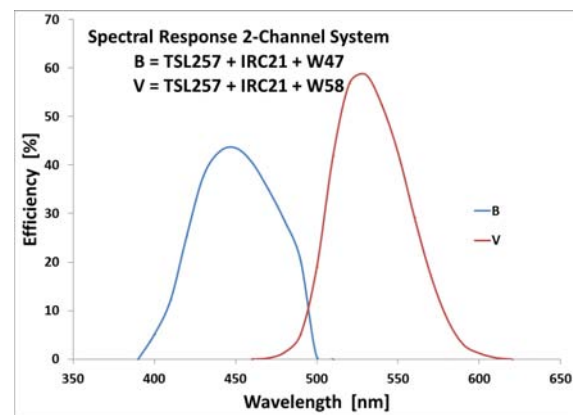


Figure 3. The spectral response curve of the LANM Model 6 photometer.

4. Aircraft Photometer Installations

The aircraft used for collecting the initial airborne data was a Mooney M231. Subsequent flight programs were conducted with a Cessna 182Q. Both are high-performance aircraft capable of cruise speeds over 150 KIAS (approximately 170 mph). Such speeds can impose high aerodynamic loads on externally mounted devices and space the data points over a widely dispersed area. A speed of approximately 100 mph over the ground has been found to work well. This requires the airspeed to be adjusted to the particular atmospheric conditions on each flight. The greatest effect comes from the winds, which may be much higher at altitude than at ground level. If the wind direction is parallel to the grid legs then the total groundspeed variation will be twice the wind speed. This can easily introduce variations of data point spacing of 20% if not corrected. An additional source of variation comes from the fact that the groundspeed will be higher for a given indicated airspeed as the airplane is operated at higher altitudes.

High-performance aircraft have been found to be particularly well suited to gathering data because they can quickly cover the distance between the base airport and the survey area and because they generally have sufficient fuel capacity for long duration flights. They have tended to be more stable than lighter aircraft, which eases pilot fatigue and yields higher quality data.

The photometers must be mounted to the airplane such that no part of the aircraft structure obscures the detector's field of view. All aircraft approved for night operations carry a variety of lights which have the potential to impact the measurements. The lights are usually arranged such that they will not affect the pilot's night vision, so mounting the photometer near the crew cabin can help minimize the effect of aircraft lighting. The surface of the airplane can be sufficiently reflective to bounce light (ambient or aircraft) into the photometer's field of view so care must be taken in planning the photometer mounting.

Two installations have been used: a cantilever mount and an in-wing mount. The cantilever mount is a dedicated bracket which bolts to the bottom of the wing, near the leading edge, and holds the photometer ahead of the wing. This allows the photometer sensors to face upward and downward without interference from the airframe. The drawbacks are that the bracket must be carefully designed to prevent adverse aerodynamic effects on the airplane. The bracket itself is subjected to aerodynamic forces as well as maneuvering forces (G-forces). The maximum operating speed of the airplane is greatly limited with a cantilever mount in place. Additionally the airplane

must be flown very gently. The existing cantilever mount has been tested at airspeeds up to 105KIAS and forces of +1.3/-0.5G.

The in-wing mount is particularly well suited for down-looking installations, though we have engineered designs for upward looking installations as well. As currently implemented, such a mount introduces no aerodynamic changes and does not impact the aircraft performance. This can be useful for making measurements at long distances from the aircraft base of operations since the full cruising speed of the airplane can be utilized.



Figure 4. LANM Model 5 and LANM Model 6 mounted on a C-182Q aircraft wing. The former is on the cantilevered mount, and the latter inside the blue wing panel.

In both cases the photometers must be mounted so that they will be oriented vertically during flight. This means that the dihedral angle of the wings must be compensated for, and average angle of attack in cruise phase flight must be considered. Note that this may be different from the level attitude when the airplane is on the ground. It is not sufficient to simply adjust the mount to level the SBM while on the ground. The external mounting bracket has been aligned with the airflow streamlines at the cruise condition to minimize aerodynamic loads.

We have simplified determination of angular displacements of the photometers during data collection by developing a three axis accelerometer device called the Time-Orientation-Position (TOP) Logger. This device automatically logs time, magnetic heading, pitch, roll, latitude, and longitude of the aircraft. This data stream can be integrated with the photometry data stream to indicate when the photometers are looking “off target”, and those data points can be removed from the analyzed data set.

5. LAN MAP 1 Protocols

Details of the airborne flight protocols generally employed by STEM can be found in Craine and Craine (2011). We summarize the key sequences for LAN MAP 1 below:

- The flight path for the survey segment to be flown is programmed into a ForeFlight moving map navigation system.
- Final weather and astronomical boundary condition checks are made.
- Photometers are installed and initiated; GPS lock and data logging are confirmed.
- Aircraft pre-flight checks are completed.
- The flight is launched and communication is maintained with local air traffic control.
- The survey path is flown typically for about 3 hours.
- A simultaneous ground mobile sky brightness measurement path is driven using a SBM Model 4 mounted on a car.
- Upon completion of the flight pattern the aircraft is returned to its home base and the photometers are shut down.
- Data files are all downloaded and storage folders are created in the Sky Brightness Data Archive (SBDA).
- Data are pre-processed.
- Data are available for processing and analysis.
- Flights are repeated as needed to achieve the desired spatial density of observations.

6. Project Status

During 2012, STEM initiated a comprehensive, community wide, light at night mapping program for the Tucson, Arizona area. In this section we show examples of some of the flight test data collected in anticipation of the official start of LAN MAP 1. The flight test data were collected over the northwestern most quadrant of the LAN MAP 1 survey area.

These data were collected with a LANM Model 5 photometer, using both zenith and nadir looking channels. The data were optically constrained by the silicon detector sensitivity curve as modified by an IRC-20 infrared cut filter as shown in Figure 2.

The test flights were for patterns flown at altitudes of 5,000, 6,500, and 8,000 ft MSL; the data

shown here were obtained at 8,000 ft MSL. Flights were timed to ensure that the aircraft arrived at the data collection Initial Point (IP) shortly after astronomical twilight. The flights were conducted in the complete absence of moonlight, and were completed prior to Pima County lighting code curfew for commercial lighting.

In Figures 5 and 6 we show sky brightness isophotal maps plotted on Google Earth aerial images of Tucson, Arizona.

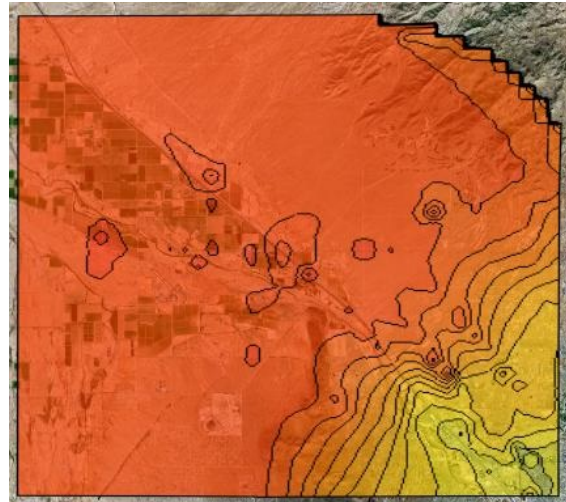


Figure 5. Sky brightness data over the NW quadrant of Tucson, Arizona plotted on a Google Earth aerial image. This plot is constructed with 15 levels of intensity resolution represented as mag/arcsec². The light yellow is the bright end of the scale.

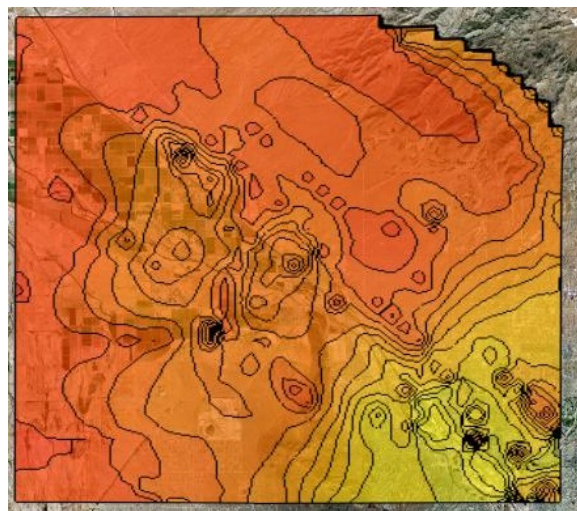


Figure 6. The same flight as Figure 5, plotted for the down-looking data.

To understand these figures one must appreciate that the isophotal contours indicate the brightness of the sky as seen by an observer looking up from each

geographical location of interest on the aerial photograph.

Even casual comparison of these up- and down-looking plots indicates localized bright areas on the ground that clearly contribute to anomalously bright areas in the sky. It is a simple matter to use the display software to zoom through the graphics overlay at those points to identify the specific contributing light sources.

In 2012 February, the first of the formal LAN MAP 1 data collection flights was conducted. The ground path for this flight is shown in Figure 7. The path data have been truncated to include only that portion of the flight conducted in the LAN MAP 1 survey area. The parallel flight legs on this flight were spaced three miles apart, and the intervening gaps will be filled by later flights. Slight deviations in the path are a consequence of Air Traffic Control vectoring in the vicinity of Tucson International Airport and Davis Monthan AFB to accommodate a simultaneous flight test program of the Boeing 787 Dreamliner.



Figure 7. The ground track of the first of the LAN MAP 1 data flights, plotted on a Google Earth satellite image.

Quick look representations of these initial data can be seen in Figures 8 and 9. In Figure 8 we show an isophotal map of the sky brightness data as seen over a substantial portion of the Tucson Basin. Figure 9 shows the same region, but looking down at the lights on the ground. These data are much more sparsely distributed than that what we expect for the completed survey, but are still quite suggestive of the lower frequency patterns of sky brightness over Tucson.

In the case of Figures 8 and 9, the data are binned at 15 levels. This is done to provide a more realistic picture of the smoothed appearance of both sky brightness and ground lights. Because the survey grid is only partially filled on this first flight, binning the data to provide more contour intervals introduces

numerous spurious features that can be very misleading in interpreting the images.

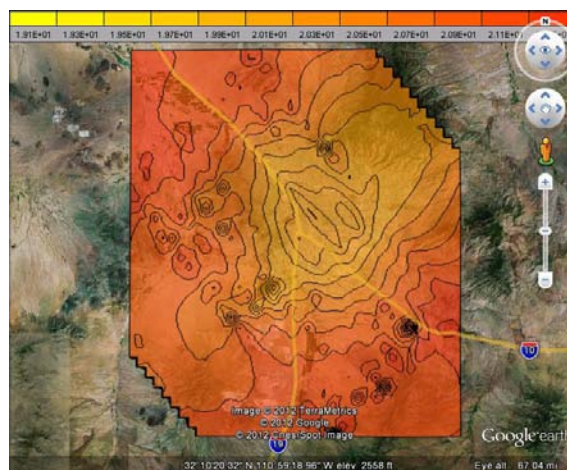


Figure 8. Sky brightness distribution over the Tucson Basin as seen from the flight of Figure 7.

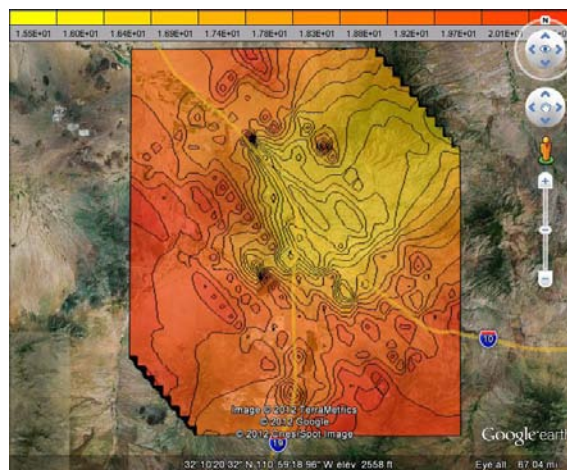


Figure 9. Ground lighting distribution as seen from the flight of Figure 7.

7. Conclusion

The tools and protocols developed by STEM to enable low-altitude wide-area-survey automatic photometry of both the ground and the sky are offering a powerful new way to look at issues of light trespass. These protocols can be applied to ground, air, and sea-going vehicles, and offer community planners, developers, and managers of light sensitive facilities a unique means of evaluating the impact and evolution of light at night.

Even a preliminary look at the LAN MAP 1 data demonstrates areas of concern for local astronomical facilities. Contrary to conventional wisdom on the population expansion of Tucson and its suburbs, the brightest expansion of the Tucson light dome is to the

northeast, where it clearly poses a threat to the University of Arizona observatories on Mt. Bigelow and Mt. Lemmon. Conversely, observatories on Mt. Wrightson, to the south of Tucson, remain in a fairly dark region. Sky brightness over Mt. Wrightson is quite likely to evolve for the worse as development expands down the I-19 corridor, and leaps over the Santa Rita Mountains to the southeast.

It will be of interest to watch annual changes in LAN MAP 1 data to the west of Tucson as well. There, development has for several years progressed west of the Tucson Mountains, and is steadily filling Avra Valley and points south and west, posing significant threats to Kitt Peak. Kitt Peak has almost certainly seen the end of large telescope installation, but preservation of existing facilities will remain a priority for at least a few more years.

8. Acknowledgements

The authors would like to thank Scott Fouts for some of the piloting duties and Ed Tuohy for mechanical assistance with one of the airplanes used in the data collection. We gratefully acknowledge an anonymous corporate donor for very generous grant support to undertake this program.

9. References

Craine, E. R., Craine, B. L., Craine, E. M. (2011). “The Sky Brightness Data Archive (SBDA).” in *Proceedings for the 30th Annual Symposium on Telescope science* (Warner *et al.*, eds). pp 45-52. Society for Astronomical Sciences, Rancho Cucamonga, CA.

Craine, P. R., Craine, E. R. (2011). “Airborne Light at Night (LAN) Photometry Protocols.” STEM TechRep-11-1203. STEM Laboratory, Tucson, AZ.

NMEA (2011). www.nmea.org

SIRF (2005). *NMEA Reference Manual*” SiRF Tech, Inc., San Jose, CA.

Observing Double Stars

Russell M. Genet

*California Polytechnic State University and Cuesta College
4995 Santa Margarita Lake Road, Santa Margarita, CA 93453
RussMGenet@aol.com*

B.J. Fulton, Federica B. Bianco, John Martinez

*Las Cumbres Observatory Global Telescope
6740B Cortona Drive, Ste. 102, Goleta, CA 93177
fbianco@lcogt.net, bjfulton@lcogt.net, jmartinez@lcogt.net*

John Baxter, Mark Brewer, Joseph Carro, Sarah Collins, Chris Estrada,

*Jolyon Johnson, Akash Salam, Vera Wallen, Naomi Warren
Cuesta Community College, Highway 1, San Luis Obispo, CA 93403
Jrbax@aol.com, mrk.a.brewer@gmail.com, jcarro@charter.net, sjcollins94@gmail.com,
pr1est0112@hotmail.com, jolyonjohnson@gmail.com, akashumm@sbcglobal.net,
jvwallen@charter.net, renoman599@gmail.com*

Thomas C. Smith

*Dark Ridge Observatory, 701 NM Highway 24, Weed, NM 88354
tcsmith@darkridgeobservatory.org*

James D. Armstrong

*University of Hawaii, Institute for Astronomy, and Las Cumbres Observatory Global Telescope
34 Ohiaku Street, Makawao, Maui, Hawaii 96768
jd@ifa.hawaii.edu*

Steve McGaughey

*Haleakala Amateur Astronomers, 5 Kamauhalii Way, #3-A, Wailuku, Maui, HI 96793
stevemcgee2@yahoo.com*

John Pye

*University of Hawaii Maui College, 310 W. Ka'ahamanu Ave., Kahului, HI 96732
jpye@hawaii.edu*

Kakkala Mohanan, Rebecca Church

*University of Hawaii, Leeward Community College, 96-045 Ala Ike St., Pearl City, HI 96782
mohanastrogglcc@gmail.com, rjchurch@hawaii.edu*

Abstract

Double stars have been systematically observed since William Herschel initiated his program in 1779. In 1803 he reported that, to his surprise, many of the systems he had been observing for a quarter century were gravitationally bound binary stars. In 1830 the first binary orbital solution was obtained, leading eventually to the determination of stellar masses. Double star observations have been a prolific field, with observations and discoveries—often made by students and amateurs—routinely published in a number of specialized journals such as the *Journal of Double Star Observations*. All published double star observations from Herschel's to the present have been incorporated in the *Washington Double Star Catalog*. In addition to reviewing the history of visual double stars, we discuss four observational technologies and illustrate these with our own observational results from both California and Hawaii on telescopes ranging from small SCTs to the 2-meter Faulkes Telescope North on Haleakala. Two of these technologies are visual observations aimed primarily at published “hands-on” student science education, and CCD observations of both bright and very faint doubles. The other two are recent technologies that have launched a double star renaissance. These are lucky imaging and speckle interferometry, both of which can use electron-multiplying CCD cameras to allow short (30 ms or less) exposures that are read

out at high speed with very low noise. Analysis of thousands of high speed exposures allows normal seeing limitations to be overcome so very close doubles can be accurately measured.

1. Introduction

Observing double stars has engaged generations of student, amateur, and professional astronomers for the better part of three centuries. Over 100,000 double stars have been discovered. As each year goes by, new doubles are discovered and the observations of already known doubles continue to accumulate.

A wide range of telescopes, instruments, and techniques are currently used to measure the separations and position angles of double stars. Telescopes range from a 3-inch Tasco refractor equipped with a \$150 astrometric eyepiece observing relatively wide optical doubles (Grisham *et al.*, 2008) to a 10-meter Keck reflector with adaptive optics/laser guide star observing very close late-M binaries (Dupuy *et al.*, 2012). Instruments include visual eyepieces and filar micrometers, regular CCD cameras, and fast, low noise EMCCD frame transfer cameras. Advanced techniques include blind or other deconvolution strategies, lucky imaging, and speckle interferometry.

Although beyond the scope of this paper, the absolute cutting edge with respect to close separation (and hence short binary periods) is amplitude interferometry arrays such as the Center for High Angular Resolution Array (CHARA) on Mt. Wilson (McAlister 1999). Six 1-meter telescopes in a “Y” configuration interferometer provide milli-arcsecond resolution allowing binaries with orbital periods of just a day to be observed. In this paper we will, after a brief history of double star observations, describe two spreadsheets we have developed to aid us in selecting doubles for observation. We will then describe both visual and CCD observations we make with students that have both scientific and educational goals. Finally, we will describe two advanced techniques we are exploring—lucky imaging and speckle interferometry—to aid us in observing close double stars. Our observations were made on 8- to 32-inch telescopes in California, and 9-inch to 2-meter telescopes in Hawaii.

Most of the coauthors of this paper will be giving talks at the Maui International Double Star Conference in February 2013. In many cases they will be meeting each other for the first time, and will also be meeting other double star observers from around the planet. For details on this conference see www.AltAzInitiative.org.

2. Early Double Star Observations

Galileo thought that the sun was the center of the universe and stars were just points of light on a nearby sphere. For those, contrary to Galileo, who thought stars were distant suns, he suggested they should look for and observe close double stars—one bright and one faint that happened, by chance, to appear close together along the line-of-sight from Earth. If the bright star was nearby and the faint one far away, then the nearby bright star should shift its position with respect to the faint star over a six month period due to the rotation of the Earth around the sun (parallax).

Following up on Galileo’s suggestion, William Herschel began measurements of the separation of position angles and separation of double stars in earnest in 1779. Three years later he reported his observations of 269 binaries to the Royal Society (Herschel 1782). Continued observations led, a couple of decades later, to the somewhat unexpected conclusion by Herschel (1803) that many double stars were gravitationally bound binaries. Interestingly, John Michel (1767) had earlier reported to the Royal Society that, based on a statistical analysis of a few bright visual double stars, he had concluded they occurred at a higher frequency than one would expect due to chance alignment alone and hence were probably truly gravitationally bound stars. It is probably a good thing that Herschel was unaware of Michel’s paper or he might not have initiated his search for and a measurement of double stars, as his goal was determining parallaxes.

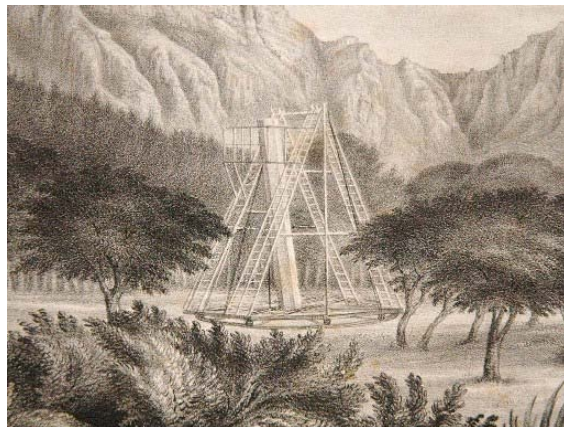


Figure 1. William Herschel’s 20-foot telescope was relocated to Table Mountain near Cape Town, South Africa, where his son John observed double stars in the southern skies.

In the mid 1800's, while he was director of the Dorpat Observatory in what was then Livonia, Friedrich Georg Wilhelm von Struve made micrometric measurements of 2,714 double stars from 1824 to 1837 and published these in his work *Stellarum duplicium et multiplicium mensurae micrometricae*. F.G.F. von Struve's son, Otto Wilhelm von Struve, (1897-1963), continued his father's work using a 15-inch refractor at the Pulkovo Observatory near St. Petersburg, cataloging several thousand double stars. Another notable double star observer was Robert Innes at the Meteorological Observatory in Johannesburg, South Africa. He compiled in 1927 *The Southern Double Star Catalog* consisting of 1,600 entries. Robert Aitken, with the help of collaborator W.J. Hussey, published in 1932 the *New General Catalogue of Double Stars within 120° of the North Pole* consisting of 17,180 doubles. The Lick Observatory at Mount Hamilton near San Jose, CA, published the 1963 *Index Catalog of Visual Double Stars*, containing 64,250 objects covering the entire sky. In 1965 it was transferred to the United States Naval Observatory as the *Washington Double Star Catalog* (WDS) which now contains over 100,000 double stars.

Observations of the double star Zeta Ursae Majoris were indirectly used by Savary (1827) to obtain an orbital solution, while a solution directly using all the observations was provided shortly thereafter by John Herschel. Orbital solutions, when combined with stellar parallaxes and other data, led to the determination of stellar masses, a key parameter influencing stellar evolution. Parallaxes were hard to come by until the Hipparcos satellite accurately determined a large number of parallaxes (Perryman 2011). The *Sixth Orbital Catalog* provides orbits for 2,187 binaries (as of 1 January 2012).

For more detailed historical expositions, please see Aitken (1918), Herrmann (1973), Couteau (1978), Argyle (1986), Tanguay (2003), and Hoskin (2011).

3. Two Spreadsheets

Students in Genet's astronomical research seminar (described below in the next section) have, for many years, used Haas' (2006) catalog of 2,100 doubles to pick out relatively bright, well-separated double stars for their first projects. The Haas catalog was convenient for students to use as it listed doubles by constellation, only provided key information, and just included relatively bright doubles observable with smaller telescopes. However, one had to "manually" page through the catalog to select observational candidates. Furthermore, some vital information, such as

SAO and other identifiers, number of past observations, etc., was not included. Increasingly sophisticated students would prefer to use their laptops to help them sort and select potential doubles for observation, while SAO or other identifiers are handy for entry into today's computerized telescopes.

Joseph Carro has prepared a spreadsheet catalog of 3,950 double stars that is ideal for student use. Carro incorporated information from SIMBAD—the astronomical data base operated at the CDS in Strasbourg, France—into a series of Microsoft Excel spreadsheets that facilitate sorting and selecting doubles for study. The spreadsheets are arranged by constellation, and include star names, common identifiers, and details on each double star. Summary tables of all 3,950 stars are sorted in various ways as a convenience for the user. A diagram showing the major stars of each constellation is provided. Using the star name as the key, a hyperlink to SIMBAD allows additional information, such as parallax, to be conveniently obtained. Carro's catalog can be accessed at www.AltAzInitiative.org, or you can contact him at jcarro@charter.net. Carro is expanding his catalog to include additional double stars and further information.

To select doubles for advanced projects, such as multiple stars across many constellations, faint double stars, etc., it is helpful to have a way to choose them quickly and easily. Tom Smith created a master catalog using a relational database engine and Structured Query Language (SQL) with the *Washington Double Star Catalog* (WDS) as the foundational catalog. Several other databases of stars were incorporated and relationally linked to the engine, including the *Sixth Catalog of Orbits of Visual Double Stars* (6th Orbital Catalog) and the *Hipparcos 2 Catalog* (Hip2). Many of the desired data fields needed in our studies were not contained directly in any of the original catalogs and were synthesized using various mathematical and astrophysical algorithms. In many cases, the units for some of the data were different across the various catalogs, so new fields were created with uniform units. Smith routinely generates Microsoft Excel worksheets that are convenient for selecting doubles for observation, data manipulations, charting, and generating population statistics.

Genet has sorted and reduced the initially large spreadsheets provided by Smith to short, compact lists of doubles for specific observational programs. This process typically involves removing columns not of interest, narrowing the columns so the relevant data appears all together on the screen, selecting a range of RA and dec of interest, and sorting and selecting on such parameters as separation, delta magnitude, parallax, proper motion, spectral type, etc. Lists have been prepared for high proper motion

pairs, faint pairs that include an M star, pairs with a white dwarf, etc.

Our research is incorporating photometry as well as the astrometry of our target double star systems. The new AAVSO Photometric All Sky Survey (APASS) catalog has secondary photometric standards in every field of view. This will facilitate transformations to the standard photometric systems. Please see <http://www.aavso.org/apass> for details.



Figure 2. The twin 8-inch APASS-North astrographs at Tom Smith's Dark Ridge Observatory in Weed, New Mexico.

4. Visual Observations and Student Education

Several different groups of students, educators, and amateur astronomers are working together to provide middle school, high school, and community college students a hands-on research experience. One group, the California Double Star Association, is centered on a research seminar offered by Genet at Cuesta College. This seminar consists, primarily, of students at Arroyo Grande High School. Another group, the newly formed Maui Double Star Association, meets at the University of Hawaii's Institute for Astronomy in Maui, and provides a research opportunity for both middle school and high school students.

In both groups, students, using a Celestron or Meade ruler/protractor astrometric eyepiece, measure the separations and position angles of visual double stars, typically following the procedures outlined by Argyle (2003). Students observe with telescopes supplied and operated by local amateur astronomers. The students analyze their data and write up brief papers describing their observations, analysis, and results. The papers are given extensive internal and external reviews, and then appropriately rewritten. Students present their results at scientific conferences and their final papers are submitted to the *Journal of Double*

Star Observations for consideration by its editor, Kent Clark. The entire process is overseen by professional educators and astronomers. See Genet *et al.* (2010) for details.

The intent of the seminar is not to recruit future astronomers, although that is certainly happening, given the enthusiasm level of some of the students. The purpose is to give the students an opportunity to conduct original science research, thus discovering how real science is done. Understanding the nature of scientific research is useful for many different careers, as well as exercising responsible citizenship in today's complex world.

Double star measurements were first made at Cuesta College on California's central coast in the Fall of 2007 (Grisham *et al.*, 2008, Johnson and Genet 2007, and Johnson *et al.*, 2008). The following year the seminar was moved to Cuesta College's South Campus at Arroyo Grande High School (AGHS), which has been the home base for this seminar for the past four years. Published papers, with AGHS students primarily as coauthors, include Alvarez *et al.*, 2009, Brewer 2011, Estrada *et al.*, 2010, Estrada *et al.*, 2011, Grisham *et al.*, 2008, Johnson *et al.*, 2008, Johnson and Genet, 2007, and Marble *et al.*, 2008. The 2011 class was the largest to date, with an enrollment of 17 students – all high school students – divided into three teams. Each team published a paper (Baxter *et al.*, 2012; Fluitt *et al.*, 2012; Warren *et al.*, 2011), and one team published a second paper (Collins *et al.*, 2011). Students may take the seminar up to three times for college credit. Students in their second or third year are team leaders for the students who are enrolled for the first time. A student research seminar was also held at Coast Union High School, in nearby Cambria (Dowdy *et al.*, 2009).



Figure 3. Cuesta College 2011 research seminar students pose in front of Nimbus II, a 22-inch Dobsonian telescope built by Reed and Chris Estrada, used to observe double stars with an astrometric eyepiece.

The seminar class is conducted as a graduate-level seminar. Several student groups are formed. The groups are given a general directive to collect position angle and separation data on a visual double star pair. Specific double star systems are selected by the students. Each group is responsible for observations, data analysis, literature research, and a written paper. The various groups are the initial editors of each other's papers. Student research is valuable in its own right as it adds to the knowledge base of double stars. It also contributes to student academic careers. It is rare indeed for a student to be a published science researcher before leaving high school, a point recognized with respect to college admissions and awarding of scholarships. Most of the seminar's graduates have been accepted to their first choice college and have also received scholarships based on their published research.

Having a local supportive community of educators and amateur astronomers has been vital. They have donated their time to instruct and demonstrate, to edit student work, and generally be science role models. Also vital are mentors—often amateur astronomers who are professional educators in fields other than astronomy. As Joseph Carro points out, the primary task of a mentor is to organize information so that a coherent and meaningful learning session can be achieved.

Based now on many years of double star seminars, the instructor and advisors note several factors that contribute to the success of published student research:

- Students can and should complete scientific research projects in a single semester. (Once the semester is over, students rarely complete projects.)
- Double star projects are more amenable to this short time frame than most others.
- Requiring the publication of research is vital, as are outside reviews prior to publication.
- It helps to have a mix of experienced and inexperienced observers.
- Student research teams can exercise their diverse talents and experience by allocating their skills to the various aspects of scientific research.

Based on the success of the early Cuesta College seminars, Genet initiated a student summer workshop in 2008 at University of Oregon's Pine Mountain Observatory east of Bend, Oregon. Although student contact hours remained the same, the summer workshop differed from the fall seminar by being concen-

trated into a single long weekend. During the four consecutive summers of 2008-2011, students and science teachers from several high schools and undergraduate colleges in Washington, Oregon, Idaho, and California participated in and successfully published double star research projects. Double star research is complex enough to challenge students without being so extensive as to require months of observation and analysis. This makes their study appropriate for students engaged in a several-day, hands-on research workshop.

At each workshop, students were broken up into research teams led by an experienced double star observer. Most attendees had never engaged in quantitative research before, so they received training in this area on the first day of the workshop prior to taking measurements that night. This was followed by daytime data analysis and paper writing and further observations, as required, at night.



Figure 4. Although they used smaller telescopes for their double star observations, students and instructors pose in front of the 32-inch telescope at the University of Oregon's Pine Mountain Observatory 2009 Student Research Workshop.

A total of eight papers have been published in the *Journal of Double Star Observations* from these Pine Mountain Observatory workshops. Most papers report on the separation and position angle of a double star such as Iota Boötes (Schrader *et al.*, 2010), Beta Lyrae (Carro *et al.*, 2012), 61 Cygni (Baxter *et al.*, 2011), and Delta Boötis (Estrada *et al.*, 2012). However, Frey *et al.* (2011) and Alduenda *et al.* (2012) reported observations of multiple star systems. Another team measured the double star STTA 123 AB and, in determining its components to be bound by gravity, estimated a rough orbit (Brashear *et al.*, 2012).

Another group, The Maui Double Star Association, consists of middle and high school students, and amateur and professional astronomers living on the island of Maui in Hawaii. Genet, who spends each winter in Hawaii, helped found and is a part-time member of the group. The students, who attend dif-

Observing Double Stars – Genet *et al.*

ferent schools, meet at the University of Hawaii's Institute of Astronomy (IfA). IfA astronomers J. D. Armstrong and Joe Ritter, and Haleakala Amateur Astronomers member Steve McGaughey lead the group.

For their visual observations they are using Steve McGaughey's Celestron C-9.25 at the Haleakala Amateur Astronomers observatory on the summit. McGaughey and Genet have developed procedures for student visual observations at the summit (McGaughey and Genet, 2012).



Figure 5. Maui Double Star Association: (back row) Eric Rohzinski, J.D. Armstrong, McKayla Wandell, Audreanna Leatualii, and Stephen McGaughey, and (front row), Noah Rohzinski, Aaron Rohzinski, and Isaac Sato.



Figure 6. Stephen McGaughey and his Celestron C-9.25 at the Haleakala Amateur Astronomers observing location at the 10,000 foot summit of Haleakala.

5. CCD Observations and Student Education

A program of student education via CCD observations of double stars was initiated this past winter at the University of Hawaii's Leeward Community College (LCC) on Oahu. LCC is one of the seven community college campuses of the University of Hawaii's system, with some 6,200 students. It is located to the west of Honolulu over looking Pearl Harbor.

LCC's Kilohoku Hale observatory is equipped with an Optical Guidance Systems 0.5-meter $f/8.2$ telescope and an Apogee Alta U6 CCD camera which was used for observations of the multiple star system Beta 321 in Lepus (Church *et al.*, 2012).



Figure 7. The Leeward Community College observatory is not far from Pearl Harbor.



Figure 8. Left to right: Rebecca Church (student), Kakala Mohanan (LCC instructor), and Russ Genet (visiting). The telescope is a 0.5 meter Optical Guidance Systems Cassegrain.

The Maui Double Star Association (MDSA) is fortunate in that 30% of the time on the Las Cumbres Observatory Global Telescope (LCOGT) 2-meter Faulkes Telescope North (FTN) has been allocated to the University of Hawaii for student education and public outreach. Thus the MDSA is in a good position to pursue advanced double star projects using this telescope. FTN can be conveniently operated in a Real Time Interface (RTI) mode from the University of Hawaii's Institute for Astronomy Maui headquarters at the base of Haleakala. Although initially clouded out, the weather was clear on the night of March 31st when J. D. Armstrong, Cindy Krach, Audreanna Leatualii, Steve McGaughey, Aron

Rohzinski, Noah Rohsinski, and McKayla Wandell, were at the controls at IfA, while Russ Genet participated via speakerphone.



Figure 9. Steve McGaughey, J.D. Armstrong, Russ Genet, and John Pye stand in front of the 2-meter Faulkes Telescope North on the summit of Haleakala. An in-person observational session scheduled for that night were clouded out but was successfully completed remotely at a later date.

Brian Mason at the U.S. Naval Observatory had suggested that observations of late M-star doubles, doubles with a white dwarf, and high common proper motion pairs—especially the faint pairs only observed a single time by Luyten (1997) could be usefully observed by the 2-meter FTN. Smith and Genet worked together to develop three observational lists—one for each of these areas. Rafael Caballero, a member of Agrupacion Astronomical Hubble in Spain, has suggested the observation of faint common proper motion pairs (Caballero, 2012). He developed a new list of high common proper motion pairs for us that contained a mix of known pairs (in the WDS) and potential new double stars that could, if observationally confirmed, be added to the WDS as new discoveries. Genet narrowed the list down to 9 “Rafa” systems (with stars from 14th to 19th magnitude) of which 7 were observed in the allotted two hour observing window. Maui students operated the telescope under the supervision of Armstrong and McGaughey, while Genet participated via speakerphone, sending Aladin Previewer images via the

Internet. A paper reporting these observations is being prepared.

6. Lucky Imaging

High spatial resolution is vital to obtaining accurate measurements of close visual double stars. The atmosphere compromises image resolution, limiting the minimum separation of the systems that can be studied. However, when short exposures—on the order of 0.1Hz or less—are collected, one is essentially imaging instantaneous atmosphere configurations. In lucky imaging (Law *et al.*, 2006), targets are observed at >10Hz cadence, and only the images least affected by the atmosphere—typically only 1% in the R band, less in bluer bands—are selected. Those “lucky” exposures, once stacked, can reconstruct a highly spatially resolved image, often diffraction limited, of a sky region of one to a few tens of arc seconds, the nominal size of an isoplanatic atmosphere patch. Note that the majority of the data is not used in the image reconstruction, thus this technique is extremely time consuming. Thus observations must be planned for 10 to 100 times the conventional image exposure required to achieve the desired signal-to-noise ratio.



Figure 10. B.J. Futon, Russ Genet, and John Martinez at the Las Cumbres Observatory Global Telescope’s BOS 32-inch telescope. With Federico Bianco, they used the EMCCD Andor Luca-R camera on this telescope for lucky imaging and speckle interferometry observations.

Lucky imaging was used as early as the 1920s for planetary observations. However, the typical brightness of close double stars and multiple star systems rendered them too faint to be imaged at the necessary high cadence. The advent of high sensitivity, low noise cameras over the last decade, particularly EMCCDs, has unlocked the potential of this technique. Although the cost of EMCCD cameras began in the \$40,000 range, new cameras can now be pur-

chased for less than \$8,000, and some used cameras have been purchased for as little as \$2,500.

On a 2-meter telescope, such as Faulks Telescope North (FTN), lucky imaging is feasible in presence of a 12th magnitude or brighter guide star within 10 or a few tens of arc seconds of the target and, provided that the pixel size is sufficiently small, the optical limit of the telescope is routinely achieved by selecting the luckiest few percent images. Furthermore, frame transfer CCD and EMCCD cameras, which can download one image while recording another, maximize the imaging duty cycle, reducing total time requirements. When a guide star – possibly the target itself – is used, the lucky exposures are selected on the basis of the Strehl ratio, a measure of the sharpness of the star image. The images are then aligned on the brightest pixel, nominally taken as the peak of the diffraction or optics limited point-spread-function (PSF), although more sophisticated methods that exploit cross correlation or wavelets can provide a more accurate reconstruction of the image.

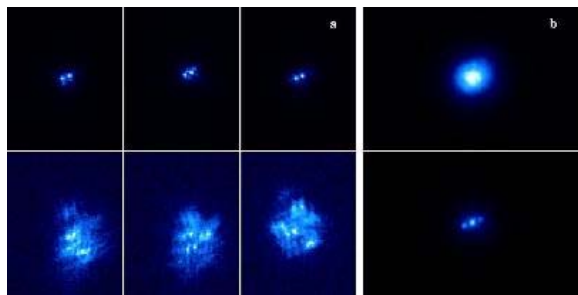


Figure 11. A selection of images of the double star Zeta Bootis from data collected at the 32-inch BOS telescope at ~30Hz cadence, and a reconstructed "lucky" image.

In the figure, panel (a) is a selection of images of the double star Zeta Bootis. The data was collected at BOS at ~30Hz cadence (each exposure was ~0.034sec) by an Andor Luca-R EMCCD camera with an SDSS r' filter and a x2 Barlow. The three sharpest, as well as the three least sharp images in the series are shown on the top and bottom respectively. Panel (b) at the top is a stack of the first 200 frames in the series, equivalent to a single 3.4 second exposure. Panel (b) at the bottom is the reconstructed lucky image – a stack of the sharpest 200 frames (a 1% selection) – for a total exposure of 3.4 seconds. Frames were selected and aligned using the brightest pixel in the star image. The ghost star appearing at the roughly 2 o'clock position in the lower right panel is an artifact of the shift-and-add these technique used to create the lucky image, known as *tripling*. The pair, which at the time of the observation had a 0.45 arc second separation, is clearly resolved.

7. Speckle Interferometry

When observed at a sufficiently high cadence, star images reveal the presence of "speckles," resulting from the atmosphere producing multiple sharp images of the target. In the case of a single star, these speckles will be randomly distributed inside the Gaussian seeing envelope on the detector. However, in the case of a binary, there will be a characteristic separation and position angle that the speckles will follow. These duplicated images of the star are randomly distributed, and simply summing the images or a long exposure will blur out this high-frequency information, leaving only a Gaussian seeing envelope.

It was first suggested by Labeyrie (1970) that Fourier analysis of speckles could allow the position angle and separations of close binaries to be measured with great precision. This technique is now known as "speckle interferometry". Harold McAlister and his associates at George State University pioneered speckle interferometry, while Brian Mason and associates at the US Naval Observatory, Elliott Horch at Southern Connecticut State University, and others have launched sizeable double star speckle interferometry observing programs. Horch (2006) reviewed the history and current status of speckle interferometry.

Since Fourier decomposition is blind to phase shifts, the location of each of the duplicated double star images on the detector is lost, but any correlations between speckles in different locations remains. By summing the 2-dimensional Fourier power spectrum of the high-cadence images, one can discern any patterns in the speckles that are common throughout the dataset.

If the target is an unresolved binary, the resulting power spectrum will form a set of fringes. The separation of these fringes is inversely related to the projected sky separation, thus making it possible to measure the separation of binaries that are closely spaced, down to the diffraction limit (or pixel scale) of the telescope.

This method of speckle interferometry creates 180 degree degeneracy in the position angle that must then be resolved using other imaging techniques (such as lucky imaging) or more advanced interferometry methods (e.g. bispectrum image reconstruction, Lohmann *et al.*, 1983). In most cases we use a combination of speckle interferometry and lucky imaging to measure the position angle, separation, and flux ratio of each binary pair.

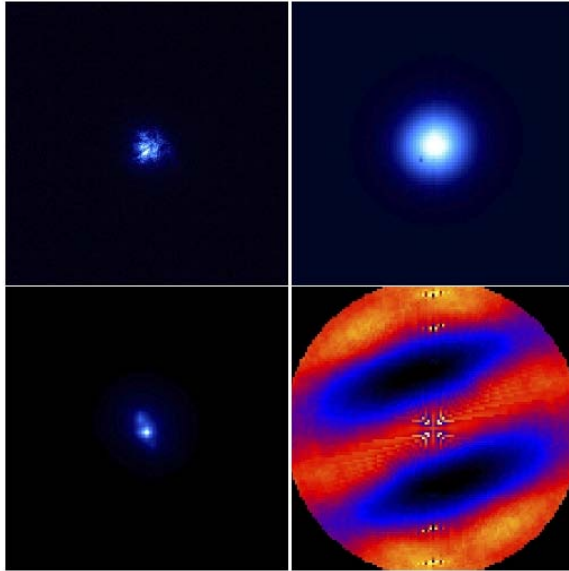


Figure 12. Results for the close visual binary HD 23985. See text for explanation.



Figure 13. The Orion Observatory's Andor Luca-S camera and 10-inch telescope equipped with a Sidereal Technology control system.

We observed HD 23985 (WDS 03503+2535AB) with LCOGT's BOS 32-inch telescope. An x2 Barlow and I filter were used in conjunction with the Andor Luca-R EMCCD camera. The components of the binary HD 23985 are reported in the WDS as magnitude 5.75 and 6.52. Referring to the figure, upper left is a single 34 ms exposure of HD23985, also known as a speckle. Upper right is a 10 second exposure of HD23985. Lower left is a 1% Lucky image of HD23985. The separation of the two components is 0.325". Lower right is a speckle interferogram of HD 23985 created by summing the 2-D Fourier power spectrum of all 5,000 34 ms images.

At Genet's Orion Observatory, an Andor Luca-S EMCCD frame transfer camera is being used for lucky imaging and speckle interferometry of double stars, as well as high speed photometry of X-ray binaries and other variables stars. The Andor Luca cameras are lightweight and are easy to transport, install on large aperture telescopes as a guest observer to achieve higher resolution, or use in portable field operations to observe asteroid or Trans-Neptunian Object occultations.

8. Conclusions

Measuring the separation and position angles of double stars is cooperative activity that has engaged many astronomers – students, amateurs, and professionals – for well over two centuries. Observations are welcome for publication in the *Journal of Double Star Observations* and similar journals. Once published, the observations are incorporated in the *Washington Double Star Catalog* along side those by William Herschel and all the other contributors.

Visual double observation projects using a low cost astrometric eyepiece on small telescopes have proven to work well for student seminars and summer camps where published results are a requirement. While somewhat more complex, CCD double star observations provide students with an opportunity to learn advanced techniques, and with larger telescopes, such as the 2-meter Faulkes Telescope North, to observe unusually faint doubles.

Finally, the advent of relatively affordable EMCCD frame transfer cameras is extending lucky imaging and speckle interferometry to fainter magnitudes, allowing atmospheric degradation to be circumvented and the resolution limits of telescopes to be achieved.

9. Acknowledgements

We thank the Las Cumbres Observatory Global Telescope for observational time on their 0.8-meter telescope at Santa Ynez and 2.0-meter telescope on Haleakala. This research was supported in part by NASA through the American Astronomical Society's Small Research Grant Program which funded the Andor Luca-S camera at the Orion Observatory. This research made use of the Washington Double Star and other catalogs provided by the U.S. Naval observatory. We thank CDS in Strasbourg, France for use of Aladan, the SIMBAD database, and access to various catalogs. Finally, we thank Richard Berry for supplying the lithograph from John Herschel's report from the Cape.

10. References

- Aitken, Robert. (1918). *The Binary Stars*. Reprinted 2012. BiblioLife. Charleston, SC.
- Alduenda, C., Hendrix, A., Hernandez-Frey, N., Key, G., King, P., Chamberlain, R., Frey, T. (2012). “Separation and position angle measurements of double star STFA 46 and triple star STF 1843.” *JDSO* **8**, 48.
- Argyle, B. (ed.). (2003). *Observing and Measuring Visual Double Stars*. Chapter 12. Springer. New York.
- Argyle, B. (2004) *Observing and Measuring Visual Double Stars*. Springer-Verlag. London, UK.
- Argyle, R. (1986). *Webb Society Deep-Sky Observer’s Handbook, Vol 1: Double Stars*. (second edition). Enslow. Hillside, NJ.
- Alvarez, P., Fishbein, A., Hyland, M., Kight, C., Lopez, H., Navarro, T., Rosas, C., Schachter, A., Summers, M., Weise, E., Hoffman, M., Mires, R., Johnson, J., Genet, R., White, R. (2009). “A comparison of the astrometric precision and accuracy of double star observations with two telescopes.” *JDSO* **5**, 60.
- Baxter, J., Collins, S., Berlin, K., Jordano, C., Waymire, T., Cardoza, C., Shore, D., Carro, J., Genet, R. (2012). “Observations of the triple star system Phi Cassiopeia.” *JDSO*, submitted.
- Baxter, A., Johnson, J., Genet, R., Estrada, C., Medley, D. (2011). “Comparison of two methods of determining the position angle of the visual double star 61 Cygni.” *JDSO* **7**, 212.
- Brashear, N., Camama, A., Drake, M., Smith, M., Johnson, J., Arnold, D., Chamberlain, R. (2012). “Observations, analysis, and orbital calculation of the visual double star STTA 123 AB.” *JDSO* **8**, 122.
- Brewer, M. (2011). “Astrometric measurements of the double star STFA 43AB.” *JDSO* **7**, 107.
- Caballero, R. (2012). “351 new common proper-motion pairs from the Sloan Digital Sky Survey.” *JDSO* **8**, 58.
- Carro, J., Chamberlain, R., Schuler, M., Varney, T., Ewing, R., Genet, R. (2012). “Measurements of Beta Lyrae at the Pine Mountain Observatory Summer Workshop 2011.” *JDSO* **8**, 150.
- Collins, S., Jananne, K., Berlin, C., Cardoza, C., Jordano, T., Waymire, D., Shore, Baxter, R., Johnson, R., Carro, J., Genet, R. (2012). “Visual astrometry observations of the binary star Beta Lyrae.” *JDSO* **8**, 153.
- Couteau, P. (1978). *Observing Visual Double Stars*. English translation 1981. MIT Press. Cambridge MA.
- Chruch, R., Mohanan, K., Genet, R. (2012). “CCD Astrometry of the Multiple Star System Beta 321 in Lepus.” In preparation.
- Dowdy, M., Heaston, N., Mathieson, C., Powell, B., Vega, E., Hodes, B., Hoffman, M., Frey, T., Johnson, J., Arnold, D., Genet, R., Hodges, L. (2009). “Astrometric measurements of the neglected visual double star ARY 54 AC.” *JDSO* **5**, 74.
- Dupuy, T., Liu, M. Ireland, M. (2012). “Testing theory with dynamical masses and orbits of ultracoal Binaries.” *ASP Conference Series*, in publication.
- Estrada, C., Gupta, A., Kohli, M., Lund, A., Stout, A., Daglen, B., Daglen, J. (2012). “Astrometric measurements of the visual double star Delta Boötis.” *JDSO* **8**, 6.
- Estrada, C., Magana, S., Salam, A., Van Artsdalen, A., Baxter, J., Brewer, M., Carro, J., Genet, R., Graf, M., Herman, D. (2011). “Astrometric measurements of the visual double star Epsilon Lyrae.” *JDSO* **7**, 195.
- Estrada, C., Johnson, J., Weise, E., Fisher, J., Howard, T., Salam, A., Almich, C., Kessinger, D., Cavnillas, S., Matakovich, T., Maly, K., Wallen, V., Genet, R. (2010). “Astrometric measurements of the visual double star H 5 12A.” *JDSO* **6**, 230.
- Frey, T. G., Bense, H., Bense, R., Muller, F., Gasik, R., Ruppe, M., Scimeca, D., Johnson, J., Medley, D. (2009). “Visual measurements of the neglected double star ARY 52 at the Pine Mountain Observatory summer research workshop 2009.” *JDSO* **5**, 212.
- Fluitt, J., Heath, E., Johnson, B., Ortiz, G., Charles, H., Estrada, R., Genet, R. (2012). “Observations of the binary star Nu Draco.” *JDSO*, submitted.
- Frey, T., Achildiyev, I., Alduenda, C., Bridgman, R., Chamberlain, R., Hendrix, A. (2011). “Visual measurements of the binary star S 654.” *JDSO* **7**, 45.
- Frey, T., Achildiyev, I., Alduenda, C., Bridgman, R., Chamberlain, R., Hendrix, A. (2011). “Visual meas-

- urements of the multiple star STT 269 AB-C and ARN 8 AB-D.” *JDSO* **7**, 50.
- Genet, R., Johnson, J., Wallen, V. (2010). “One-semester astronomical research seminars.” in *Small Telescopes and Astronomical Research*. Collins Foundation Press. Santa Margarita, CA.
- Grisham, D., Johnson, J., Genet, R., Arnold, D. (2008). “Double star measurements with a three-inch Tasco telescope.” *JDSO* **4**, 10.
- Haas, S. (2006). *Double Stars for Small Telescopes*. Sky Publishing. Cambridge, MA.
- Herrmann, D. (1973). *The History of Astronomy from Herschel to Hertzprung*. English translation 1984. Cambridge University Press. Cambridge MA.
- Herschel, W. (1782). “Catalogue of double stars.” *Philosophical Transactions of the Royal Society* **72**, 112-162.
- Herschel, W. (1803). “Account of the changes that have happened, during the last twenty-five years, in the relative situation of double stars.” *Philosophical Transactions of the Royal Society* **93**, 339.
- Horch, E. (2006). “The Status of Speckle Imaging in Binary Star Research.” *RevMexAA* **25**, 79-82.
- Hoskin, M. (2011). *Discoverers of the Universe: William and Caroline Herschel*. Princeton University Press. Princeton, NJ.
- Johnson, J., Genet, R. (2007). “Measurements of the visual double star STF 2079.” *JDSO* **3**, 147.
- Johnson, J., Frey, T., Rhoades, S., Carlisle, J., Alers, G., Genet, R., Atkins, Z., Nasser, M. (2008). “Student group measurements of visual double stars.” *JDSO* **4**, 52.
- Labeyrie, A. (1970). “Attainment of diffraction limited resolution in large telescopes by Fourier analyzing speckle patterns in star images.” *Astron. Astrophys.* **6**, 85.
- Law, N., Mackav, C., Baldwin, J. (2006). “Lucky imaging: high angular resolution imaging in the visible from the ground.” *Astron. Astrophys.* **446**, 739.
- Lohmann, A. W., Weigelt, G., Wirtitzer, B. (1983). “Speckle masking in astronomy: triple correlation theory and applications.” *Applied Optics* **22**, 4028.
- Luyten, W. J. (1997). *LDS catalog: Doubles with common proper motion (Luyten 1940-1987)*. On line catalog in SIMBAD based on *Publ. Astr. Obs. Univ. Minnesota*.
- Marble, S., Gonzalez, C., Cameron, C., Johandes, J., Chapman, B., Fishbein, S., Johnson, J., White, R., Genet, R. (2008). “High school observations of the visual double star 3 Pegasi.” *JDSO* **4**, 24.
- McAlister, H. (1985). “High angular resolution measurements of stellar properties.” in *Annual Review of Astronomy and Astrophysics* **23**, 59.
- McAlister, H. A. (1999). “The CHARA array on Mt. Wilson: an overview.” in *Optical and IR Interferometry from Ground and Space*. ASP Conference Series **194**.
- McGaughey, S., Genet, R. (2012). “Observation of STF 2686 from Haleakala.” *JDSO*, submitted.
- Michell, J. (1769). “An inquiry into the probable parallax, and magnitude of the fixed stars, from the quantity of light which they afford us, and the particular circumstances of their situation.” *Philosophical Transactions of the Royal Society* **57**, 234-264.
- Law, N. (2006). *Lucky Imaging: Diffraction-Limited Astronomy from the Ground in the Visible*. Cambridge University thesis.
- Perryman, M. (2010). *The Making of History’s Greatest Star Map*. Springer. New York.
- Savary, F. (1830). *Connaissance des Tems pour Pan.* Bachelier. Paris, France.
- Schrader, A. B., Walker-LaFollette, A. M., Johnson, J. M., Medley, D. J., Genet, R. M. (2010). “Measurements of visual double stars with a NexStar 6 SE at the Pine Mountain Observatory Summer Research Workshop 2009.” *JDSO* **6**, 225-229.
- Warren, N., Wilson, B., Estrada, C., Crisafi, K., King, J., Jones, S., Salam, A., Warren, G., Collins, S., Genet, R. (2012). “Astrometric observations of Delta Cepheus.” *JDSO* **8**, 140.

Amateur Image Pipeline Processing using Python plus PyRAF

Wayne Green
Boulder Astronomy and Space Society
7131 Oriole Lane
Longmont, CO 80503
dxwayne@gmail.com

Abstract

A template pipeline spanning observing planning to publishing is offered as a basis for establishing a long term observing program. The data reduction pipeline encapsulates all policy and procedures, providing an accountable framework for data analysis and a teaching framework for IRAF. This paper introduces the technical details of a complete pipeline processing environment using Python, PyRAF and a few other languages. The pipeline encapsulates all processing decisions within an auditable framework. The framework quickly handles the heavy lifting of image processing. It also serves as an excellent teaching environment for astronomical data management and IRAF reduction decisions.

1. Introduction

The project's goal is to assist the amateur astronomy community – with little computing experience – to develop a highly scripted solution to match their observing environment to their reporting needs. Python is a platform-agnostic environment growing in popularity with professional astronomers. It provides a framework to allow the Image Reduction and Analysis Facility (IRAF) to be combined with powerful libraries for mathematical analysis, astronomical computation and publication.

Python is a mature language with widespread use in systems administration, academia, science, engineering, business and industry. It has a rich suite of libraries, including SciPY for scientific mathematics, matplotlib for producing publication ready graphics, and specialized astronomy libraries including the IAU Standards of Fundamental Astronomy (SOFA) (SOFA Board 2010), USNO Novas C and Novas-Py (novas module) (Barron et al 2011). SOFA manages time and earth-pointing modeling to high precision. Novas allows using the JPL DE-405 solar-system model and provides other astrometric capabilities.

The complexity of IRAF is both its strength and its weakness. IRAF was started in 1981, extending best practices from prior years and becoming a serious service in 1984 (Tody, 1993). Today IRAF is a large collection of algorithms and techniques used for a consistent analysis of astronomical data. IRAF is large (approximately 40,700 files with approximately 3,450 help files) making it difficult to learn and easy to make mistakes.

IRAF is the primary core for undergraduate and graduate courses in observing and instrumentation. IRAF is one of the ‘gold standards’ of professional astronomy. It provides analysis for both photometry and spectroscopy.

The pipeline described here is the result of observing sessions for the novae 2011dh and 2011aj. The main goal of the campaign was to ring out issues with the instrumentation, data capture and the analysis environment at the Sommers-Bausch Observatory (SBO).¹ Lots of images and very repetitive analysis activities led to developing this pipeline. Some serious defects were uncovered, as discussed below.

A pipeline represents a “closed framework of accountability” where symbols (elements of instrument configuration and the analysis process) are managed by a ‘framework’ (a documented archive). The pipeline is ‘closed’ in the sense that all original data and germane intermediate results are retained. It is ‘accountable’ since steps of the process may be audited and any errors identified, understood and corrected. Thus all aspects of the system are available through configuration management; no questions about the veracity of results should remain unanswerable.

2. Pipeline Overview

Planning an observation develops several of the files used later in the process. The ‘rawdata’ directory is created and includes a special ‘etc’ directory storing the star catalog’s ‘.tsv’ file and a reference image. The catalog and image may be augmented with ds9 (SAOImage) ‘regions’ to locate the camera’s field-of-

¹ University of Colorado, Boulder, CO USA

view relative to comparison stars, to show known bad areas of a chip, or to set the slit orientation for spectroscopy. A special ‘observations.txt’ file contains FITS header entries (Pence, 2010), encoded as one *keyword:value:comment* per line, and is applied by the *fittofits* script. Anything else, like the time allocation request document, may be added as well. The project’s ‘etc’ directory is the place where cooked zero, dark and normalized flats are placed.

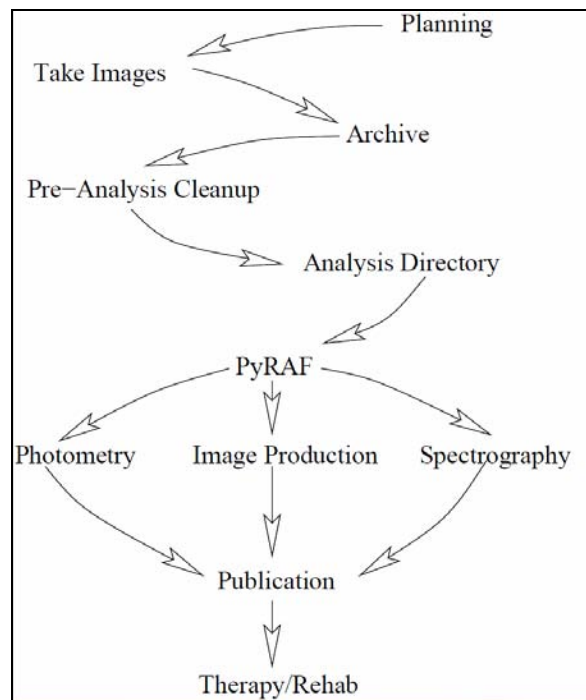


Figure 1. Overview of the pipeline process.

It is of value to be able to move the ‘etc’ directory contents across sites and share material in a way that is insensitive to the platforms and software releases encountered. Develop on Linux at the office, move to a Windows/Sun observatory, and share with Windows/Mac/Linux users.

2.1 Raw Data

Observations are made and the raw telescope image files are copied into the rawdata directory. At this time, the directory is frozen (made read-only) and an archive copy is made. The rawdata directory is copied to a preanalysis directory before any changes are made.

2.2 Preanalysis Directory

The purpose of this directory is to support cleaning of file names and augmenting them with proper header information. This makes them ready for processing.

The “FIT” files are converted from the Amateur Astronomical Instrument Processing Package (AIP) format (Longmire, 2003) to match the pipeline FITS keyword policies (NRAO, 2011). Verbose file names are edited down to a manageable size. The *fitserial* script prepends a small serial number to all files in the order specified by observation time FITS header keywords. Special FITS keywords are added that describe the filters, their serial numbers, the RA/Dec of the target(s), spectrograph settings and site and instrument data. This is mostly handled by the *fit2fits* script. Special header values for equipment’s manual settings are made with the *fitsrewrite* script on a file by file basis.

The results may be checked with a *fitsls* and *fitsgrep* program. The HEASARC program *fitsverify* (see NASA HEASARC) may be used as well.

The pipeline = policy+algorithms+data and the *fit2fits/fitsrewrite* scripts are designed to align local conventions to IRAF conventions. The *fit2fits* script copies all files to a special ‘attic’ directory prior to making changes. This retains the original files in a handy location for reference.

This pre-analysis directory is frozen and an archive copy is made.

2.3 Analysis Directory and Analysis

The pre-analysis directory is then copied to the analysis directory and work begins in earnest. At this point if a misstep is made in the process the effort of cleaning and augmenting files is not lost. Simply re-copy the pre-analysis directory and start again. The scripts run quickly and little time is lost.

The *fitsort* program is executed first. It reads the header keywords and builds a directory substructure. The subdirectories hold images by type, filter, binning and exposure time. In each created subdirectory a special ‘l.l’ file is created that contains the pertinent file names. This file is a ‘batch’ file or ‘at’ file used as ‘@l.l’ in IRAF.

The pipeline script traverses the directory and cooks all the zeros, darks, flats, comparison files, etc. It copies these files to the project’s ‘etc’ directory. It then applies these files to all the science images.

At this point all the data are inspected for the kind of gross defects that crop up – with hot pixels and atmospheric artifacts being the most dangerous.

The core analysis process is now performed. This varies with the target and observing program. Photometry proceeds along one path while spectrographic analysis follows its own path. Other examples include high-cadence observations of CV or Be stars and cases where targets overlap nebula or galaxy structure.

2.4 Photometric Analysis

The next phase uses *daofind/daophot* or *sextractor* (Linux) to extract instrumental magnitudes. The ‘.tsv’ catalog files are used to acquire reference magnitudes for stars. At this stage the point-spread function (PSF) for images becomes critical.

Additional finishing steps are performed as needed.

3. Developing Pipeline Steps

The 2011dh campaign's data analysis started by hand in the usual way, with an eye open to ways to code the steps into scripts. The scripts were desired as a framework for other projects – especially those involving undergraduate research assistants.

One key aspect about IRAF is its ‘unlearn’ command. This cleans out all hidden ‘sticky’ parameters from the system. Analysis was done by taking the ‘epar quiz’ and filling in all the parameters. The epar command opens into hidden subordinate parameter files shared across common stages of analysis where defaults are not announced. For example average vs. median combining with the *imcombine* command. Once acceptable results were obtained and the parameter files were deemed correct the ‘lpar’ command was used to list the parameters for a script. This information was cut and pasted into the script and edited to meet specific needs.

In this way scripts for creating reduced zero, dark and flat files were made. It was during zero file production that we noticed structure in the zero files. This was in the form of noisy pixels that appeared hot, but not always in the same place. Thus pixel-masks would not work. Dark images suffered the same effects.

3.1 Writing Basic IRAF Oriented Scripts

As an example, the cooking of image zero reference files is explored. Once PyRAF is started, the IRAF *lpar zerocombine* command produces the listing in column 1 of table 1 (lpar’s comments deleted). Each lpar line is edited to produce a Python dictionary shown in column 2.

Within the *masterzeros* script the source line:

```
iraf.zerocombine(**zerocombine_keywords)
```

passes the dictionary to the zerocombine function. That is all that is needed to cause Python’s iraf module to process all the files listed in the *LI* file to produce a single file called ‘raw_1x1_zeromaster.fits’.

Another dictionary is passed to `iraf.imsurfit(**surfit_keywords)` applying the

Gaussian smoothing function to the raw image. This removes structure as well as hot and cold pixels.

The results are shown in figures 2 and 3. There is a small corner-to-corner bias structure in the com-

lpar zerocombine	zerocombine_kw = {
input = "@l.l"	'input' : iname,
(output = "zmaster")	'output' : rawname,
(combine = "average")	'combine' : "average",
(reject = "minmax")	'reject' : "none",
(ccdtype = "zero")	'ccdtype' : "zero",
(process = no)	'process' : iraf.no,
(delete = no)	'delete' : iraf.no,
(clobber = no)	'clobber' : iraf.no,
(scale = "none")	'scale' : "none",
(statsec = "")	'statsec' : "",
(nlow = 0)	'nlow' : 0,
(nhigh = 1)	'nhigh' : 1,
(nkeep = 1)	'nkeep' : 1,
(mclip = yes)	'mclip' : iraf.no,
(lsigma = 3.0)	'lsigma' : 3.0,
(hsigma = 3.0)	'hsigma' : 3.0,
(rdnoise = "0.")	'rdnoise' : "0.",
(gain = "1")	'gain' : gain,
(snoise = "0.")	'snoise' : "0.",
(pclip = -0.5)	'pclip' : -0.5,
(blank = 0.0)	'blank' : 0.0,
(mode = "a1")	'mode' : "a"
	}

Table 1. Convert IRAF lpar to Python Dictionary

bined zero file. The smoothing of outlier pixels in the overall image removed artifacts from later processing steps.

During processing, the special feature from CL/ECL that prepends a pattern to a file name is retained in Python’s iraf module. Thus IRAF’s command:

```
imarith @l.l-cooked_masterzero.fits z_//@l.l
```

subtracts the ‘cooked_masterzero.fits’ from each file in ‘l.l’ and prepends a ‘z_’ to each new file. When dark subtracting:

```
imarith z_//@l.l-cooked_darkmaster.fits d_//@l.l
```

followed by

```
imarith d_//@l.l / masterflat.fits f_//@l.l
```

produces a set of ‘f_’ files that are normalized and ready for later processing. In a similar policy: ‘c_’ represents *imcombined* files; ‘a_’ means *imaligned* files, etc. While the commands are shown in “command-line” form, each is scripted to identical behavior within the Python code. The prepending feature only requires the one file, ‘l.l’, that holds the base file

names to guide the various steps of the pipeline. This alleviates the need for numerous files (or lists) with multiple variations of the file names.

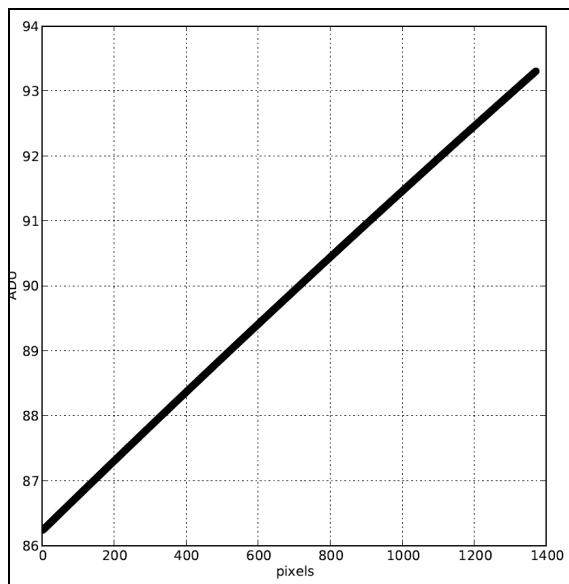


Figure 2. Raw zero image.

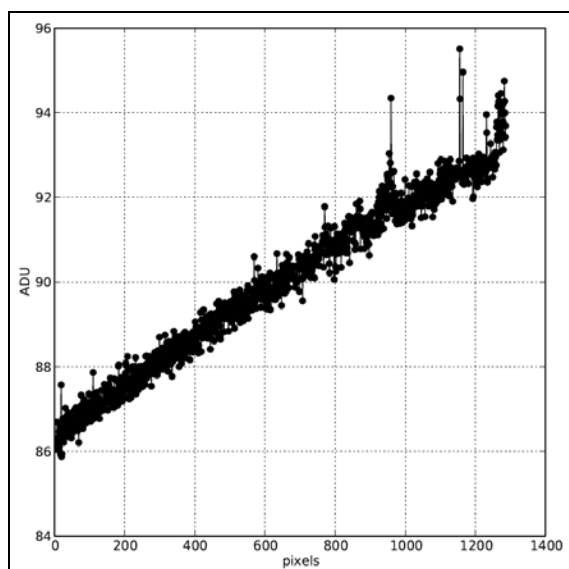


Figure 3. Zero image cooked with imsurfit.

3.2 A More Complex Script

In a more sophisticated application: Green *et al.* (2009) applied line strengths from Osterbrock (1989) to images of the Bubble Nebula (NGC 7635), giving the ratio of Hydrogen alpha to Hydrogen beta based on $d = \text{ratio of the relative line strengths}$.

The ratio $d = 1 - (4.861 \times 10^{-5} / 6.563 \times 10^{-5})$ is computed and used to calculate column density as

$[\log(\alpha/\beta) - \ln(3)] / d$. This simple formula is easily applied to two combined FITS images.

Two programs were written in Python. The first applies this equation to the arrays of the values in the Hydrogen alpha and beta images. The second makes a surface plot of these data using matplotlib.

Figure 4 is the Hydrogen alpha image; Figure 5 is the Hydrogen beta image; Figure 6 is the ratio; Figure 7 is the surface plot of the results. The plot in Figure 7 reveals the column density of the nebula in a very visceral way.

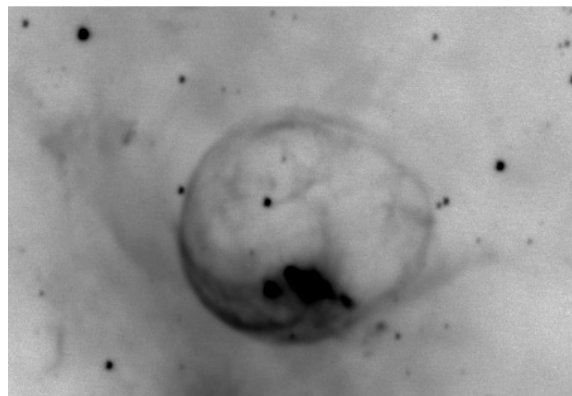


Figure 4. Hydrogen alpha image.

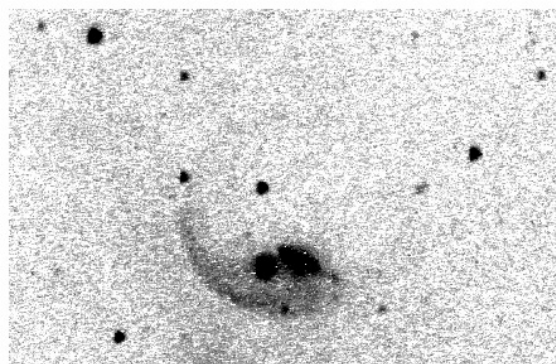


Figure 5. Hydrogen beta image.

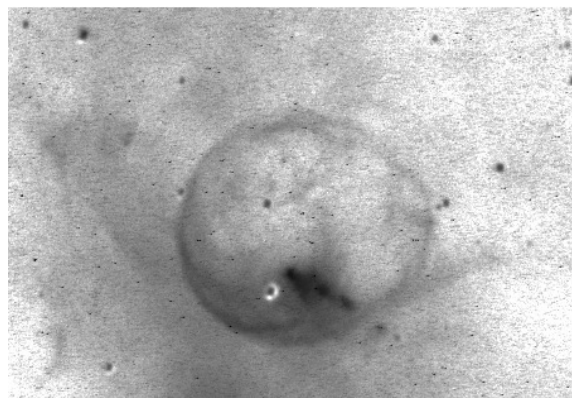


Figure 6. Column density ratio of images.

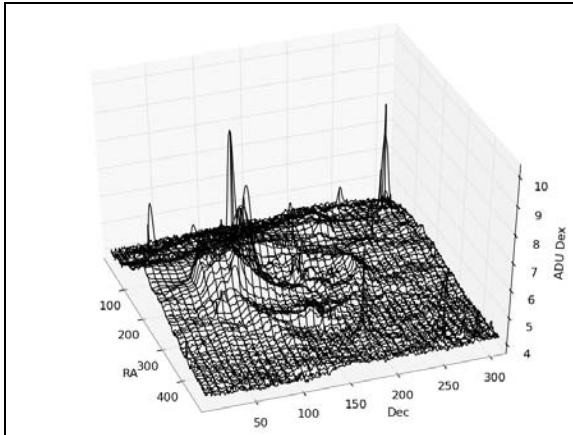


Figure 7. Surface plot of ratios.

4. Issues Uncovered Using the Framework

During the 2011dh campaign, issues with the camera's chip and very dirty filters pushed analysis of the images to the breaking point – that of losing confidence in reductions. Several times, sticky IRAF parameters led to erroneous results. The pipeline was created and refined to support auditing work needed to understand the problems with the manual process, equipment and images.

The IRAF program *imsurfit* was discovered and applied to the zeros and darks. The functionality was easily added to the pipeline, removing the problems we encountered.

An outstanding issue is with the 'goose-footed' PSF for star images with SBO's mis-collimated Boller and Chivens 24-inch. The PSF does not match any pre-packaged software. Special handling of the telescope's PSF was needed.

The third issue involved the filthy filters – great for teaching but lousy for science. New filters are ready for use, together with new filter parameters for IRAF.

5. Conclusions

The pipeline provides a fully accountable way of managing data and processing for observations. IRAF provides a rich 'kit' of resources for dealing with problems and delving into image issues. The Python environment and special Python libraries allow developing and sharing programs between computing operating systems. The scripting forces each parameter to a known state and provides a more consistent session-to-session analysis framework. The solutions to newly identified problems can be easily integrated into the framework by using rich features of the existing IRAF code.

6. References

- Barron, E. G., Kaplan, G. H., Bangert, J., Bartlett, J. L., Puatua, W., Harris, W., Barrett, P. (2011) "Naval Observatory Vector Astrometry Software (NOVAS) Version, 3.1, Introducing a Python Edition". *Bull. AAS* **43**, 2011.
http://aa.usno.navy.mil/software/novas/novas_py/novaspy_intro.php
- IAU SOFA Board. IAU SOFA software collection. Issue 2010-12-01. <http://www.iausofa.org>
- Green, W., Stiner, J., Davis, M. (2009) "Study of NGC 7635." Unpublished.
- Longmire, M. (2003). "SBFITSEXT Version 1.0 A Set of FITS Standard Extensions for Amateur Astronomical Processing Software Packages." Santa Barbara Instruments Group, Santa Barbara, CA.
- FITSVerify. FITS file verification tool. NASA Goodard Space Flight Center.
<http://heasarc.gsfc.nasa.gov/docs/software/ftools/fitsverify/>
- IRAF (2011). National Radio Astronomy Observatory.
 National Radio Astronomy Observatory.
<http://iraf.noao.edu/>
- Osterbrock, D. (1989). *Astrophysics of Gaseous Nebulae and Active Galactic Nuclei*. (Table 4.1). University Science Books, Mill Vally, CA.
- Pence, W. D., Chiappetti, L., Page, C. G., Shaw, R. A., Stobie, E.. "Definition of the Flexible Image Transport System (FITS), version 3.0." (2010). *Astron. Astrophys.* **524**, A42.
- Tody, D. (1993). "IRAF in the Nineties." in *Astronomical Data Analysis Software and Systems II* (R. J. Hanisch, R. J. V. Brissenden, J. Barnes, eds.). *A.S.P. Conference Series* **52**, 173.

High Time Resolution Astronomy or High Speed Photometry

Gary A. Vander Haagen
Stonegate Observatory
825 Stonegate Rd, Ann Arbor, MI 48103
garyvh2@gmail.com

Abstract

High Time Resolution Astronomy (HTRA) or High Speed Photometry offers opportunity to investigate phenomena that take place at timescales too fast for standard CCD imaging. Phenomena that occur within fractional-seconds to sub-millisecond timescales have been largely overlooked until recently due to technology limitations and/or research priorities in other areas. Discussed within the 1-second to millisecond range are flares, oscillations, quasi-periodic oscillations (QPOs), and lunar occultations. A Silicon Photomultiplier (SPM) detector with associated pulse amplifier and high-speed data acquisition system were used to capture stellar intensities at rates up to 1000 samples/sec on stars to 8 V-mag. Results on YY Gem flares, exploratory searches for oscillations on AW Uma, BM Ori, and X Per, and lunar occultations are discussed along with data reductions techniques. Opportunity for future study is also discussed.

1. Introduction

Our fascination with solar the system, star systems and their evolution, asteroid tracking, rotation, sizes, and composition as a few examples have led us to fainter and fainter objects, larger optics, and longer exposures. With longer exposures, events that take place in the fractional-second to millisecond time-scale are averaged and lost.

Interest in this area opens up a whole new range of possible explorations. High speed photometry or high time resolution astronomy (HTRA) can fill an area of scientific exploration that complements conventional CCD imaging and offers unique insight into relatively unexplored areas. Richichi (2010) presents a good overview of how HTRA augments astronomical research. Figure 1 shows research areas versus timescale and the regions of study. Pulsars, oscillations, quasi-periodic oscillations (QPOs), and occultations push the millisecond and beyond range. These represent significant equipment challenges requiring very fast and sensitive photo detectors and larger aperture optics for 8-9 magnitude and beyond. In addition, with data rates in the kilohertz range there are challenges in coping with the storage and analysis of the data. With intensity sampling at 1000 samples/sec a two-hour data collection run generates 7.2 million data points for storage and subsequent analysis.

For the slower oscillations, transits, flares, and flicker events, data rates in the 10 to 100 Hz range still present the same equipment challenges but offer opportunity for the study of fainter objects. The previously cited Stellar Oscillation and Occultation arti-

cle presents numerous examples for study in these areas.

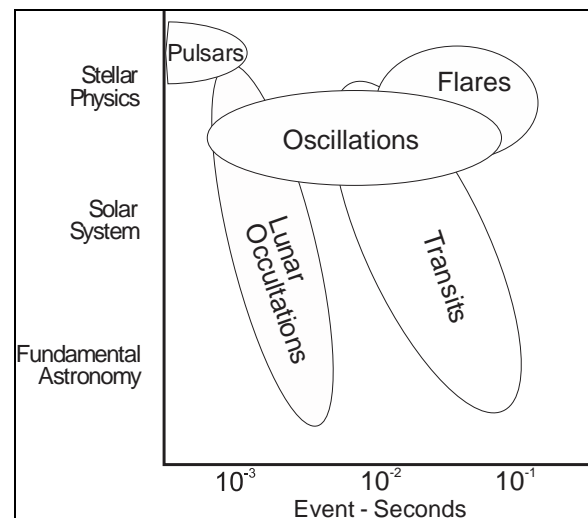


Figure 1. Research opportunities at various timescales, facsimile reproduced by permission from A. Richichi.

The trade-off between sampling rates and S/N is shown in Figure 2 for sampling rates of 10, 100, and 1000 samples/sec. This graph shows ideal conditions using a clear filter with minimal scintillation noise. The telescope has a 17-inch aperture and a silicon photomultiplier detector (SPM) with an internal gain in excess of 10⁶. At 1000 samples/sec the measurement limit is approximately 8th magnitude.

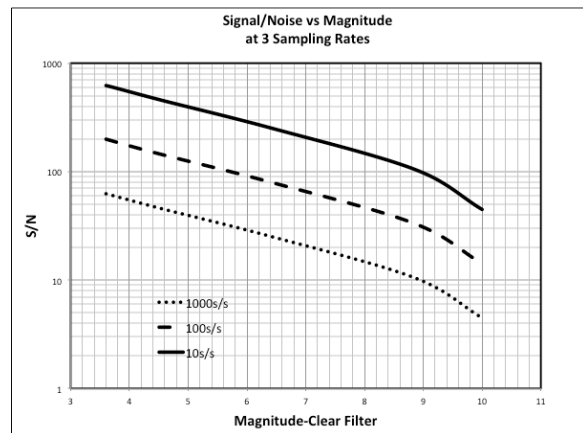


Figure 2. S/N versus magnitude for 3-sampling rates with clear filter and low scintillation noise

When pursuing fast events bandwidth (BW) is limited by our sampling rate. To avoid aliasing during analysis, the sampling rate (f_s) must exceed the Nyquist rate (f_n),

$$f_s > f_n$$

where $f_n = 2BW$

Or, for a BW of 1000 Hz the sampling rate must be greater than 2000 Hz. Literature places a number of the oscillations events in the mHz-1900 Hz region for x-ray binaries (XB) (Warner, 2008). Targeting of the 1900 Hz oscillation dictates a minimum sampling rates of 3800 samples/sec thereby limiting objects to approximately 6th magnitude or brighter for 14-17-inch scopes. For slightly less demanding lunar occultation studies a resolution of 1-3 milliseconds is required for diffraction fringe capture. This places sampling rates in the 300 to 1000 samples/sec range. These rates and the slightly slower flares and flickers can push the upper limit to as high as 10th magnitude under ideal conditions.

Target	Type	V Mag
X Per	HMXB Pulsar	6.7
AW UMa	CV	6.9
BM Ori	EB, X-ray source	8
YY Gem	EB, X-ray source	9.8
RZ Cas	EB, X-ray source	6.2
Moon Occultations	Single & double stars	<8.0

Table I. HTRA study targets

With an practical upper limit of 9th magnitude the initial candidates for fast event studies are shown in Table I.

2. The Optical Train for High Speed Photometry

Key components of the optical system include a telescope with 10" or greater aperture, a fast response detector system with internal gain, data acquisition system and analysis software.

The detector represents the biggest challenge for HTRA. While there are several CCD cameras available with internal gain (electron multiplication) they are expensive and do not provide the S/N of photomultiplier type sensors. However, they do provide a mechanism for obtaining a reference star and using more conventional data reduction techniques. The discussion presented in Vander Haagen (2011) provides an overview of numerous sensor types and their performance. The characteristics that make the Silicon Photomultiplier (SPM) most attractive are high internal gain (10^{6+}), good noise performance, wide bandwidth and insensitivity to overloading, troublesome with conventional vacuum photomultipliers.

The SPM used was manufactured by sensL (2012). Figure 3 shows both the unpackaged sensor along with it fully enclosed and cooled and attached to a nose piece with filter and f-stop. The output of the SPM is millivolt level pulses at rates up to 10 MHz depending on the equivalent photon count per second, one photon per count. These low voltage pulses are fed to a wideband pulse amplifier to provide a logic level signal for the data acquisition system. The amplifier provides a voltage gain of 2500 at a bandwidth of 10 MHz necessary for undistorted photon pulse counts. This is a higher performance version of the previously used amplifier. The new amplifier provides about double the BW and greater stability to temperature and input-output loading changes. A schematic of the circuit may be requested from the author.

The initial optical train used had a field of view of 80 arcseconds. The configuration used a video camera for alignment and relied on accurate tracking from the mount for extended periods. Without guiding, tracking errors were excessive for multiple-hour data collection runs. The optical train was modified to improve ease of initial alignment and provide continuous autoguiding. The modified optical train is shown in Figure 4.

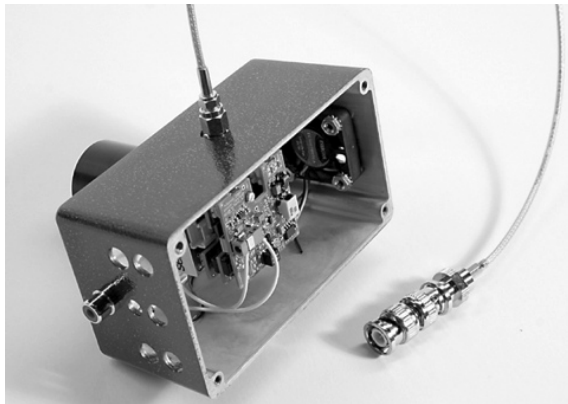
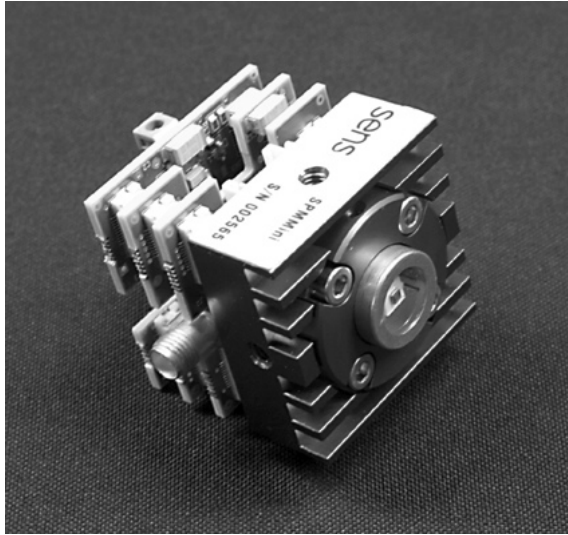


Figure 3. Top: SPM module. Bottom: SPM module packaged with cooling fan, nosepiece, f-stop and filter. A cooling fan is required to keep the thermoelectric cooler operating at 30 C below ambient.

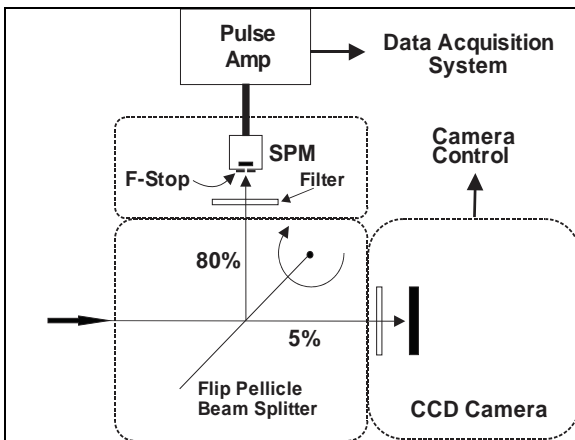


Figure 4. Optical train with flip pellicle beam splitter, SPM module, and CCD camera for alignment and guiding

The light enters and strikes a 5-micron pellicle beam splitter, National Photocolour (2012). Approxi-

mately 80% of the light is reflected 90°, passing through the optical filter, f-stop, and onto the SPM. The CCD camera for initial set up and autoguiding uses the 5% transmitted light. A software controlled servo motor positions the pellicle for either beam splitting mode or 100% pass through for normal CCD camera operation. The optical train has demonstrated easy initial alignment and guiding for the long data collection runs.

The f-stop most generally used was 750-micron diameter providing a field of 57-arcseconds. A smaller 400-micron diameter f-stop was required for lunar occultation work.

The full optical train is shown in Figure 5 mounted on the 17-inch PlaneWave scope.

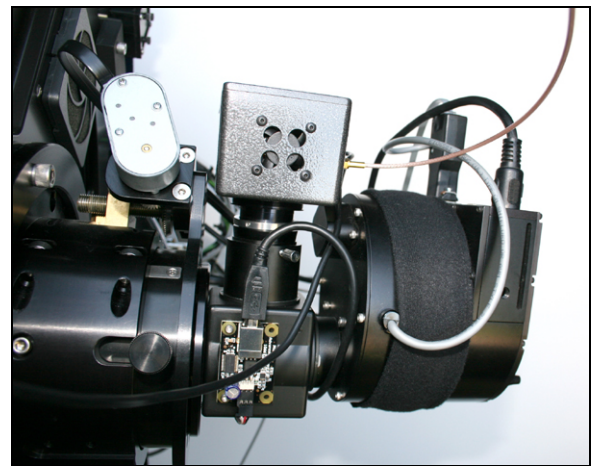


Figure 5. Optical train showing SPM and CCD camera attached to software controlled pellicle beam splitter

3. High Speed Data Acquisition and Analysis

The basic data collection sequence will operate without a reference star. Since we are operating with a single pixel camera there is no option for a reference without adding a second complete optical train with associated equipment and alignment issues. In addition, the two data streams are generally correlated in real time. Such a setup is described in Uthas (2005) and is generally not necessary for the higher frequency data particularly where data is at a frequency substantially higher than the scintillation noise. An alternative calibration option will be discussed in Section 7.

The data acquisition system used was from, Measurement Computing Corporation (2012), a DaqBoard/1000 series data acquisition board. The PCI board takes one PC slot with the data inputted through a standalone connection board. Important features of the data acquisition system include:

1. Easy connection and use with PC at lowest system cost
2. Bandwidth capability to at least 8×10^6 -photon integration counts per second.
3. Ability to totalize counts over any period; micro-seconds to seconds
4. Ability to trigger data collection on a count, count rate or analog event and employ a caching technique for pre-trigger data capture
5. Integrated DaqView software for real time data storage and review of events

The integrated DaqView software met all the data acquisition requirements but did not include a suite of digital signal processing (DSP) subroutines for Fourier transforms, power spectral density, filtering, smoothing, etc. Sigview 2.3, a DSP package by SignalLab (2012) had the required capability. Sigview has an intuitive structure and easily imports ANSI data from the MC data acquisition system. This software provides capability for all the filtering modes such as low pass, high pass, band pass, fast Fourier transforms (FFT), spectrograms, statistical analysis, amplitude and frequency measurements, adding and parsing of data runs, etc. This capability helps to reduce the dependency on a secondary reference star, to some extent, as will be described later.

4. Exploratory Look at Rapid Events in Eclipsing and X-ray Binaries

The primary interest of this study is the stellar physics events as shown in Figure 1. The focus will be on cataclysmic variables (CVs) particularly X-Ray binaries (XB) exhibiting QPO or suspected optical oscillations. Current models suggest magnetically controlled accretion onto a rapidly rotating equatorial belt of gas. These energetic events may generate RF, X-Rays, and occasionally modulate emitted light in the form of oscillations or QPOs with signatures varying widely, Uthas (2005) and Warner (2008).

Flares are well known events for our Sun and other stars and CVs with strong magnetic fields at their surfaces. An energetic flare can produce luminosity increases of many orders of magnitude on time scales of seconds to days. Flickering is a smaller outburst of a few tenths of a magnitude over a much shorter time, generally seconds to minutes.

Be it oscillations, flares, or flickering events they occur rapidly such that detailed high-speed data is necessary for capture. These data are used to develop or validate models for the stellar systems. For the oscillations, target frequencies range from 40-2000

Hz placing these frequencies generally beyond the worst of the scintillation noise. Targeted will be those stars or star systems with suspected or verified events and at data rates necessary to capture the oscillation. The limiting factor will be target brightness necessary to support the fast exposures. The data will be captured at data rates as high as possible in segments of 10^6 data points for each file. The data acquisition system supports continuous data collection but limits the file size for analysis purposes. The prime tool for identifying the oscillations will be the Fourier transform power spectral density (PSD) of the amplitude-time data and the Spectrogram or a time sequence PSD showing where in time the frequency occurred.

For flares and flickering events the time domain data will be reviewed directly or bandpass filtering and/or resampling of the data will be used to reduce the high frequency variations. The same segmenting of data will limit individual files to 10^6 points.

Data collection objectives will be exploratory in nature:

1. Confirming the range of data gathering of both magnitude and BW.
2. Learning to separate noise from stellar information focusing on XB with known oscillations in the X-Ray spectrum and “suspect” in the optical.
3. Refining equipment and procedures for improve results.
4. Firming up a plan for next steps including working with a researcher.

4.1 AW UMa

AW UMa is a cataclysmic variable; HMXB targeted because of its general classification and previous interest by other researchers. The first run of AW UMa was at 200 sample/sec and the initial look at the data generated considerable excitement. Figure 6 shows an expanded section of the 3600-second run.

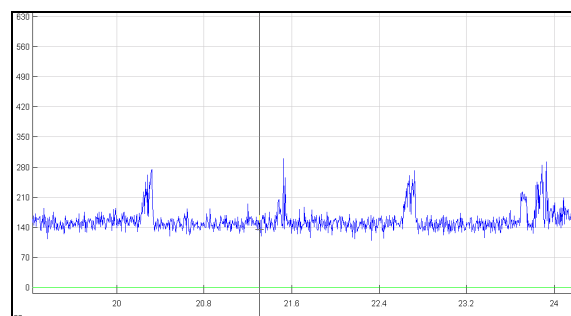


Figure 6. AW Uma data at 200 samples/sec, 7-second section noting periodic pulses

These periodic pulses were found later to originate from an open ground on a coax connection. Considerable attention is necessary to address noise across the full spectrum prior to any data collection. Flipping the pellicle to the pass through position blocks the sensor and helps to confirm proper noise performance. This step was accidentally omitted prior to this run. Three additional 1-hour runs were completed on a second night. No high frequency components were detected.

4.2 X Per

X Per is a HMXB, Pulsar, and gamma-ray source and suitable classification for high frequency activity. The 6.7 V magnitude allowed for data collection at 1000 samples/sec. All runs were with Astrodon Johnson-Cousins blue filters. Run #1 on 2012 March 7 was 6 segments of 1 million data points each. The files are seamless from one to the next so no data is lost. Run #2 on 2012 March 9 was 8-segments of 1-million points each. A PSD of a typical run is shown in Figure 7.

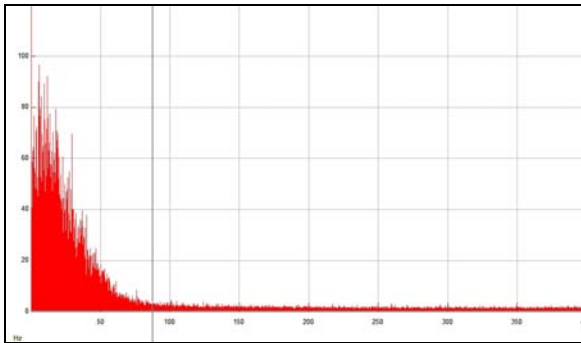


Figure 7. X Per PSD data at 1000 samples/sec, typical spectra with no high frequency components to 500 Hz

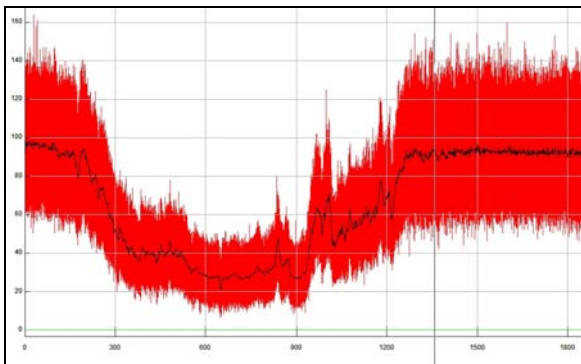


Figure 8. X Per data at 1000 samples/sec, composite of 4 segments. The smooth data were resampled at 1-sample/sec

Another X Per run occurred on 2010 March 15. 10 segments of 1 million points each. A composite of the first 4 segments is shown in Figure 8.

The data encompasses a short eclipse that seems unreported in the literature. The cloud sensing system showed no change in the sky condition during the period. Note also what appear to be small flares during the eclipse. A PSD of the flare section is shown in Figure 9.

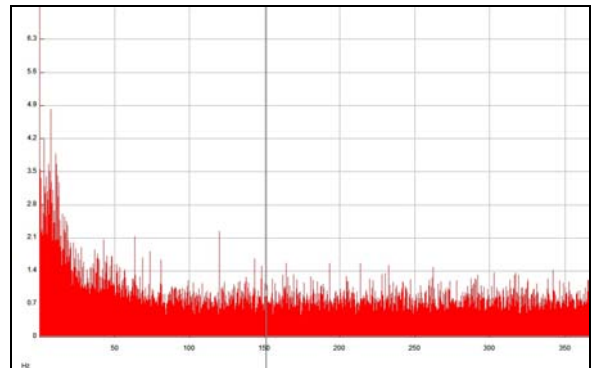


Figure 9. X Per PSD of flare section

Figure 9 shows no identifiable high frequency components. However, on run #6 there was an identifiable peak at 383 Hz as shown in Figure 10, a potential QPO.

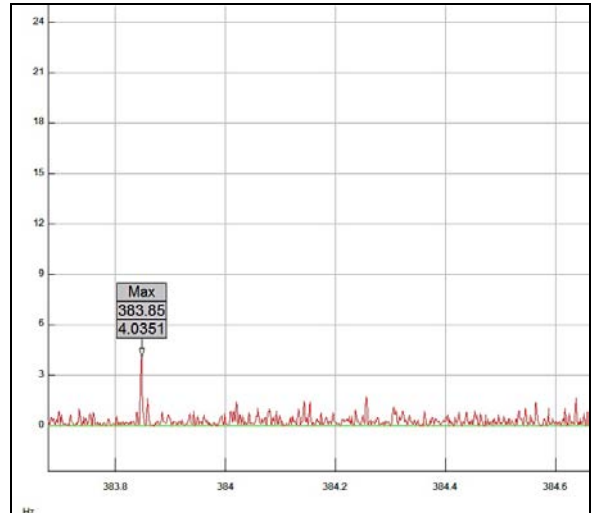


Figure 10. X Per PSD data at 1000 samples/sec, run #6; a potential QPO at 383.85 Hz

A very high amplitude peak was detected during segment 5. With the mean count running at approximately 100, just after 306 seconds on segment 5 the counts peaked over 3200. Figure 11 shows this event. The signal profile does not match a flash tube typical of emergency vehicles. No clouds were present for possible lightning flash. A possible explanation is a

stray emergency vehicle rotating light flash from a nearby road. These data will be investigated further.

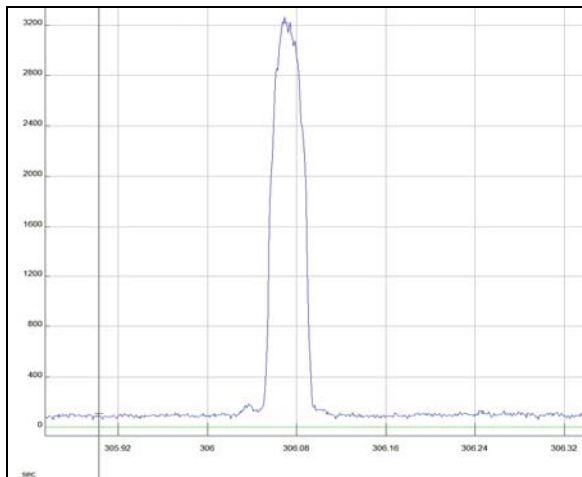


Figure 11. X Per data for segment 5 showing very high peaking near 306 seconds

4.3 BM Ori

BM Ori is an eclipsing binary and X-Ray source with good sky position for long runs. The EB was studied two nights 2012 March 17/20 at 1000 samples/sec. On the first run PSD analysis showed peaking of data at 167 Hz on three of the 1-million data point segments. Figure 12 shows both the full PSD and a section focused on 168.6 Hz. The same peak occurred in all the other segments of this run. On 2102 March 20 another run was completed with 8 segments of 1 million points each. The data looked similar with the 167 Hz components showing in all 8 segments. Figure 13 shows the PSD and a spectrogram of segment 8.

With so little data available at these data rates it is difficult to validate and exciting to see what is captured on each nights runs.

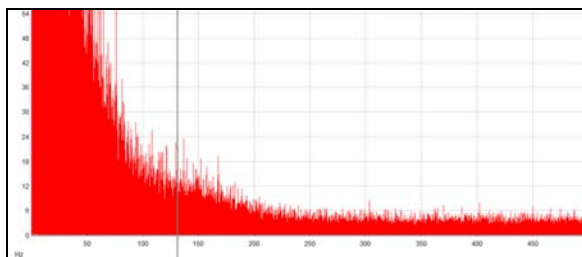


Figure 12a. BM Ori PSD data. Full 500 Hz BW.

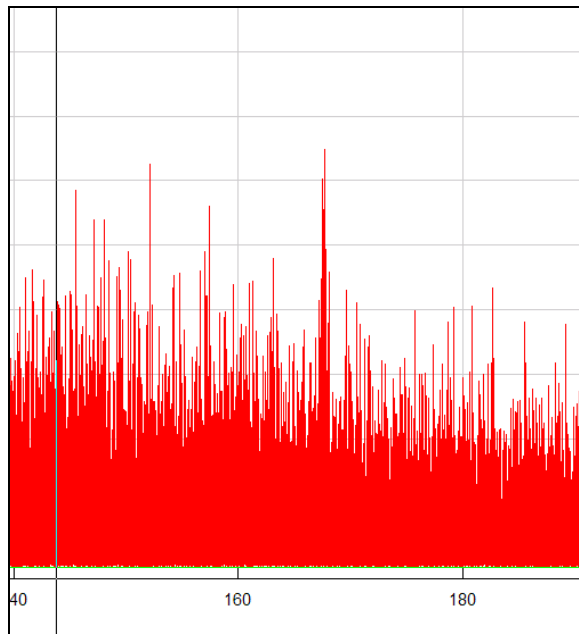


Figure 12b. BM Ori PSD data. Region around 167.6 Hz.

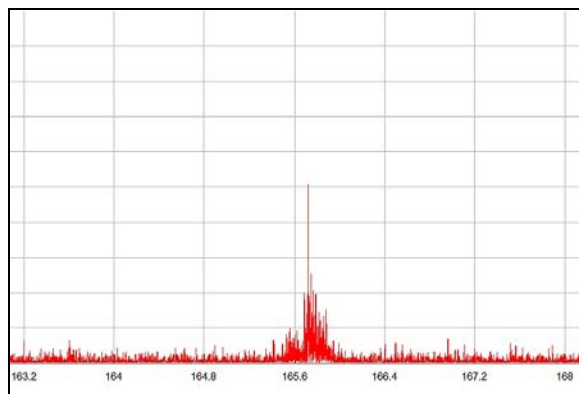


Figure 13a. BM Ori PSD and Spectrogram. Region around 166 Hz.

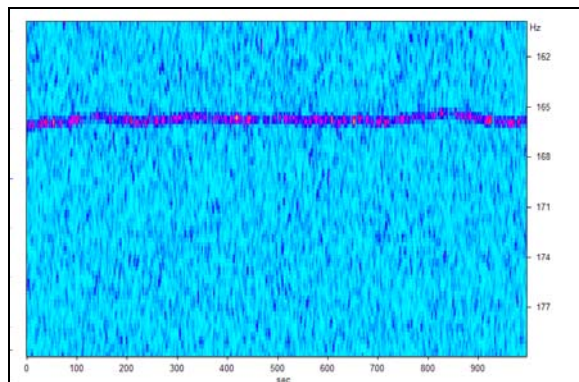


Figure 13b. Spectrogram showing the distribution of the 166 Hz oscillation over 1000 seconds. The spectrogram's brighter spots indicate higher concentration of the oscillation. Note small frequency change over the 1000-second period.

4.4 YY Gem

As a clouded-in participant of the YY Gem photometric team, this star generated considerable interest for future study of its active flares. YY Gem is an M dwarf eclipsing binary and known flare star. With its 9.8 V magnitude, data was collected at 200 samples/sec giving a BW of 100 Hz. Data were collected for a 2-hour and 6-hour run on two nights. Figure 14 shows the full 3600 seconds of data for 2012 March 13.

With data compressed it looks noisier than would be expected. However, with an average count of 600+ the S/N was 15 and acceptable. The PSD of the same data is shown in Figure 15.

The FFT shows strong components below 5 Hz and reaching background levels by 25 Hz. There were two low level components at 65 and 98 Hz at very low power density.

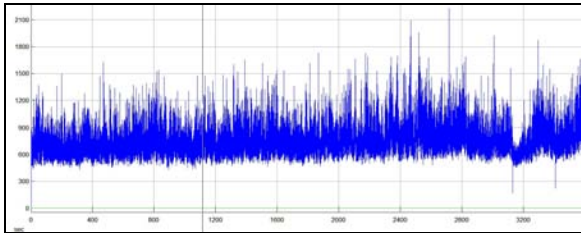


Figure 14. YY Gem data for 2012-02-13, blue filter, 200 samples/sec, with 3600-second trace

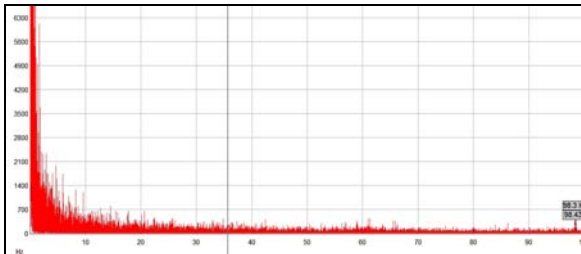


Figure 15. YY Gem PSD data for 2012-02-13, blue filter, 200 samples/sec, BW = 100Hz

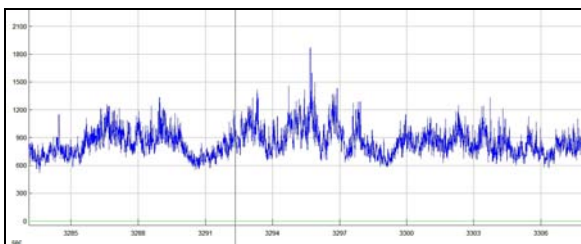


Figure 16. YY Gem flicker event

Figure 16 shows a flicker event with a total duration of less than 10 seconds at approximately a magnitude brightening at the peak. This star warrants

longer data runs through multiple eclipses (0.814 days primary) to increase the chase of flare and flicker capture.

5. Lunar Occultations: a High Accuracy Measurement Tool

The Moon has held all those studying the heavens for thousands of years in great fascination. However, it has only been in the last 60 years that the Moon’s predictable and known apparent angular rate of motion (0.4”/sec) and accurately known distance has been augmented by a well-understood occultation process, Nather *et al.* (1970a,b). With good physical data, timing to 1-millisecond, and a detailed model of the diffraction pattern created by the lunar edge, occulted object angular diameters and double star separations can be calculated with high accuracy (Richichi, 2005).

The limitation of this tool is that the lunar occultations cover about 10% of the sky area over its 18.6-year cycle. Furthermore, many occultations occur during the day, are reappearances and require accurate off axes guiding for the hour or more the star is behind the Moon, and the light scattered from the illuminated portion has to be sufficiently low to yield adequate S/N. And, then there are still sky conditions and the instrumentation. The author recommends reading a good primer “Lunar Occultations” (Blow, 1983), that sets the stage well. “Combining optical Interferometry with Lunar Occultations” (Richichi, 2004), is also very informative. With all these difficulties lunar occultations still present an exciting challenge and area for accurate measurement of star diameters and separations using HTRA techniques.

The lunar occultation sequence can be seen in Figure 17 where a moving diffraction pattern is generated on the earth’s surface by the star prior to the geometric shadow. The pattern and shadow is moving at approximately 750 meters/sec dependent upon the limb contact angle. To illustrate, a simple diffraction pattern $F(w)$ for a monochromatic point-source the intensity is given by

$$F(w) = \frac{1}{2 \left[\left(\frac{1}{2} + S(w) \right)^2 + \left(\frac{1}{2} + C(w) \right)^2 \right]}, \quad w = x \sqrt{\frac{2}{\lambda D}}$$

where $S(w)$ and $C(w)$ are the Fresnel sine and cosine integrals.

This shows that the diffraction intensity is a function of both the wavelength λ of observation and the lunar distance D . The Fresnel integrals can be calculated with a MathCad type program or using Keisan (2012). The results are shown in Figure 18.

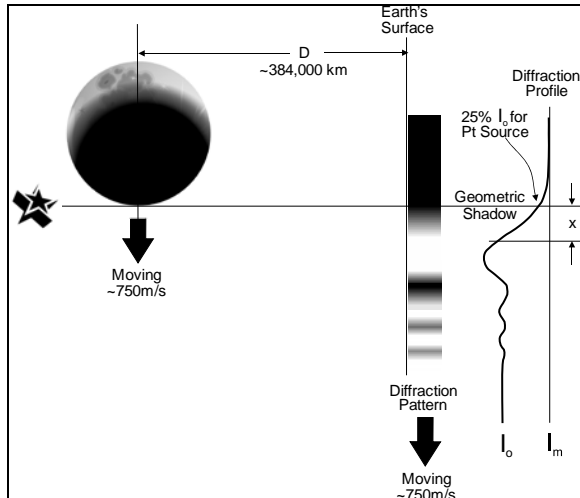


Figure 17. Lunar occultation of star showing moving diffraction pattern on earth's surface

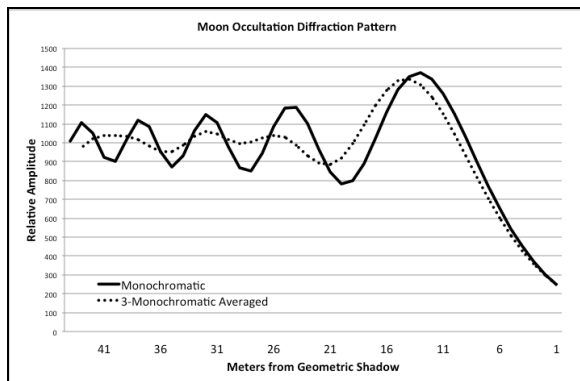


Figure 18. Single and multiple colors diffraction patterns formed on earth's surface, distance in meters from the geometric shadow

The solid line shows a monochromatic pattern for source at 430 nm. Clearly defined interference fringes exist past 41 meters from the geometric shadow. With the fringes moving at 750 m/s the fringe rate is 0.75 m/millisecond or the first fringe passes in about 12 milliseconds. Since our stars are anything but monochromatic we average three monochromatic wavelengths, to keep the math simple, and get the dotted interference pattern. Note the significant blurring of the fringes. It only gets worse as we integrate all the fringes over the BW of a typical narrow band filter and increase the diameter of the source to something finite. A good set of pictorials illustrating the effects of wavelength, BW, and star diameter is presented by Richmond (2005).

Nather and Evans (1970) developed one of the first diffraction models of the occultation event leading to more than two decades of refinements. A least squares fit to the data is made using model parameters such as star brightness profile, sky background,

detector and filter response, integration time, Moon's physical parameters, etc. The stars diameter is an additional parameter to be varied to find the best chi-squared fit of the diffraction pattern to the data. A further refinement of the least squares model came with the "composed algorithm" (CAL), Richichi (1989), which incorporates an iterative algorithm to select the "most likely" brightness profile of the source thereby yielding correct solutions over a much wider range of noise levels. Researchers have reported angular diameters to 0.5% uncertainty using the CAL approach (Richichi, 2005). In my brief contact with researchers these models are not available for general use and require collaboration with the researcher. With good models and millisecond data, a measurement range in angular diameters/separation from 2 to 300 milli-arcsecond (MAS) is possible (Richichi, 2012).

As a simple example of how the fringe analysis process works using only one element of the diffraction profile, Richmond (2005), presents a simulation of a uniform circular disk on the fringe pattern. Figure 19 estimates the angular size of a disk based on the height ratio of the first fringe, $I_{\text{fringe peak}}/I_0$. For a point source the ratio is 1.31. For a 20 MAS diameter the ratio is 1.08.

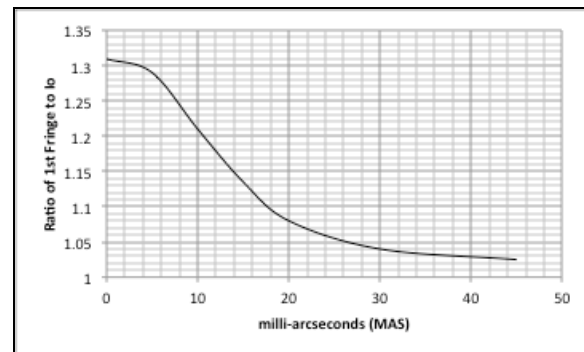


Figure 19. Angular size of a disk using only the ratio of first fringe height to steady state I_0

As seen this relies on only one characteristic of the data's profile and provides limited utility.

The video occultation measurement software LiMovie (Miyashita, 2008), offers a graphing and diffraction matching routine. To date it has not been possible to use non-video data as a source for this program.

Two excellent references for lunar occultation predictions include: The International Occultation and Timing Association, IOTA (2012) and the Dutch Occultation Association with their Lunar Occultation Workbench, DOA (2012). The Lunar Occultation Workbench (LOW) was found particularly user friendly and included many helpful cross-references.

Initial occultation data collection using a 750-micron f-stop proved unsuccessful for a 7.05 V-mag star due to excessive dark limb illumination of the field. A second 150-micron f-stop, 11 arcseconds field, proved nearly impossible to align and focus. Use of the 150-micron diameter pinhole required a precision focuser in the SPM path, which could not be accommodated due to insufficient optical path length. A compromise 400-micron f-stop, 30 arcseconds field, gave acceptable S/N for lunar phases to around 50% and 6⁺ magnitude. Further work is necessary to determine the range of illumination and star magnitudes for the two smaller pinholes.

Occultation of XZ-5588, 53 Tauri, SAO-76548, a 5.5 V-mag star is shown in Figure 20.

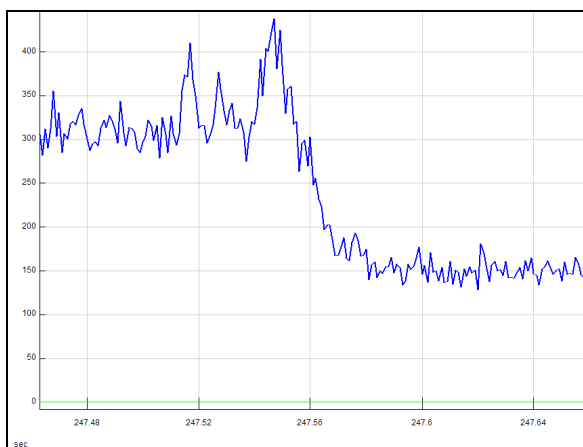


Figure 20. Occultation of XZ-5588 at 1000 samples/sec using a blue J-C filter exhibiting 3-diffraction fringes

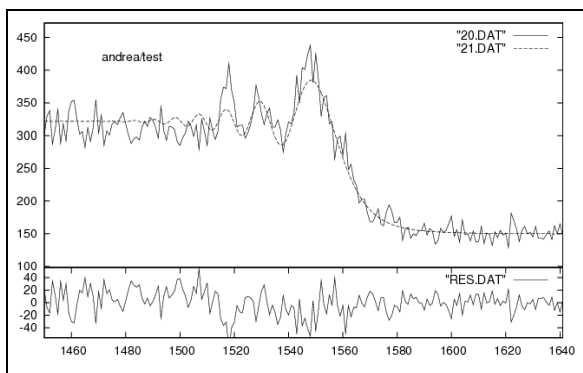


Figure 21. Occultation of XZ-5588 with point source diffraction pattern shown (dotted) as determined by the CAL model, first trial.

Using the first fringe ratio of 410/310 counts = 1.32, Figure 19 would place the star angular diameter at a point source or too small to be measured. A large amount of uncertainty results in this calculation due to the curves irregularity and simplicity of the model.

Referring to Fig. 21, a CAL diffraction model was run on XZ-5588 data with an estimate of the

SPM system parameters. The model found a point source assumption provided a good data fit with chi-squared of 0.97. The SPM system parameters are being reviewed and the model rerun to confirm the stars angular diameter.

6. Future Study Opportunities

Target	Type	V Mag.
X Per	HMXB Pulsar	6.7
AW UMa	CV	6.9
CygX-1	HMXB	8.9
YY Gem	EB, X-ray source	9.8
Vela X-1	XB	6.9
RZ Cas	EB, X-ray source	6.2
Lunar Occultations	Single & double star detection and measurement	< 8.0

Table II. Candidates for future HTRA study

Table II summarizes several good candidates for future study. The X-Ray binaries and cataclysmic variables are candidates that exhibit short or even extended periods of rapid variability in both the RF and the optical spectrum. Star systems such as Cygnus X-1 have exhibited modulation at frequencies in the 100 to 1300 Hz frequency range. This remains an opportunity for work in late summer and early fall when at its highest altitude. Vela X-1, HD77581, is another candidate for lower latitude study. Detection of these signals are challenging due to their low intensity, high frequency, and unpredictable occurrence. A study by Uthas (2005) and summary by Warner (2008) give some insight into this very interesting study group.

Flaring stars such as YY Gem are exciting study opportunities and allow for higher magnitude targets with sampling rates as low as 10 samples/sec.

The website ephemerides by Kreiner (2004), are excellent for identifying EB targets and timing as is the AAVSO (2012) for observing campaigns, descriptions of star types and their characteristics, classifications, outbreaks, data, charts, etc.

Occultations are a source of major interest at the higher sampling rates. The International Occultation and Timing Association, IOTA (2012) provides targets, technical assistance, and a depository for data.

7. Discussion and Conclusions

The SPM proved a capable detector for photon counting, high-speed photometric study. The use of the flip pellicle and capability for continuous guiding made set up easy and long term data acquisition pos-

sible without intervention. A setup modification using a helical focuser in the SPM's optical path would improve focusing for the smaller f-stop apertures. The focuser would also greatly reduce the wobble and misalignment that accompanies the sliding-tube focusing technique used. Field stops of 750, 400, and 150-micron proved a reasonable choice. Modification of the optical train for quick change and registration of the f-stops would significantly reduce down time.

The absence of a reference star is problematic when lower frequency phenomena are investigated, e.g., flares, eclipses. One solution is use of the intensity data from the guide star as a reference. These data could be easily stored on one of the extra channels of the data acquisition system and used to eliminate the slower variability from atmospheric transmission changes occurring over periods of seconds.

Considering the 5-study objectives:

1. Confirm the range of data gathering of both magnitude and BW.

Sampling rates to 1000 samples/sec were possible to 8th magnitude providing the filter used matched the spectral characteristics of the target. A magnitude dimmer is possible without a filter. For brighter targets sampling rates to 10,000 samples/sec are possible.

2. Learn to separate noise from stellar information focusing on XB with known oscillations in the X-Ray spectrum and "suspect" in the optical.

Stellar oscillations were found on X Per at 383.86 Hz, and on BM Ori at 166-7 Hz, possible QPOs. No literature confirmation was found for these frequencies. Use of digital filtering and FFT processing easily separates these signals from the lower frequency scintillation noise. Attention must be given at all times for elimination of system noise from ground loops, other electronic equipment, and optical sources visible to the sensor.

3. Refine equipment and procedures for improve results.
Changes to the optical path for better initial alignment and tracking were successful.
4. Confirm the capability for data collection on lunar occultation events and processing of data.

The lunar occultation data for XZ-5588 was

analyzed with the CAL model and found to be an unresolvable point source at high confidence.

5. Firm up plans for next steps including working with a researcher .

Identification of a researcher for collaboration on HTRA in high frequency oscillations and/or flaring is underway. Additional data collection on lunar occultations will also be pursued.

8. Acknowledgements

The author thanks Larry Owings for his development of the control software for the flip pellicle beam splitter. His speed and thoroughness on the project was greatly appreciated. Thanks and appreciation to Andrea Richichi of the European Southern Observatory and National Astronomical Research Institute of Thailand for his use of Figure 1 and CAL model data reduction for occultation of XZ-5588.

9. References

- AAVSO (2012). American Association of Variable Star Observers. <http://www.aavso.org/>
- Blow, G. L. (1983). *Lunar Occultations. Solar System Photometry Handbook*. (R. M. Genet, ed.) pp. 9-1 to 9-25.
- DOA (2012). The Dutch Occultation Association. Lunar Occultation Workbench, LOW Software v. 4.1. <http://www.doa-site.nl/>
- IOTA (2012). International Occultation and Timing Association. <http://lunar-occultations.com/iota/iotandx.htm>
- Keisan (2012). High accuracy scientific calculations. <http://keisan.casio.com/has10/SpecExec.cgi?id=system/2006/1180573477>
- Kreiner, J. M. (2004). "Up-to date linear elements of close binaries." *Acta Astronomica* **54**, 207-210. <http://www.as.up.krakow.pl/ephem/>
- Measurement Computing Corporation (2012). IO-Tech Data Acquisition Equipment. http://www.mccdaq.com/products/daqboard_series.aspx
- Menke, J., Vander Haagen, G. A. (2010). "High speed photometry detection and analysis techniques."

- The Alt-Az Initiative*. (R. M. Genet, J. M. Johnson, V. Wallen, eds.) pp. 443-469.
- Miyashita, K. (2008). LiMovie software for video analysis of occultation events. http://www005.upp.soc-net.ne.jp/k_miyash/occ02/limovie_en.html
- Nather, R. E., Evans, D. S. (1970a). *Astron. J.* **75**, 575-582.
- Nather, R. E., McCants, M. M., (1970b). "Photoelectric Measurement of Lunar Occultations IV. Data Analysis." *Astron. J.* **75**, 963-968.
- National Photocolor, Inc. (2012). Manufacturers of pellicle mirrors and beam splitters. <http://www.nationalphotocolor.com/specs.html>
- Richichi, A. (1989). "Model Independent Retrieval of Brightness Profiles from Lunar Occultation Light Curves in the Near Infrared Domain." *Astron. Astrophys.* **226**, 366-372.
- Richichi, A. (2004). "Combining Optical Interferometry with Lunar Occultations." *ASP Conference Series* **318**, 148-156.
- Richichi, A., Roccatagliata, V. (2005). "Aldebaran's angular diameter: How well do we know it?" *Astron. Astrophys.* **433**, 305-312.
- Richichi, A. (2010). "Stellar Oscillations and Occultations. High Time Resolution Astrophysics IV." Agios Nikolaos, Crete, Greece, May 5, 2010.
- Richichi, A. (2012). Personal communications.
- Richmond, M. (2005). Diffraction effects during lunar occultations. <http://spiff.rit.edu/richmond/occult/bessel/bessel.html>
- sensL Technologies Ltd. (2012). Manufacturers of SPMs. <http://sensl.com/products/silicon-photomultipliers/>
- SignalLab (2012). Sigview 2.3 software for DSP applications. <http://www.sigview.com/index.htm>
- Soydugan, E., Soydugan, F., Demircan, O., Ibanoglu, C. (2006). "A catalogue of close binaries located in the δ Scuti region of the Cepheid instability strip." *Not. R. Astron. Soc.* **370**, 2013-2014.
- Uthas, H. (2005). *High-Speed Astrophysics: Rapid Events Near compact Binaries*. Lund Observatory, Sweden.
- Vander Haagen, G. A. (2008). "Techniques for the study of high frequency optical phenomena." in *Proceedings for the 27th Annual Conference of the Society for Astronomical Sciences*. (Warner *et al.*, eds.) pp 115-122. Society for Astronomical Sciences, Rancho Cucamonga, CA.
- Vander Haagen, G.A. (2011). "The Silicon Photomultiplier for High Speed Photometry." in *Proceedings for the 30th Annual Conference of the Society for Astronomical Sciences*. (Warner *et al.*, eds.) pp 87-96. Society for Astronomical Sciences, Rancho Cucamonga, CA.
- Warner, B., Woudt, A. (2008). *QPOs in CVs: An executive summary*. Dept. of Astronomy, University of Cape Town, South Africa.

Photon Counting – One More Time

Richard H. Stanton
 JPL Retired
 43665 Oak Leaf Trail
 Three Rivers, CA 93271
 rhstanton@gmail.com

Abstract

Photon counting has been around for more than 60 years, and has been available to amateurs for most of that time. In most cases single photons are detected using photomultiplier tubes, “old technology” that became available after the Second World War. But over the last couple of decades the perfection of CCD devices has given amateurs the ability to perform accurate photometry with modest telescopes. Is there any reason to still count photons? This paper discusses some of the strengths of current photon counting technology, particularly relating to the search for fast optical transients. Technology advances in counters and photomultiplier modules are briefly mentioned. Illustrative data are presented including FFT analysis of bright star photometry and a technique for finding optical pulses in a large file of noisy data. This latter technique is shown to enable the discovery of a possible optical flare on the polar variable AM Her.

1. Introduction

An ideal photon counting system has at least four properties making it attractive for astronomical photometry:

1. Given 100% quantum efficiency and zero noise, one can do no better than count the arriving photons vs. time
2. Since all information is contained in short duration photon pulses (~30ns), very high-speed photometry is possible, *without any increase in measurement noise*, simply by sampling these counts at a high rate.
3. These count samples start out as digital data that can be binned to give several views of the same data with different time resolutions. Subsequent analyses can draw directly on powerful digital processing techniques, such as filtering and FFT analysis, to bring out additional information.
4. Being digital in nature, photon counting is inherently linear over a large brightness range, typically on the order of ten stellar magnitudes.

Of course real devices have neither 100% quantum efficiency nor zero noise. But modern detectors can come close to this ideal. CCDs have pushed quantum efficiency beyond the 70% level while photomultiplier tubes often achieve respectable levels of

25 to 30%. The very low noise readout electronics in many CCD cameras make them ideal for a wide range of astronomical applications, including photometry (Howell, 2000). But most CCD systems are not configured for fast photometry, or for counting individual photons. Video camera systems can do an excellent job of recording high-speed events such as asteroid occultations (Menke, 2007), but they usually operate at fixed bandwidth and also don't count single photons. Finally, newer devices such as the Silicon Photomultiplier described by Vander Haagen (2011), have interesting potential, but are apparently not yet demonstrating performance competitive with readily available commercial photomultiplier tubes (PMTs).

PMTs have long boasted the ability to count individual photons with essentially zero noise. Now the availability of modern tube modules with integrated electronics means that amateurs no longer have to deal with high voltage power supplies and high-speed amplifier/discriminator electronics. Simply plug in a 5V supply and you are ready to start counting photons!

This paper focuses some aspects using PMTs for astronomical photometry, a few of the interesting objects one can observe and example techniques for analyzing large files of count data. Finally, a brute force but effective way to search for pulses in noisy data is presented, along with an unanticipated “success story”.

2. Early Years

When the author started counting photons in the mid-seventies there were many obstacles to overcome. One needed a PMT specifically designed for photon counting, a high-voltage power supply, an amplifier / discriminator to generate countable pulses, a high-speed counter and a computer to store the data. Since personal computers were just arriving on the scene, some assembly-level coding was needed to make it all work. The author (Stanton, 1983) has described some of this early complexity. With luck and a lot of soldering and programming, one might be able to gather and store 10,000 points of photon data in a single run. Although this system was complex and strictly limited in the data capacity, it did demonstrate some of the strengths of photon counting. The next four figures illustrate the power of this early system for low noise photometry.

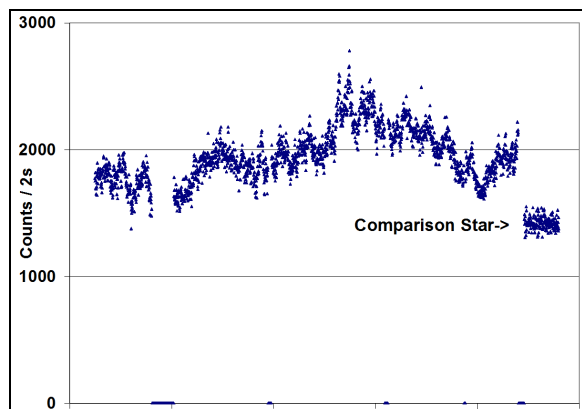


Figure 1. The polar variable AM Her in an active state on June 14, 1983. Points are photon counts per 2s, no filter with sky background subtracted.

Figure 1 shows approximately one hour of the count rate for the variable AM Her in an active state. All data in this paper were taken using a 16-inch Cassegrain telescope built in the 1960s by Cave Optical Co. For polar variables stars like AM Her, material falling from the secondary star to its white-dwarf companion is channeled by an intense magnetic field to a small spot on the dwarf's surface. The obvious flickering seen here is believed to be due to changes in the rate of material flowing in this process.

A second example from this early system is the light curve of the cataclysmic variable HT Cas, captured during one of its rare outbursts (Figure 2). This light curve shows the deep eclipses that occur every orbit when the system's bright accretion disk is eclipsed by the darker secondary star. Also seen are the transient "superhumps" that move through the light-curve with a period somewhat longer than the system's 106 minute orbit.

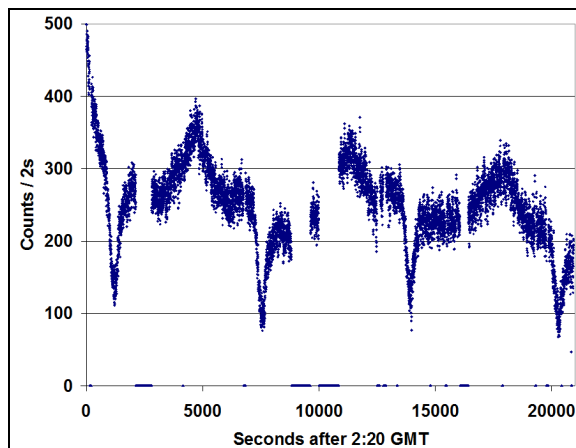


Figure 2. Variability of cataclysmic variable HT during outburst on 1985 January 20. V-filter with background counts subtracted. Note motion of the bright superhumps relative to the eclipses.

These days light curves like these can be readily duplicated using CCD imaging. The greater quantum efficiency of these devices, the relative ease of recording repeated frames of data, and the ability to simultaneously measure an entire field of comparison stars, give CCDs a clear edge for observing faint stars at this time resolution.

The next two figures illustrate a regime where the advantage still belongs to PMTs. As mentioned above, one of the advantages of a photon counting system is its ability to acquire data at high time resolution without introducing extra noise into the signal. Figure 3 illustrates this with count data gathered with millisecond resolution during a lunar occultation of 75 Tau. Note that the main Fresnel diffraction peak is clearly visible at this resolution.

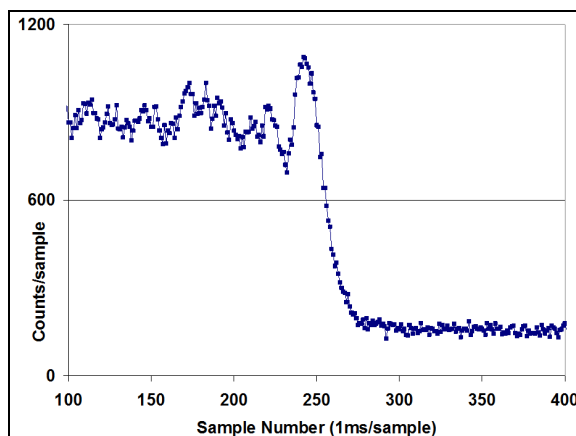


Figure 3. Lunar occultation of 75 Tau on 1979 March 5.

Figure 4 illustrates the serendipitous "discovery" of the close binary Hu 1080 made the same night as the moon passed through the Hyades. This binary is not well known to amateurs since the separation of its

6.6 and 7.3 magnitude components varies in the range 0.04" to 0.4" over its 40 year orbital period. It was apparently near its widest separation when this occultation occurred.

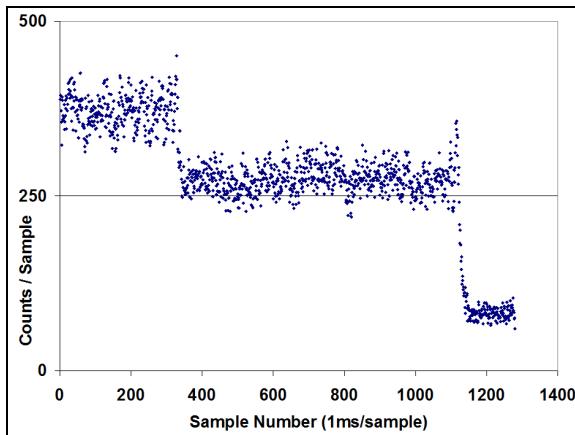


Figure 4. Lunar occultation of binary star Hu 1080 on 1979 March 5. Note that both components exhibit brightening just before disappearing due to Fresnel diffraction.

3. Hardware

Modern technology has made photon counting much easier to implement:

1. Photomultiplier, high-voltage supply and amplifier /discriminator electronics are now available encapsulated in a small, light weight package. One literally inputs 5V and gets photon pulses out with these modules. The author currently uses a Hamamatsu H8259-01 which gives a broad spectral response, QE peak of ~25%, a pulse-pair resolution less than 30 ns.
2. High speed, multiple channel counters are now available as relatively inexpensive PC boards. These boards feature DMA data transfer to the host computer, software-controlled functionality, and the ability to resolve pulse pairs separated by as little as 15 ns (see for example, National Instruments PCI-6602 Counter Timer board).
3. In conjunction with these counters, modern PCs can gather and store files of hundreds of millions (even billions) of data points per run. And the processing power of PCs enables efficient analysis of these huge files.

What can all this capability do for the amateur? It gives him a tool for going after **known** high-speed optical phenomena, such as lunar and asteroid occultations and more exotic targets such as the Crab Neb-

ula pulsar. But it also has the potential for finding **currently unknown** fast signals that professional astronomers simply don't have the time or inclination to look for. Jocelyn Bell Burnell, discoverer of pulsars 45 years ago, more recently (2004) put it this way:

"...we have neglected, incidentally, time-variability. The X-ray astronomers are alert to it, the radio-pulsar people are alert to it; gamma-ray astronomers are too, but only now are the optical astronomers starting to study things that go bump in the night. It's a fascinating and under-researched topic."

4. Data Analysis

4.1 Analysis Approach

In addition to hardware for generating time series of photon data, there are powerful analysis tools available that can help make sense out of the vast data files these systems generate. Two of these tools, digital filtering and FFT analysis, are illustrated here. Except where noted, all data in the remainder of this paper were gathered using the same set of timing parameters to give a consistent starting point for analysis. These parameters, a 3- μ s sample time and 300-second observation duration, result in files of 100 million data points each. While the resulting files dramatically over-sample any expected target brightness variation, they provide ample data for testing various data processing techniques. Of course one can select almost any desired time resolution by simply combining the 3 μ s samples into longer sample bins.

4.2 Digital Filtering

Figure 5 illustrates a small segment of data taken of the bright star (21 Lyr) and binned to give 96- μ s samples. The average photon rate for this star was approximately 3.5×10^6 counts/s. Both dark count (typically 10/s) and sky background (around 5000/s) are negligible in his case. As can be seen in Figure 5, two types of noise dominate this data. The first is the large amplitude, low frequency variation due to atmospheric seeing. The second, high frequency point-to-point variation, is due to statistical "shot" noise. Shot noise is always present in photon count data since it is inherent in the statistical nature of the incoming light itself.

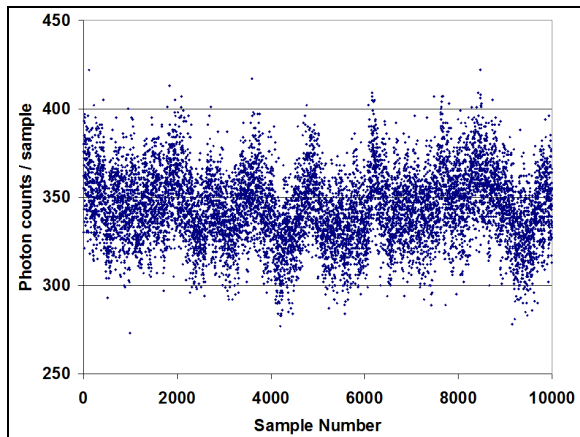


Figure 5. A small section of count data for the bright star 21 Lyr, binned to 96 μ s per sample.

The seeing signature can be easily eliminated with a high-pass digital filter. Finite Impulse Response (FIR) digital filters can be designed as high-pass, low-pass or band-pass using readily available software programs (Rabiner and Gold, 1975). Typically these filters can achieve a high level of attenuation for stop-band frequencies, while having a negligible effect in the pass-band.

Figure 6 shows the result of passing the raw data (Figure 5) through a high-pass digital filter cutting off frequencies below about 300 Hz. While this filter removes all trace of seeing from Figure 5, it also eliminates any low-frequency information that was also in the signal. Note that, with the removal of seeing noise, shot noise alone is responsible for the significant scatter still seen in Figure 6. The mean data value is now zero since the lowest frequency (zero Hz) has also been removed.

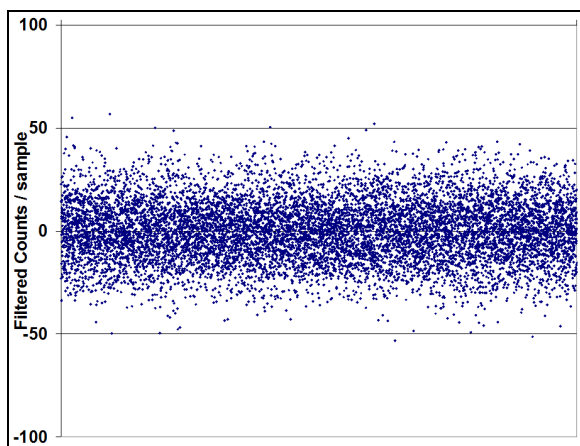


Figure 6. Data from Figure 5 after passing through a high-pass digital filter.

4.3 Frequency Spectrum Analysis

These two sources of noise also leave clear signatures in the frequency spectrum of the data. Figure 7 gives the power spectrum of the original 21 Lyr data, calculated using an FFT program available on the Internet (Ooura, 1998). In this case the original 3- μ s samples are combined into samples 768 μ s long. Note that while each FFT spectrum uses only 2048 of these samples, the final curve averages about 380 of these individual spectra. This technique greatly reduces the noise content in the final spectrum.

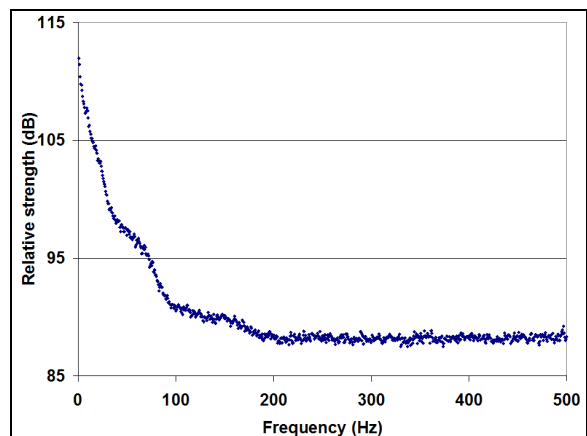


Figure 7. Power spectrum of the 21 Lyr data, after binning to 768 μ s per sample.

The spectrum in Figure 7 can be understood in terms of the two noise sources discussed above. The increasing power level at low frequencies is clearly due to atmospheric turbulence. As frequency increases, the atmosphere makes less of a contribution until it has essentially no effect on the data above 200 Hz. The interesting wiggles in this curve are almost always present, perhaps due to the interaction between seeing cell size and the telescope aperture and obscuration.

In the right half of Figure 7, the detection floor is determined by the shot noise in the signal. This noise is sometimes referred to as “white noise” since it makes an equal power contribution to all frequencies. Any signal that produces a power level significantly below this “floor” will not be detected. However, a small signal that rises above this level can be found, even though it is totally invisible in the original time-series data.

Such a case is shown in Figure 8. This figure again uses the 21 Lyr input data, this time binned to 192- μ s samples to show higher frequencies. This plot dramatically illustrates that the atmosphere’s influence is totally absent for higher frequencies. We

would get the same spectrum above 200 Hz even if the data were taken on the moon!

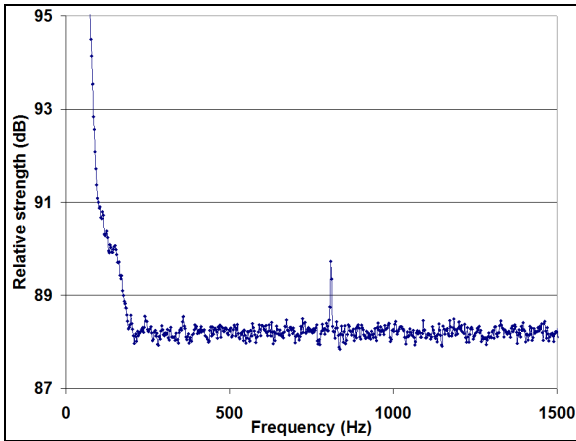


Figure 8. Power spectrum of the 21 Lyr data, after binning to 192- μ s samples to show higher frequencies (note that the vertical scale has also been expanded relative to Figure 7).

The resonance seen near 800 Hz was a total surprise. Could this be a message sent by an advanced civilization orbiting 21 Lyr? Perhaps some optical tone sent to attract our attention? Alas, not this time. After looking at the data from other stars brighter and fainter than 21 Lyr it became clear that this was some type of instrument artifact that only affects data from the very brightest stars. Whether this artifact arises from the PMT module, the counter module, or some defect in the setup, it has not been seen in data from stars 6th magnitude or fainter.

4.4 Searching for Pulses

While the power spectrum can reveal the presence of a low-level repeating waveform, other approaches must be used to find isolated pulses in noisy data. The author developed a program to search for pulses, assuming that nothing is known *a priori* about the pulse. The program uses an intuitive approach, rather than one based on mathematical theory. The following unknown parameters must be considered in the search:

- Pulse amplitude
- Pulse duration
- Position relative to discrete samples

The amplitude of the pulse must be large enough to be detected above the noise. It is assumed that an isolated pulse that is smaller than the peak noise pulses will not be found. If it is a repeating pulse it may be detected in the power spectrum, but this search assumes that only single, isolated pulse exists.

Pulse duration is also a key parameter. A long pulse might not be detected with a short sample time. Conversely, a short pulse smeared out over a long sample period might also escape detection.

Finally, the amplitude of a pulse centered exactly on the boundary between two samples will be cut in half relative to a more fortuitous positioning. The result could be that a perfectly viable pulse passes undetected.

The algorithm described graphically in Figure 9 can address each of these concerns. Starting with a nominal file of 10^8 samples, the data are searched for the largest count value. This value and position of this maximum is saved, along with related statistical data (mean and variance). Next, samples in the original file are combined, two at a time, to provide an input file for the next iteration. In order to increase the chance of detecting a pulse split between two samples in this new file, a second binned file is computed, staggered by one input sample.

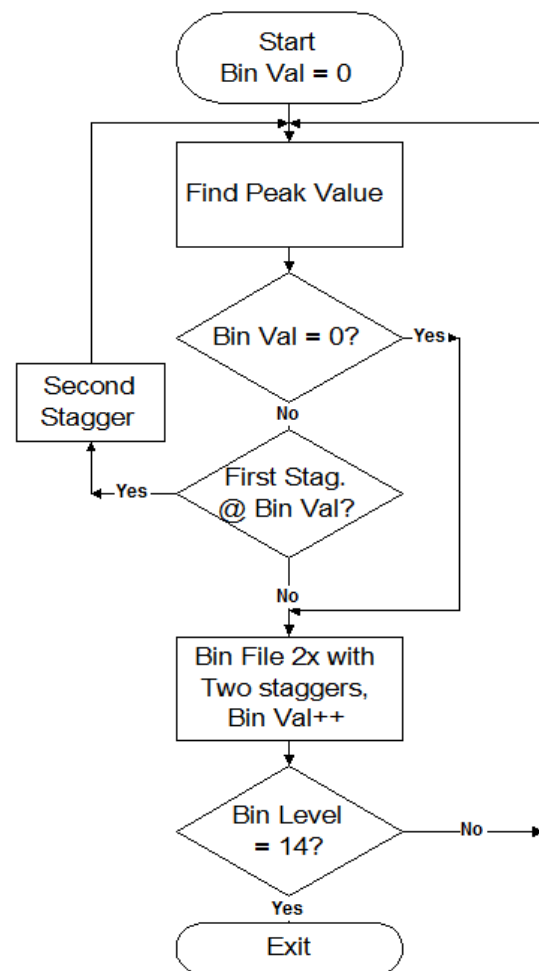


Figure 9. Program flowchart for finding peak values in a data file.

Each of these two new files is then treated as a new input file, and the process of identifying the peak repeated for both files. The result of this process for through 13 iterations of a faint test “star” is illustrated in Figure 10.⁹ The peak value for each iteration is plotted against the number of original samples summed (Bin Ratio). Since each iteration doubles the length of the count sample, the largest sample size corresponds to $2^{13} = 8192$ samples of the original $3\mu\text{s}$ data added together. Note that, except for the initial point, there are two points for each bin ratio, corresponding to the two staggers mentioned above. In this case, for many of the bin ratios, the measured peaks for the two staggers fall on top of each other.

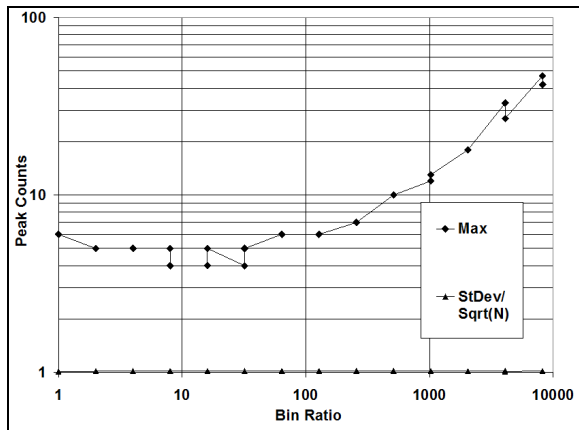


Figure 10. Peak values found vs binning ratio for file of highly attenuated sunlight (equivalent to a 15th magnitude star).

The second curve in Figure 10 plots the ratio standard deviation divided by the square root of the mean value. For purely random shot noise this value should be unity. If seeing or source variability add to the measured standard deviation, this ratio rises above 1.0. Some instrument effects (e.g. deadtime) can drive it below unity. It is plotted here as a check on data randomness.

As one might expect, the peak value increases as the sample length increases. But since the count rate is very low (0.0028 per $3\text{-}\mu\text{s}$ sample) it doesn't increase dramatically even after 8192 samples are binned together. Note that the number of samples drops proportionally as longer samples are created from the same input data. With fewer samples, one expects the probability of a truly large false signal (noise pulse) to decrease.

But what does statistics tell us to expect? We know that the Poisson distribution should apply for counting random events, even when the mean value is very small. For this distribution, the probability P

⁹ This “star” was actually attenuated sunlight to reduce seeing effects for this special test case.

of finding a value of k counts, given a mean count value of λ is given by

$$P(k, \lambda) = \frac{\lambda^k e^{-\lambda}}{k!} \quad (1)$$

Given N data points in a run, the number of these points expected with exactly k counts per sample is simply

$$n(N, k, \lambda) = N P(k, \lambda) \quad (2)$$

One can use the probability of having a single pulse in the data ($1/N$), and the mean count value λ , to calculate the peak value k , that is likely to occur, on average, once in that pass. Although k is an integer in Poisson's equation it is possible to construct a continuous curve by interpolation. If this is done correctly, one would expect measured peaks in a set of *random* count values to all fall close to this curve. If a measured peak value for one or more bin levels falls well above the curve it should be looked at as a possible optical pulse. Of course for longer pulses, atmospheric seeing may also play a role.

Figure 11 shows the results of this calculation for the test case previously described. The solid curve shows the expected peak value vs. bin ratio, agreeing quite well with the data except for bin levels less than 10. This agreement suggests that this automated approach to searching huge files of photon count data can reliably locate pulses that are larger than expected statistically. The dashed curve in the Figure 10 shows the peak size predicted the Gaussian distribution. As expected, this distribution does not work well for small mean count values but approaches Poisson for larger values.

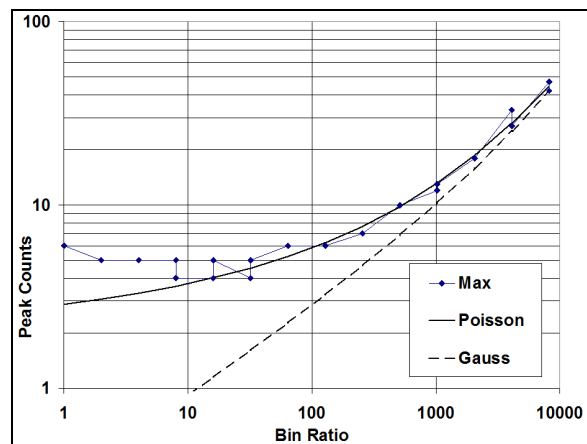


Figure 11. Predictions of Poisson and Gaussian distribution compared to data in Figure 10.

Why are the peak values for bin levels less than 10 significantly higher than predicted? One might argue that we're only talking about samples that are

one or two photons larger than predicted. Is this really important? Perhaps not, but this effect is seen for virtually every faint star case measured to date. No good explanation has yet been found for this deviation.

Setting aside these very small pulses, one can get a sense of the power of this process at separating real pulses from noise by looking at some numbers. Consider the bin level 1024 in Figure 11, corresponding to $1024 \cdot 0.002838 = 2.906$ counts per sample. The number of samples at this level is $10^8/1024 = 97,656$. Using these values the computer estimated a value of $k \sim 13$ as the count value that is likely to occur only once in this data set (solid curve in Figure 11). Equation (2) gives the following expected number of occurrences for this case:

Pulse size (k)	Expected # of pulses (n)
12	4.0
13	0.9
18	0.00018

Evidently pulses significantly larger than predicted by the Poisson curve are statistically very unlikely to be due to random noise, at least above bin level ~ 10 .

5. AM Her Pulses

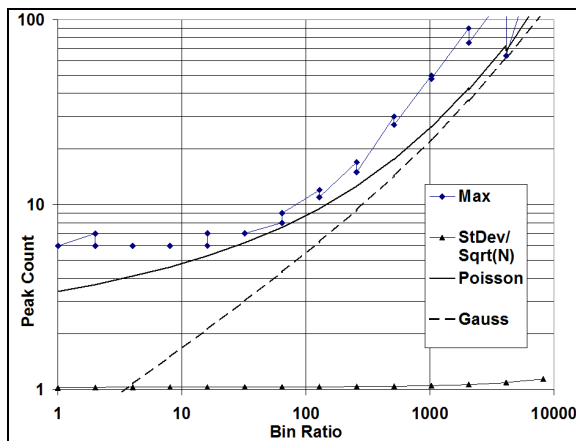


Figure 12. Pulse search results for a file of AM Her data. Divergence from Poisson curve at bin ratios above 100 indicates presence of peaks far larger than those expected for random noise.

Over the last few months, the analysis tools described in Section 4 were applied to photon data from a variety of bright and faint stars. For the most part the pulse search results were consistent with Poisson statistics of random noise, except for very low bin ratios, as discussed above. This included a number of observations of the AM Her. A notable exception occurred for one observation made on 2011 Sept. 4.

The pulse size plot for this observation shows a significant deviation from Poisson expectations, par-

ticularly for pulses corresponding to a bin ratio around 1000 (Figure 12). The plot indicates that the pulse(s) found are about twice as large as noise peaks predicted by Poisson (or Gauss), far larger than anything expected statistically.

When the time series data for this bin ratio is examined, two very large pulses are found (Figure 13). Unlike the flickering usually associated with this variable (Figure 1) these appear to be short, intense flares corresponding to a brightness increase of at least two magnitudes with durations of roughly 36 and 66 ms. Are these pulses real? There is little doubt that they are caused by actual optical pulses, not noise or some system artifact. But are they associated with AM Her? Could they just be light from a passing airplane or distant lightning? At least one other instance of a strong optical flare from this star has been reported (Cherepashchuk *et al.*, 1996), but it's not certain that this flare was anything like those shown in Figure 13.

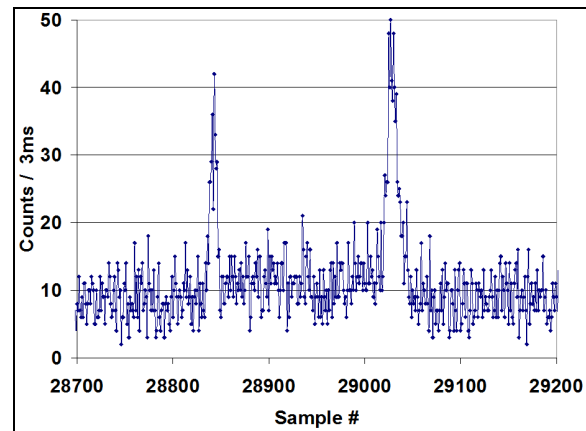


Figure 13. Pulses responsible for the non-random signature in Figure 13. These are roughly twice the size of the largest pulse expected at this resolution, a huge difference.

More observations are needed! But this event emphasizes a very real problem when searching for isolated pulses or other transient events. How does one separate “noise” such as airplanes, satellites, lightning, illuminated birds, etc., from a real signal? Having two widely separated telescopes that simultaneously observe the same target could eliminate most artifacts. The author is currently implementing another approach, monitoring the light level reflected off of the photometer diaphragm. Any pulse that appears in this reflected light is clearly not associated with the target star.

6. Conclusion

There is much that can be done by amateurs using photon counting. Very capable equipment is now

available at moderate prices. Combined with a mid-size telescope such equipment can observe many interesting, rapidly varying objects. The possibility certainly exists that an appropriately equipped observer will someday discover some previously unknown class of fast astronomical phenomena.

7. References

Burnell, J. B. (2004). "Pliers, Pulsars, and Extreme Physics", in *Radiations of Sigma Pi Sigma* **10**, pp 5-10.

Cherepashchuk, A, *et al.* (1996). *Highly Evolved Close Binary Stars: Catalog*. Gordon and Breach Publishers, p. 291.

Howell, S. B. (2000). *Handbook of CCD Astronomy*. Chp. 5. Cambridge University Press, Cambridge.

Menke, J. (2009). "The Addictive Properties of Occultations." in *28th Annual Conference of the Society for Astronomical Sciences* (Warner et al., eds.). pp. 9-17. Society for Astronomical Sciences, Rancho Cucamonga, CA.

Ooura, T., (1998). Freeware program `fft4g.c`

Rabiner, L., Gold, B. (1975). *Theory and Application of Digital Signal Processing*. Chp. 3. Prentice-Hall. New York.

Stanton, R. H., (1983). "Design and Use of a Computer-Based Photon Counting System" in *Advances in Photoelectric Photometry—Volume 1* (R.C.Wolpert, R. M. Genet, eds.). pp. 87-129.

Vander Haagen, G. A. (2011), "The Silicon Photomultiplier for High Speed Photometry." in *30th Annual Conference of the Society for Astronomical Sciences* (Warner *et al.*, eds.) pp. 87-96. Society for Astronomical Sciences, Rancho Cucamonga, CA.

Tracking Bolides, 3D Visualization and Data

Thomas G. Kaye
Foundation for Scientific Advancement
7023 Alhambra Dr., Sierra Vista, AZ 85650
tomkaye@u.washington.edu

Robert Crawford
Tucson AZ

Mark Bowling
Tucson AZ

John Kalas
Tucson AZ

Abstract

For the past decade progress has been made in using consumer-grade low light video cameras to watch the night skies for meteor trails. Sophisticated software can now monitor the video stream in real time and parse out the events of interest from a continuous recording. Sandia Laboratories has funded over 100 of such cameras spread throughout the country. Their primary purpose has been to record large fireballs. The fireball data is primarily used to compare with space based observatories that are watching for nuclear explosions on Earth. The Desert Fireball Array in southern Arizona has deployed three of these cameras in overlapping visual fields. The mutual detection of events allows for three-dimensional reconstruction of the entry angle, speed, brightness and spectroscopy. The stated goal of the project is to use the tracking information to locate and recover a meteorite that was tracked through the atmosphere. The acquired data would allow direct comparison of atmospheric ionization characteristics to ground based laboratory analysis using simulated ablation of the same meteorite. To achieve this goal, high precision calculations and final analysis using 3D projections in Google Earth will be described.

1. Introduction

Meteors are the least expensive “sample return missions” available on Earth. Known meteor showers have been a subject of intensive studies especially in Europe (Berezhnoy, 2010; Borovička, 1994). The sporadic meteors however present a challenge for research due to the random nature of their arrival and difficulty of recovery. While many large random bolides have been captured on home video, comparatively few have been recovered and almost none with reliable reentry data. Most data available from previous studies consists of velocity and brightness information (Borovička, 2007). Spectroscopic data is available for showers (Madiedo, 2011) but almost non-existent for sporadics. The upper atmosphere where bolides begin ionization is molecularly extremely thin and is at a higher vacuum than can be achieved on Earth. This leads to unusual ionization species that normally recombine instantly in a lower vacuum plasma environment but in the upper atmosphere, live long enough to display “forbidden lines” in their spectra.

Velocity upon reentry while consistent in meteor showers varies widely with sporadics and has not been well characterized. Velocity and entry angle combine to influence the survival potential of a meteor through the burn phase. Certain orbit trajectories can closely match Earth’s orbital velocity and are very favorable for meteor survival. These bolides exhibit slow apparent velocity and deep penetration before dark flight.

For the past three years the group known as the Desert Fireball Array has been running three cameras on a triangular 100 kilometer baseline that covers the south eastern corner of Arizona.

2. Materials and Methods

The initial Sandia Labs camera is pictured in Figure 1. The housing uses standard PVC fittings with an acrylic dome. Self-contained in the housing is the camera, power supply, heating unit and temperature control module. It is powered by 120 VAC and feeds an analog video signal via the coax cable to a commercial computer video card at video frame rates.

The software is proprietary to Sandia and scans each series of 5-10 frames looking for brightness changes above a certain threshold. It is continuously recording and holds approximately the last 30 seconds in a memory buffer at all times. Once an event is triggered, the buffered recording allows the entire event to be saved with no clipping due to detection lag. The resulting data file displays a subframe of the video with the target centered in the field. A key-stroke will provide a light curve for the duration of the burn.



Fig. 1. Sandia video camera housing. System incorporates PVC fittings for waterproofing with internal heater and power supply.

Figure 2 shows the second generation housing developed by the Fireball Array team. It is based on an inexpensive waterproof electrical enclosure that has been modified with an optically flat side window. The heater and onboard power supply have been dispensed with in order to save space and it is now powered by an external supply. The original camera utilized a 360-degree fisheye lens for horizon-to-horizon coverage. In practicality, bolides close to the horizon are typically many hundreds of kilometers away and do not produce useful data. The horizon in view also creates multiple false triggers from cars etc. Experimentation showed that three cameras using lenses with a 120 degree field-of-view, in a triangular deployment, provided a higher resolution image. In this arrangement, each pair of cameras looks “over the

shoulder” of the third camera to maintain a 360 degree mutual detection zone as shown in Figure 3.



Fig. 2 Second generation camera housing with 100 degree field of view.

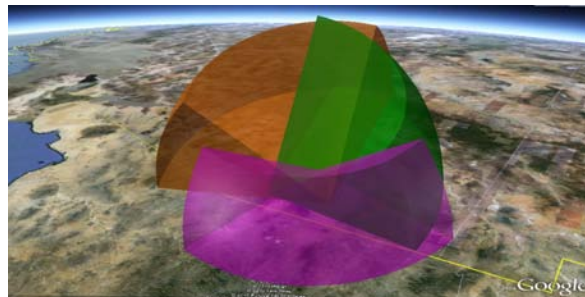


Fig. 3 The three cameras overlap the field of view within the 100 kilometer baseline. Dual camera detections are possible out to several hundred kilometers.

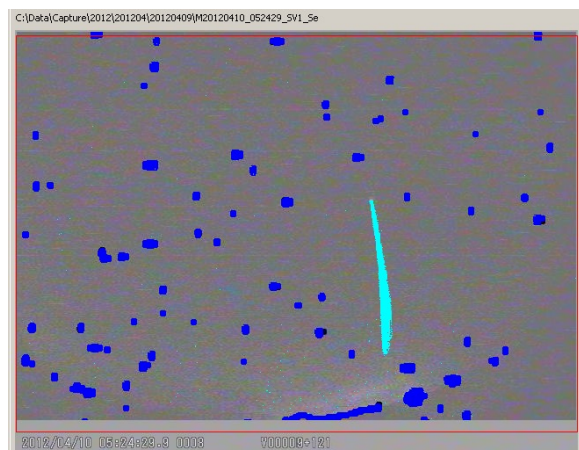


Fig. 4 Automatically generated masking in UFO Capture in dark blue. This reduced the number of false hits by approximately 95%. Light blue is a captured meteor trail.

The Sandia software has now been replaced with UFO Capture (Sonotaco.com) that was developed in

Japan. The new software features a self generating mask that blocks areas of twinkling lights such as stars or streetlights that continually vary (Fig. 4). This very powerful feature eclipses other software and drastically reduces the number of false detections, which can easily fill a hard drive in one night. Astrometric calibrations are handled by matching a star field to the mask. A least-squares calibration between the field and the mask determines RA and DEC for each pixel. In Japan, UFO Capture is used primarily with narrow field camera lenses (25~40 degree field of view). It remains to be determined whether the camera model used in the astrometric calibration can represent the greater distortions present in fisheye lenses.



Fig. 5 Reconstructed path through the atmosphere in Google Earth. The position data was extracted for each frame.

Combining the astrometric position information from two or more cameras allows for a three dimensional reconstruction of the bolides path through the atmosphere. In order to determine a potential impact zone, Google Earth data files were created from the multi-camera reentry data (Fig. 5).

The 3D rotation in Google Earth allows rotation in order to “sight down the barrel” of the bolide’s trajectory and define a spot on the ground as the maximum, or farthest point of impact for the search ellipse (Fig 6.) Additional rotation allows for the end of the burn phase to be viewed normal to ground, thereby determining the minimum, or nearest position for the ellipse discounting wind.

The light curve for the bolide is extrapolated from each frame of the video stream. The light curve is superimposed three dimensionally on top of the trajectory again using Google Earth. Penetration into the atmosphere is then visually correlated with brightness (Fig. 7).

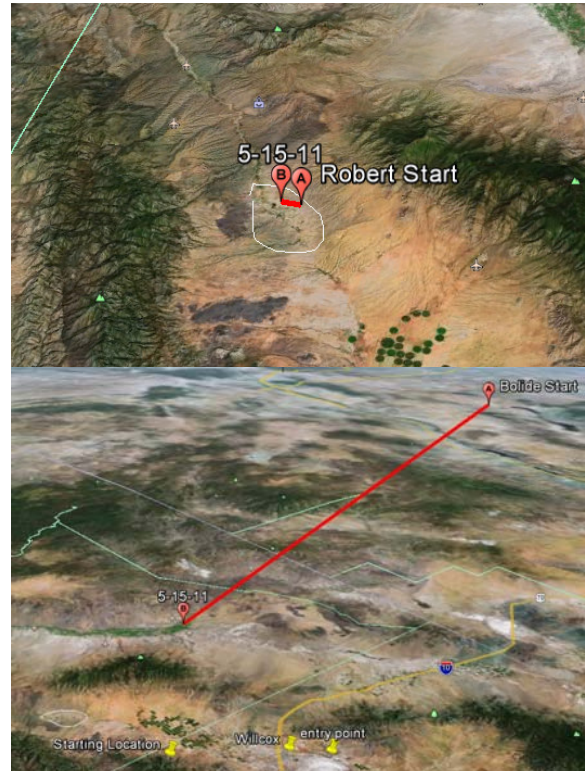


Fig. 6 Using Google Earth to calculate the search area for a fall. Upper image is “looking down the barrel” of the bolide path in order to determine the furthest extent of the strewn field. Lower image is a side view of the trajectory in order to determine the minimum starting point for the ellipse of the strewn field.



Fig. 7 White vertical lines above the red reentry path indicated the relative brightness during the burn phase. In this configuration the light curve can be visually correlated to the penetration into the atmosphere.

Proprietary software has been created in Matlab to triangulate a bolide's position in three dimensional space on a frame-by-frame basis. For events seen by two or more stations, the video recordings are aligned in time to sub-frame accuracy ($<1/30^{\text{th}}$ second) by correlating the light curves. The bolide's pixel position in each video frame is turned into a line-of-sight vector based on the astrometric calibration of each camera's orientation on the sky. The lines of sight from two or more stations are then intersected to find the estimated location of the bolide that approaches all lines of sight most closely at that instant in time. The triangulation takes account of the geographic location of each station, the rotation of Earth, and the location of Earth in its orbit around the Sun to compute the instantaneous position of the bolide in Cartesian XYZ coordinate systems, both geocentric and heliocentric. Frame-to-frame differences in the positions are used to compute the bolide's velocity. With careful astrometric calibration of each camera's orientation on the sky, scientifically useful data on bolide dynamics can be extracted from the video frames.

Spectroscopy is accomplished through a stand-alone system that incorporates a CCD camera with a low F-number lens in front of a transmission grating. The camera is set to continuously expose 30-second images through the night. This system's visual field overlaps the center of the three detection cameras. A detection from one of the other systems is time stamped and allows the proper frame to be extracted from the night's sequence of frames. Figure 8 shows a reentry and its associated spectra. Each horizontal row of pixels produces a spectrum so the entire evolution of the ionization and ablation process can be analyzed.

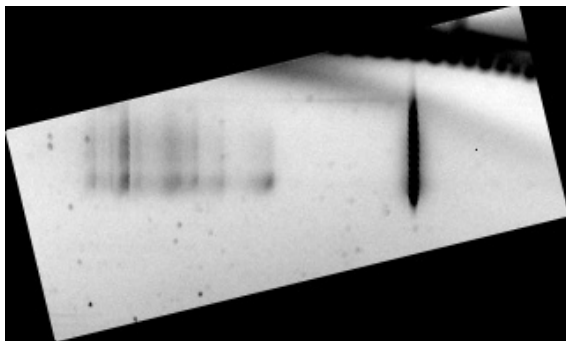


Fig. 8 Spectrum of bright bolide.

3. Discussion

Data on meteor showers is available for virtually all of the major events. Efforts in the 1980's and 1990's centered around film and continuously recorded video, which were cumbersome and lacked

sensitivity. Recent interest in sporadics has been helped by the marriage of computer recorded video and low light video cameras bringing new technology to bear on the problem. The original systems brought out for meteor detection were either proprietary or Linux-based, which made wide-scale deployment difficult (ASGARD). The second generation of software described here, makes video integration much easier and the detection algorithms are much more robust.

This project's first goal is to acquire as much data as possible including vector, velocity, brightness and spectroscopic information. This data has been available before but never has the actual meteorite that generated the data been available for analysis. Using the 3D reconstruction, a search ellipse becomes apparent and a local team of searchers is standing by to fulfill the second goal, which is to acquire the meteor that generated the data.

Once in hand, laboratory analysis of the material can be directly compared to reentry data to "ground truth" the observations. Laboratory work can identify limits of detection, anomalies in the spectra, temperature and ablation characteristics which can all be compared to the atmospheric data. This will allow refinement of the characteristics of bolide reentry and, with further processing, the reentry vector can be extrapolated into orbital parameters as is currently being done by NASA to determine the original source of the bolide (NASA).

4. Conclusions

The technology for full-time automated detection of meteors has finally come of age. The combination of inexpensive low light cameras and high performance real-time analysis of the video stream, creates a powerful tool for bolide research. Visualization tools such as Google Earth are bringing the data to life in simple but effective ways and allowing an unprecedented look into all aspects of Earth crossing bolides. The instrument infrastructure is now in place and all that is necessary is the cooperation of a random bolide to enter the atmosphere in the right area. In the last several years at least three large bolides have fallen inside the detection area. One of these was recovered and is now known as the Whetstone fall (Wikimedia.org). Unfortunately, technical problems had cameras off-line during these events and a mutual detection was not recorded. The technical difficulties have now been overcome and multiple cameras are scanning the skies on a regular basis just waiting for the next big event.

5. References

ASGARD, All Sky and Guided Automatic Realtime Detection. Meteor detection software.
meteor.uwo.ca/~weryk/asgard

Berezhnoy, A. A. (2010). “Formation of molecules in bright meteors.” *Icarus* **210**, 150–157.

Borovička, J., Spurný, P. (2007). “Atmospheric deceleration and light curves of Draconid meteors and implications for the structure of cometary dust.” *Astron. Astrophys.* **473**, 661-672.

Borovicka, J. (1994). “Two components in meteor spectra.” *Plan. Space Sci.* **42**, 145-150.

Madiedo, J. M. (2011). “Emission Spectra of Geminid Fireballs from 3200 Phaeton: Preferential Depletion of Volatile Phases.” IAU Symposium.

NASA, All Sky Fireball Network,
<http://fireballs.ndc.nasa.gov>

Sonotaco.com, UFO Capture Software.

Trigo-Rodriguez, J. M., ed. (2008). *Advances in Meteoroid and Meteor Science*, Springer Pub. 564 pgs.

Wikimedia.org, Whetstone Mountains Meteorite,
http://commons.wikimedia.org/wiki/File:Whetstone_Mountains_meteorite.jpg

Tools and Techniques for Measuring Asteroid Occultations with DSLR and CCD Cameras

*John E. Hoot
SSC Observatory
615 S. El Camino Real
San Clemente, CA 92672
Observatory@ssccorp.com*

Abstract

Currently most asteroid occultations are measured with video equipment. This technique is limited to stars bright enough to be measured at 30 frames per second and limits participation to observers that have portable low-light video and time standard tagging equipment. This paper presents new observation tools and analysis methods that allow the larger community of astroimagers to make precise occultation measurements with tracking telescopes and DSLR or CCD integrating cameras.

1. Introduction

Occultation events occur when one body, typically non-luminous, passes directly between an observer and a more distant luminous body, completely blocking the distant body's radiation. Occultations are a sub-class of transit events. This special alignment of the observer, distant object, typically a star, and the occulting body provides an opportunity to determine the shape of the occulting body. The most typical forms of occultation measurements are performed on asteroids passing in front of stars and lunar limb features passing in front of stars.

For the case of asteroids, if we know the orbit of the asteroid with sufficient precision to predict the transit, we also know its distance to the observers and its apparent velocity in the plane perpendicular to the observer's line of sight. With this information, simple algebra and multiple observers it is possible to accurately render the cross sectional profile of the asteroid.

With the advances in precision stellar and asteroid astrometry in combination with low cost computing power, it is now possible to predict, with reasonable accuracy, many more occultation events than ever before. For lack of sufficient observers, many of these events are under recorded.

Currently, most occultation observers are diligent shadow chasers. They are typically equipped with telescopes, low light video cameras, a time standard capable of imprinting accurate time codes onto the video, and a video recording system. With this equipment they do fantastic work. This type of equipment is pretty specialized and requires a commitment to this type of observation that not many observers are going to make. At the same time tele-

scopes, DSLR cameras, CCD cameras and computers proliferate.

Drift scan imaging is a known technique for using this most common type of astroimaging of equipment to measure occultation events. The method allows integrating cameras to make accurate occultation observations. Historically, the precision of this method was limited due to time jitter in the observation. This situation has changed with the proliferation of smart-phones, GPS's, computers and wireless networks.

This paper presents an overview of how to make drift scan occultation measurements using modern timing and geodesy technology. It also presents an overview of currently available free computing tools to assist in making these measurements. Finally, it introduces a set of freely distributed tools developed by the author to facilitate occultation planning, observing and data analysis.

We are near a tipping point in occultation astronomy. The correct equipment is in enough hands. Enough events are being predicated with sufficient accuracy that observers may wait for events to come to them. The tools are freely available. The time has come when drift scan occultation observation now belongs in every astroimager's repertoire. And perhaps soon it will become the predominant method for occultation observation.

2. Drift Scan Fundamentals

Traditional video occultation measurement methods point a telescope at the star to be occulted and record the star's image 30 frames or 60 fields per second. To measure an occultation one examines the video frame by frame measuring the star's brightness.

The brightness of the star is plotted against the time coded frames to look for the time and duration of the star's dimming or complete disappearance. This is a mechanization of the visual method of calling out the events seen through the eyepiece, recording the observations on audio tape, while a time signal plays in the background.

Drift scanning uses a different method. One starts to make a traditional long exposure image, but at a precise moment prior to the predicted occultation the user disables, or retards, the clock drive of the telescope. This results in stars being trailed. In some variations of the method, the drive is re-enabled. By measuring the star trail's flux versus position in the image, the precise time and duration of the occultation can be determined.

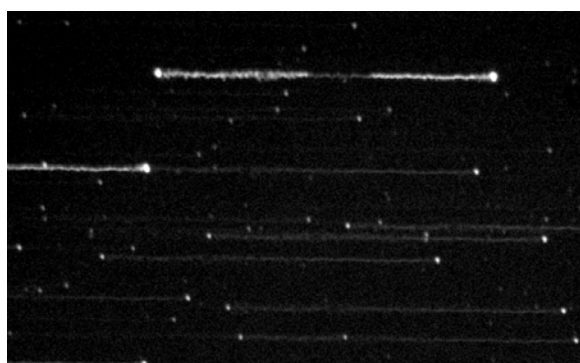


Figure 1. Drift Scan Occultation Observation Example

Figure 1 shows an example of how a drift scan observation appears in an image. In order to determine the precise time and duration of the occultation, the observer needs to know the time that the drifting began, and the rate of drift. Provided the observer knows the rate of drift in pixels/second, reduction becomes a straight forward measurement and calculation.

3. Drift Scanning vs. Video

Drift scanning has both disadvantages and advantages when contrasted with video measurements. The greatest strength of the drift scan method is that integrating cameras, particularly in the case of CCD cameras, have better signal to noise ratios than video cameras. Video signals rarely approach 10 bits signal to noise ratios. DSLR cameras typically have 12 to 14 bits S/N ratios, and cooled CCD's can have 14 to 16 bits S/N ratios. Additionally, since you read out your imager only once, you have only one unit of readout noise per pixel, as opposed to 60 per second. This latter advantage is only significant if your drift rate is less than 60 pixels/second. The other strength of this method is that by varying your plate scale or

drive speed, you have complete control over the drift rate. This allows you trade off timing accuracy for improved signal to noise ratios by lowering your drift speed.

These two advantages provide the ability to measure events, albeit to lower resolution, than are simply inaccessible to video, for a given aperture of telescope.

The method's greatest weakness is that time jitter in the triggering of the drift tends to be larger than in video measurements. Even if the power to the telescope drive is interrupted, flywheeling of the motors and energy stored in the scope power supply capacitors will cause the drifting to begin some time later than when it is triggered. In the case where the drive servos are commanded to stop or retard, the delay in the servo motor loop will cause the drifting to be delayed by the servo latency.

4. Drift Scan Planning

The first step in making an occultation observation is to locate events proximate to you. IOTA, the *International Occultation Timing Association*, has a wonderful web site that will show you predicted events in your vicinity. I am particularly fond of Steve Preston's *Worldwide Occultation Prediction Page*. It provides a concise summary of upcoming events with a notation of the broad geographical regions from which the event is expected to be visible. If an event is going to be visible in your broad geographical region, you can then link to a more detailed map of the shadow's path across the Earth. If this looks like something accessible to you, you can then download a summary of the occultation event and the visible path with 1 sigma error margins.

Upcoming Events:

April 2012

Event Date/Time	Rank/Asteroid	Star	Visibility	HM D.A	Details
07 Apr. 12:40 UT	53 (161) Athor mag 12.8	UCAC2 21109150 mag 10.9	N Mexico, New Zealand	2.1m 8.3s 81°	[Mar 31 23:03]
07 Apr. 12:54 UT	45 (78) Theobalda mag 15.5	UCAC2 15772656 mag 10.9	Australia	4.6m 7.1s 74°	[Feb 09 08:07]
08 Apr. 03:38 UT	99 (165) Loreley mag 13.7	UCAC 3878763 mag 13.2	SW USA, Mexico, Venezuela	1.0m 18.2s 68°	[Mar 31 23:07]
08 Apr. 05:02 UT	10 (3346) Oryta mag 16.4	UCAC 11856137 mag 9.9	Brazil, Argentina	6.9m 2.6s 56°	[Jan 10 11:46]
08 Apr. 06:49 UT	42 (341) California mag 13.3	TYC 5545-00242-1 mag 10.0	N Canada	3.4m 1.5s 25°	[Mar 31 23:09]
08 Apr. 07:41 UT	0 (120061) 2003 CO1 mag 20.5	UCAC2 23171710 mag 13.2	South America	7.1m 8.5s 88°	[Mar 10 09:44]
08 Apr. 08:07 UT	67 (196) Philomela mag 12.1	UCAC 22091680 mag 12.5	SE USA	0.6m 11.1s 52°	[Feb 11 03:33]
08 Apr. 13:18 UT	16 (2388) Karolinum mag 16.0	HIP 91652 mag 10.1	S Pacific	5.9m 1.5s 54°	[Jan 10 11:49]
08 Apr. 15:36 UT	99 (70) Alauda mag 12.8	TYC 7890-01339-1 mag 12.0	Antarctica, SW Australia	1.2m 39.8s 50°	[Feb 11 03:33]

Figure 2. Occultation Event Summaries

Once you have located an event, you need to pick a site from which it will be observed. If you are fortunate, the site may be your own back yard, or your observatory site. More likely you will need to travel some distance, so prior planning is key. To facilitate this effort the author has developed a utility that converts occultation event summaries to “.kml”

files that load as overlays to Google Earth's application.

The application is titled *Occultation Maps*. When run from a PC it presents a screen as shown in Figure 3.

Once you have loaded an event, the header summary of the event shall appear in the dialog's main window. Assuming you already *have Google Earth* on your computer, simply click on the "Convert and View" button. Shortly, the globe will be displayed with the shadow path and 1 sigma error estimate imposed over it

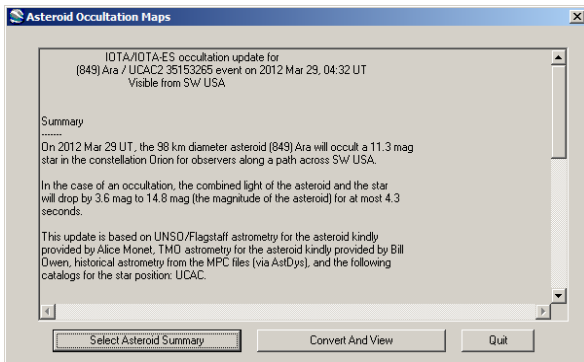


Figure 3. Google Earth Map Generator

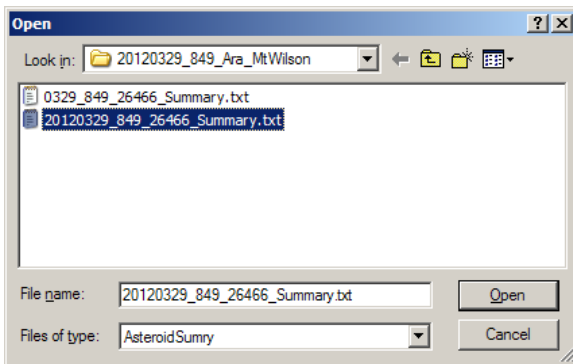


Figure 4. Loading An Event

Once you have the path in *Google Earth*, it is easy to use the interactive controls and overlays to locate an observing site that provides you with convenient access and infrastructure. For the event pictured in Figure 5, it was fortunate that the path of expected visibility passed directly over the Mount Wilson Observatory.

With the permission of the facility superintendent, I was able to set up in their 16-inch dome to attempt to view this event.

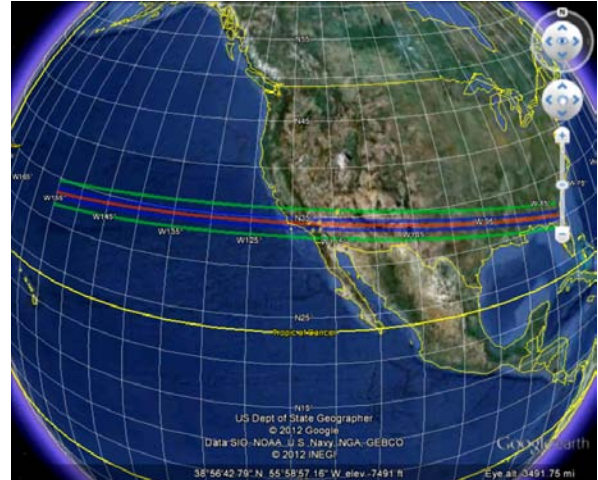


Figure 5. Shadow Path In Google Earth



Figure 6. Site Selection

5. Making The Observation

Since you should have selected your opportunity well in advance, best practice is to setup and configure your gear a week or so ahead of time and rehearse. This will prevent nasty surprises, such as overcrowded star fields, poor signal to noise ratios, faulty cables, missing software, over filled disk drives, etc.

The keys to making a good observation are being on target, getting a good exposure, accurate timing, and precise geodesy. All of these can be practiced in your backyard BEFORE you go, should travel be required. Once you can do it perfectly in your yard, you can pack everything that is there and know you will have all the tools required when you get to your site. Even if the site is your own yard, you will have worked out all the kinks when you are not under the gun.



Figure 7. Cell phone GPS/Compass

First, work out the exact location from which you will observe. This is easy if you are already using Google Earth. Just put a pushpin on your site and read out the latitude and longitude. Alternatively, if you must change locations at the last minute, you can retroactively locate the site in Google Earth, or often smart cell phones now contain GPSs that can give you exact location.

Next, select your drift method. The two primary choices are “Drive Off” or “Drive Guided”. The “Drive Off” method simply removes power from your telescope and lets the Earth’s rotation move the stars across your image frame. This is absolutely the simplest method. It can be as simple as:

1. Centering Your Star
2. Starting Your Exposure
3. Punching off the power switch on your telescope as you listen to WWV on a shortwave radio.
4. Waiting for your exposure to finish.

A more complicated method may use a computer triggered switch or relay to interrupt the power to your scope. This approach takes human reaction times out of the equation and does not impart motion to the scope. Regardless of the method used to perform a “Drive Off” observation, the drift rate will be

a function of your plate scale and the declination of the target star.

The formula to convert pixels to time for “Drive Off” observations is:

$$\frac{PS \times Length}{15.041 \times \text{Cos}(Dec)} = T$$

Where :

- PS* = Plate Scale (arc sec/pix)
- Dec* = Declination of Target Star
- T* = Duration of Event
- Length* = Length of Event In Pixel

While this method is easy, it does mean that you will need to employ focal reducers and/or binning of your images to adjust the plate scale to fit the brightness and duration of your event.

The other observing method, that I call “Guided Drift”, requires you to have a telescope with either an autoguider port, computer commanded tracking rates or slewing. In this method you command the telescopes servo system to alter its drive rate by initiating a guiding command, or altering the drive rate for a fixed amount of time, starting before the event and ending after the event. This method requires a computer with a connection to your telescope, but has the advantage that you can precisely tailor the drift rate to suit your instrument’s sensitivity. Additionally, data reduction does not require any astrometry to solve plate scales on your images.

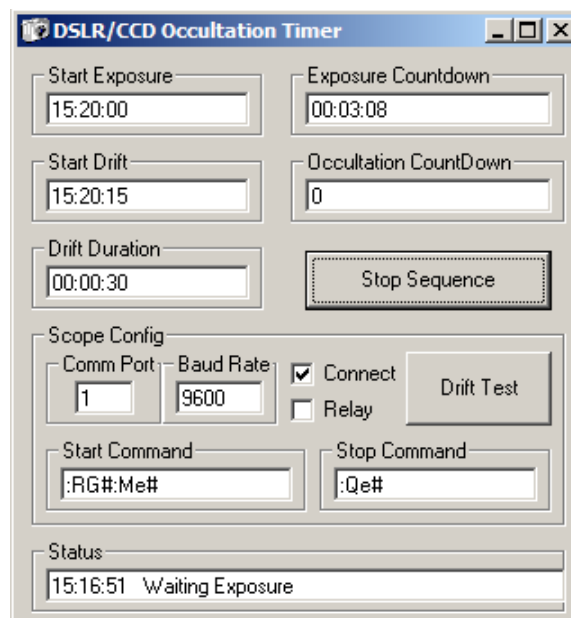


Figure 8. Drift Scan Trigger Screen Shot

The author has developed a PC application that controls this process. Once you have entered your event parameters, the software alerts you as to when to start your exposure. After that, all the key timing events are triggered automatically. The application is titled *Drift Scan Trigger*. Figure 8 shows a screen shot of the application.

To use the “drift scan trigger” program with telescopes that accept guiding and tracking commands directly from their serial ports, simply connect your PC to you telescope. The command sequences to start and stop drifting can be entered in the “Start Command” and “Stop Command” windows.

In the example in Figure 8, the program is configured to command a generic Meade telescope to apply east guiding for the drift duration. Since my Meade telescope hand controller lets me specify a guide rate from 1 to 100 percent of sidereal rates, I can pre-configure my scope with a tracking rate appropriate to my target. A guide speed setting of 100% effectively halts the drive system on my scope.

If your scope lacks the ability to serially command the drive system, it may still be equipped with an auto guiding port. Typically, these are presented as modular phone connectors where the grounding individual pins cause the scope to slowly guide east and west in RA and north and south in DEC. In these systems, you can build a simple serial port controlled switch to interface with the scope’s guider port. A schematic for a simple control is shown in *Figure 9*.

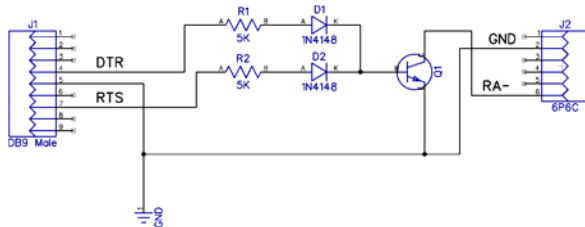


Figure 9: Guider Input Interface

Finally, you can modify the circuit in *Figure 9* to activate a relay interrupting power to your telescope.

If you are using the guider interface or a relay, you need to check the relay box in the program to change the way the serial port is commanded. Otherwise, uncheck the relay box if you are serially commanding your telescope.

To use the Drift Scan Trigger program, synchronize your computer’s time with a standard time signal (see section 6). Next determine how long you want to drift. Your drift time should be longer than the expected occultation duration plus 2-sigma of the expected time and an additional margin for trigger.

Configure the start time to be at least 15 second prior to the start of the drift timing, and be sure your total exposure time leaves some additional time at the

end of the drift sequence. This will cause you to have two bright images of your target star in your exposure with a thread of light between recording the target star’s flux during the drift interval.

There is a Drift Test button that allows you to simulate the event instantly. This allows you to frame your target. Start your exposure and click on “Drift Test”. The program will command your telescope through the same sequence of commands that will be sent during the event. It allows you to inspect your result and if necessary adjust the position of the target star in the frame or modify your drift rate or plate scale to optimally capture the event.

When your occultation event time nears, click the “Start” button. The status line will count down the time until the start of the exposure. Starting 6 seconds before the exposure, the computer will start beeping at one pulse per second to prepare you to start the exposure. As the program counts to 0, start your exposure. From here on, all the critical actions will be triggered under computer control.

6. Precise Computer Time

The key to success with drift scan method is having the computer clock maintain as precise a time as possible. If you computer has a broadband Internet connection, keeping precise time is easy. There are a number of excellent programs that will synchronize your computer’s clock with the National Institute of Standards and Technology’s atomic clock. My personal favorite is *Dimension 4*. Once loaded, it runs in the background, waking up at programmable intervals, pinging the Atomic clock and updating your PC’s clock.

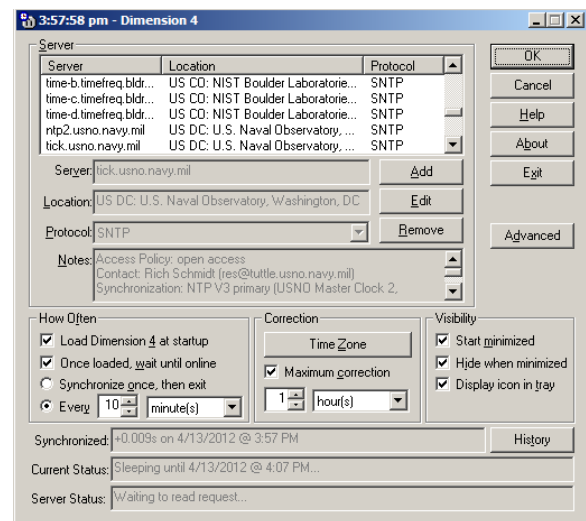


Figure 10. Dimension 4 Screen Shot

Asteroid Occultation Techniques - Hoot

One of its excellent features is keeping a running history of its corrections so you can get an estimate of the drift rate and the statistical accuracy you may expect from your observations.

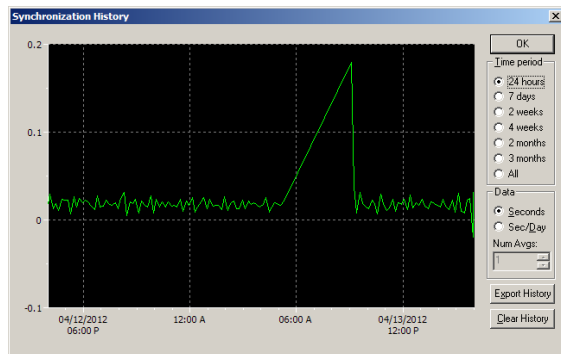


Figure 11. Time Correction History.

Figure 11 indicates that my machine tends to stay within 10 msec of standard time as long as I maintain an Internet connection. Left on its own, it drifts at a rate of 180 msec in 3 hours, or 60 msec per hour.

This tool is even useful in the field. As long as your observing location has 3G or 4G cell phone service, you can tether your phone to your computer, run *Dimension 4* and have time accurate to 10 msec.



Figure 12. USB GPS Receiver

In the event you do not have network connectivity, there are two other methods that are very reliable. First is WWV and WWVB, the NIST radio stations that transmit time signals on 2.5MHz, 5MHz, 10 MHz and 15MHz. When using these sources, I turn on only the computer and radio and keep them as far apart as I can and still hear the radio. My experience is that these signals can be difficult to use near computers, telescopes and cameras that all emit radio interference. But if you use WWV to sync your clock

shortly before observing and have characterized the clock drift with *Dimension 4* previously, you can still get pretty accurate results.

NEMA GPS signals are the final option. An inexpensive USB GPS module runs about \$25 from various Internet vendors. It looks to the computer just like a serial port connected to a GPS receiver.

Several years ago the author developed a utility to capture locations information and synchronize computer clocks from GPS serial data streams.

One of the well known problems with GPS/NEAM data streams is that they show a delay between the correct time and the output of the time string that is device dependent. However it is the author's experience that while these delays differ from device to device. For a given device the delays are relatively constant. For that reason, the *GPS Geodesy* program includes a "Delay" parameter field. It contains a static correction to be applied to the GPS time standard prior to its being applied to the PC clock.

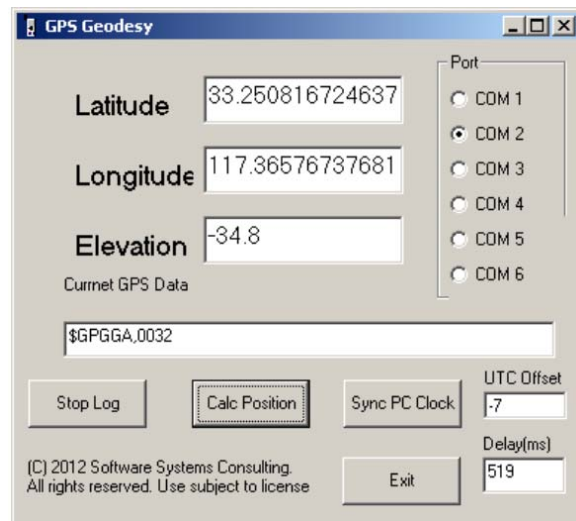


Figure 13. GPS Geodesy Screen Shot

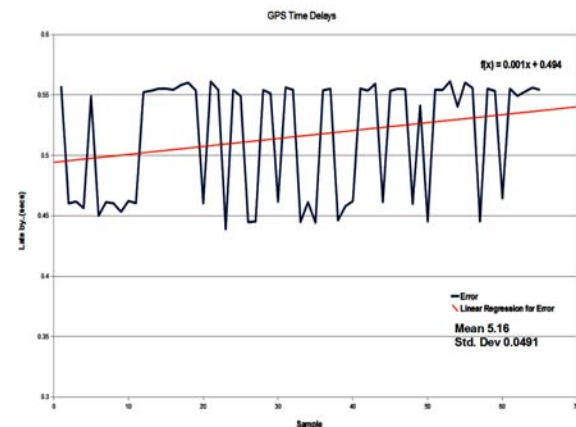


Figure 14. GPS-NEMA Jitter

Figure 14 shows the results of 60 trials of applying GPS serial time corrections versus Dimension 4 network time standards. It demonstrated that GPS serial data streams provide accurate timing to ± 50 milliseconds, $1/20^{\text{th}}$ of a second accuracy from virtually any location.

To characterize a new device, simply connect yourself to the Internet and put the GPS where it can get enough satellites to get a fix. Often you can obtain a fix in a wood frame structure. Then bring up both *Dimension 4* and *GPS Geodesy* on your system. Set the GPS delay to 0 and alternate between synchronizing to network time and GPS time. About 50 or so tries will get you a statistically useful sample population. Now go to *Dimension 4*'s history window and export the history file as a CSV file and use your favorite spreadsheet to analyze the results. Take the simple mean and plug it into the *GPS Geodesy* program's delay parameter and you are ready to go into the field.

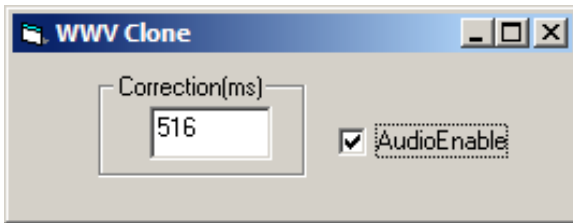


Figure 15. Virtual GPS

The final time tool, developed by the author, is titled *virtual WWV Clone*. It uses the PC's clock and the audio system in a computer, to create a fake WWV audio stream. It assumes the computer has been synchronized with some time standard. The PC itself has some delay inherent in the multimedia system, so the best way to calibrate a computer is to set the computer time via your preferred method and then tune WWV in on a good radio. You can then adjust your correction factor so that your computer's time signals sync with WWV's. The human sense of rhythm is accurate to better than 10 milliseconds. So, when it sounds good, it is good.

With a PC and a WWV clone, you can make drift scan observations by simply watching the PC's clock. Open the shutter on your camera and pull the plug on the right WWV time tick.

Regardless of the drift scan exposure method you employ, the duration of the occultation will be measured very precisely. The primary error will be the time displacement of the observation related to the jitter in the drift triggering mechanism.

7. Data Reduction

The ultimate product of your observation will be the duration and start time of the occultation at your observing location, or lack thereof. Data reduction is the process of extracting that information from your drift scan image.

The steps in data reduction of a drift scan CCD image start out as in any other CCD image, by calibrating for bias, dark current and potentially flat fielding the optics.

To facilitate the easy extraction of the event data, the next step is to rotate the image such that the star trails are precisely horizontal. The tool used to do this should be flux conserving, so as not to corrupt the photometric information in your image.

Next you want to extract the brightness history versus position in your image. Most astronomical image processing tools provide a method for this process.

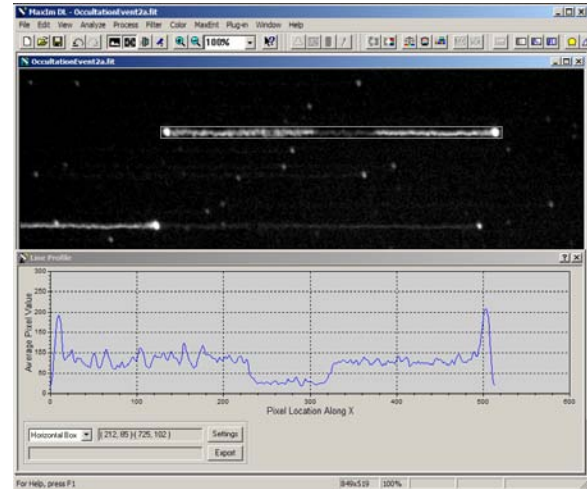


Figure 16. Line Profile Extraction

Figure 16 shows how to accomplish this in Maxim/DL. Using the cursor, box the target star's trail including both the start and end points. From within the "View" menu, select "Line Profile". Finally, within the line profile dialog box, select "Horizontal box".

At this point you have a graph of the sum of the columns within the box plotted against the row pixels. To maximize signal to noise ratios you want to box the star trail while encapsulating as few of the background pixels as possible.

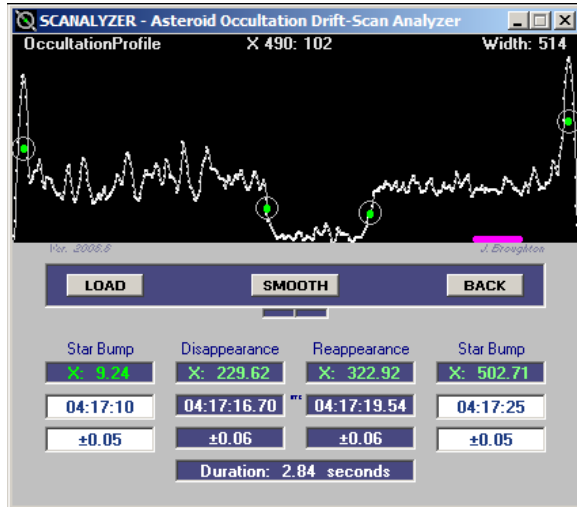


Figure 17. Scanalyzer Screen Shot

Similar graphs can be extracted by IRAF and IRIS. Both are free image analysis software.

At this point there are a couple of different ways to go. Easiest in Maxim/DL is to move over the graph, reading out values. Locate the center of the star before and after the drift. The drift time divided by the difference in pixels between the two star images is your *SecondsPerPixel* coefficient. Now measure the pixels between start of drift and the midpoint of the occultation ingress. Next measure the duration of the occultation in pixels. Multiplying both values by the *SecondsPerPixel* coefficient to get the timing of the events.

Alternatively, you can export the data to a “.CSV” file and perform similar computations in your favorite spreadsheet.

Finally, John Broughton has developed an easy interactive drift scan analysis tool called *Scanalyzer* that he distributes for free from his website. It takes exported profile drift scan text or .CSV files as input and provides an interactive means to calculate the occultation timing and the error bars associated with the observation. It also has advanced features including time corrections for non linear plate scale distortions.

8. Tool Links

John Broughton. Drift scan tools: Scanalyzer & ScanTracker
<http://www.asteroidoccultation.com/observations/DriftScan/Index.htm>

Christian Buil. Iris CCD and DSLR image processing and analysis software
<http://www.astrosurf.com/buil/us/iris/iris.htm>

Cyanogen Systems. Maxim/DL Image Reduction and Analysis Software
<http://www.cyanogen.com/>

Google. Google Earth Download
<http://www.google.com/earth/index.html>

Meade Instrument. Planetarium and Image Processing: AutostarSuite 5.5
<http://meade.com/software-manuals>

NOAO. IRAF- Image Reduction and Analysis Facility
<http://iraf.noao.edu/>
<http://acs.pha.jhu.edu/~shy/x-iraf-windows/>

Steve Preston. Worldwide Occultation Prediction Site
<http://www.asteroidoccultation.com/>

Space Telescope Science Institute. STSCI Data Analysis System - IRAF Extensions
http://www.stsci.edu/institute/software_hardware/stsdas

SSC. Occultation Tools: GPS Geodesy, Asteroid Occultation Maps, Drift Scan Trigger
<http://www.sccorp.com/Observatory>

Thinking Man's Software. Dimension 4 - Network Time Synchronizer
<http://www.thinkman.com/dimension4/>

Do not forget to report your observations. There is strength in your numbers, but only if you share them. For full instructions on reporting your observations see:

<http://www.asteroidoccultation.com/observations/>

9. Conclusion

The odds are that if you are reading this article, you have all the necessary equipment and expertise to observe an occultation. Give it a try. You may not always see the occultation, but that is where the asteroid isn't and that fact is worth reporting. And you may find that measuring an asteroid's cross section is exciting. You and a handful of collaborators can solve the cross section of an asteroid with observations that span a handful of seconds. Shape modelers spend a lot more time for their results!

10. Acknowledgements

The author would like to thank the Mount Wilson Institute for the use of its facilities while developing and testing the tools referenced in this paper.

11. References

Brown, M. E., Rajuillo, C. A. (2004). "Direct Measurements of the Size of the Large Kuiper Belt Object (50000) Quaoar." *Astron. J.* **127**, 2413-2417

Buie, M. W., Millis, R. I., *et al.* (1993). "CCD Camera Occultation System." *Bull. Am. Astron. Soc.* **25**, 1115.

Chen, W. P., *et al.* (2003). "Fast CCD Photometry in the Taiwan American Occultation Survey." *Baltic Astronomy* **12**, 568-573.

Cooray, A. (2003). "Kuiper Belt Object Sizes from Occultation Observations." *Astrophys. J.* **589**, L97-L100.

Dunham, E. W., Baron, R. I., *et al.* (1985). "A High Speed Dual-CCD Imaging Photometer." *PASP* **97**, 1196-1204.

Fors, O, Nunez, J. Richichi, A. (2001). "CCD Drift-scan Imaging Lunar Occultations." *Astron. Astrophys.* **378**, 1100-1106.

Massey, P. (1997). *A User's Guide to CCD Reductions with IRAF*. IRAF Documentation.

Millis, P., Dunham, D. W. (1989). "Precise Measurement of Asteroid Sizes and shapes from Occultations." in *Asteroids II* (Shingley *et al.*, eds.). pp. 148-170. University of Arizona Press. Tucson.

Nuggent, R. (ed.) (2007). *Chasing The Shadow: The IOTA Occultation Observation Guide*. International Occultation Timing Association.

Olkin, C. B., *et al.* (1996). "Astronomy of Single-cord Occultations: Application to the 1993 Triton Event." *PASP* **108**, 202-210.

Papers without Presentation and Posters

A Virtual Astronomical Research Machine in No Time (VARMiNT)

John Beaver
University of Wisconsin – Fox Valley
1478 Midway Rd.
Menasha, WI 54952
john.beaver@uwc.edu

Abstract

We present early results of using virtual machine software to help make astronomical research computing accessible to a wider range of individuals. Our Virtual Astronomical Research Machine in No Time (VARMiNT) is an Ubuntu Linux virtual machine with free, open-source software already installed and configured (and in many cases documented). The purpose of VARMiNT is to provide a ready-to-go astronomical research computing environment that can be freely shared between researchers, or between amateur and professional, teacher and student, etc., and to circumvent the often-difficult task of configuring a suitable computing environment from scratch. Thus we hope that VARMiNT will make it easier for individuals to engage in research computing even if they have no ready access to the facilities of a research institution. We describe our current version of VARMiNT and some of the ways it is being used at the University of Wisconsin – Fox Valley, a two-year teaching campus of the University of Wisconsin System, as a means to enhance student independent study research projects and to facilitate collaborations with researchers at other locations. We also outline some future plans and prospects.

1. Introduction

Astronomical research is very much tied to computing. For a professor or graduate student at a research institution, there is an existing shared computing infrastructure, with networked computers already configured for a variety of research tasks, and a local community of support to assist beginners. But for amateur astronomers or faculty and students at small colleges, the lack of an existing research computing environment can be a serious obstacle to conducting astronomical research.

The actual physical computing power necessary for many research tasks is now easily available; even a low-cost netbook may have enough power for some data reduction and analysis tasks. The difficult part is the initial setup and configuration of the software and necessary dependencies, along with the tutorials and documentation necessary for those beginning in research computing. The lack of a common infrastructure also makes it difficult for people to help each other.

Toward addressing this need, we have developed our Virtual Astronomical Research Machine in No Time (VARMiNT). The purpose of VARMiNT is to provide a ready-to-go research computing environment, mostly for astronomy, that can be freely shared between researchers, or between professional and amateur, teacher and student, etc.

VARMiNT is a fully-configured Ubuntu Linux virtual machine (VM) that can be booted and run

from any computer that has VMware Player installed. VMware Player is proprietary software from VMware (www.vmware.com), but it is available for free (with registration) for MS Windows and Linux. We have attempted to create VARMiNT with an operating system (OS) and installed software that are free and open-source, mostly under the Gnu Public License (Kuhn *et al.*, 2008).

Since individual copies of VARMiNT act as independent computers, they can be customized for particular uses. Thus a particular copy of VARMiNT may be modified for a particular combination of project and user, with appropriate documentation and data installed for that particular project, customized to fit with the experience of the intended user. In this way a given VM can spawn clones that evolve over time according to local needs.

We hope that VARMiNT can be a useful tool for extending astronomical research computing to individuals who currently lack the resources to set up such an environment themselves. We also hope VARMiNT can facilitate (and thus encourage) new collaborations that bring research in astronomy to individuals not affiliated with research institutions. Here we describe some of the properties and possibilities of sharable virtual machines and our VARMiNT in particular.

2. Virtualization Software

VARMiNT is set up as a VMware Virtual Machine. It can be run directly with several VMware products, including the free (with registration) VMware Player, which is available for most MS Windows and Linux host operating systems.

VMware was chosen because their virtual machines are portable and can be self contained within one directory. Thus VARMiNT can be shared simply by copying it to, for example, an external USB hard drive. The copy can then be moved freely back and forth between host computers, even across platforms. Simply shut VARMiNT down on one host, disconnect the drive, reconnect it to another host, and boot it back up.

The other popular choice for virtualization software is VirtualBox (www.virtualbox.org). VirtualBox has the advantage that it is open-source GPL software, and it is available for Mac OSX as well as MS Windows and Linux. VirtualBox virtual machines, however, are not truly portable; they must be created new on each host computer. It is fairly easy however, to create a VirtualBox virtual machine from a VMware VM. One can simply create a new VirtualBox VM, but instead of creating a new virtual disk, simply use the disk from a VMware VM. At present, this is the only way we know to run VARMiNT on a Mac OSX host.

3. VARMiNT 1.0 Operating System and Installed Software

VARMiNT 1.0 is a VMware VM, designed to run directly on VMware Player or VMware Workstation. The OS is Ubuntu 11.04, 32 bit, and it can be run on both 32 and 64-bit host machines. VARMiNT is configured with a single 40-GB capacity virtual disk that is also the boot disk (additional virtual disks can easily be added). The entire VM is contained within one folder and sub-folders. The current size of the virtual disk is about 12 GB.

Since VMware support of graphics acceleration is uneven, the VARMiNT's desktop manager (Gnome Classic) is configured to run without effects. It can be reconfigured to run with effects if your virtualization software can handle 3D graphics acceleration. We have had some success in running VARMiNT with 3D acceleration under VirtualBox and with the most recent version of VMware Player.

Many useful computing tools and software packages are already installed and configured in VARMiNT, including the basic utilities that would be present on any Linux system. The list below gives a

brief description of some of the most important packages.

- The Ubuntu Software Center, which gives easy categorized access to a central repository of free software. This combined with the Synaptic Package Manager allows the user to easily (and safely) install software and manage dependencies.
- The LibreOffice suite (an open-source fork of Open Office)
- A full Latex environment, including the excellent Texmaker source code editor, and the Jabref bibliography manager
- GIMP, an open-source alternative to Photoshop.
- The astronomical image viewers Aladin, DS9 and ImageJ. All three of these include some basic image processing capabilities.
- IRAF, v2.15.1a, 32-bit, with the STSDAS and TABLES external packages. This is the venerable NOAO Interactive Reduction and Analysis Facility for all types of astronomical image processing.
- STScI Pyraf and Pyfits. These allow one to integrate Python programming with IRAF or to access FITS data directly from Python.
- STScI Specview, a free utility for display and simple analysis of spectra.
- GDL, the Gnu Data Language, a free and open-source alternative to IDL.
- CLOUDY, the photoionization modeling code of Gary Ferland
- A Python/Pylab/Matplotlib programming environment, with the Ipython interface. The R programming language is also included as an alternative.
- Scilab and Octave, open-source (and mostly compatible) clones of Matlab; and WxMaxima, an open-source alternative to Mathematica.
- The popular open-source graphics utility Gnuplot, as well as SciDavis, a useful data management facility combined with an object-oriented plotting package.

4. Modes of Use

One reason for using a virtual machine is to use a different operating system from the one that is natively booted on your host computer. For example, one might want to use a Linux virtual machine in order to gain access to Linux programs on a MS Windows computer.

But even if the virtual machine uses the same OS as the host computer, there still may be advantages to the VM approach. In particular, a virtual machine can be kept “lean” as it can be configured around a particular subset of possible uses. The VM need not perform all possible computing tasks, and so it can be kept small (and thus easily backed up), uncluttered, and customized for the project at hand.

Thus one may find it useful to do most of one's work on a choice of a few different customized virtual machines, each booted when needed on a host computer that can also be kept lean and uncluttered. If the host computer has enough resources, both VMWare and VirtualBox allow the user to have multiple VM's booted simultaneously on the same host.

Another possible advantage, with VMWare VM's in particular, is portability. Thus one can, for example, easily move a project, contained within a VM stored on a usb hard drive, back and forth between computers at home and work. This portability also makes it easy to share projects between users.

5. License Issues

We have made every attempt to include only GPL, or GPL-compatible, open-source software in VARMiNT. The Ubuntu OS was configured without the installation of proprietary hardware drivers. This is possible because the virtualization software (e.g., VMWare or Virtual Box) used to boot the VM creates its own virtual hardware drivers. A new user of VARMiNT has the option to install free software (called “Guest Additions” for Virtual Box or “Vmware Tools” for VMWare) to better integrate the guest VM and the host OS. These proprietary (but free) add-ons then allow for such features as copy and paste or click and drag between the guest VM and the host OS.

Information on the licenses for installed software on VARMiNT is contained within a text file, prominently linked by a launcher on the initial desktop. Since these are all GPL, or GPL-like, license agreements, then this should satisfy the license agreements when VARMiNT is copied and shared between users.

For a particular use, one may want to install software that while free, requires the active acceptance of a license agreement in order for it to be in-

stalled (we believe there is no such software on the current version of VARMiNT). In that case, copying and sharing the VM may violate that agreement, as the new user has not actively accepted the license agreement.

But even with this restriction, the VM approach still provides advantages for potential users to share this software (perhaps it is a necessary piece of software for a desired research collaboration), even if it cannot be installed on the VM before sharing. The usual method for “sharing” such software between potential users is to provide a set of detailed instructions explaining step-by-step how to install the software. The problem is that the instructions often fail in practice, because of different hardware and software configurations, different versions of software appearing on a given download server, etc.

In the case of a VM, the installation instructions can be included, and they can be specific to the initial state of that particular VM. And so the instructions can be tested beforehand to be sure they work on that particular shared VM. In fact the entire installation process can be tested, and then the software uninstalled before sharing. Since the active acceptance of a license agreement usually occurs at the installation stage, while there are often no restrictions on downloading the necessary installer files, this can be done ahead of time to be sure the tested version is the actual version installed by the new user.

In principal, the entire installation process could be scripted. And so when a new user of a recently copied and shared VM first boots the machine, a script runs that carries out the installation process from previously downloaded installer files, prompting the new user to accept the license agreements as they appear. A second script could even be included to undo this process and reset the VM to its initial state for further sharing.

6. Examples of Uses of VARMiNT

VARMiNT and its predecessors have been used heavily at the University of Wisconsin – Fox Valley (UWV), a two-year campus of the University of Wisconsin system, with the primary mission of transfer of students to one of the four-year campuses.

UWV has no institutional research computing infrastructure, let alone one specifically geared toward astronomy. Faculty office computers are not suitable for research, in large part because the individual researcher has no control over the installation of software (let alone the OS) on their computer. And so VARMiNT was developed by the author partly to address his own research computing needs, and re-

cent work by the author (Beaver and Conger, 2012; Beaver *et al.*, 2012; Beaver and Robert, 2011) has been carried out almost entirely on VMs similar to VARMiNT.

A project currently under development to perform spectrophotometry of point sources at extremely low cost (Beaver and Conger, 2012) uses VARMiNT heavily, as this allows diverse users to carry out the rather complex data reduction and calibration procedures within a commonly shared computing environment. Since the point of this project is to bring stellar spectrophotometry to those who would otherwise have no access to the technique, VARMiNT is a necessary part of the project.

Here are a few other scenarios that come to mind:

- A researcher establishes collaborations with individuals who lack the institutional resources to set up their own research computing environment, simply by sending USB hard drives containing VMs back and forth through the mail.
- A graduate student, as part of her own dissertation research, creates and maintains a VM environment and then trains a couple of local amateur astronomers to use it in order to help with some of the labor-intensive aspects of her research. The astronomy department thereby strengthens relationships with the amateur astronomers, the amateurs get a unique experience and their names included on published work, and the graduate student gains valuable experience as a teacher and research team leader. Several years later another graduate student does the same, but this time the now-experienced amateurs help train the graduate student.
- An instructor at a small two-year college designs VMs specifically for student independent study projects in astronomy. The computing environment is custom made for the particular project and configured to a point appropriate to the level of the students and the fact that they will only be around for two years at most. The student keeps the machine on a USB hard drive connected to their home computer, but disconnects it and brings it to the instructor's office when needing help. A copy of the machine is later modified by the instructor so it will be appropriate for a different student project.

7. Future Prospects

VARMiNT 1.0 is designed to provide a rather generic environment for astronomical research, in

particular for the reduction of astronomical image data and spectra. We are currently customizing versions of VARMiNT specifically for our ongoing projects in Stromgren CCD Photometry and extremely low-cost point-source spectrophotometry. In particular, we hope to make these VMs more user friendly for amateur astronomers or for beginning students through further work on the documentation and tutorials, and by writing appropriate scripts.

We hope to see VARMiNT and similar VMs foster collaborations that perhaps would not have taken place otherwise due to the stumbling block of sharing computing facilities with individuals not associated with a research institution. One could envision the construction of a central repository of VM's geared toward different types of astronomical computing, in order to facilitate such access.

Much further work would be needed in order to realize the widespread adoption of VMs for research collaborations, particularly to ensure compatibility with existing institutional research programs while still maintaining free and open-source VMs that can be shared without running afoul of license agreements. As an example, many institutions rely heavily on the proprietary IDL. VARMiNT 1.0 is equipped with GDL, an open-source alternative that, although incomplete, is mostly compatible with IDL. This incompleteness means much work would need to be done in order to get the GDL environment on VARMiNT ready for a particular project of active research, as many common publicly-available procedures would likely need to be modified somewhat.

8. Conclusions

Virtual Machines provide an elegant solution to the problem of bringing astronomical research to a greater diversity of individuals. Our VARMiNT can provide a ready starting point for those who wish to set up an astronomical research computing environment that is customized for a particular combination of project and user. For inquiries about how to obtain a copy of VARMiNT, or for suggestions for future versions or desires to collaborate, please contact the author.

9. Acknowledgements

Dale Thibideau, Network Administrator at the University of Wisconsin Fox Valley, first introduced me to virtualization software, and his continuing help and insight have been invaluable. Chuck Conger, (UW Fox Valley) and Dan Phiel (UW Oshkosh) have both tested early versions of VARMiNT and offered helpful suggestions.

This work was supported in part by the following grants:

- UW Fox Valley Foundation Grant (2010)
- UW Fox Valley Professional Development Grants (2010, 2012)
- UW Colleges Department of Computer Science, Engineering and Physics Professional Development Grants (2010, 2012)
- NSF ROA Supplement, AST 1135760 (2011)

VMware, VMware Player and VMware Workstation are registered trademarks of VMware, Inc.

10. References

Beaver, J. E., Conger, C. (2012). "Extremely Low Cost Point-Source Spectrophotometry (ELCPSS)." in *Proceedings for the 31st Annual Symposium on Telescope Science* (Warner *et al.*, eds.). pp. 113-120. Society for Astronomical Sciences, Rancho Cucamonga, CA.

Beaver, J. E., Piehl, D., Kaltcheva, N., Briley, M. (202). "Strömgren-H photometry of the galactic cluster M 11." In preparation.

Beaver, J. E., Robert, D. M. (2011) "A CCD Spectrograph for One Dollar." in *Earth and Space Science: Making Connections in Education and Public Outreach*. ASP Conference Series **433**, 425.

Kuhn, B. M., Williamson, A, Sandler, K. M. (2008). "A Practical Guide to GPL Compliance." Software Freedom Law Center.
www.softwarefreedom.org (retrieved 12 April 2012).

The Confusing Case of 16666 Liroma

*Robert K. Buchheim
Altimira Observatory (G76)
Coto de Caza, CA 92679 USA
Bob@RKBuchheim.org*

*John Ruthroff
H60
Carmel, IN USA
John@theastroimager.com*

Abstract

In late 2011, asteroid 16666 Liroma made a very favorable apparition with unusually bright magnitude and passing through near-zero solar phase angle. This opportunity prompted a project to determine the rotation period, lightcurve shape, and phase curve parameters (H , G) of this asteroid. The rotation period $P = 112 \pm 5$ h that we find, with amplitude $\Delta m \approx 0.45 \pm 0.05$ mag (peak-to-peak) seems to be well-justified. The lightcurve gives a fair fit to almost all of the data gathered on 21 nights over an period of 2 months. However, three nights at the largest phase angle (at the end of the observed apparition) fall significantly “off” the lightcurve. An attempt to fit the lightcurve to a two-period model gives a somewhat better fit, but still leaves substantial deviations from a model lightcurve, thus presenting an unresolved mystery.

1. Introduction

The 2011-2012 apparition of 16666 Liroma presented an unusually favorable set of circumstances: a close approach to Earth (making the asteroid bright enough for photometric study with small telescopes), and a presentation at nearly zero solar phase angle (offering the prospect of monitoring the asteroid’s opposition surge, and determining its phase curve). The authors independently began observations of this object and then collaborated by merging our data sets and jointly analyzing (and struggling over) the results.

2. Data, Reduction, and Analysis

Differential photometry was collected on different nights at our two observatories, using similar equipment (both telescopes were 0.3m Schmidt-Cassegrain telescopes operating at $f/6$, with CCD imagers). RKB used multiple filters (typically either V-R or R-C, depending on the night), while JR used only V-band. Images were reduced in the standard way with flat, dark, and bias frames, and “censored” to eliminate any images that were adversely impacted by cosmic rays, aircraft lights, bad tracking, etc. Differential photometry was done with MPO Canopus.

Because it turned out that we had a hard time finding a period with a plausible lightcurve, one of us (RKB) undertook to “calibrate” the magnitudes of all comparison stars from all nights onto a local R-band

system; the idea being that this would facilitate “bridging” the asteroid magnitude across widely-separated fields of view. All comp stars were selected to have similar color indices of about $[V-R] \approx 0.45 \pm 0.1$, using the MPO Comp Star Selector; so there is little color difference between the comp stars and the asteroid. It seemed simplest to leave the comp-star data on the local “Altimira observatory R-band” photometric system to avoid any errors or offsets introduced by transformation to the standard system. We note that this is quite close to the standard system (the color terms in Altimira Observatory transforms are small).

Three clear and stable nights were devoted to calibrating the comparison stars, by imaging one or two Landolt fields and the comp-stars. The Landolt fields were imaged both near culmination and lower in the west to determine the atmospheric extinction in V-, R- and C-bands. The observed instrumental magnitude of each comp star was extrapolated to its exo-atmospheric value by:

$$\begin{aligned} R_0 &= R - k_R \cdot X \\ C_0 &= C - k_C \cdot X \end{aligned}$$

where R and C are the observed instrumental magnitudes [i.e. $2.5 \log(\text{ADU}/t)$], X is the air mass of the observation, and k_R , k_C , are the atmospheric extinction parameters (in mag/air-mass).

The values of R_0 , C_0 are, of course, sort of inconvenient (of order -6 to -10). In order to translate them to more “conventional” values, one comp star

was selected as the “anchor star”, and all other comp stars from all nights were assigned magnitudes anchored to this star, as:

$$R_{\text{comp}} = R_{\text{anchor}} - [R_{0,\text{anchor}} - R_{0,\text{comp}}]$$

and a similar equation for C band.

The zero-point of the C-band magnitudes was selected so that $C \approx R$ for solar-color stars (not surprising, since there is not much color term between C and standard-R in the Altimira Observatory system).

JR’s data was taken only in V-band. His fields and comp stars were imaged in Altimira V- and R-bands on one of the “calibration nights”. This provided the comp star magnitudes on the “Altimira R” system; and since the asteroid and the comps are nearly solar-color, it is reasonable to assume that $\Delta\text{mag} = V_{\text{ast}} - V_{\text{comp}}$ can be treated as being equal to $\Delta\text{mag} = R_{\text{ast}} - R_{\text{comp}}$. (A few nights with both V and R-band data were examined, to confirm that there is no evidence of the asteroid changing color as it rotates).

With this approach, all of the asteroid sessions were put onto a single, consistent “local” photometric “R-band” system.

3. A Differential-Photometry Lightcurve

With all comp stars on the “Altimira R” system, the asteroid differential magnitudes were placed on a consistent baseline

The resulting “raw” lightcurve for 2011 late November and early December is shown in Figure 1.

This shows a sequence of alternating “upward” and “downward” slopes that suggests a period of about 4 days.

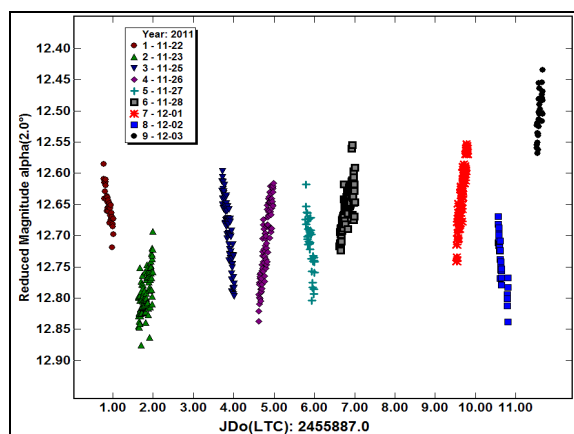


Figure 1: “Raw” lightcurve of 16666 Liroma (in terms of “reduced magnitude” (using $G = 0.15$), for UT 2011 Nov 22 through 2011 Dec 03

The solar phase angle was minimum ($\alpha \approx 0.97$ deg) on 2011 Nov 25 (JD ≈ 2455890.5). Over the

interval of time plotted in Figure 1, the solar phase angle changed from $\alpha \approx -2$ deg through zero, to $\alpha \approx +6$ deg. Figure 1 is plotted as reduced-magnitude, using an assumed $G = 0.15$.

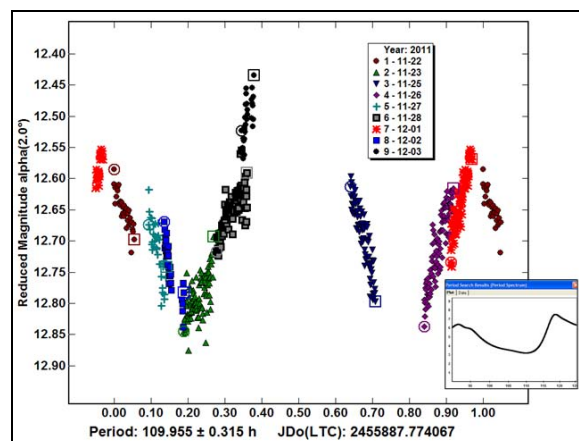


Figure 2: “First estimate” of phased lightcurve of 16666 Liroma, based on 9 nights near opposition. The inset shows the results of the MPO Canopus period-search algorithm.

The MPO Canopus period-search routine was used on these 9 sessions, and found a plausible fit at $P \approx 110$ h, as shown in Figure 2. Phasing the observations to this period results in a double-peaked lightcurve, although this set of nights did not capture the maximum brightness of the lightcurve.

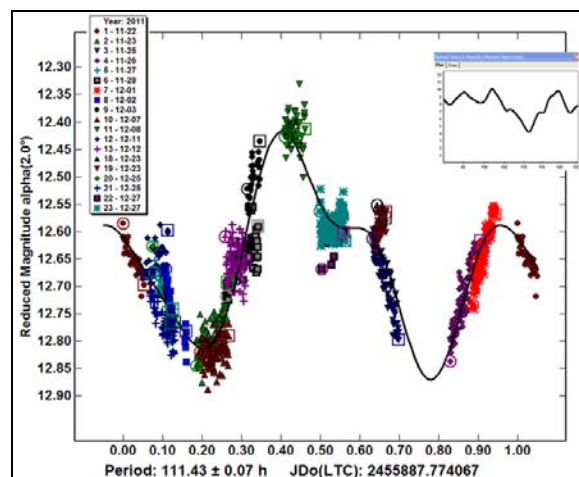


Figure 3: Phased lightcurve of 16666 Liroma, using differential photometry from 16 nights over 1 month, showing best-fit lightcurve period $P = 111.43$. Solar phase angles range from $\alpha = -1.96$ to $\alpha = +21$ degrees. Inset shows the results of the MPO Canopus period-search algorithm.

Adding data gathered from 7 additional nights over the following three weeks resulted in only a slight change in the estimated period, and the lightcurve shape can be reasonably fit by a 4th order Four-

rier curve, as shown in Figure 3. Some of the photometric data is noisier than we would normally like, because the asteroid was getting pretty faint as its distance from Earth increased.

This lightcurve has no arbitrary “delta-comps”, is a plausible double-peak shape, and gives a reasonably good fit to the data (RMS = 4.2, in units of 0.01 mag). The only poorly-justified parameter hidden within it is that it uses the “default” phase-curve parameter of $G = 0.15$ to compensate for the changing solar phase angle.

We also tried several numerical experiments by applying more-or-less arbitrary “delta-comp” adjustments (up to 0.3 mag) to groups of nightly data. The net result of these experiments was that the best-fit lightcurve periods ranged from 109 to 115 h, so we conclude that the best-estimate lightcurve period is $P = 112 \pm 5$ h.

4. Phase Curve Determination

The lightcurve shape in Figure 3 (described by a 4th-order Fourier curve) was used with the data of asteroid R-brightness vs. time to determine the asteroid’s phase curve. The method invented by Harris (1989) and applied by Buchheim (2010) was used. In this method, each night’s data (asteroid magnitude vs. time) is lined up with the appropriate portion of the lightcurve shape, and the implied rotational brightness maximum for that rotational cycle is found by extrapolating along the lightcurve shape. An example of this procedure is illustrated in Figure 4.

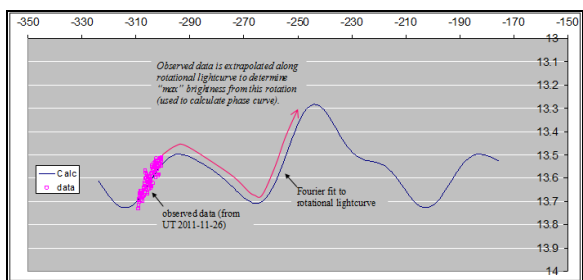


Figure 4: Example of the implementation of the procedure from Harris, et al (1989) to extrapolate “observed” data to determine the “max” brightness of the rotational phase curve on the indicated rotation. The solar phase curve is formed by plotting R_{max} vs. α

The values of R_{max} found in this way are then plotted against the solar phase angle at the time of observation, to create the phase curve. The result is shown in Figure 5.

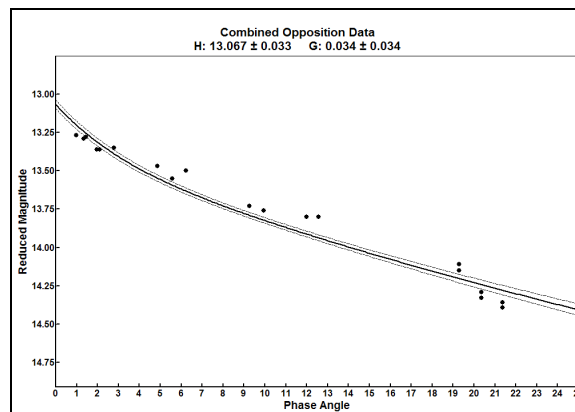


Figure 5: Phase curve (R_{max} vs. α) derived for 16666 Liroma.

Taken at face value, this gives an unusually low “slope parameter” $G = 0.03 \pm 0.03$.

The Harris *et al.* (1989) method to determine G becomes iterative at this stage – the lightcurve shape is re-determined based on the “found” value of G , and then the extrapolated “maximum” brightness for each observation night is re-calculated. The iteration continues until mutually-consistent lightcurve and phase curve are achieved. As Harris *et al.* (1989) point out, this process normally converges within just one or two iterations.

As it turned out for this project, re-plotting the lightcurve using this value of $G = 0.03$ did not make a significant change in the derived period or the shape of the lightcurve, but it did result in a very slightly poorer RMS “fit” to the data.

5. Discordant Results Late in the Apparition

Additional data was gathered in the hope of filling in the gaps in the rotational lightcurve, and extending the coverage of the phase curve to larger solar phase angles. Alas, rather than helping, this additional data is a source of confusion. Altimira Observatory gathered R- and C-band data on UT 2011 Dec 28, 2012 Jan 18, and 2012 Jan 19 (at solar phase angles of $\alpha \approx 22$ to 30 degrees).

When this data is plotted on the previously-found lightcurve with $P = 111.43$ h, it falls badly off the curve, and at least in the case of 2012 Jan 18 and 2012 Jan 19 no arbitrary “delta-comp” would bring the data into alignment with the lightcurve. Worse, a period search that includes this data results in a complete garble, with no plausible lightcurve found at any period between 40 hr to 250 h.

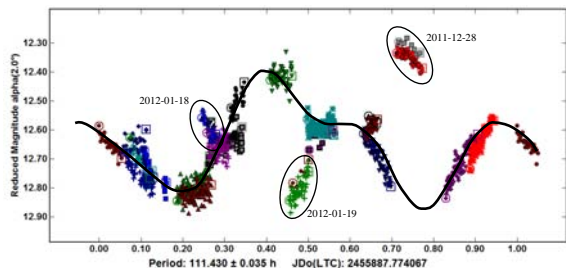


Figure 6: Lightcurve data, showing the nights – late in the apparition, at phase angles $\alpha \approx 22$ to 30 degrees – that “don’t fit” the lightcurve formed by the other nights

What is going on with these nights?

One might suspect that there is a problem with the comp-star magnitudes (i.e. adjusting the delta-comp might bring these nights “into line”). There are a couple of factors that argue against this suspicion. First, nights 2012 Jan 18 and 2012 Jan 19 used the same comp stars: adjusting them up or down together is not going to improve the overall situation. In addition, the calibration of the comp stars for all three nights was done in a single observing session, with the comp star fields for 2012 Jan 18/19 and 2011 Dec 28 imaged only about 30 minutes apart. There were no apparent changes in atmospheric conditions during this time interval, and the images of Landolt standard field SA-95 taken both before and after the images of the comp-star fields showed no anomalies. Other comp stars that were imaged and calibrated on that same night, within an hour of the images of these “problem” fields, show no discrepancies. Finally, the comp stars for 2012 Jan 18 and 19 were re-imaged on the next night, and these images gave essentially identical exo-atmospheric instrumental magnitudes.

		cal'd on 2012-01-26				
FOV night		C1	C2	C3	C4	C5
2012-01-18		-7.625032	-6.586032	-7.195032	-6.923032	

		cal'd on 2012-01-27				
FOV night		C1	C2	C3	C4	C5
2012-01-18		-7.588731	-6.544731	-7.203731	-6.886231	
	delta	0.036301	0.041301	-0.008699	0.036801	

Considering that these two independent calibrations yielded the same comp-star magnitudes (± 0.02 mag), it is hard to argue that they are discrepant. By extension, the calibration of the comp stars for other nights (done in the same way, with the same instrument) is given some additional credibility.

It is possible that the shape of the lightcurve changes at large solar phase angles ($\alpha \approx 22$ deg to $\alpha \approx 30$ deg). Shadowing effects can certainly cause significant changes in the shape of a lightcurve from opposition to large solar phase angle. We attempted to test this notion by examining alternate lightcurve

shapes, or slightly different periods, using only the half-dozen nights at the end of the apparition (i.e. large solar phase angles). This did not provide any useful clues.

Could the asteroid have undergone some sort of cometary activity? There is no evidence of any coma or emission on the images. The asteroid appears as a normal star-like point spread function. Plus, although it is easy to imagine how a comet-like activity might make the asteroid appear brighter than expected (e.g. 2011 Dec 28), it is more difficult to imagine that dust or gas emission could make it appear fainter than expected (e.g. 2012 Jan 19).

6. Tumbling?

Liriope’s relatively long primary period (assuming $P \approx 112$ h to be at least approximately correct) makes it a good candidate to be a non-principal axis rotator (i.e. a “tumbler”).

We are not qualified to assess whether these anomalous data points might be related to complex (rotation + precession) motion of the asteroid. However, as a first step to investigate this possibility, a “two-period search” was conducted with the utility in MPO Canopus. The results were not spectacularly successful, but were intriguing. The best combination of primary and secondary periods was:

$$P_1 = 107.44 \text{ h (‘‘rotation’’ period?)}$$

$$P_2 = 198.80 \text{ h (‘‘precession’’ period?)}$$

Figure 7 shows the brightness vs. time $[H(0,1,1)]$ predicted by this two-period model. In the top panel the two-period brightness model is compared to the simpler single-period ($P_1 = 107.44$ h) model. This illustrates the complexity of the resulting brightness vs. time profile that is caused by introducing the second period, compared with a single-period model. The bottom panel of Figure 7 compares the observed asteroid brightness with the prediction of the two-period model. (“Observed” data points are the measured magnitude adjusted to zero-solar-phase angle, assuming a slope parameter of $G = 0.03$). The early portion of this shows that the two-period model is a nice fit to the data – a noticeably better fit than is achieved using just the “ P_1 ” curve. Late in the curve, the distinction between the single-period and the two-period predictions is not as clear, but again the two-period model seems to fit the data nicely. The complexity of the two-period brightness curve might explain why it was so difficult to find a “single-period” model that could fit all of the data, even near opposition.

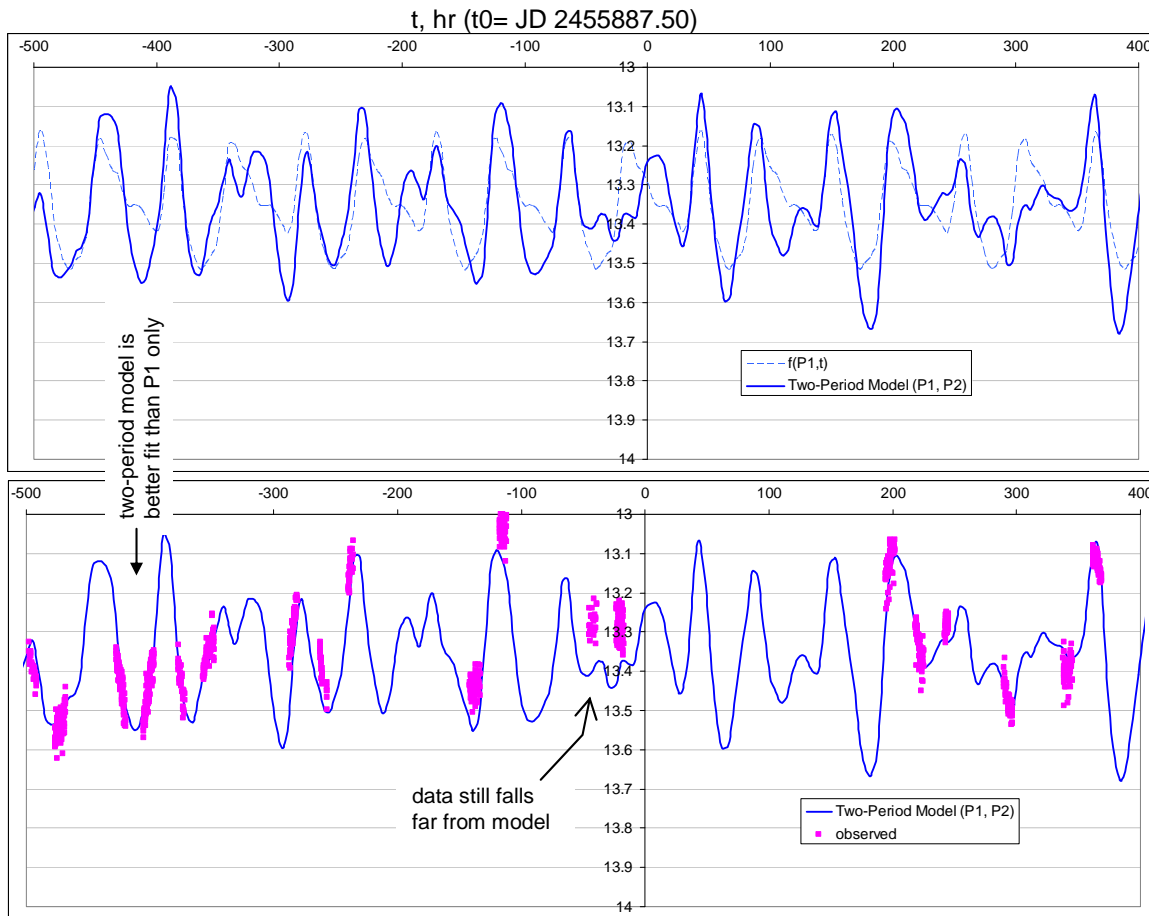


Figure 7: A “two-period” lightcurve model offers an intriguing (but not completely successful) explanation of the complex brightness changes of 16666 Liroma

Unfortunately, around $t = 0$ (UT 2011 Dec 08), the observed points lie significantly above the predicted curve. Worse, very late in the apparition (not shown in Figure 6), the final two nights of data (UT 2012 Jan 18 and 19) are substantially fainter than the prediction of a $G = 0.03$ phase curve. So, the “two-period” model doesn’t completely resolve the confusing case of this asteroid’s lightcurve.

Phase Curves.” in *Proceedings for the 29th Annual Symposium on Telescope Science* (Warner et al., eds.) p. 101. Society for Astronomical Sciences, Rancho Cucamonga, CA.

Harris, A.W., et al. (1989). “Phase Relations of High Albedo Asteroids. The unusual opposition brightening of 44 Nysa and 64 Angelina.” *Icarus* **81**, 365.

7. Availability of Data

All of the differential photometry data from this project has been uploaded to the ALCDEF database, so it can be examined and used by anyone who is interested in re-analyzing it, or combining it with other data sets.

8. References

Buchheim, R. K. (2010). “Methods and Lessons Learned Determining the H-G Parameters of Asteroid

Student Project and Curriculum Based on Light at Night Data Collection

Erin M. Craine
STEM Laboratory, Inc.
4681 N. Cerritos Dr. Tucson, AZ 85745
ecraine@dakotacom.net

Jennifer C. DeBenedetti
Catalina Foothills School District
9566 N. Marsh Wren Pl. Tucson, AZ 85742
jennifercraine@yahoo.com

Abstract

There is a growing movement in the educational field to promote science, technology, engineering and math studies, stemming from a concern about waning understanding and interest among K-12 students in these topics. STEM Laboratory, Inc. (STEM) has developed a Sky Brightness Meter (SBM) that can be used with ease yet produces complex information relating to light at night monitoring. STEM sees the SBM and its corresponding data archive as a means to involve students in projects that relate to scientific method exploration, makes science more accessible, and encourages a life long appreciation and understanding of scientific endeavors. In this paper we present an example of a project template that could be used by students studying effects of artificial light on sky brightness. STEM has developed several outreach lessons aligned with the National Common Core Curriculum, Systems Thinking concepts and local standards to be implemented in classrooms or independent youth organizations.

1. Introduction

This paper is intended to serve as a general guide for students contemplating conducting and writing their own report using light at night data collected with the STEM Sky Brightness Meter or from the STEM Sky Brightness Data Archive (SBDA), c.f. Craine *et al.* (2011). It provides a basic overview of the methodology and procedures for collecting and reducing data, and gives an example of the sort of information and product students could potentially develop.

Additionally, this paper provides some sample classroom applications, relating to light and light at night, that teachers could apply and adapt to their grade level. It is by no means a complete representation of all potential projects, but it does give an idea of the types of lessons possible at a variety of grade and age levels.

2. Methodology

The first step in this type of research project is to determine the site to be monitored. Such a selected site should be of some scientific interest, for example, due to environmental and ecological reasons or new development going in. The site can be a small sampling to be monitored multiple times, can be a

comparison of multiple sites, or may be a large area monitored once to identify lighting fluctuations within that zone. It is up to the student to decide what sort of site and monitoring schedule best suits their own research goals.

Alternatively, the student may choose to mine the STEM Sky Brightness Database Archive (SBDA) to utilize and analyze already collected light at night data. This provides a good option if the student does not have the means to collect their own original data.

Once a site has been selected for monitoring, a detailed route should be established prior to the commencement of data collection. This ensures consistency if the site is to be measured multiple times, minimizes confusion during the actual collection, and maximizes the use at the other end by guaranteeing a logical and thorough data set. Table I is an example of part of a pre-planned, written route that we followed when collecting data around Salpointe High School in Tucson, Arizona. For additional ease, a Google map with the exact route highlighted may be used.

The Sky Brightness Meter (SBM) is designed to be mounted at either a fixed location or on a moving vehicle, depending on the specific goals of the project. In this example, to collect data we mounted the SBM on the roof of an automobile using a plethora of

electrician’s tape. The photocell unit should be pointed at the zenith to give sky brightness overhead.

1	E. on Blackledge to Campbell
2	S. on Campbell to Grant
3	W. on Grant to Park
4	N. on Park to Adelaide
5	E. on Adelaide to Campbell
6	S. on Campbell to Spring
7	W. on Spring to Fremont
8	N. on Fremont to Mitchell
9	W. on Mitchell to Via Encantadora
10	N. on Via Encantadora to Glenn
11	E. on Glenn to Martin
12	S. on Martin to Spring
13	W. on Spring to Highland
14	N. on Highland to Copper
15	W. on Copper to Mountain

Table I. A portion of the Salpointe High School planned route.

To commence collection it is simply a matter of powering on the unit and confirming that satellite locks have been achieved to trigger GPS signals to the unit. Data acquisition and logging are completely automatic, and it is only necessary to position the unit on the vehicle. Ideally, data should be collected after local astronomical twilight and should be completed before moonrise. For consistency, it is desirable to collect data on clear, cloudless nights. At the end of the data collection session the data must be downloaded as a comma delimited text file for import into MS Excel for data manipulation.

3. Data

The original document produced from the data collection session is a comma delimited text file (.csv) of the raw data information. This file should be saved in its original state; any subsequent data manipulations should be done in a new Excel (.xls or .xlsx) file. The information downloaded from the SBM in which we are primarily interested includes the date, time, longitude, latitude, and magnitude per square arc second for each data point.

In order to extrapolate more useful information from the raw data it is necessary to conduct some data manipulation. In the new Excel working document added information includes the longitude and

latitude in decimal form, and elapsed time for the entire data collection session.

From this additional data we can now create a variety of graphs that serve as useful visual representations for analysis of that night’s data collection session. Plotting the decimal longitude and latitude of each data point gives us a visual image of our exact route for each session (see Figure 1).

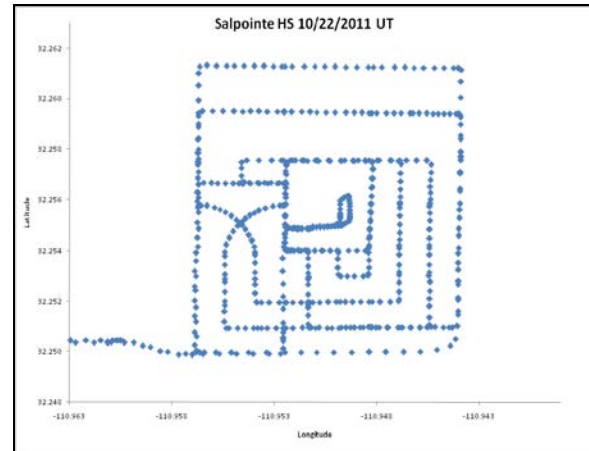


Figure 1. Ground track of the Salpointe High School route

With this graph we have multiple options for data comparisons and interpretations. For example, we could overlay this route with another of the same location on a different night to compare exactly where on the route data were collected. We could isolate certain areas of interest, and look at data from that specific leg of the route.

4. Comparison and Analysis

There is a wide range of possibilities for papers and topics derived from data collected with the sky brightness meter. Monitoring can be done to look at sky brightness for seasonal cycles or as a function of weather and air pollution. Observations can be made over a lengthy period of time, to monitor long term changes in light output as a function of population or area growth or to determine efficacy of lighting ordinances. Key sites, due to their ecological importance, can be observed to analyze lighting effects on environment and animal behavior. These are just a few examples of potential studies and papers that can be pursued by students.

Here we present one example using data collected around Salpointe High School in Tucson, AZ. We compare the sky brightness levels of the area collected over a period of two, non-sequential nights; one night with the football stadium lights on and the other night with those lights off. We export the data

extracted from the Excel file into the downloaded EarthPlot program. In this program, we set our parameters for creating an isophotal map of the area. We select “contour” as the plot type, change the opacity to approximately 45 percent, and select the number of contour levels to be plotted. We then export this .kml file to be mapped on Google Earth.

Looking at the different isophotal maps for each night (Figures 2 and 3), we can visualize the brightness levels depending on location and environmental factors.

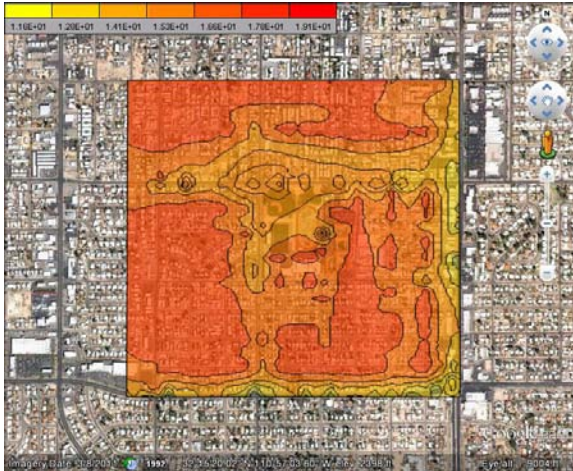


Figure 2. A 7-Level isophotal map showing Salpointe High School with stadium lights off

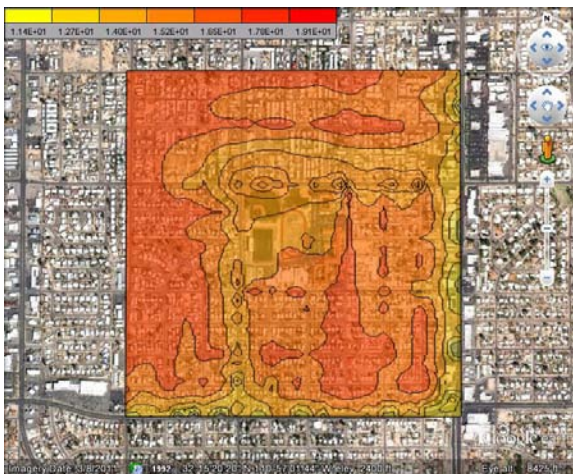


Figure 3. A 7-Level isophotal map showing Salpointe High School with stadium lights on

In this instance, we can easily see the brightness levels recorded on the night with the ball field lights on are much higher than the night with the lights off. This may perhaps be an obvious and expected occurrence but it does provide useful concrete data to support the assumption. Because there is a calibration scale of brightness, it is possible to calculate the

magnitude of the change. In addition, we can see changes in local traffic patterns indicative of increased activity near the stadium and reduced traffic in some side streets.

5. Tools and Equipment

In order to collect light at night data, analyze the findings and make a report, we used the following materials:

- STEM Lab Sky Brightness Meter (SBM)
- Vehicle for mobile collection
- Computer
- Microsoft Excel software
- Earth Plot software
- GoogleEarth software

6. In The Classroom

The previous segment of this paper described an example project that could be pursued by an older student on an independent study basis. The remainder of the paper proposes similar projects based on the SBDA and other materials put together by STEM, to be undertaken by a range of grade levels under the guidance of the teacher or by extracurricular instructors.

6.1 Education Standards

The goals in the K-12 curriculum are rooted in the Scientific Inquiry Process and the history of science as a human endeavor. While there are a variety of content specific goals for each grade level, varying from state to state, these two concepts are the underlying directive.

6.1.1. Concept I

The Scientific Inquiry Process includes the following performance objectives:

- Observations, questioning, and hypothesizing
- Investigating and modeling
- Analysis and conclusion
- Communication

6.1.2. Concept II

History of Science as a Human Endeavor focuses on change over time, advancements individuals have made in science and mathematics, and ultimately the technology and engineering their discoveries enable.

6.2 Educational Applications

Projects and lessons at the elementary grade school level will be less broad in scope, and focus more on specific and directed tasks and skill sets. Teachers will be provided with targeted sky brightness data in an Excel spreadsheet, containing information on date, time, and brightness levels. Students will be asked to create a bar graph in the excel program, charting brightness levels according to data and/or time.

If the computer technology or time for instruction is not available, students may create the bar graph on standard graph paper or poster sized paper to deliver as a possible presentation. Students should be able to make observations and compare the data and bar graphs (using their previously learned understanding of light behavior) to make inferences or draw conclusions about why the same area would have such differences in night sky brightness.

These observations should be recorded in a data table and the conclusions written in paragraph form, under a self-generated topic sentence to be supported by students' individual observations and bar graph.

At the middle school level instructors will be provided with data files for date, time, latitude, longitude, and sky brightness levels. Instructors will need to download Google Earth and Earth Plot for students to create a sky brightness isophotal map. Students will use this to calculate the areas with the most and least saturation. Students will then create a scatter plot using a random sampling of data points from these two areas. This can be created with an Excel program, standard graph paper, or poster sized paper, for a possible presentation.

Because this is a blend of teacher provided information and student analysis, this lesson would serve as a beginning of the year project to commence understanding of the inquiry process while linking to some of the Earth, Solar System and Energy performance objectives.

At the high school level students or student groups may isolate a variable to analyze sky brightness as a function of that variable. Students may collect their own data using the SBM (as described earlier in this paper), compare different data sets from the SBDA, or use a combination of the two. Students may question and hypothesize: sky brightness as a

function of weather, air pollution, seasonal cycles, building/development codes, or protected lands. Students will independently gather data, model the data in appropriate graph form for analysis, and draw conclusions based on their observations of the data. Students will then present their findings in the form of a written report, and an oral classroom presentation.

Any grade level may examine a timeline of significant individuals advancing math, science and technology. Students will observe we are approaching a new frontier in scientific endeavor in this field, in which they can actively participate. They may be the next Galileo or Newton in an upcoming age of research and discovery; students may create a resume of their scientific exploits and add their own biography to the timeline at the end of they year.

7. Conclusion

The Sky Brightness Meter and Sky Brightness Data Archive are innovative technologies and tools which encourage student participation and interest in the field of science. The STEM Educational Outreach Program recognizes the importance of engaging learners of all ages and abilities. The SBDA brings real scientific data directly to students, sparking an enthusiasm at an early age. The SBM allows students of higher levels to target and direct their own projects and collect data accordingly.

The Methodology, Data and Comparison and Analysis sections of this paper serve as an introductory guide to potential student-driven scientific inquiry projects. The In the Classroom section provides classroom ready SBM and SBDA based projects linked to science standards. These suggested projects represent a portion of the opportunities STEM provides for students and educators.

8. References

Arizona Department of Education

<http://www.azed.gov/standards-practices/common-standards/>

Common Core Curriculum Standards

<http://www.corestandards.org/the-standards>

Craine, Eric R., Craine, Erin M., Craine, Brian L. (2011). "The Sky Brightness Data Archive (SBDA)" in *Proceedings for the 30th Annual Symposium on Telescope Science* (Warner et al., eds.). pp 45-52. Society for Astronomical Sciences, Rancho Cucamonga, CA.

Enhancing the Educational Astronomical Experience of Non-Science Majors with the use of an iPad and Telescope

*Robert M. Gill, Michael J. Burin
California State University, San Marcos, Physics Department
rgill@csusm.edu, mburin@csusm.edu*

Abstract

General Education (GE) classes are designed to broaden the understanding of all college and university students in areas outside their major interest. However, most GE classes are lecture type and do not facilitate hands on experimental or observational activities related to the specific subject matter. Utilizing several astronomy application programs (apps), currently available for the iPad and iPhone, in conjunction with a small inexpensive telescope allows students unique hands on experiences to explore and observe astronomical objects and concepts independently outside of class. These activities enhance the students overall GE experience in a unique way not possible prior to the development of this technology.

1. Introduction

Small telescopes have become reasonably priced and readily available. The iPad has gained popularity through the thousands of applications (apps) that have been written for almost any subject imaginable. We have taken advantage of an inexpensive telescope, the Celestron “Firstscope” (Figure 1) and several of the astronomy related apps available for the iPad (Figure 2) to enhance college and university students General Education (GE) experiences allowing them the unique opportunity to observe astronomical objects independently outside of the classroom with little or no background knowledge of the operation of a telescope or the location of objects in the sky.

Ten iPads and telescopes were purchased by the Physics Department and are available for the students to check out from Instructional Technology (IT) and the library Reference Desk. Specific astronomy apps have been loaded onto the iPads for our activities. Since the iPads also allow access to the students email and internet, IT personnel clean and reinstall all apps on the iPad prior to each checkout to ensure the integrity and security of the devices. The students can check them out for three day periods.

2. The Activities

With the availability of iPads and inexpensive telescopes it has become possible to develop self-guided activities. They can be used with the telescope alone, with the iPad alone or with the telescope and iPad together (the preferred situation) depending on the availability of the equipment at checkout.

It is assumed that the students have never used a telescope or iPad previously. The activities begin with a familiarization of the equipment. This is quite detailed and takes them through the activity step by step. Safety is always a concern; the students are reminded never to look at the Sun.

The telescope is set up in the daylight using a terrestrial object like a distant tree, building, lamp post, etc. This allows the student to become familiar with locating objects, changing eyepieces and focusing.



Figure 1. Celestron “Firstscope” telescope.



Figure 2. The iPhone and iPad.

The students also familiarize themselves with the iPad prior to using it with the telescope. “Playing” with the apps is encouraged.

The first activity is to observe the moon. The telescope is set up and aimed at the moon. The iPad app “Moon Globe” is opened and a detailed map of the moon is available (Figure 3). The students can move around the iPad screen and zoom in on the region of the moon that they are looking at in the telescope.

The students must locate several objects, e.g., mare, craters, etc. and record their observations. They may make sketches or take a photo through the telescope eyepiece if they wish. Photography is explained in the familiarization.

The next activity uses a planetarium program, “GoSkyWatch” (Figure 4) that displays the night sky. However, the iPad utilizes the GPS and accelerometer orientation system to give you a correct view of what you are looking at when you point the iPad in a particular direction in the sky. The app is powerful in that it includes many databases of information and can be used for reference and determining what you are looking at or looking for.

This is the most useful of the apps since one need only point the iPad at a location in the sky and that portion of the sky is displayed on the screen. Stars, constellations and other objects are also identified and labeled on the screen.

The image on the screen can be “zoomed” in or out to assist in the identification of objects (Figure 5). The iPad may also be used during the daytime. The suns location and zodiacal constellation can be obtained being careful to block the sun with the iPad. Other activities with this app include the identification of bright stars, finding your zodiacal constellation, finding and identifying planets and the identifi-

cation and location of reference lines like the celestial equator, ecliptic and meridian.

Access to any of the apps databases yields additional information on other astronomical objects (Figure 6). This concludes our “GoSkyWatch” app activity. The activities allow additional explorations for the student to discover other interesting aspects of the night sky on their own. These explorations should of course, be recorded and included in their reports.

The remaining activities are associated with what we call “specialty” apps. Most include reference material which we felt could augment the hands on experience. The students must at least open each of these apps and answer a few questions about them.

The “Messier List” app (Figure 7) contains a complete list of the Messier “M” objects and can be used in conjunction with the “GoSkyWatch” app.

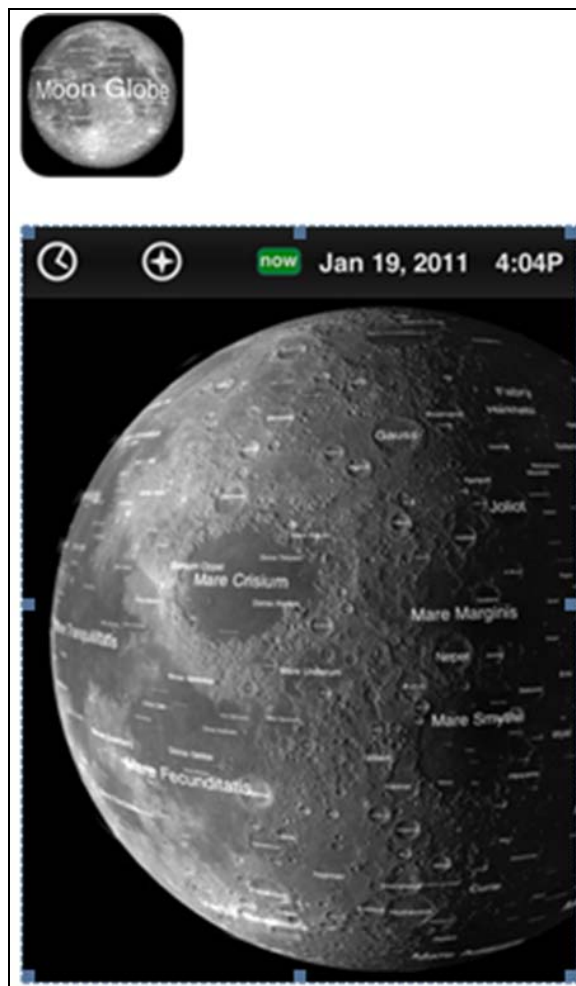


Figure 3. “Moon Globe” app and moon map.

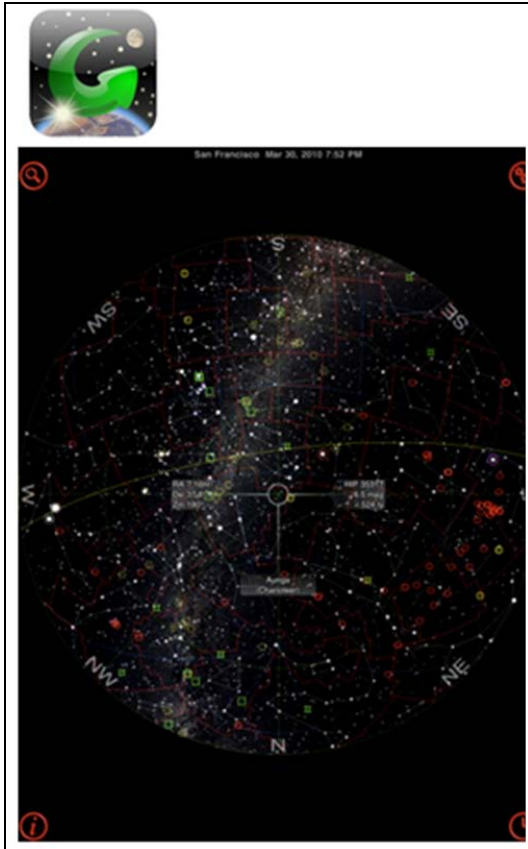


Figure 4. “GoSky Watch” app and sky map.

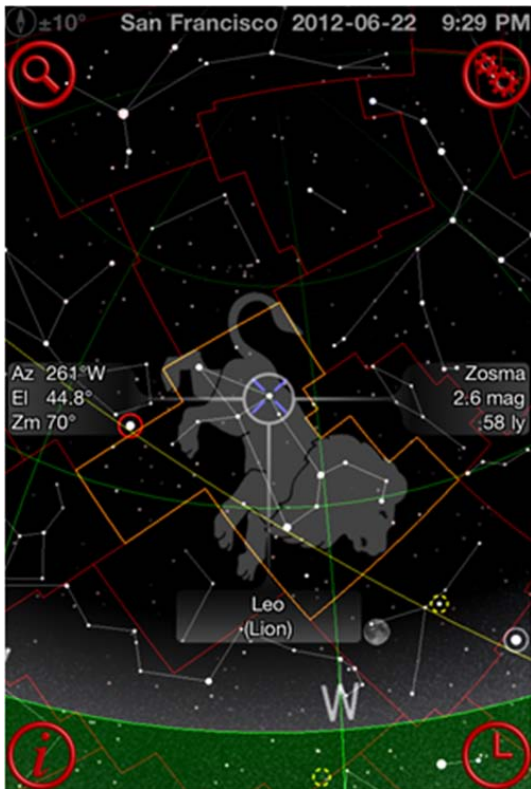


Figure 5. Zoomed-in screen.



Figure 6. Moon data.



Figure 7. “Messier List”.



Figure 8. “M” object photo and description.

The app includes technical information about each “M” object and includes a photograph of the

object. This is very helpful in observing the object with the telescope (Figure 8).

Are the planets visible? If Jupiter is in the night sky, what moons are visible? It is convenient to know “what’s up” in the sky on the night of your observations. An excellent reference source for that information is the “SkyWeek” app (Figure 9), presented by Sky & Telescope. It presents a detailed look at today’s happenings which might include star maps and photo images (Figure 10).



Figure 9. “Sky Week” app.



Figure 10. “Sky Week” maps and photos.

“3D Sun” is a very useful app (Figure 11). It digitally reconstructs images downloaded from NASA’s “STEREO” satellites to show details about the current status of the sun. Images of the sun in different wavelengths are also presented (Figure 12) and the students are asked to look at each one and compare them. Evidence of sunspots and flare activity can be observed. There is also a gallery of images that highlight past solar activity. This allows the students another insight into astronomical methods and techniques (Figure 13).



Figure 11. “3D Sun” app.

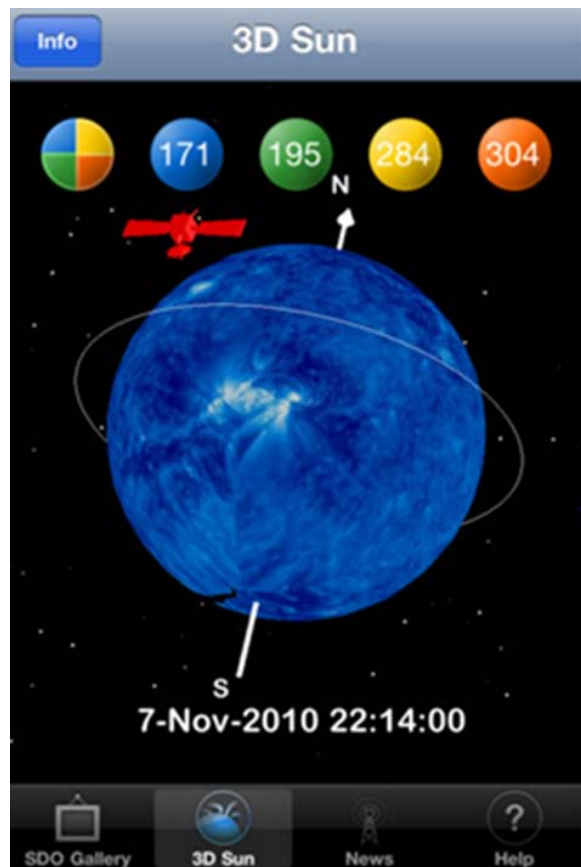


Figure 12. The Sun in different wavelengths.

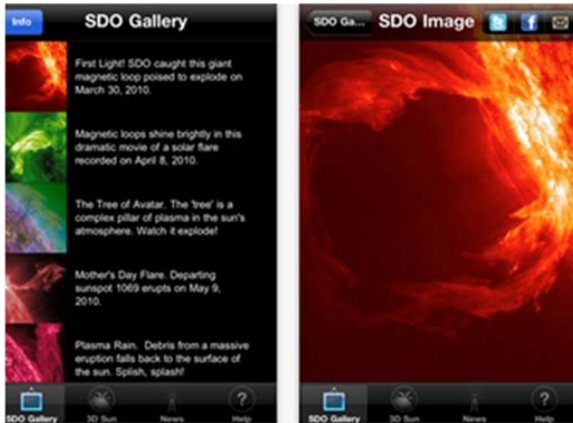


Figure 13. Gallery of solar images.

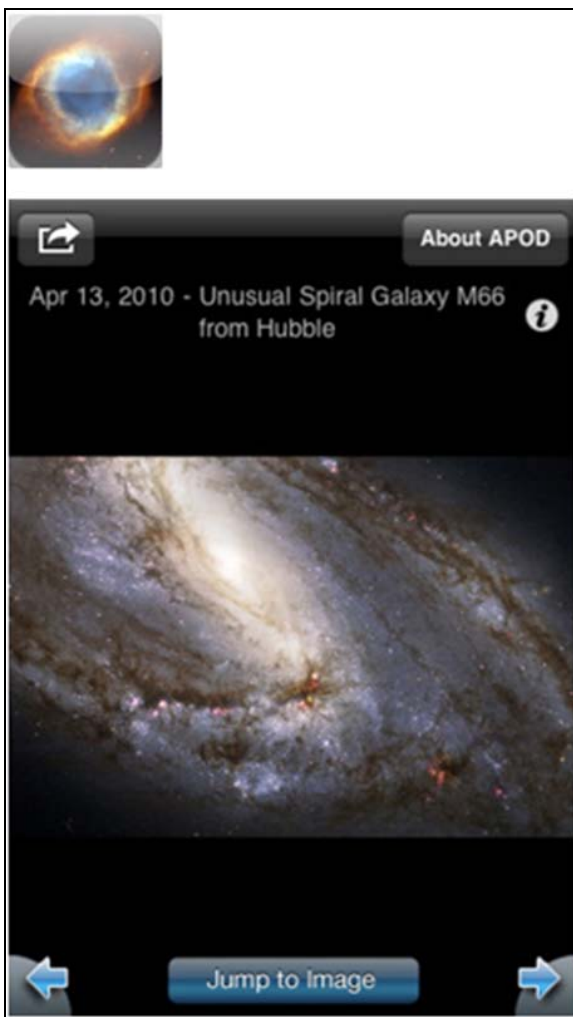


Figure 14, "APOD" app image.

Last but not least, the "APOD" app (Figure 14) Astronomy Picture of the Day was added for a bit of fun. This app is presented by NASA and displays amazing images from all areas in astronomy. A new

image appears every day with a detailed explanation. Within the explanation are hyperlinks to terms and other related information. All the old images are archived and accessible as well. We not only get pretty pictures but a good educational reference.

3. Results

The activities were completed by approximately one-third of the astronomy class and were well received. Questionnaires were completed by each student attempting the activities (39 participated in these activities) and have been analyzed in an attempt to validate the project. Keep in mind that these students are non-science majors and have little to no background in astronomy and observational methods or techniques.

The following questions were asked of the students:

1. How likely are you to use a small telescope again if you have the opportunity? Why or why not?
2. If so, will you bring an iPad or iPhone along (or similar device) if you have one? Why or why not?
3. There are many variants of astronomy apps out there, and the list is growing.
4. Please comment on any that you have used (if any) that were not included in these observational exercises. Is there one that is similar to the ones that we use here that you prefer? If so, why? You may comment on any significant differences and make recommendations (if you have any).

79% of the students indicated that they would definitely like to use a telescope again. 21% indicated that they would not; however, 63% of those, noted problems with locating objects with the small telescope and would have liked the use a larger one. The Celestron Firstscope is very small and does not have setting circles, an adequate finder scope or a go-to system for positioning. 8% of the students said they used another telescope (belonging to a relative or friend). Interestingly, 8% indicated that they were going to buy a telescope for future observations.

92% of the students indicated that they liked using the iPad with the activities. They enjoyed pointing it at the sky to locate objects. 8% indicated that it was not helpful. It was found that a majority of those who disliked the iPad activities had problems with the telescope.

The students were asked if they would look at other astronomical apps in the future if they had access to an iPad. 41% said yes and 41% said no they wouldn't but didn't give a reason why. 18% didn't respond on this question. It is possible that the response to this question may have resulted from the students misunderstanding what was really asked.

4. Conclusion

These telescope and iPad activities were considered successful after reviewing the initial semester trial data. The majority of the students liked the activities and found them useful. They particularly enjoyed pointing the iPad at the sky and identifying what it was pointed at. Problems operating the small telescope contributed to some student's comments.

Minor modifications are planned for the activities instructions and the questionnaire to eliminate possible confusion in the future. We may be able to eliminate some of the problems the student's had with the telescope. Purchasing more iPads and telescopes would also increase the availability of the equipment for more student participation.

It is often difficult to stimulate a GE student's interest in subject matter that they may not have an interest in. It was refreshing to see the non-science major student response to the use of these technologies, especially those few who stated they were going to buy their own telescopes.

We also realized that regular structured astronomy laboratory class exercises could benefit from the integration of the iPad telescope applications.

The reasonable cost of the iPad apps makes it easy to afford. Most of the apps used in the activities were free. The remaining apps cost is reasonable, between \$5 and \$40. Additional apps may be utilized in the future.

Integrating astronomy apps into teaching activities should increase drastically in the future. To assist faculty with the many possibilities for student activities, catalogs of astronomy apps have already been published, *Franknoi*.

A copy of the activities is available upon request from the authors.

5. Acknowledgements

We would like to thank the Physics Department for funding the purchase of the telescopes and the iPads and Colin McDonnell, Instructional Technology, for his preparation and maintenance of the iPads and their apps.

6. References

Franknoi, A. (2011). "Astronomy Apps for Mobile Devices, a First Catalog." *Astronomy Education Review* **10**, 010302-1, 10.3847/AER2011036

6.1 Apps / Equipment

3D Sun

Dr. Tony Phillips, LLC

<http://itunes.apple.com/us/app/3d-sun/id347089078?mt=8>

Apple iPad

http://store.apple.com/us/browse/home/shop_ipad/family/iPad?afid=p219/GOUS&cid=AOS-US-KWG-BOPIS

Apple iTunes

www.apple.com/itunes

Astronomy Picture of the Day

Concentric Sky

<http://itunes.apple.com/us/app/astronomy-picture-of-the-day/id304006512?mt=8>

Celestron Firstlight Telescope

Celestron, LLC. , 2835 Columbia St. Torrance, CA

GoSkyWatch Planetarium,

GoSoftWorks

<http://itunes.apple.com/us/app/goskywatch-planetarium-for/id364209241?mt=8>

Messier List

Scot Spencer

<http://itunes.apple.com/us/app/messier-list/id364899443?mt=8>

Moon Globe

Midnight Martian

<http://itunes.apple.com/us/app/moon-globe/id333180321?mt=8>

S&T SkyWeek

Sky & Telescope Media, LLC

<http://itunes.apple.com/us/app/s-t-skyweek/id398252674?mt=8>

The Rotational Period of the Sun Using the Doppler Shift of the Hydrogen alpha Spectral Line

Robert M. Gill
 California State University, San Marcos, Physics Department
 Merritt Observatory
 5034 Hill Ranch Dr. Fallbrook, CA 92028
 rgill@csusm.edu

Abstract

The fact that the sun rotates is obvious by observing the daily motion of sunspots. The overall sunspot movement to the west is a result of this solar rotation. However, solar rotation can also be determined by observing the solar spectrum at the solar limbs. The absorption lines in the spectrum will display a Doppler shift since the east limb is coming toward the observer and the west limb is moving away. The velocity of the limb, relative to the observer, can be determined from these spectral line shifts. Knowing the solar radius, the rotational period can be calculated.

1. Introduction

The observation of sunspots demonstrates solar rotation. The overall sunspot movement to the west is a result of this solar rotation. Galileo calculated the sun's rotational period in 1610 using these observations.

The utilization of high resolution spectroscopic analysis employing small aperture telescopes (0.35m) can also be used to measure the sun's rotational period.

The rotational velocity can be calculated by using the observed Doppler Effect. Observations of the Hydrogen α absorption line at the limb shows a small spectral shift to shorter wavelengths as the east limb is coming toward the observer and to longer wavelengths as the west limb is moving away. Comparing these wavelength differentials from the laboratory standard of the $H\alpha$ line, the rotational velocity can be calculated. Knowing the solar radius and the rotational velocity, the rotational period can be calculated.

2. Observations, Measurements and Calculations

Hydrogen absorption spectral lines are quite obvious in both low and high resolution images of the solar spectra and can be measured quite easily using available computer software programs (Figure 1).

High resolution spectra of the sun's $H\alpha$ absorption line were obtained using the Merritt Observatory 0.35m Schmidt Casagrain telescope and the Merritt Spectrograph. Spectra were taken on the eastern and western limb of the sun (Figure 2).

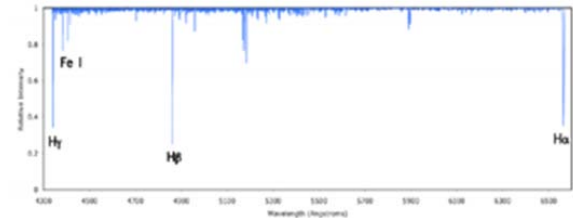


Figure 1. Low resolution solar spectra showing hydrogen alpha absorption lines (McMath-Pierce Solar Observatory).



Figure 2. High resolution $H\alpha$ absorption line.

The spectra were profiled for analysis using *RSpec Real Time Spectroscopy* software (Figure 3). The $H\alpha$ absorption line wavelength was determined after the spectra was calibrated using a neon standard (Figure 4).



Figure 3. Profiled spectra.

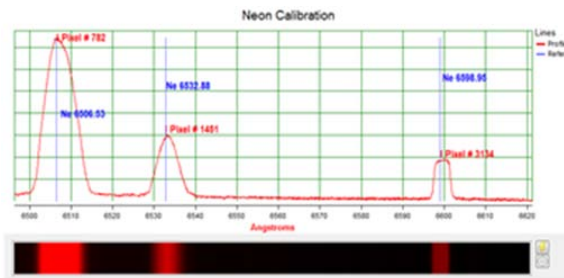


Figure 4. Neon calibration spectra.

From the profiled spectra above, H α wavelength values were obtained:

$$\begin{aligned} \text{H}\alpha \text{ eastern limb} &= 6562.757 \pm 0.005 \text{ \AA} \\ \text{H}\alpha \text{ western limb} &= 6562.837 \pm 0.005 \text{ \AA} \\ \text{H}\alpha \text{ lab standard} &= 6562.797 \pm 0.001 \text{ \AA} \end{aligned}$$

Calculating the rotational velocity using:

$$C = 2.99792458 \times 10^8 \text{ ms}^{-1}$$

and

$$V_{\text{rot}} = \frac{\lambda - \lambda_0}{\lambda_0} C = 1999.9 \text{ ms}^{-1}$$

Calculating the rotational velocity error using:

$$V_{\text{rot}} \text{ published} = 7.189 \times 10^6 \text{ ms}^{-1}$$

then

$$\text{Error, } V_{\text{rot}} = 2.99 \text{ ms}^{-1}$$

Calculating the rotational period using:

$$R_s = 6.955 \times 10^8 \text{ m}$$

and

$$T_{\text{rot}} = \frac{2\pi R_s}{V_{\text{rot}}} = 25.3 \text{ days}$$

Calculating the rotational period error using:

$$T_{\text{rot}} \text{ published} = 25.05 \text{ days}$$

then

$$\text{Error, } T_{\text{rot}} = 0.25 \text{ days}$$

3. Results

The values calculated apply to the equatorial region of the Sun; the rotational angular velocity varies across the surface of the Sun from the equator to the poles. This is referred to as differential rotation.

At the equator the solar rotation period is 25.05 days. This is the sidereal rotation period (Figure 5), and should not be confused with the synodic rotation period of 26.91 days; which is the time for a fixed feature on the Sun to rotate to the same apparent position as viewed from Earth. The synodic period is longer because the Sun must rotate for a sidereal period plus an extra amount due to the orbital motion of the Earth around the Sun.

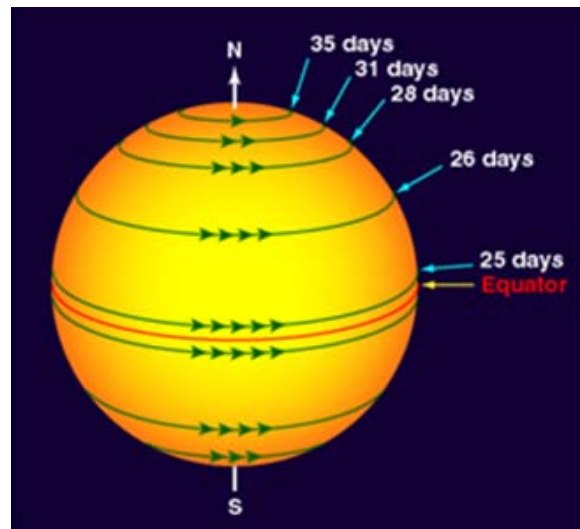


Figure 5. Differential solar sidereal rotation.

4. Conclusion

Significant assumptions have been made when measuring the solar spectral lines. Physical effects such as temperature, pressure, elemental abundance, density and surface gravity have been ignored. These properties affect the width and the height as well as the shape and position of the spectral lines.

Considering that these assumptions and constraints would drastically complicate this exercise, they have been excluded. This technique yields a satisfactory value for the rotational period of the sun considering that the Doppler shifts obtained were at the limits of the resolution of the Merritt Spectrograph. This technique and apparatus can be used as in a simple laboratory exercise for physics and astronomy classes demonstrating the methods and techniques utilized by astronomers.

5. Acknowledgements

I would like to thank Michael Burin, *CSUSM Physics Department*, for his insight and willingness to utilize this exercise in his astronomy laboratory class.

6. References

Gill, R. M. (2011). "Construction of an Inexpensive High Resolution Littrow Spectrograph for Be Star H Alpha Analysis." in *Proceedings of the 30th Annual Symposium on Telescope Science* (Warner et al., eds.). Society for Astronomical Sciences, Rancho Cucamonga, CA.

RSpec. Real time spectroscopy.
<http://www.rspec-astro.com/>

Fast Spectrometer Construction and Testing

John Menke
22500 Old Hundred Rd
Barnesville, MD 20838
john@menkescientific.com

Abstract

This paper describes the construction and operation of a medium resolution spectrometer used in the visual wavelength range. It is homebuilt, but has built in guiding and calibration, is fully remote operable, and operates at a resolution $R=3000$. It features a fast $f3.5$ system, which allows it to be used with a fast telescope (18 inch $f3.5$) with no Barlow or other optical matching devices.

1. Background

Five years ago I completed an 18inch $f3.5$ Newtonian for use primarily in asteroid and stellar photometry as described in

<http://menkescientific.com/18inchescope.pdf>.

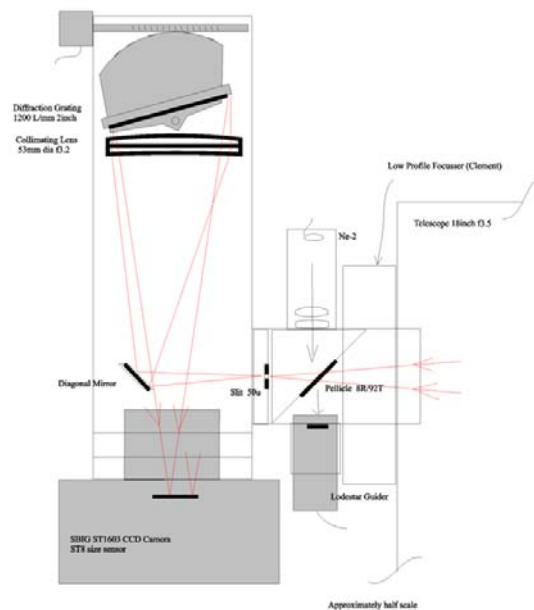
Soon after, I obtained an SBIG DSS7 low resolution $R = 100$ (5A) spectrometer. While the DSS7 is capable of very good work, one of the difficulties of using the DSS7 with the Newtonian was that it is an $f10$ instrument, thus requiring use of a $2.7x$ Barlow.

After several years, I saw the benefits of an instrument with increased resolution. The goals for the instrument design would be

- Native operation at $f3.5$, ie., no Barlow needed.
- Resolution $R=2-3000$ (approximately $2A$)
- High Stability to allow precise wavelength measurements and tracking
- Self Guiding in a closed loop
- Full remote operation
- Integral calibration source
- Inexpensive
- Reasonable weight and with good balance
- Construction using basic machine shop practices
- Operable with almost any CCD camera

2. Spectrometer Design

Figure 1 shows the overall spectrometer layout roughly to scale. The figure shows the optical elements and surfaces as heavy black.



Fast Spectrometer $f3.5$ $R=3000$

Figure 1.

The biggest design challenge was to accommodate the fast f -ratio. The problem is not so much the optics, as it is that such a fast converging light beam from the telescope allows very little space for optical elements once it leaves the telescope and before it enters the slit. While one could build a spectrometer into the telescope, this would make instrument changeover very cumbersome. After considering a variety of designs, I settled on my own version of a Littrow design (in which the light from the grating reflects back at approximately the entering angle) that appeared to meet the design goals.

2.1 Focuser

A key element in the design is the focuser itself. The focuser is an early Clement design featuring a highly constrained and stiff kinematic design that is only 1inch high at minimum and 4inches high fully extended. As manufactured, the focuser uses an **external** 4inch high post and screw to vary the focus with virtually no backlash. While the mechanism works extremely well, its placement interfered with mounting a spectrometer. To correct this, I modified the focuser drive by making a new adjusting screw which projects *into* the telescope (rather than external), and indeed, I also mounted the remote controlled (RoboFocus) stepping motor inside (powered off except when changing focus). The focuser surface is now completely clear.

2.2 Guider

The telescope must be actively guided to keep the star on the slit. The telescope is approximately 1 a-s/pixel, and the slit opening at 50u would be about 5.5 pixels wide. After examining alternatives, I chose a partially reflecting pickoff mirror in the optical path. This is a simple system to build and allows the guider camera potentially to see a large field. I used a 8% reflection, 92% transmission pellicle (super thin mirror) for the optical element. This is mounted on a PVC carrier installed in the inlet 2inch tubing. The guide camera is a Starlight Express Lodestar camera, uncooled, no shutter, 8.5u pixels (closely matching the 9u pixels of the imaging camera). In practice, it has no trouble guiding on mag12 stars using 5 sec exposures.

2.3 Calibrator

I also built a simple neon calibrator that uses the *rear* of the pellicle mirror to reflect light into the slit. The Ne-2 neon bulb is driven by a 12VDC to 120VAC converter (remote controlled). Its light passes through several small diffusing sheets to create a reasonable area source, then through a lens that focuses at about f3-f4 off the back of the pellicle into the slit.

2.4 Slit

The slit is a 50u 3mm high air (not glass) slit mounted in a PVC carrier in the inlet tube. The star image from the telescope is approximately 2.5a-s FWHM, which translates to about 25u. Thus, a 50u slit allows virtually all of a reasonably well focused

star to enter the spectrometer, while allowing for some pointing and guiding error.

2.5 Spectrometer Body

The spectrometer is built of 1/8in aluminum round and square tubing. The elliptical flat reflecting mirror for the incoming light from the slit is mounted on a simple section of aluminum angle and is adjusted by hand to that it picks up all the incoming light while sufficiently offset to allow the light from the grating to miss it on the way to the camera.

The light from the slit diverges toward the collimating lens. This is a simple achromat of 55mm dia and 170mm focal length mounted on a simple PVC holder that can slide along the long axis of the spectrometer. Adjustment screws allow the lens carrier to be tilted and turned approximately 3deg. The light passes through the collimating lens as a parallel beam. It then reflects off the grating (1200L/mm, 2inch square, blazed for 5000A), converges back through the collimating lens, bypasses the elliptical flat, and enters the main camera (which is on axis). The camera (I use an ST1603 w/ST8 size sensor) is mounted to the spectrometer body using a machined block of PVC.

Returning to the grating, it is attached to 1/8in aluminum plate (using a relatively soft 5 minute epoxy), which in turn is mounted on a piece of aluminum angle with three sets of push/pull screws. This allows the user to tilt the grating and to tightly lock the setting. The aluminum angle containing the grating is mounted on a home-cut sector of worm wheel that is pivoted under the center front surface of the grating. The worm wheel was made from 1/4 in. aluminum plate held in a jig while a small lathe drove a hand tap to cut the teeth. The wheel is turned by a small stepper motor driving a length of 1/4-20 threaded rod acting as the worm. The system allows easy shift of the wavelength band, is stable in a given position, and has fairly small, easy to compensate backlash. The section of worm wheel was trimmed to allow the grating to be turned square to the light beam (ie, as a simple reflector in Order Zero) as well as to turn far enough to reach the beginning of second order.

A serial controlled RoboFocus controller drives the stepping motor to the desired center wavelength for the spectral region of interest as predetermined using the neon calibrator. The controller incorporates anti-backlash logic so that all moves finish in the same direction. The controller also controls remote operation of the neon calibrator.

3. Setting Up the Spectrometer

Setting up the instrument requires establishing the positions and orientations of the optical elements appropriately. I used several simple devices in the alignment and testing process including the neon calibrator and other light sources, plus a variety of cheap red lasers for ray tracing to assure proper component orientations.

Once a good spectrum is obtained, one can use the neon calibrator to measure the calibration and dispersion in A/pixels. For this, one has to identify a series of lines unambiguously. This does take some practice, using frequent reference to web sites, e.g.,

<http://astro.u-trasbg.fr/~koppen/discharge/index.html>

and various tables of emission lines. A sodium flame provides the D lines at 5889 and 5895 which helps verify operation of the spectrometer (this spectrometer will easily split these two lines).

Finally, one has a choice of alignment of the spectrograph—will the slit be E-W or N-S on the sky? For several reasons, I prefer E-W so that variations in clock drive move the star along the slit, rather than off the slit.

4. Initial Targeting in the Field

The problem of getting the target star onto the slit the first time may appear intimidating because the user cannot image the target star and slit at the same time. However, the process is in fact quite easy if one follows a step by step approach that is detailed in the article on our website. Subsequent aiming and focus verification typically takes 2-5 minutes at the beginning of an observing session.

5. Conclusion

This project has been fun and satisfying, and has resulted in a fully usable instrument that can easily track below mag12 and take good spectra to about mag8. The cost was about \$500 for materials, and required about 150 hours of work (of course, a second one would be much faster to build and debug). The spectrometer met or exceeded all the goals, and will be used to supplement the DSS7 spectroscopy at our observatory.

A much more detailed version of this paper with photos is on www.menkescientific.com/John'sPage.

ADILS: An Amateur Dual Imaging Littrow Spectrograph

Wayne Green

Boulder Astronomy and Space Society, Boulder, CO
dxwayne@gmail.com

ADILS An Amateur Dual Imaging Littrow Spectrograph

Wayne Green
Boulder Astronomy and Space Society, Boulder Colorado



Goals

- Demonstrate design and prototyping of a complex spectrograph
- Two views of a single spectrum dispersion axis: red and blue
- Simultaneous red/blue image with a single exposure
- Uses include: astrophysical line ratios; $H\alpha/H\beta$ column density and, SNe classification
- f ratio adaptable, $f/15$ to $f/4.8$ instruments
- Platescale adaptable, and
- Light weight with management of center of mass

Design

- ADILS has three main blocks: re-imaging, littrow spectrograph and dual band selection blocks.
- Pre-slit re-imaging to manage platescale of object
- Small slit capability only
- Dichroic mirror for red/blue separation and managing order overlap
- Low cost 3000 /cm order 1 grating, and 6000 /cm order 2 grating to match resolution and exposure time to instrument, and
- Band selection mechanism with optical path-length management
- ADILS images with a single camera. Long slit spectroscopy possible by altering the dual band selection block and adding a second camera
- ADILS does not require special handling for spectra reductions

System Overview

The 500 nm focal length of ADILS makes for 0.07λ per μm at the focal plane, or $0.54 \mu\text{m}$ per $9 \mu\text{m}$ pixel. However, the slit image is 1:1 with the littrow design so a $25 \mu\text{m}$ slit spans 3 pixels.

Seeing and focal length conspire to make point sources at the telescope's focal plane larger than practical slit diameters. So focal plane image re-imaging is required to match the slit diameter. Astronomical objects with small sizes are minimal in spectroscopy.

Airy Disc: perfect seeing – Rayleigh resolution (in radians)

$$\theta = 1.22 \frac{\lambda}{D} \times F \tag{1}$$

$$= 1.22 \frac{5 \times 10^{-5}}{25 \text{ cm}} = 2.44 \times 10^{-5} \times 2,500,000 \mu\text{m} = 6.1 \mu\text{m} \quad 25\text{cm } 2.5\text{m FL}$$

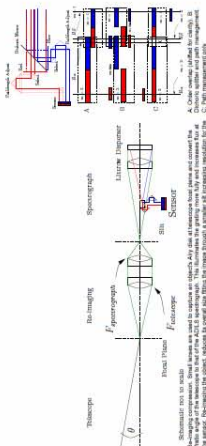
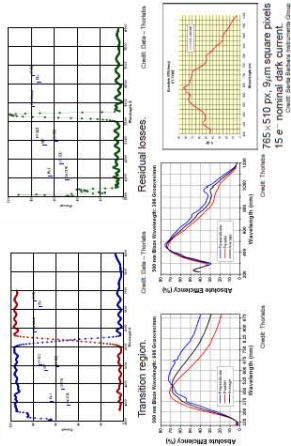
$$= 1.22 \frac{5 \times 10^{-5}}{61 \text{ cm}} = 1 \times 10^{-5} \times 4,800,000 \mu\text{m} = 4.8 \mu\text{m} \quad 60\text{cm } 4.8\text{m FL}$$

$$= 1.22 \frac{5 \times 10^{-5}}{122 \text{ cm}} = 1.22 \times 10^{-5} \times 16,459,200 \mu\text{m} = 8.23 \mu\text{m} \quad 122\text{cm } 16.4\text{m FL}$$

Perfect resolution is well within the pixel sizes for telescopes in the amateur range.

Beam Separation and Optical Path Management

Dichroic mirror transition above $0.01 \mu\text{m}$, 4363.2, 4958.9, 5005.8 Å.

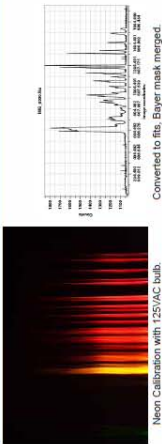


The dichroic splitter together with path management, allows selecting two widely separated areas of the dispersion axis. Gratings with lines/cm $\sim 4,500$ exhibit overlap between $m=1$ and $m=2$ orders. Case A shows axis before management where $H\alpha$, $m=1$ is confused with $H\beta$, $m=2$. In case B with dichroic splitter and path management, the orders are separated, allowing exposures at same order (reducing anamorphic distortion). In case C, the confusion persists, but while the sensor may acquire $H\beta$, $m=1$ and $H\alpha$, $m=2$, blaze angle efficiencies and flux, per $\Delta\lambda$, $\Delta\theta$ by order is dramatically different affecting analysis ability.

Analysis Issues

- Field Curvature ($f(r, \theta)$) (r parallel, θ perpendicular to dispersion)
- Vignetting (spectro-photometric calibration)
- Continuum matching over narrow interval (littrow's high dispersion)
- Line Bridging (line wings, bisector symmetry)
- SNR (high dispersion/narrow telescope aperture)
- Pixel size (classing, Nyquist), well depth, QE, and dark current

Prototype Test



Bench Results

- Scale tested with basic alignment using spectratch
- roughly 1 1592 Å over 3472 pixels: $0.458 \text{ \AA} / 6.4 \mu\text{m px}$, $0.072 \text{ \AA} / \mu\text{m}$, and
- 859 Å over 57.7 sensor. Clear need for dual mode

Conclusions

The littrow spectrograph offers higher resolution at the expense of slit-width, flux and line access (one widely separated line per exposure). The ADILS offers the ability to examine lines without order overlap by folding and stacking areas along the dispersion axis separated by more than the width of the sensor. Line ratio analysis often samples widely separated lines ($H\alpha/H\beta$ column density for example).

Higher resolution, as a function of the focal length of the spectrograph, means lower flux not suited to smaller apertures of amateur telescopes. Thus the 8cm f/6.3 optics of ADILS matches amateur instruments well. This instrument is suited as a teaching mechanism for undergraduate observation and instrumentation lab courses.

As mentioned – the author would like to thank the ADS faculty and the staff of the Space Based Astronomy Laboratory at Colorado for their support of BASS. Data and images about the gratings and filter used in the design by permission from Thorlabs, Inc.

High Accuracy RA/Dec Encoders for a ca 1890 GEM

Wayne Green
 Boulder Astronomy and Space Society, Boulder, CO
 dxwayne@gmail.com



High Accuracy RA and Dec Encoders for ca 1890 German Equatorial Mount
 Wayne Green, John Doran
 Denver Astronomical Society, Denver Colorado

Goals

- High precision rapid pointing of telescope manually
- Increase number of objects viewed during public event
- Locate faint objects in light polluted city skies **Special targets, Comets, Novae, Asteroids, Planet Oppositions** and stars purchased from grifters
- Wireless connection to hand held devices
- Display, to public queued at telescope

Historic Chamberlain Observatory, University of Denver, Denver Colorado

First light July 14, 1894 [1]

- 20-inch f/15-Saegmuller GEM Mount with Alvan Clark optics.
- Original right clock-drive replaced with modern drive
- Original RA/Dec brass setting circles viewable with periscopes still in use
- 7.8m focal length for **26.6 arcsec/mm plate scale**
- Electronic encoders added at cost of \$8,000USD in 1990's

Electronics

Control System

- Industry Standard **ABZ quadrature** encoders
- 1-Wire™ temperature sensor (circle's expansion over 1.72 meters and 30K on order 20µm/K/mieler for roughly 1.034µm or 775 arcseconds/1's increments.)
- Processors: Cyclone III FPGA™
- State Machine, structural and VHDL blocks
- Support circuitry to handle buffering and level shifting

Outputs:

- Tricks reported as ARA ADec slew rate
- Encoder alarms for signal strength, and level shifting
- RS-232 DE-9 DCE output (TxRx/Ground), feeding **Orion Wireless Network Bog™** using SkySafari™
- Display via AppleTV™ to dome monitors for public.

System Block Diagram



Sample FPGA Development:



Prototype



FPGA Prototype in Rack (shown with optical encoder attached to motor)

MPU vs. MPU

MPU

- RTOS latency is an issue
- PSOC OS may garbage collect
- Hardware interface limited, bit-banging often employed, but
- Good inter-system communications

FPGA

- Totally asynchronous interface, no lost signals
- Off-the-shelf low cost hardware development platforms
- Excellent no-cost development tools
- Development using schematic capture or VHDL code files
- Extremely fast execution
- VHDL main with rails, integers and arrays
- Commonly employed control-flow tests and operators
- Code extremely close to hardware, and
- Use PSOC for inter-system communications!

Summary and Conclusion

Summary

- Open Hardware and semi-open Software solution
- Simplifies telescope operations, increases useful observing time
- Provides a full STEM™ demonstration for K-12 Students
- Makes 1890's telescope fully usable for today's students

Future

- Add additional linear encoders to tangent arms to track slow motion adjustments
- Add motor controller capabilities for tracking
- Add GoTo to telescope for future.
- DC-Servo motors tied to pinion slew gears
- Reuse/expansion of open-hardware design

Electronics

Control System

- Industry Standard **ABZ quadrature** encoders
- 1-Wire™ temperature sensor (circle's expansion over 1.72 meters and 30K on order 20µm/K/mieler for roughly 1.034µm or 775 arcseconds/1's increments.)
- Processors: Cyclone III FPGA™
- State Machine, structural and VHDL blocks
- Support circuitry to handle buffering and level shifting

Outputs:

- Tricks reported as ARA ADec slew rate
- Encoder alarms for signal strength, and level shifting
- RS-232 DE-9 DCE output (TxRx/Ground), feeding **Orion Wireless Network Bog™** using SkySafari™
- Display via AppleTV™ to dome monitors for public.

Mechanical Overview

Encoder Attachment

- Encoder tape, aggressive adhesive
- Tape will replace chain
- Brackets to accommodate run-out in setting circles
- Tangent Arms (Future)
- Linear encoder best choice
- Movement adds scaled delta to output ticks



Encoder attachment, back connection with hardware blocks



Encoder attachment, front connection with hardware blocks



Dec Encoder



Dec Encoder

System Overview

Old Configuration

- Old DFM system:
- Positive belt (chain) glued to setting circle with cog-wheel follower
- \$50USD encoder with 2048 ticks per rev, total of 26,000 ticks per RA revolution
- same encoder, smaller radius for Dec
- one-off Software Bisque™ BBox with 1,296,000 arcs/circle = **0.175 arcsec/tick** (usual caveats)
- Used to the Sky™ Ver. 5, required vendor special update to Ver. 6.

New Configuration

- Donated unobtrusive COTS Renshaw™ encoders \$2000USD including read heads and 1µmeter tape
- RA radius 10.8 inches for 1,725,604 µm ticks per revolution divided by **1,296,000 arcs/circle = 0.175 arcsec/tick** (usual caveats)
- 661,672µm ticks per revolution divided by 1,296,000 arcs/circle = **1.95 arcsec/tick** (usual caveats)
- Wireless tie to planetarium packages via phones/tablets at telescope tail-stock

Acknowledgments

Special thanks to the University of Denver for their support of public education in astronomy and to the Denver Astronomical Society as DU's current preferred partner in outreach. Together they reach roughly 4,000 people during 12 scheduled events per year.

Thanks to Renshaw plc for donation of encoder read heads, encoder tape, technical support and participation with installation of the equipment.

References:

[1] Claire M. Stencel and Robert E. Stencel, Denver's Great Telescope. Glenn E. Montgomery, pub. 2006.

WWW: <http://TheIAS.org> Joint Meeting: Society for Astronomical Sciences 2012 Symposium and AAVSO Spring Meeting, Big Bear City, CA USA

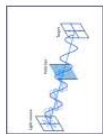
234

A Single Beam Polarimeter

Jerry D. Horne
 jdhorne@hotmail.com

A Single Beam Polarimeter

Jerry D. Horne



Abstract

As Astronomical Polarimetry is an emerging field of study for amateur astronomy, the background, theory, and instrumentation of astronomical polarimetry is reviewed. Additionally, the design and construction of a simple single beam polarimeter is presented, together with the results of its initial calibration.

1. Background:

The birth of Astronomical Polarimetry can be traced to Chandrasekhar in 1946, when he predicted the linear polarization of electron-scattered starlight coming from eclipsing binaries. This prediction was quickly confirmed just three years later, Hiltner (1949) and Hall (1949).

Over the past sixty years, Astronomical polarimetry has progressed from being primarily in the domain of the radio astronomer, to being an integral component of most of the major observatories in the world.

2. Polarized Light from Astronomical Objects

A common explanation for this resultant polarization is that interstellar dust grains are not spherical in shape, so that light is absorbed more along one axis than another, and that the dust grains generally become aligned with a magnetic field. Hence, some percentage of extinction, and in-turn polarization, occurs along a particular direction. (Ponthieu and Lagache, 2004). The known processes of astronomical polarization are: (Moran, 2006)

Process	Cause	Seen in
Extinction	Aligned Dust Grains	Interstellar Polarization
Scattering	Dust	Reflection Nebulae, T-Tauri Stars
Scattering	Rayleigh	Cool Stars
Scattering	Electron	Hot Stellar Envelopes
Scattering	Resonance/Raman Line	Comet, Sun / Synthetic Stars
Emission	Aligned Dust (Thermal)	Molecular Clouds
Emission	Cyclotron/Synchrotron	All Her stars, Blazars, GRBs

3. Polarization theory and the Stokes Parameters

Classically, light can be considered a transverse electromagnetic wave. As such, the wave has X and Y vector components. Unpolarized light exhibits rapidly fluctuating vector components, so no net polarization can be measured. Linearly polarized light has defined components for the X and Y axis that are in phase with each other...

Mathematically, polarized light can be described in terms of the Stokes parameters: I, Q, U & V, where I is the total intensity, Q & U are vectors which describe linear polarization, and V represents circular polarization. Two other important measures are the polarization position angle (PA), and the degree (%) of polarization (P). These two quantities can be derived as:

$$PA = \frac{1}{2} \arctan(U/Q)$$

$$P = \sqrt{(Q^2 + U^2 + V^2)} / I$$

In considering just linear polarization,

$$V = 0,$$

$$P = \sqrt{(Q^2 + U^2)} / I$$

Measurement of these quantities follows from the fact that the total intensity I, is a sum of the orthogonal intensities.

$$I = I_0 + I_90 = I_{45} + I_{135}$$

Where 0, 45, 90, and 135 are different angular orientations of the polarizing filter or analyzer. The Stokes parameters, Q and U are defined as, and in-turn, can then be measured as:

$$Q = I_0 - I_90$$

$$U = I_{45} - I_{135}$$

4. The Single Beam Polarimeter

This type uses a polarizing filter to detect linear polarization. The basic elements, (Figure 1) are the detector and the polarizing filter. The detector is ordinarily a CCD camera. The prime advantage of it is that it is very simple in design and very easy to construct, under \$200

The principle disadvantages of the single beam polarimeter are: (1) The filter only allows one component (U or Q) of the polarization through the filter at a time. For elements are needed (0, 45, 90, and 135 degrees) to complete the polarization data set for one object. (2) The polarizing filter is not sensitive to circular polarization.

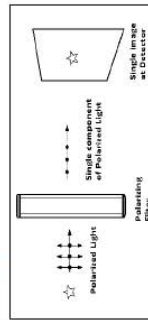


Figure 1: Basic design of a Single Beam Polarimeter

5. The Dual Beam Polarimeter

The dual beam device (Figure 2) utilizes a 1/2 wave retarder plate to allow circular polarization to enter the detector, and also uses a Wollaston prism to split the beam into two orthogonal components, representing the I₀ and I₉₀ intensities (or I₄₅ and I₁₃₅). Allowing simultaneous measurement of both these intensities. A disadvantage is that its construction costs can easily exceed \$3000.

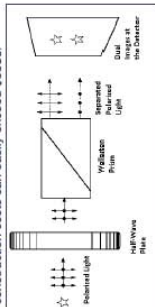


Figure 2: Basic design of a Dual Beam Polarimeter

6. Construction of a Single Beam Polarimeter

This device can be constructed from a few readily available and/or obtainable parts. The detector should be a quality CCD camera. The polarizing filter can be obtained from multiple telescope and optics sources, but is generally inexpensive.

A key part of the system is a goniometer, which is an instrument that allows the polarizing filter to be rotated to a precise angular position. Thor Labs, in Newton, NJ, has a number of gaged rotation mounts (for ~\$100) that fit a 1.25 inch polarizing filter. Polarimeter also involves the use of photometric filters, primarily B and V. Finally, some sort of metal housing or framework is required to assemble and hold all of the components into a rigid structure. A few spare CCD adapter/connectors are quite useful for this purpose. A drawing of a working prototype is seen in Figure 3.

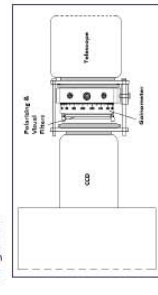


Figure 3: A Single Beam Polarimeter Prototype

7. Data Gathering and Calibration

Since polarimetry measures the differences in intensity between different settings of the polarizing, the same principles of high precision photometry apply to polarimetry. The object should be centered in the CCD fov, to minimize effects of filter rotation. Multiple images at each rotation angle should be obtained.

Calibration is made using polarization standards and null standard stars, for example Sierkowski et al. (1975) and Hsu & Breger (1982). Polarization values of these stars range from 1% to 6%, and have a range of polarization angle values. Null standards exhibit no polarization. Calibration results for the single beam polarimeter are presented in Figures 4 and 5.

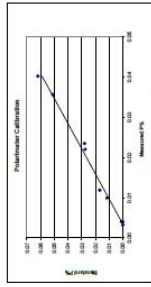


Figure 4: Measured vs Standard Polarization %, for the Single Beam Polarimeter

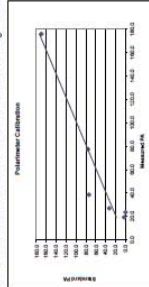


Figure 5: Measured vs Standard Polarization Angle for the Single Beam Polarimeter

The calibration of the polarimeter is quite good for the polarization percentage, but there is some scatter in the current polarization angle calibration. The instrument has a polarization bias of approximately 0.4%, with that same degree of measurement uncertainty.

8. References

- Chandrasekhar, S., 1949, *Astrophys. J.*, 103, 165
- Hall, J.S., *Science*, 1949, 109, 166
- Hiltner, W.A., *Science*, 1949, 109, 65
- Hsu, J.-C. & Breger, M., 1982, *ApJ*, 262, 732
- Moran, J., 2006, University of North Carolina at Chapel Hill, 7
- Ponthieu, N., Lagache, G., 2004, *Dust Polarization*, <http://hir.planck.fr/article263.html>
- Sierkowski, K., Mathewson, D. S., & Ford, V. L., 1975, *ApJ*, 196, 261

